

BULGARIAN CHEMICAL COMMUNICATIONS

2021

Volume 53 / Number 2

*Journal of the Chemical Institutes
of the Bulgarian Academy of Sciences
and of the Union of Chemists in Bulgaria*

Evaluation of sonocatalytic degradation of phenol in the presence of zirconium oxide and cerium oxide nanocatalysts

F. Ghasemi¹, A. Naghizadeh^{1,2*}, G. A. M. Ali^{3,4}, V. K. Gupta^{5*}, Shilpi Agarwal⁵, B. Mansouri²

¹ Department of Environmental Health Engineering, Faculty of Health, Birjand University of Medical Science, Birjand, Iran

² Medical Toxicology and Drug Abuse Research Center (MTDRC), Birjand University of Medical Sciences, Birjand, Iran

³ Chemistry Department, Faculty of Science, Al-Azhar University, Assiut 71524, Egypt

⁴ The Smart Materials Research Institute, Southern Federal University, Sladkova Str. 178/24, Rostov-on-Don, Russian Federation

⁵ Department of Biological Sciences, Faculty of Science, King Abdulaziz University, Jeddah, Saudi Arabia

Received: January 27, 2020; Revised: December 17, 2020

This study investigates the phenol sonocatalytic decomposition in the presence of zirconium oxide and cerium oxide nanoparticles. Different parameters, such as contact time, pH, phenol density, catalyst dose, and temperature on phenol degradation, were investigated. All experiments were performed at ultrasound frequency of 37 kHz. The results show that the maximum degradation of phenol in the presence of zirconium oxide and cerium oxide nanocatalysts was 23.64 and 19.01%, respectively. The optimum conditions were: phenol concentration 10 mg/L, time 30 min, pH 3, catalyst dosages 0.4 g/L, and temperature 30 °C. The findings recommend using both zirconium and cerium oxides as nanocatalysts for phenolic compounds degradation.

Keywords: Phenol, Zirconium oxide, Cerium oxide, Sonocatalysis.

INTRODUCTION

Water contamination with aromatic compounds such as dyes and phenols and their derivatives with a long half-life are sustainable in the environment and supposed to be a potential danger for humans and the environment [1-4]. These compounds exist in industrial wastes and are the main source of water pollution [5-8]. Phenol and its derivatives enter surface waters naturally through plants and algae decomposition and non-naturally through industrial wastewaters [9-11]. Phenol major pollutant sources include color manufacturing industries in a water environment, production of pesticides, gasoline, steel, oil and petrochemicals, leather, detergents, synthetic textiles, electronics, glass, explosives, cosmetics, and medical preparations [12-14]. Phenol compounds are considered priority pollutants due to their toxicity to the organism [15-17]. These compounds at low concentrations in drinking water can cause taste and odor changes [18]. In addition, they are toxic to aquatic plants and human life. Phenol and its derivatives are potentially carcinogenic. Swallowing phenols at a 10 to 240 mg/L concentration for a long time can cause mouth inflammation, diarrhea, dark urine, and visual problems. Toxic phenol concentration in blood is approximately in the range of 4.7 to 130 mg/L [19]. Exposure to excessive phenol can affect the brain,

gastrointestinal system, eyes, heart, liver, lung, skin, kidney, and pancreas [20]. According to the World Health Organization recommendation, an acceptable concentration of phenol in drinking water is 1 µg/L [21]. The United States environmental protection agency determined allowable phenol levels in industrial wastewater discharged into the rivers as less than 0.1 mg/L [22].

Different methods were proposed for phenol removal, such as oxidation, photocatalytic degradation, biodegradation, chemical coagulation, solvent extraction, burning, reverse osmosis, microfiltration, ultrasonic irradiation, ozonation, and absorption [5, 14, 18, 23-30]. Nevertheless, these methods are increasingly limited due to the high cost. Moreover, such methods are non-destructive because they just transfer the organic compound from water to another phase, thus easily making secondary pollutions [31]. Using new approaches based on ultrasound waves with advanced oxidation processes is remarkable [32, 33]. Soundwave may have more advantages against other advanced practical treatment methods because of the accelerating decomposition of organic compounds that resist water. Practical advanced treatment methods need chemical materials and input energy to achieve an acceptable level for decomposition [34]. In the present method, under ultrasound wave performance, vapors and trapped gas in a liquid,

* To whom all correspondence should be sent:
E-mail: al.naghizadeh@yahoo.com
vinodfcy@gmail.com

created by cavitation phenomena and through very high temperature, organic pollutants instantly decomposed directly or indirectly using hydroxyl radicals within collapsing cavitation bubbles [21, 35-37].

However, organic pollutants decomposition using ultrasound usually needs high energy and high reaction time [38]. To overcome this problem, the sonocatalytic destruction process was extended [39, 40]. The sonocatalytic method has high safety, simplicity, and efficiency [41]. The nanoparticles used in this study are zirconium oxide (ZrO₂) and cerium oxide (CeO₂). ZrO₂ nanoparticles are used as a catalyst because of their low price, non-toxicity, high chemical stability, hydrophilicity, catalyst activity, etc. [23, 42]. CeO₂ is another effective catalyst for organic materials oxidation, such as phenol and cyclohexane [43]. Several studies about phenol removal were conducted through sonocatalysis, but there is no publication related to phenol removal by sonocatalysis in the presence of CeO₂ and ZrO₂. Therefore, this study investigates the efficiency of CeO₂ and ZrO₂ nanoparticles as catalysts for phenol degradation through the sonocatalytic method.

MATERIAL AND METHOD

This practical study was performed experimentally on a laboratory scale. In this work, ZrO₂ and CeO₂ with 99.95 and 99.97% purity, respectively, were used as catalysts. At first, a stock solution (500 mg/L) was prepared by dissolving 0.5 g of phenol in 1000 mL of distilled water. The phenol removal experiments were performed in the presence of nanoparticles of ZrO₂ and CeO₂ in Erlenmeyer flasks. The used frequency was 37 kHz, and the studied pH values were in the range of 2-11. After finding the optimal pH, the optimal dose of the catalyst was determined. Five dosages of catalyst (0.1, 0.2, 0.3, 0.4, 0.5 g/L) were examined. After determining the optimal pH and catalyst dosage, contact time (10, 20, 30, 40, 50 min) and initial phenol concentration (10, 20, 30, 40, 50 mg/L) were optimized. Finally, the experiments were performed at different temperatures (20, 30, 40, 50, and 60 °C), and the optimal temperature was found. In the different stages of research, phenol concentration was determined on a spectrophotometer at a wavelength of 500 nm. The structure and morphology of ZrO₂ and CeO₂ nanocatalysts were characterized using X-ray diffraction (XRD) and scanning electron microscopy (SEM).

RESULTS AND DISCUSSION

ZrO₂ and CeO₂ nanocatalysts characterization

XRD patterns and SEM images of ZrO₂ and CeO₂ nanoparticles are shown in Figs. 1 and 2, respectively.

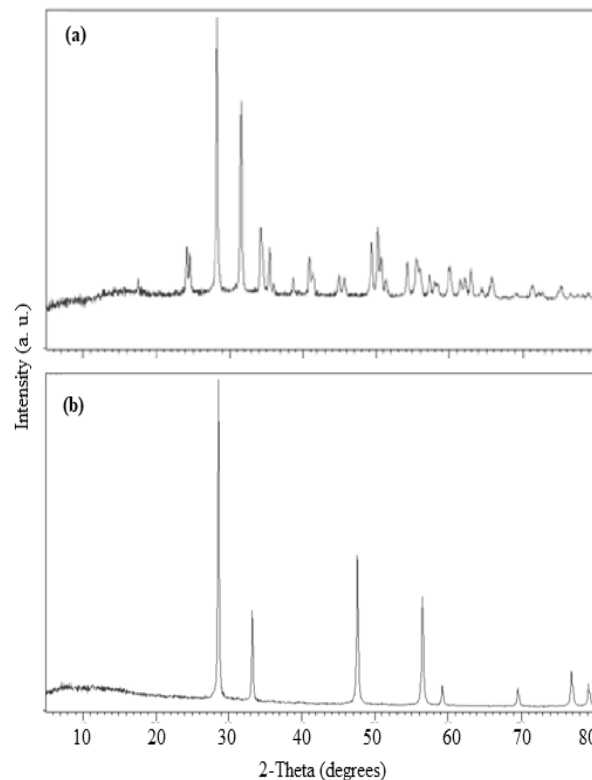


Fig. 1. X-ray diffraction patterns for ZrO₂ (a) and CeO₂ (b).

XRD is a technique that is used widely for determining structural specifications. SEM is used for investigating surface specifications and nanoparticle shape. In the two patterns, the number of peaks and the number of diffraction angles are different which shows a unique and completely different crystalline structure. ZrO₂ and CeO₂ XRD patterns are shown in Figs. 1a and 1b, respectively. Peaks related to ZrO₂ are located at 24.14, 28.27, 31.56, 34.25, 34.50, 40.83, 49.34 and 50.21°. For CeO₂, the peaks are located at 28.64, 33.17, 47.56, 56.41, 59.16, 69.49, 76.73, and 79.15°, which shows the tetragonal and cubic property of these nanoparticles [23, 44, 45]. Data on particle size (Ps), obtained based on peaks width, show that ZrO₂ size is smaller than that of CeO₂ (38 and 46 nm for ZrO₂ and CeO₂, respectively) using the Scherrer equation ($P_s = k\lambda / \beta \cos\theta$, where $k = 0.9$, λ is the Cu-target wavelength, β is the full-width at half-maximum of the diffraction peak, and θ is the diffraction angle [46-48]).

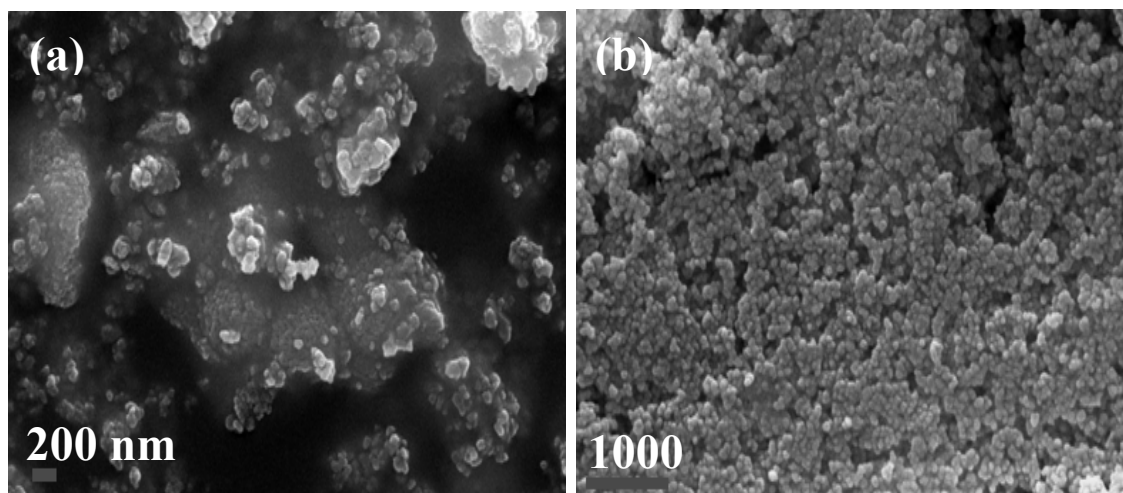


Fig. 2. SEM images of ZrO₂ (a) and CeO₂ (b).

CeO₂ nanoparticles are light yellow, of spherical shape, and the density is equal to 7.132 g/cm³, while ZrO₂ nanoparticles are white, of approximately spherical shape with a density of 5.890 g/cm³, as can be seen from Fig. 2. The smaller spherical particles of ZrO₂ (Fig. 2a) are widely distributed, providing a larger amount of active centers.

Effect of pH on phenol degradation by sonocatalytic process

In this study, the amount of phenol removal in the pH range from 2 to 11 was investigated in the presence of ZrO₂ and CeO₂ nanoparticles. As displayed in Fig. 3, the maximum amount of phenol removal by a sonocatalytic process using ultrasound (US) only and in the presence of ZrO₂ and CeO₂ is at pH 3. The removal ratio was 14.6, 13.73, and 0.38% using ZrO₂, CeO₂, and US, respectively. pH has an essential effect on phenol destruction.

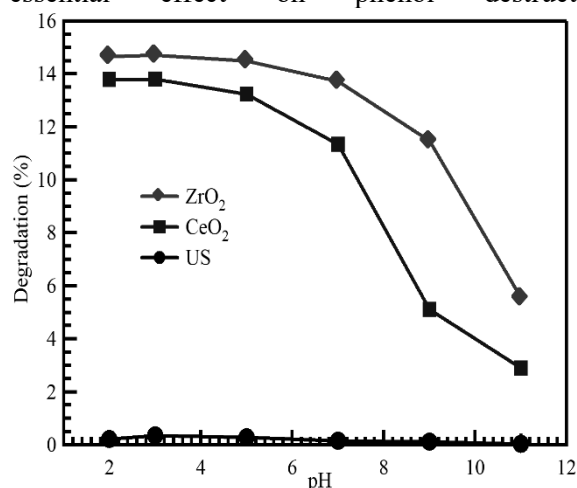


Fig. 3. pH effect on phenol removal by nanocatalytic process in the presence of ZrO₂ and CeO₂ nanoparticles.

Phenol adsorption and catalyst surface charge will vary with changes in the pH value. This factor affects the interpretation of removing pollutants through the sonocatalytic method because of different functions of surface ionization, hydroxyl radical formation, particle aggregation, and pollutant specifications, which can affect catalyst adsorption and congestion [49]. It is known that the degradation reactions can be accelerated under acidic conditions while under strongly alkaline conditions; due to the repulsion force from the negatively charged surface, phenol anions in aqueous solution are mainly degraded through radical (OH) oxidation, which is a slow-motion degradation process [5]. When catalysts are released in the water environment, they have a tendency to accumulate, which leads to an increase in catalyst dispersion in the acidic environment due to the repulsion between catalyst surfaces. Also, in an acidic environment, hydroxyl radical production increases, which leads to stronger decomposition of the nanocatalysts [50]. In alkaline conditions, the generated phenol ions are concentrated between water and gas and cannot enter the cavitation bubbles, and they react with OH radicals outside the cavitation bubbles; hence the rate of degradation is lower [51]. These results agree with those reported by MacManamon *et al.* about phenol photocatalytic decomposition in the presence of TiO₂ and ZrO₂, which showed a stronger phenol removal in the acidic environment [52, 53].

Effect of initial dose on phenol degradation by sonocatalytic process

Fig. 4 shows the removal percentage of phenol at different concentrations and different times in the presence of ZrO₂ and CeO₂.

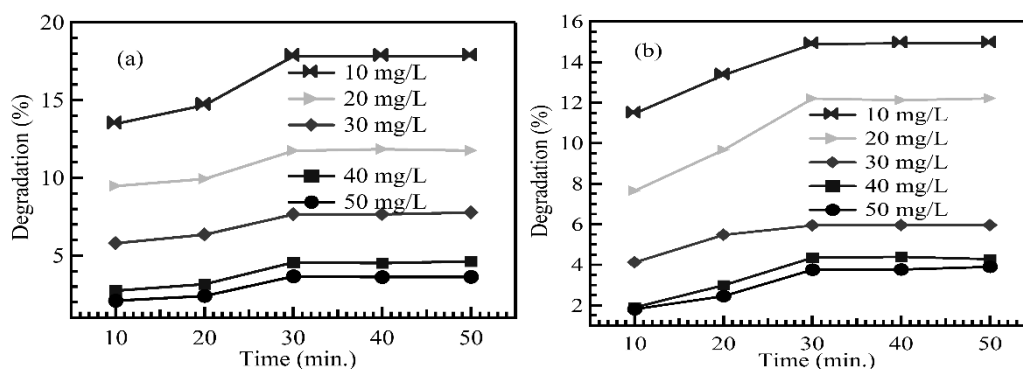


Fig. 4. Effect of time on phenol removal by sonocatalytic process in the presence of ZrO₂ (a) and CeO₂ (b) nanoparticles.

The phenol removal percentage reaches a maximum in 30 min, and at 10 mg/L concentration, which equals 17.77% and 14.98%, respectively. After this time, the removal is constant. With regard to Fig. 4, phenol removal amounts of 10, 20, 30, 40, 50 mg/L after 30 min, equal to 14.98, 12.23, 6.06, 4.30, and 3.88%, respectively. As observed, phenol removal percentage until 30 min, for all concentrations increases, and there is no increment beyond this time. In Fig. 4, phenol removal amounts at 10, 20, 30, 40, 50 mg/L concentrations after 30 min equal to 17.77, 11.71, 7.77, 4.58, and 3.64%, respectively. Also, in Fig. 4, after 30 min, the phenol removal reaches a constant value. The reason for decreasing decomposition efficiency with increasing primary concentration can be explained as follows: at the same nanoparticles concentration, constant time, and pH, the hydroxyl free radical density in solution is equal, therefore phenol reaction with OH⁻ radicals at low concentration increases and leads to increasing phenol decomposition by free radicals [50]. In addition, when phenol concentration increases in the liquid phase, it may increase the partial pressure in cavitation bubbles, and finally, the decreased solvent temperature can be effective for dissolution. Another reason for these phenomena is that comparing with lower phenol concentration, fewer sound waves in the solution can destruct these molecules because produced sound waves are constant at different concentrations. Finally, sound waves do not reach the fundamental particle's surface, and this factor causes decreasing oxidation. It can be seen that with increasing contact time, removal amount increases and then reaches a plateau. The most important reason for this phenomenon can be that with passing the time, more hydroxyl free radicals are produced, which are spent for phenol molecules oxidation, and as a result, phenol concentration decreases, moreover in primary moments, pollutant concentration is high, and it is possible that more collisions between phenol molecules and hydroxyl free radicals occur.

With time passing, the concentration of pollutants decreases, and the existing hydroxyl free radicals are spent on phenol metabolites oxidation, which causes slowing down of the removal amount.

From these data, we can conclude that the sonocatalytic process is more efficient in phenol removal in the presence of CeO₂ and ZrO₂ nanoparticles. In the study of Mahvi *et al.* performed in 2015 on tetracycline removal by chemical sonoprocess they concluded that the percentage of removed tetracycline increases [50]. A study conducted by McManamon *et al.* on phenol removal by photocatalysis process showed that up to 25 mg/L concentration, phenol removal increased, but after that decreased [52]. Research performed by Khataee *et al.* in 2015 on color removal by the sonocatalytic method revealed that with increasing color concentration, color removal decreased [54]. Another study performed by Hamdaouui *et al.* using the sonochemical method for removing tetrachlorophenol showed that the efficiency decreased with increasing pollutant concentration [55]. Chowdhury *et al.* also reported in their study in 2009 about the sonochemical decomposition of organic compounds in which, with increasing concentration of organic compounds, removal efficiency decreased [56].

Effect of catalyst dose on phenol degradation by sonocatalytic process

As shown in Fig. 5 phenol removal efficiency with increasing CeO₂ nanoparticles and ZrO₂ particles dose increases from 0.1 to 0.4 g/L and then is constant. The maximum percentage of phenol removal is in a 0.4 g/L catalyst for CeO₂ and ZrO₂ nanoparticles, 19.0 and 23.6%, respectively.

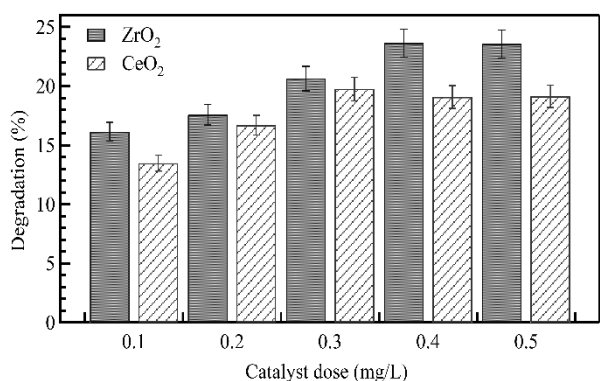


Fig. 5. Catalyst dose effect on phenol removal by sonocatalytic process in the presence of ZrO₂ and CeO₂.

This can be attributed to the fact that when all phenol molecules are sitting on the catalyst, adding more catalyst, because of the absence of phenol molecules does not affect removal efficiency [50]. Increasing phenol removal by increased catalyst dose can be stated because of increasing active sites, and more hydroxyl radicals produced [54]. As specified, with increasing catalyst dose from 0.4 g/L, the amount of removal phenol remained constant because of decreasing ultrasound waves to nanoparticles, this action leads to catalyst aggregation, and finally, available and active sites decreased [20, 57]. Babuponnusami *et al.* studied the phenol removal and showed that phenol removal up to 0.5 g/L of zero-valent iron nanoparticles increased [58]. Bansal *et al.* also reported increasing color removal with increasing the amount of ZrO₂ nanoparticles [23].

Effect of temperature on phenol degradation by sonocatalytic process

Fig. 6 shows the temperature effect on phenol removal by sonocatalytic process in the presence of ZrO₂ and CeO₂ nanoparticles. Unlike the current reaction system, the rate of sonochemical reactions decreases by increasing the solution temperature beyond a certain limit. Due to the effects of cavitation, increasing the temperature to reach the desired level increases covariance activity due to sufficient energy generation. Subsequently, it increases the number of cavity bubbles in sonocatalysis, resulting in an increase in the production of radicals and the degradation of pollutants. A higher temperature increase (higher than optimal) causes a higher solvent vapor pressure inside the cavitation bubbles filled with water vapor and leads to increased resistance to movement within the bubble during the collapse of cavitation cavities and cavitation energy dissipates [59, 60].

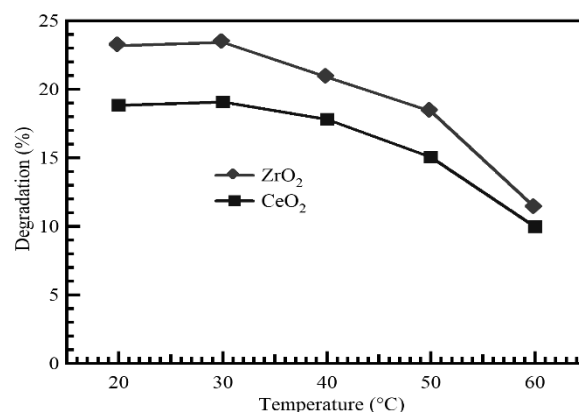


Fig. 6. Investigation of temperature effect on sonocatalytic phenol removal in the presence of ZrO₂ and CeO₂.

In this study, the amount of phenol sonocatalytic destruction at 20, 30, 40, 50, and 60 °C was investigated, and we can see that increasing temperature does not create a notable difference in phenol removal slightly increased up to 30 °C and then decreased. The increase occurred because of increasing reaction speed and, on the other hand, in this process, increasing water vapor leads to decreasing sonocatalysis activity and finally decreasing phenol removal [61]. Combining these two actions makes very little increase in phenol removal. Golash *et al.* on ultrasonic analysis of sewage showed an increase in decomposition rates up to 25 °C followed by a decrease [62]. Also, the results of the study by Barik *et al.* on the degradation of 2,4-dichlorophenol showed the temperature of 34 °C as optimal for decomposition [59].

Comparison of the activity of various processes in phenol removal

Under optimal conditions, phenol removal was performed in the presence of ultrasound waves, and the efficiency of its removal by CeO₂ and ZrO₂ nanoparticles was determined and compared with that of the sonocatalysis process. As shown in Fig. 7, the amount of phenol removal in the presence of ultrasound waves is very low (0.68%) while the amounts of phenol removal in the presence of CeO₂ and ZrO₂ nanoparticles were 4.79 and 9.41%, respectively. This value for the sonocatalytic process using ultrasound in the presence of CeO₂ and ZrO₂ equals 19.01 and 23.64%, respectively. The decomposition of organic pollutants by ultrasound usually needs high energy and high reaction duration time [38].

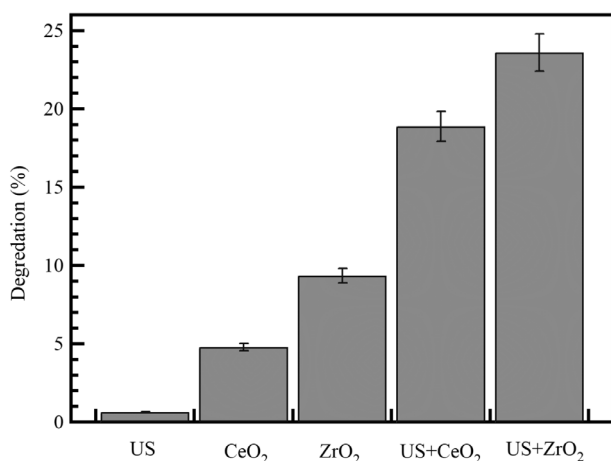


Fig. 7. Comparing phenol removal in the different processes.

The reasons behind the higher catalytic activity of ZrO₂ than CeO₂ are the wider bandgap (5 and 3.1 eV, for ZrO₂ and CeO₂, respectively) and higher stability [63, 64]. In addition, larger amounts of active centers are available on the smaller particle size of ZrO₂ than CeO₂ (38 and 46 nm, respectively).

Only sonowaves cannot decompose phenol to a stable compound; therefore, we can add a catalyst to increase phenol removal efficiency [65]. In the study of Yehia *et al.* on phenol removal by a Fenton-process in the presence of ultrasound it was reported that the amount of phenol removed in the presence of ultrasound waves in 60 min is 20% (less than the Fenton-process) [5].

CONCLUSIONS

ZrO₂ and CeO₂ nanocatalysts show tetragonal and cubic structures with particle size of 38 and 46 nm, respectively. ZrO₂ and CeO₂ nanocatalysts show an excellent catalytic performance for phenol degradation using the sonocatalytic method. The optimum conditions were: phenol concentration 10 mg/L, time 30 min, pH 3, catalyst dosages 0.4 g/L, and temperature 30 °C. The maximum amounts of phenol removal using ZrO₂ and CeO₂ were 23.63 and 19.01%, respectively. According to these research results, ZrO₂ has a higher potential than CeO₂ as a catalyst for phenol decomposition using the sonocatalytic method. The findings recommend using both zirconium and cerium oxides as nanocatalysts for phenolic compounds degradation.

Acknowledgements: The Medical Science University of BIRJAND, Iran, supported this work, hereby we appreciate many experts and officials of the research laboratory of the School of Public Health.

REFERENCES

- H. H. Abdel Ghafar, G. A. M. Ali, O. A. Fouad, S. A. Makhlof, *Desalin. Water Treat.*, **53**(11), 2980 (2015).
- V. K. Gupta, S. Agarwal, H. Sadegh, G. A. M. Ali, A. K. Bharti, A. S. Hamdy, *J. Mol. Liq.*, **237**, 466 (2017).
- S. Agarwal, H. Sadegh, Monajjemi Majid, A. S. H. Makhlof, G. A. M. Ali, A. O. H. Memar, R. Shahryari-ghoshekandi, I. Tyagi, V.K. Gupta, *J. Mol. Liq.*, **218**, 191 (2016).
- I. Fatimah, R. Nurillahi, I. Sahroni, G. Fadillah, B.H. Nugroho, A. Kamari, O. Muraza, *Journal of Water Process Engineering*, **37**, 101418 (2020).
- F. Z. Yehia, G. Eshaq, A. M. Rabie, A. H. Mady, A. E. ElMetwally, *Egypt. J. Pet.*, **24**(1), 13 (2015).
- S. M. Seyed Arabi, R. S. Lalehloo, M. R. T. B. Olyai, G. A. M. Ali, H. Sadegh, *Physica E*, **106**, 150 (2019).
- Y. L. Qi, G. Han, X. C. Song, *Mater. Res. Bull.*, **102**, 16 (2018).
- M. Solehudin, U. Sirimahachai, G. A. M. Ali, K. F. Chong, S. Wongnawa, *Adv. Powder Technol.*, **31**(5), 1891 (2020).
- S. Yapar, V. Ozbudak, A. Dias, A. Lopes, *J. Hazard. Mater.*, **121**(1-3), 135 (2005).
- D. G. Aseev, M. R. Sizykh, A. A. Batoeva, *Russ. J. Phys. Chem. A*, **91**(12), 2331 (2017).
- G. Eshaq, S. Wang, H. Sun, M. Sillanpää, *Sep. Purif. Technol.*, **231**, 115915 (2020).
- M. Ahmaruzzaman, *Adv. Colloid Interface Sci.*, **143**(1-2), 48 (2008).
- S.-H. Lin, R.-S. Juang, *Journal of Environmental Management*, **90**(3), 1336 (2009).
- M. Kilic, E. Apaydin-Varol, A. E. Pütün, *J. Hazard. Mater.*, **189**(1-2), 397 (2011).
- R. I. Yousef, B. El-Eswed, A. a. H. Al-Muhtaseb, *Chem. Eng. J.*, **171**(3), 1143 (2011).
- S. Yao, Y. Zhang, Z. Shi, S. Wang, *Russ. J. Phys. Chem. A*, **87**(1), 69 (2013).
- G. Eshaq, S. Wang, H. Sun, M. Sillanpää, *J. Hazard. Mater.*, **382**, 121059 (2020).
- N. N. M. Zain, N. K. Abu Bakar, S. Mohamad, N. M. Saleh, *Spectrochim. Acta, Part A*, **118**, 1121 (2014).
- I. Z. Shirgaonkar, H. S. Joglekar, V. D. Mundale, J. B. Joshi, *J. Chem. Eng. Data*, **37**(2), 175 (1992).
- Q. Jia, A. C. Lua, *J. Anal. Appl. Pyrolysis*, **83**(2), 175 (2008).
- P. Singh, Sonu, P. Raizada, A. Sudhaik, P. Shandilya, P. Thakur, S. Agarwal, V. K. Gupta, *J. Saudi Chem. Soc.*, doi.org/10.1016/j.jscs.2018.10.005 (2018).
- H. B. Senturk, D. Ozdes, A. Gundogdu, C. Duran, M. Soylak, *J. Hazard. Mater.*, **172**(1), 353 (2009).
- P. Bansal, G.R. Chaudhary, S.K. Mehta, *Chem. Eng. J.*, **280**, 475 (2015).
- L. Svoboda, P. Praus, M. J. Lima, M. J. Sampaio, D. Matýsek, M. Ritz, R. Dvorský, J. L. Faria, C. G. Silva, *Mater. Res. Bull.*, **100**, 322 (2018).
- Y. Li, Q. Du, T. Liu, J. Sun, Y. Jiao, Y. Xia, L. Xia, Z. Wang, W. Zhang, K. Wang, H. Zhu, D. Wu, *Mater. Res. Bull.*, **47**(8), 1898 (2012).

26. A. M. Asiri, M. S. Al-Amoudi, T. A. Al-Talhi, A. D. Al-Talhi, *J. Saudi Chem. Soc.*, **15**(2), 121 (2011).
27. H. Bashiri, M. Rafiee, *J. Saudi Chem. Soc.*, **20**(4), 474 (2016).
28. W.-M. Liu, *Chem. Res. Chin. Univ.*, **29**(2), 314 (2013).
29. A. S. Ethiraj, P. Uttam, V. K. K. F. Chong, G. A. M. Ali, *Mater. Chem. Phys.*, **31**(5), 1891 (2020).
30. A. Sharifi, L. Montazerghaem, A. Naeimi, A. R. Abhari, M. Vafaei, G. A. M. Ali, H. Sadegh, *Journal of Environmental Management*, **247**, 624 (2019).
31. J. Wang, Y. Jiang, Z. Zhang, G. Zhao, G. Zhang, T. Ma, W. Sun, *Desalination*, **216**(1-3), 196 (2007).
32. M. Papadaki, *Sep. Purif. Technol.*, **34**(1-3), 35 (2004).
33. F. Hayati, A. A. Isari, B. Anvaripour, M. Fattahi, B. Kakavandi, *Chem. Eng. J.*, **381**, 122636 (2020).
34. N. H. Ince, G. Tezcanli, R. K. Belen, İ. G. Apikyan, *Appl. Catal., B*, **29**(3), 167 (2001).
35. K. S. Suslick, S. J. Doktycz, E. B. Flint, *Ultrasonics*, **28**(5), 280 (1990).
36. M. Sivakumar, A. B. Pandit, *Ultrason. Sonochem.*, **8**(3), 233 (2001).
37. B. Nanzai, K. Okitsu, N. Takenaka, H. Bandow, Y. Maeda, *Ultrason. Sonochem.*, **15**(4), 478 (2008).
38. M. T. Taghizadeh, A. Mehrdad, *Ultrason. Sonochem.*, **10**(6), 309 (2003).
39. M. Kubo, K. Matsuoka, A. Takahashi, N. Shibasaki-Kitakawa, T. Yonemoto, *Ultrason. Sonochem.*, **12**(4), 263 (2005).
40. J. Wang, Z. Pan, Z. Zhang, X. Zhang, F. Wen, T. Ma, Y. Jiang, L. Wang, L. Xu, P. Kang, *Ultrason. Sonochem.*, **13**(6), 493 (2006).
41. J. Wang, B. Guo, X. Zhang, Z. Zhang, J. Han, J. Wu, *Ultrason. Sonochem.*, **12**(5), 331 (2005).
42. X. Yu, W.-C. Zhu, S. Gao, L.-l. Chen, H.-J. Yuan, J.-H. Luo, Z.-l. Wang, W.-X. Zhang, *Chem. Res. Chin. Univ.*, **29**(5), 986 (2013).
43. H. Zhao, G. Zhang, Q. Zhang, *Ultrason. Sonochem.*, **21**(3), 991 (2014).
44. S. Lu, K. Li, F. Huang, C. Chen, B. Sun, *Appl. Surf. Sci.*, **400**, 277 (2017).
45. N. C. S. Selvam, A. Manikandan, L. J. Kennedy, J. J. Vijaya, *J. Colloid Interface Sci.*, **389**(1), 91 (2013).
46. A. Patterson, *Physical Review*, **56**(10), 978 (1939).
47. O. A. Fouad, S. A. Makhlof, G. A. M. Ali, A. Y. El-Sayed, *Mater. Chem. Phys.*, **128**(1), 70 (2011).
48. O. A. Fouad, G. A. M. Ali, M. A. I. El-Erian, S. A. Makhlof, *Nano*, **7**(5), 1250038 (2012).
49. N. Ghows, M. H. Entezari, *J. Hazard. Mater.*, **195**, 132 (2011).
50. M. Hoseini, G. H. Safari, H. Kamani, J. Jaafari, A. Mahvi, *Iran. J. Health Environ.*, **8**(2), 141 (2015).
51. K. P. Jyothi, S. Yesodharan, E.P. Yesodharan, *Ultrason. Sonochem.*, **21**(5), 1787 (2014).
52. C. McManamon, J. D. Holmes, M. A. Morris, *J. Hazard. Mater.*, **193**, 120 (2011).
53. M. Giahhi, D. Pathania, S. Agarwal, G.A.M. Ali, K.F. Chong, V.K. Gupta, *Studia Universitatis Babeş-Bolyai, Chemia*, **64**(1), 7 (2019).
54. A. Khataee, M. Sheydaei, A. Hassani, M. Taseidifar, S. Karaca, *Ultrason. Sonochem.*, **22**, 404 (2015).
55. O. Hamdaoui, E. Naffrechoux, *Ultrason. Sonochem.*, **15**(6), 981 (2008).
56. P. Chowdhury, T. Viraraghavan, *Sci. Total Environ.*, **407**(8), 2474 (2009).
57. S. G. Anju, S. Yesodharan, E. P. Yesodharan, *Chem. Eng. J.*, **189-190**, 84 (2012).
58. A. Babuponnusami, K. Muthukumar, *Sep. Purif. Technol.*, **98**, 130 (2012).
59. A. J. Barik, P. R. Gogate, *Ultrason. Sonochem.*, **36**, 517 (2017).
60. M. Chiha, O. Hamdaoui, S. Baup, N. Gondrexon, *Ultrason. Sonochem.*, **18**(5), 943 (2011).
61. J. Wang, Z. Jiang, Z. Zhang, Y. Xie, Y. Lv, J. Li, Y. Deng, X. Zhang, *Sep. Purif. Technol.*, **67**(1), 38 (2009).
62. N. Golash, P. R. Gogate, *Ultrason. Sonochem.*, **19**(5), 1051 (2012).
63. J. Wang, Y. Lv, L. Zhang, B. Liu, R. Jiang, G. Han, R. Xu, X. Zhang, *Ultrason. Sonochem.*, **17**(4), 642 (2010).
64. Y. Kristianto, R. Saleh, Effect of CeO₂ promotion on the sonocatalytic performance of ZrO₂ nanoparticle catalysts, AIP Conf. Proc., AIP Publishing LLC, 2018, p. 020042.
65. M. H. Entezari, C. Pétrier, P. Devidal, *Ultrason. Sonochem.*, **10**(2), 103 (2003).

The effect of effluent on the water quality in the Nišava

J. M. Veličković^{1*}, S. D. Stevanović², M. Lutovac³

¹Department of Chemistry, Faculty of Sciences and Mathematics, University of Niš, Višegradska 33, Niš, Serbia

²Faculty of Medicine, University of Niš, Bulevar D r Zorana Đinđića 81, 18000 Niš, Serbia

³Faculty of Management, University of Union – 'Nikola Tesla' Beograd, Njegoševa 1a, 21205 Sremski Karlovci, Serbia

Received: March 31, 2020; Revised: December 03, 2020

From a general perspective, the sewage system in Niš is a combined-type system. After mixing with fecal and atmospheric water the effluent is directly discharged into the Nišava *via* two main outlets (the left and right collectors). This research studies the influence of untreated wastewater on the recipient's (surface water) quality. The analysis of the samples was done by application of a standard spectrophotometric method, with validation reports and measurement uncertainty evaluation reports. Surface and wastewater quality testing was carried out in accordance with the relevant directives, national and international regulations. Physical (temperature, turbidity, pH and electrical conductivity) and chemical (chlorides, ammonia, nitrites, nitrates, sulfates, iron, manganese and chromium as Cr⁶⁺ and Cr³⁺ ions) parameters were analyzed as indicators of quality. Yearly sample quality monitoring indicated river water degradation, which necessitates wastewater treatment in the left and right collectors before the discharge into the Nišava.

Keywords: wastewater and surface water, monitoring, spectrophotometry

INTRODUCTION

Wastewater is any water that has been adversely affected in quality by anthropogenic influence. The sewage from communities, as well as the effluent from industrial units have been identified as the main cause of water pollution across our country. Sewage is a water-carried waste in a solution or suspension that is intended to be removed from a community. It is also referred to as wastewater and it is characterized by volume or flow rate, physical condition, chemical constituents, and bacteriological organisms that it contains. During recent years, there has been an increasing awareness and concern about water conservation all over the world. Hence, new approaches towards achieving sustainable development of water resources have been internationally advanced [1].

Due to industrial development, domestic effluent and urban run-off account for the bulk of the wastewater generated in Niš. Based on its origin, wastewater can be categorized as sanitary, commercial, industrial, agricultural or surface runoff. The term wastewater needs to be differentiated from the term sewage. Because pathogens are excreted in feces all sewage from cities and towns is likely to contain pathogens of some type, potentially presenting a direct threat to public health. Putrescible organic matter has posed a different sort of a threat to water quality in recent years. There has been an increasing awareness and concern about water conservation all over the world [2]. Water management poses a major challenge in

many densely populated countries throughout the world. In Europe, and due to the WFD [3], stewardship of water resources is of paramount importance now and in the future. The major aim of the WFD is to reach good water quality in all European waters by managing water bodies, i.e., lakes, rivers, groundwater bodies, transitional waters and coastal waters by 2027 at the latest.

In Europe, the state of the aquatic environment is controlled by legislation outlined by the European Commission. Directive 2000/60/EC setting out the framework for community action in the field of water policy has reformed the water quality policy of the community, and is the first attempt to move towards ecosystem-based management that should ensure a good ecological status [3, 4]. Its aim is the prevention of water pollution within the European Union through such steps as identifying the pollutants which pose the greatest risks to or *via* the water environment. A supplementary of WFD is Directive 2008/105/EC of the European Parliament and of the Council of December 2008 on environmental quality standards in the field of water policy and Directive 2013/39/EU of the European Parliament and of the Council of August 2013 amending Directives 2000/60/EC and 2008/105/EC as regards priority substances in the field of water policy which includes a list of 45 priority substances. Requirements for the quality of wastewater discharged from plants are included in Council Directive 91/271/EEC of May 1991 concerning

* To whom all correspondence should be sent:

E-mail: jasminka@frad.rs

urban wastewater treatment. The Directive determines the *inter alia* requirements for discharges from urban wastewater treatment plants, including emission limit values for these [4].

Municipal wastewater is one of the largest sources of pollution, in volume. Therefore, it is necessary to treat any type of wastewater to produce an effluent with good quality. “The higher the level of treatment provided by a wastewater treatment plant, the cleaner the effluent and the smaller the impact on the environment” (US EPA 1999).

To remove soluble organic matter and possibly also nitrogen from wastewater, biological treatment is often the second step and is followed by a disinfection unit (chlorine contact tank) [5, 6].

From a general perspective, the Niš sewage system is a combined-type system. A large section of the city, in particular, the central region of the city on the left and right banks of the Nišava, possesses general (mixed)-type collectors whereas for Niška Banja and certain peripheral and newly-built parts of the city a separation system was constructed. After mixing with fecal and atmospheric water the wastewater is directly discharged into the river Nišava *via* the two main outlets: outlet 1 - the left collector in Ivan Milutinović street and outlet 2 - the right collector in Beograd mahala.

The purpose of this study is to estimate the effect of untreated sewage effluent on the recipient’s water (the Nišava) quality *via* physical and chemical water quality indicators.

EXPERIMENTAL

Materials and methods

Water quality was tested according to the corresponding directives and regulations of national and international authorities – regulations (Official Gazette of RS, No: 33/2016; 67/2011, 48/2012 1/2016; 50/2012; 24/2014; 74/2011 and Official Gazette of SRS, No. 31/82).

The Nišava water quality was also monitored following drinking water regulations (EU Council Directive 98/83/EC 1998; Official Gazette SRJ No: 42/1998, 44/1999, 28/2019; WHO 2011a; US EPA 1999a; US EPA 2012) considering that river water (at the entrance to the city) is used as the water intake.

The quality analysis of the wastewater in the left (L) and right (R) city collectors and the Nišava water quality analysis before (N- the water intake) and after the discharge of the left city collector (Nk - around 300 m downstream) (Fig. 1), was carried out at the Laboratory of the sanitary control sector with the JKP ‘Naissus’ laboratory in Niš. The laboratory is accredited according to the standard SRPS ISO/IEC 17025:2006. Fig. 1 shows Nišava-water intake (locality 3), and Nišava downstream from the left collector (locality 10).

The water samples for physico-chemical examinations were taken by experts in accordance with the standards: SRPS EN ISO 5667-1:2008, SRPS EN ISO 5667-3:2017, SRPS EN ISO 5667-4:1997, SRPS EN ISO 5667-6:1997, SRPS EN ISO 5667-10:1997.



Fig. 1. Nisava River - locality 3 and locality 10.

The analysis of wastewater and surface water encompassed the appointment of the following parameters:

Physical parameters (methods): water temperature (SRPSH.Z1.106:1970), turbidity (EN ISO 7027: 1999); pH value (EN ISO 10523: 2008) and electrical conductivity (SRPS EN 27888:2009).

Chemical parameters (methods): chloride (SRPS ISO 9297/1:2007 revision 1); ammonia (SRPS.H.Z1.184:1974); nitrite (SRPS ISO 26777:2009); nitrate (standard methods for testing hygienic correctness "Drinking water"1990); sulfate (USEPA 375.4:1978); iron (SRPS ISO 6332:2003); manganese (standard methods for testing hygienic correctness "Drinking water"1990); and chromium as Cr⁶⁺ and Cr³⁺ ions (ISO 11083:1994(E)).

Physical methods

The wastewater and surface water quality analysis was conducted from January to December 2017 with a monthly sampling frequency.

Temperature measurement - the standard SRPSH.Z1.106:1970 method was validated. Measurement uncertainty was determined (2.26%). The measuring apparatus was standardized.

Spectrophotometric determination of color - by the 2120C SMEWW 21 method which is non-standard, validated as confirmed by the validation and measurement uncertainty reports. The limit of quantification was 5 units of Co-Pt scale, the coefficient of variation (CV) was 0.42%, measurement uncertainty was 9.6%. Internal control was conducted and the equipment was standardized.

Determination of turbidity - by a turbidimeter, the lab used the standard EN ISO 7027: 1999 method for ascertaining turbidity. This method was validated, which was confirmed by the validation and measurement uncertainty reports. The limit of quantification was from 0.20 NTU, CV was 0.80%, and measurement uncertainty was 6.37%. Turbidity was measured with a turbidimeter HACH 210ANIS. The laboratory used certified reference materials.

Potentiometric determination of the pH value - the laboratory used the standard EN ISO 10523: 2008 method for ascertaining pH, which was validated as confirmed by the validation and measurement uncertainty reports: accuracy was 98-99%, CV was 0.23%, measurement uncertainty was 3.0%. The measuring equipment was the pH meter WTW Level 1. The instrument was standardized, marked.

Conductometric determination of electrical conductivity - the laboratory used the standard and validated SRPS EN 27888:2009 method. Measurement uncertainty was 3.68%. CV was

0.25%, the limit of quantification was 0.01 $\mu\text{S}/\text{cm}$. The instrument measuring electrical conductivity was the Inolab Cond Level 1 WTW conductometer. The range was from 1 to 1999 $\mu\text{S}/\text{cm}$. The instrument was standardized.

Chemical methods

Chloride determination (Mohr's method) - the volumetric method, SRPS ISO 9297:1997, SRPS ISO 9297/1:2007 revision 1. The laboratory utilized the standard method which has verification and measurement uncertainty estimation reports. CV was 0.64%, measurement uncertainty was 10.02%. The range of chloride detection in water was 5-300 mg/L.

Ammonia determination (Nessler reagent method) - the spectrophotometric method SRPS.H.Z1.184:1974. The laboratory used the standard method with verification and uncertainty reports. A report verified the method's suitability: CV was 2.5%, the limit of quantification was 0.04 mg/mL, measurement uncertainty was 11.4%. The equipment for performing this method was standardized. The parameter was in the range between 0.004-4.88 mg/L.

Nitrite determination - the laboratory used the standard spectrophotometric method SRPS ISO 26777:2009 with validation reports and measurement uncertainty evaluation reports CV was 0.95%, measurement uncertainty was 5.16%. The parameter was measured in the range between 0.005-0.300 mg/L.

Nitrate determination - the laboratory relied on a non-standard (Manual P-V-31/C) spectrophotometric method for nitrate determination which was validated as stated in the validation and measurement uncertainty estimation reports. CV was 0.21%, measurement uncertainty was 10.16%, the limit of quantification was 0.4 mg/L.

Sulfate - the turbidimetric USEPA 375.4:1978 method. Validation and measurement uncertainty reports were issued. CV was 12.5%, measurement uncertainty was 8.86%. The equipment used in the laboratory for this method was a turbidimeter HACH 2100 ANIS. Sulfate measurement range in water was 1.0-40 mg/L.

Calcium determination - the volumetric USEPA 215.2:1978 method and magnesium content determination (by calculation from calcium) VMK. Validation and measurement uncertainty reports were issued. For LGS QCI-715, code 82724, Ca (54 \pm 0.5mg/L), Mg (13.2 \pm 0.1mg/L); Ca: CV was 2.21%, Mg: CV was 1.28%, measurement uncertainty: for Ca=5.25%, for Mg=6.20%. Calcium

was determined in the range of 0.6-200 mg/L and magnesium – in the range of 0.4-200 mg/L.

Iron determination - the spectrophotometric standard method SRPS ISO 6332:2003. Measurement uncertainty was 6.7%, accuracy 4%, the limit of quantification was 0.010 mg/L, CV was 2.82%. The measuring range was 0.010-2.00 mg/L.

Manganese determination - the laboratory used a non-standard spectrophotometric P-V-26A method for measuring manganese. This method was validated as confirmed by validation and measurement uncertainty reports. Measurement uncertainty was 12.9%, for a sample concentration of 0.025 mg/L (CV 7.9%), for sample concentration of 0.050 mg/L (CV 7.6%), the limit of quantification was 0.025 mg/L. The parameter was measured in the range of 0.025-4.0 mg/L.

Aluminum determination - the standard spectrophotometric ISO 10566:1994 method which has validation and measurement uncertainty reports. A report on method suitability was issued. The limit of quantification was 0.02 mg/L, CV was 1.38%, measurement uncertainty was 10.8%. The parameter was measured within the range of 0.020-0.500 mg/L.

Chromium determination - the laboratory used the standard spectrophotometric ISO 11083:1994(E) method which has verification and measurement uncertainty estimation reports. The limit of quantification was 0.01 mg/L Cr for a sample concentration of 0.0012 mg/L, CV was 2.3%, for CRM 0.050 mg/L Cr, measurement uncertainty 7.60%.

Copper determination – the standard method 3113-B-APHA/WWA-WEF 2005, atomic absorption spectrometry, VARIAN, was used.

The apparatus used in the laboratory for spectrophotometric methods was UV/VIS spectrophotometer Analytic JENA.

Statistical analysis

The experimental results were expressed as mean value \pm standard error of three replicates. In order to statistically estimate any significant differences among mean values, where applicable, the data were subjected to a one-way analysis of variance (ANOVA) test [7].

RESULTS AND DISCUSSION

The results of the physical and chemical parameters are shown in Tables 1, 2 and 3. The highest surface water and wastewater temperatures were measured in the wastewater samples (R) 23.8°C in August while the lowest water temperature was measured in the samples of surface water at the water intake location (N) 6.4°C in December (Table

1). With a change in temperature, there is a change in the chemical composition of water, the content of gases and especially of oxygen. No national or international standards have been set for the temperature of surface water and wastewater (US EPA 1998 and Official Gazette SRJ no 42/98; 44/99) because they don't have an immediate effect on human health, but they influence the chemical and microbiological processes in water. The turbidity values measured in each surface water sample ranged from 1.80 NTU (nephelometric turbidity units) at the water intake area to 30.00 NTU in the Nišava downstream from the wastewater discharge point (Table 1), which points to the deterioration of river water quality. Turbidity is lower than 10 NTU in the water samples (N) from low water level periods, while in rainy periods particles from the Nišava banks get washed away and dissolved in the water. The water becomes muddy and colored and consequently even turbidity at the water intake increases.

The toxicity of many components depends on the pH value. For instance, HCN toxicity increases with the decline of pH values while the toxicity of NH₃ grows with the elevation of pH values. Simultaneously with the elevation of pH values, heavy metals in effluent get deposited in the form of their hydroxides. The measured pH values (Table 1) in all effluent and surface water samples with the highest value of 8.39 were within the recommended values (Official Gazette of RS, No: 50/2012; 74/2011 and Official Gazette SRJ No: 42/1998, 44/1999, 28/2019).

The electrical conductivity of water depends on the geology of the area through which water flows and the ionizing particles in it. It was confirmed that warmer water has higher conductivity. The highest values of electrical conductivity in the wastewater were 1289 μ S/cm (the right collector), which did not affect the drastic increase of conductivity in the surface water: from the highest value 471 μ S/cm at the water intake (N) to the highest value of 522 μ S/cm in the river downstream from the discharge point (Nk) (Table 1). The EU directive (1998) limited conductivity to 2500 μ S/cm at 20 °C under the condition that the water is not aggressive. In Kanoja, Turkey, in 177 samples of groundwater the electrical conductivity was within the interval of 332 μ S/cm to 3004 μ S/cm with the average value of 1573 μ S/cm [8]. In Lahore, the Punjab, Pakistan, the electrical conductivity in groundwater samples before and after monsoons ranged between 455 μ S/cm to 16700 μ S/cm and from 315 μ S/cm to 13445 μ S/cm, respectively, where more than 50% of the samples had a conductivity of about 1000 μ S/cm

[9]. Chloride concentrations in all river water samples (N and Nk) (Table 2) were below the maximum allowed concentration values of 100 mg/L (Official Gazette of RS, No: 50/2012; 74/2011). In

natural water, chloride is present in low concentrations, usually below 100 mg/L. Chloride concentration increased with the rise of mineral content.

Table 1. Yearly temperature, turbidity, pH values and electrical conductivity of surface and wastewater: (N) Nišava-water intake, (L) left city collector, (R) right city collector, (Nk) Nišava downstream from the left collector.

Month	Temperature (°C)				pH value				Turbidity (NTU)		Electrical conductivity (µS/cm)			
	N	L	D	Nk	N	L	D	Nk	N	Nk	N	L	D	Nk
January	11,2 ±0.1	14,0 ±0.14	14,1 ±0.04	13,8 ±0.21	7.9 ±0.11	7.96 ±0.09	7.95 ±0.09	8.02 ±0.02	22,1 ±0.22	28,9 ±0.13	352 ±0.75	886 ±0.32	1062 ±0.43	468 ±0.09
February	6,5 ±0.2	13,2 ±0.21	15,6 ±0.24	8,9 ±0.11	8.18 ±0.12	8.00 ±0.08	8.00 ±0.01	8.30 ±0.01	12,6 ±0.08	10,4 ±0.21	375 ±0.24	922 ±0.41	1072 ±0.28	400 ±0.22
March	8.0 ±0.2	14.9 ±0.07	13.8 ±0.09	9.5 ±0.15	7.79 ±0.10	7.60 ±0.10	7.95 ±0.07	7.90 ±0.03	15.2 ±0.24	27.0 ±0.18	354 ±0.15	727 ±0.21	933 ±0.19	412 ±0.25
April	9.8 ±0.1	16.2 ±0.11	15.1 ±0.45	11.4 ±0.31	8.02 ±0.08	7.61 ±0.11	7.82 ±0.12	8.06 ±0.02	5.2 ±0.05	11.1 ±0.04	384 ±0.31	870 ±0.22	1184 ±0.31	398 ±0.42
May	12.0 ±0.3	15.9 ±0.3	16.1 ±0.42	14.3 ±0.7	8.01 ±0.11	7.90 ±0.12	7.50 ±0.07	8.04 ±0.31	17.1 ±0.08	25.0 ±0.31	372 ±0.41	860 ±0.27	1022 ±0.20	407 ±0.19
June	17.2 ±0.5	18.1 ±0.3	17.7 ±0.51	19.1 ±0.4	8.10 ±0.11	7.92 ±0.10	7.52 ±0.05	8.39 ±0.04	16.1 ±0.28	16.7 ±0.14	467 ±0.51	803 ±0.13	1027 ±0.14	513 ±0.33
July	19.5 ±0.1	21.8 ±0.2	22.5 ±0.24	21.7 ±0.5	8.04 ±0.12	7.80 ±0.17	7.87 ±0.01	8.30 ±0.02	11.1 ±0.21	30.0 ±0.17	457 ±0.27	840 ±0.39	1045 ±0.38	522 ±0.10
August	16.9 ±0.7	18.8 ±0.1	23.8 ±0.16	18.2 ±0.3	8.00 ±0.09	7.81 ±0.12	7.94 ±0.11	8.10 ±0.08	6.0 ±0.06	26.0 ±0.08	403 ±0.24	876 ±0.17	1008 ±0.07	464 ±0.24
September	17.4 ±0.3	22.7 ±0.2	23.18 ±0.41	17.7 ±0.4	8.08 ±0.12	7.80 ±0.04	7.94 ±0.10	8.20 ±0.14	1.8 ±0.05	4.4 ±0.12	411 ±0.11	884 ±0.34	970 ±0.35	460 ±0.10
October	13.2 ±0.2	17.6 ±0.6	14.7 ±0.07	13.8 ±0.2	8.05 ±0.08	7.65 ±0.03	7.62 ±0.11	8.06 ±0.10	4.3 ±0.11	4.4 ±0.01	471 ±0.11	886 ±0.24	1289 ±0.25	491 ±0.17
November	8.2 ±0.4	14.4 ±0.12	13.8 ±0.28	8.6 ±0.5	7.96 ±0.11	7.88 ±0.12	7.65 ±0.11	7.72 ±0.22	10.2 ±0.24	15.2 ±0.05	380 ±0.11	823 ±0.16	840 ±0.12	405 ±0.09
December	6.4 ±0.5	12.4 ±0.11	11.3 ±0.17	6.7 ±0.09	7.98 ±0.21	7.85 ±0.25	7.94 ±0.11	8.20 ±0.08	18.3 ±0.34	25.1 ±0.21	307 ±0.11	890 ±0.10	792 ±0.21	328 ±0.13

Table 2. Yearly chloride, ammonia, nitrite and nitrate ion concentration in surface and wastewater: (N) Nišava - water intake, (L) left city collector, (R) right city collector, (Nk) Nišava downstream from the left collector.

Month	Cl ⁻ (mg/L)				NH ₄ ⁺ (mg/L)				NO ₂ ⁻ (mg/L)	NO ₃ ⁻ (mg/L)			
	N	L	D	Nk	N	L	D	Nk	Nk	N	L	D	Nk
January	<5.0	45.8 ±0.74	67.5 ±0.21	12.8 ±0.13	0.2 ±0.12	35.7 ±0.42	30.6 ±0.27	7.9 ±0.11	<0.71	4.7 ±0.13	7.1 ±0.15	10.6 ±0.16	7.5 ±0.31
February	6.6 ±0.15	53.7 ±0.45	62.7 ±0.43	7.5 ±0.14	0.1 ±0.02	26.7 ±0.16	30.1 ±0.31	0.6 ±0.01	<0.65	4.5 ±0.17	4.5 ±0.08	6.3 ±0.12	4.8 ±0.11
March	<5.0	62.6 ±0.32	84.0 ±0.45	5.2 ±0.22	0.1 ±0.01	35.6 ±0.19	28.9 ±0.16	0.5 ±0.02	<0.03	4.5 ±0.11	7.1 ±0.23	11.2 ±0.27	5.4 ±0.06
April	<5.0	46.8 ±0.28	81.9 ±0.46	5.1 ±0.22	0.1 ±0.01	30.8 ±0.24	34.4 ±0.32	6.1 ±0.05	<0.85	3.8 ±0.12	3.6 ±0.24	3.7 ±0.08	3.7 ±0.33
May	6.5 ±0.03	45.5 ±0.31	63.1 ±0.38	7.4 ±0.21	0.2 ±0.01	45.3 ±0.51	60.0 ±0.01	3.9 ±0.02	<0.75	5.4 ±0.13	3.0 ±0.17	4.5 ±0.11	21.3 ±0.47
June	6.7 ±0.35	42.8 ±0.33	50.9 ±0.42	8.5 ±0.14	0.1 ±0.01	24.7 ±0.18	28.3 ±0.15	0.7 ±0.04	<1.15	6.5 ±0.12	2.7 ±0.10	2.5 ±0.06	5.5 ±0.19
July	6.5 ±0.35	40.8 ±0.22	77.5 ±0.55	6.6 ±0.18	0.1 ±0.01	25.6 ±0.18	26.5 ±0.06	6.2 ±0.07	<2.24	5.0 ±0.10	1.1 ±0.08	1.9 ±0.13	4.9 ±0.14
August	5.3 ±0.05	42.0 ±0.19	55.0 ±0.42	14.7 ±0.07	0.1 ±0.03	31.2 ±0.31	35.1 ±0.15	6.7 ±0.06	<0.22	4.9 ±0.09	1.1 ±0.09	0.7 ±0.05	4.5 ±0.13
September	6.5 ±0.09	54.3 ±0.56	59.5 ±0.15	12.2 ±0.14	0.1 ±0.08	23.5 ±0.24	27.4 ±0.12	1.4 ±0.21	<0.17	4.3 ±0.16	1.3 ±0.09	6.3 ±0.13	5.4 ±0.12
October	6.6 ±0.05	57.3 ±0.36	140.5 ±0.72	11.4 ±0.04	0.1 ±0.07	33.5 ±0.29	42.9 ±0.16	2.3 ±0.06	<0.14	7.7 ±0.11	6.0 ±0.11	4.3 ±0.08	7.7 ±0.25
November	5.2 ±0.08	41.2 ±0.22	92.8 ±0.72	5.1 ±0.08	0.1 ±0.19	26.2 ±0.02	36.2 ±0.27	0.4 ±0.04	<0.62	4.8 ±0.08	5.2 ±0.08	6.1 ±0.06	2.2 ±0.05
December	<5.0	44.8 ±0.33	107.2 ±0.52	<5.0	0.1 ±0.11	29.1 ±0.15	39.2 ±0.05	2.3 ±0.09	<0.88	3.8 ±0.05	4.2 ±0.55	8.4 ±0.31	3.9 ±0.23

Chloride increases water's electrical conductivity and thus corrosiveness in water is also increased [10]. In metal pipes, chloride reacts with metal ions forming soluble salts (WHO 1996a) and consequently increasing metal levels in the water. Wastewater samples (L and R) contained chloride in a higher concentration, but lower than 100 mg/L in the left collector (Table 2), while the right collector contained concentrations above the maximum allowed in only two samples (October and December), which is understandable because they are untreated wastewater (Table 2). The increased concentration of chloride in wastewater comes from industrial wastewater, galvanization and other technological processes. In Banat, Serbia, groundwater has low chloride content ranging from 5 mg/L to 50 mg/L [11].

The presence of ammonia in concentrations higher than the geological level is an important indicator of fecal contamination and can be utilized for the assessment of overall water quality [12]. Ammonia nitrogen concentrations ($\text{NH}_4^+\text{-N}$) in all wastewater samples ranged from 23.5 (L) to 60.00 mg/L (R) (Table 2) and this affected the increase of this parameter in the river: from 0.1 mg/L (at the water intake) to 7.9 mg/L in the Nišava after the wastewater discharge, which is considerably higher than the maximum allowed concentration in a river (Official Gazette of RS, No: 50/2012; 74/2011 and Official Gazette of SRS, No. 31/82).

Nitrates and nitrites in wastewater and surface water can appear naturally but anthropogenic processes like the overuse of inorganic nitrogen fertilizers, municipal wastewater, septic tanks, farm runoff, industrial effluent, and others comprise the most common causes. Inorganic nitrogen analysis enables the assessment of these activities' influence on water quality [13]. The highest nitrate nitrogen ($\text{NO}_3^-\text{-N}$) concentration of 21.3 mg/L and nitrite nitrogen ($\text{NO}_2^-\text{-N}$) concentration of 2.24 mg/L in the Nišava (Table 2) show water quality deterioration after the discharge of untreated wastewater into the river. These values are above the maximum allowed concentrations for surface water (Official Gazette of RS, No: 50/2012; 74/2011 and Official Gazette of SRS, No. 31/82). In the United States of America, Texas, a region that aside from oil and natural gas production also engages in agriculture, the groundwater nitrate concentration varied from <0.44 mg/L to 149 mg/L whereby in 3 out of 40 water samples nitrate concentration exceeded the national standard of 44 mg/L. Statistics show that nitrate concentration drops with well depth [14].

Sulfates are the least toxic anions (US EPA 1999a). Available literature does not indicate a sulfate concentration in water that may be detrimental to health. Studies suggest that in concentrations between 1000 mg/L and 1200 mg/L sulfates have a laxative effect but without diarrhea, dehydration and weight loss (WHO 2004b). Also, sulfates may contribute to corrosion in distribution systems (WHO 2004b). Sulfate concentration in each sample ranged: (N) (8.4-24.5) mg/L; (Nk) (9.1-28.7) mg/L; (L) (51.8-141.1) mg/L and (R) (16.9-178.7) mg/L (Table 3). The highest concentration of sulfate was measured in (R) (16.9-178.7) mg/L in March while the lowest sulfate concentration was measured in (N) (8.4 mg/L) in September. The increased concentration of sulfate in wastewater comes from industrial wastewater of galvanization, chemical and electrochemical degreasing in the metal industry and other technological processes [14]. Despite the mild increase of sulfate after the wastewater discharge all measured values at this location were far below the maximum allowed concentration of 100 mg/L for surface water (Official Gazette of RS, No. 50/2012). Sulfate concentrations are a consequence of leaching from agricultural land or originate from industrial waste and municipal waters [14]. These are wastewaters and their composition is of variable quality, so the results are varied.

Iron concentration (Table 3) in all surface water samples (the Nišava after wastewater discharge) was (0.05-0.39) mg/L, below the maximum allowed concentration (<0.5 mg/L) (Official Gazette of RS, No. 50/2012). Iron does not pose a risk to human health in concentrations it appears in natural water. However, if the concentration is above 0.3 mg/L it may cause turbidity and coloration, and as a consequence of the increase of iron-oxidizing bacteria pipes are lined with mucous layers. U.S. EPA (2012) considers iron a secondary contaminant and sets a secondary maximum contaminant level (MCL) of 0.3 mg/L in drinking water. The reason behind this limit is its influence on organoleptic features of water: rusty color, metallic taste, red or orange coloration. Iron promotes the reproduction of iron-oxidizing bacteria. These bacteria rely on the oxidation process of Fe^{2+} into Fe^{3+} ions for energy. This leads to clogging and the formation of a mucous layer in water system pipes [15]. On the North of Serbia, in Subotica, iron concentration in groundwater samples ranges from 0.04 mg/L to 0.96 mg/L [11].

Table 3. Yearly iron, manganese, chromium, copper and sulfate ion in surface water: (N) Nišava-water intake, (Nk) Nišava downstream from the left collector.

Month	Fe	Mn	Cr ⁶⁺	Cr ³⁺	Cu	SO ₄ ²⁻			
	(mg/L)	(mg/L)	(mg/L)	(mg/L)	(mg/L)	(mg/L)			
	NLDNk	NLDNk	NLDNk	NLDNk	NLDNk	N	L	D	Nk
January	<0.35	<0.025	<0.010	<0.010	<0.021	13.2±0.41	58.2±0.55	50.±0.05	22.9±0.17
February	<0.16	<0.025	<0.010	<0.010	<0.026	21.3±0.52	141.6±0.72	178.9±0.72	21.2±0.61
March	<0.06	<0.025	<0.010	<0.010	<0.018	10.0±0.36	34.7±0.21	18.1±0.10	10.9±0.24
April	<0.08	<0.025	<0.010	<0.010	<0.012	9.4±0.31	93.0±0.44	143.0±0.62	16.5±0.06
May	<0.11	<0.025	<0.010	<0.010	<0.017	15.3±0.08	46.3±0.31	71.8±0.47	14.1±0.07
June	<0.12	<0.025	<0.010	<0.010	<0.010	14.9±0.16	46.4±0.32	65.2±0.08	18.9±0.13
July	<0.13	<0.025	<0.010	<0.010	<0.027	24.5±0.34	45.7±0.31	70.1±0.15	28.7±0.08
August	<0.22	<0.025	<0.010	<0.010	<0.010	16.9±0.07	35.7±0.06	47.4±0.16	17.3±0.11
September	<0.15	<0.025	<0.010	<0.010	<0.010	13.6±0.06	29.9±0.26	16.9±0.09	20.4±0.16
October	<0.39	<0.025	<0.010	<0.010	<0.030	16.4±0.15	15.8±0.11	28.9±0.11	13.1±0.03
November	<0.21	<0.025	<0.010	<0.010	<0.010	8.4±0.13	24.8±0.08	19.5±0.29	11.6±0.08
December	<0.05	<0.025	<0.010	<0.010	<0.010	8.9±0.15	31.8±0.52	29.6±0.07	9.1±0.04

Manganese concentration in all samples of analyzed surface water was <0.025 mg/L (Table 3) and thus satisfies the recommended values and the maximum allowed concentration (0.1 mg/L) (Official Gazette of RS, No. 50/2012). Manganese is one of the elements the presence of which is considered natural in water (WHO 2011a). Of course, it can appear in water as a consequence of anthropogenic actions. Manganese in water behaves similarly to iron. It also promotes the proliferation of manganese-oxidizing bacteria. These bacteria rely on the oxidation process of Mn²⁺ to Mn³⁺ for energy which leads to the formation of a mucous layer in pipes. This problem occurs at manganese concentrations that exceed 0.1 mg/L. (WHO 2011a). Although these bacteria are harmless to humans they may cause clogging in water systems [16], WHO 2011a. In the groundwater of the Pannonian Basin (eastern Hungary and western Romania), manganese concentrations vary from <0.001 mg/L to 0.336 mg/L [17].

The Cr³⁺ and Cr⁶⁺ concentrations in all water samples from the river Nišava was <0.01 mg/L (Table 3) and therefore they meet the recommended values and the maximum allowed concentration (0.05 mg/L) (Official Gazette of RS, No. 50/2012). The distribution of compounds containing Cr³⁺ and Cr⁶⁺ depends on the reduction potential, pH value, oxidizing and reducing compounds presence, kinetics of reduction reactions, the formation of Cr³⁺ complexes or insoluble Cr³⁺ salts and the total chromium concentration. When chromium concentration is low, Cr³⁺ is present as a monovalent HCrO₄⁻ below the pH value of 6.5 and divalent CrO₄²⁻ at a pH value between 6.5 and 10 [18]. In water without oxygen or with a very low concentration of it, Cr³⁺ is a dominant particle that occurs in cationic (Cr³⁺, CrOH₂⁺ or Cr(OH)) or neutral (Cr(OH)₃) form depending on the pH value.

Cr³⁺ is insoluble (<20 µg/L) within the pH range of 7 to 10, with the minimum solubility at the pH value of 8 (1 µg/L) [18]. In natural minerals, chromium mostly appears as Cr³⁺. The results of studies in Croatia have shown that contaminated groundwater (Fe, Pb, Ni, and Cr) becomes a large hygienic and toxicological problem since it considerably impedes groundwater utilization [19]. Even though all of these contaminants have not yet reached toxic levels, they still represent a long-term risk for the population's health [20].

Copper concentration (Table 3) in all surface water samples (the Nišava after wastewater discharge) was (0.01-0.03) mg/L, below the maximum allowed concentration (<0.25 mg/L) (Official Gazette of RS, No. 50/2012). Copper does not pose a risk to human health in concentrations it appears in natural water.

Although the determined concentration values of Fe, Mn and Cr were below the maximum allowed concentrations, an increase in river water turbidity, as well as elevated values of nitrogen (ammonia ion, nitrates) indicated that the untreated wastewater discharge continually deteriorates the Nišava water quality. Due to higher values of ammonia ions, which indicate fecal contamination, there is a risk of pathogenic bacteria. Numerous studies [21] show the efficacy of various technical and technological wastewater treatment processes. They mostly refer to filtration, aeration, disinfection [6] and other processes depending on the degree and type of wastewater contamination. This is certainly applicable to the wastewater in Niš and the result would be the preservation of the environment and river water quality.

CONCLUSION

The physical and chemical analyses of the wastewater and surface water quality indicate deterioration in the Nišava water after the discharge from the city wastewater collectors. Contaminant concentration in the effluent has been a factor in the deterioration of the recipient's water quality. This can be stated because of the elevated turbidity values and fecal contamination indicators (ammonia ion, nitrates) in the river after the discharge from the collectors. These values are considerably increased in comparison to the values before the discharge of wastewater and in comparison to the limit values for a good ecological status according to the regulation on contaminant limits in surface water, groundwater, sediment and the time limit for reaching them (Official Gazette RS no 50/12) - for a good ecological status, i.e. class II - river type 2; natural level.

As the aforementioned regulations stipulate time limits for reaching the threshold values, in the following period it is necessary to adjust the emissions of contaminants to the threshold values. To achieve this, a central wastewater facility must be constructed with the view of preserving water from contamination and maintaining public health.

Compliance with ethical standards

Financing: No funding was used.

Conflict of interest: No conflict of interest.

REFERENCES

1. F. Burton G. Tchobanoglous, H. D. Stensel, Comp. Limited, New Delhi, 2010.
2. A. Funk, A. Wagnall, *Sci. Total. Environ.*, **332**, 13 (2004).
3. Water Framework Directive, European Union (WFDEU) Brussels, *Off.J. Europ. Commun.*, **L327**, 22 (2000).
4. L. Corominas, V. Acuña, A. Ginebreda, M. Poch. *Sci. of the Total Environ.*, **446**, 185 (2013).
5. A. Gallego, A. Hospido, M. T. Moreira, G. Feijoo, *Plant. Resour., Conservat. Recycl.*, **52**, 931 (2008).
6. A. H. Mahvi, *Iranian J. Environ. Health Sci. Engineering*, **5** (2), 79 (2008).
7. Statistical Analysis and Reporting System, ser. Guide, Version 1.0, IBM, 1999.
8. K. D. Tank, S. C. P. Chandel, *Nat. and Science*, **8** (10), 1 (2010).
9. M. Naeem, K. Khan, S. Rehman, J. Iqbal, *Pakistan J. Applied Sciences*, **7**(1), 41 (2007).
10. E. G. Stets, C. J. Lee, D. A. Lytle, *Sci. Total Environ.*, **614**(1), 1498 (2018).
11. P. Papic, M. Cuk, M. Todorovic, J. Stojković, B. Hajdin, N. Atanacković, D. Polomčić, *Pol. J. Environ. Stud.*, **21**(6), 1783 (2012).
12. T. Maekawa, N. Omura, K. Fujita et al. *Environ. Technol.*, **22**(2), 157 (2001).
13. V. Furtula, H. Osachoff, G. Derksen, H. Juahir, A. Colodey, P. Chambers, *Water. Res.*, **46**(4), 1079 (2012).
14. P. F. Hudak, *Texas Int. J. Environ. Res.*, **6** (3), 663 (2012).
15. A. Wilson, K. Parrott, B. Ross, Virginia Cooperat. Extens., Petersburg, VA, 1999, p. 356.
16. H. Tong, P. Zhao, H. Zhang, Y. Tian, X. Chen, W. Zhao, M. Li, *Chemosph.*, **119**, 1141 (2015).
17. H. A. L. Rowland, E. O. Omoregie, R. Millot, Ch. Jiminez, J. Mertens, C. Baciu, S. J. Hug, M. Berg, *Appl. Geochem.*, **26**(1), 1 (2011).
18. D. Rai, B. M. Saas, D. A. Moore, *Inorg. Chem.*, **26**(3), 345 (1987).
19. V. Gvozdic, L. J. Caciv, J. Brana, D. Puntaric, D. Vidosavljavic, *MedGlas Ljek*, **9**(1), 96 (2012).
20. E. Amanatidou, G. Samiotis, E. Trikoilidou, D. Tzelios, A. Michailidis, *Environ. Technol.*, **37**(2), 265 (2016).
21. X. Hao, D. Wang, P. Wang, Y. Wang, D. Zhou, *Environ. Monit. Assess. Chinese Univ.*, **188**(1), 24 (2016).

Regulations

- European Union Council Directive 98/83/EC of 3. November 1998 on the quality of water intended for human consumption. Drinking Water Directive (DWD), Official Journal L, 1998, 330:32.
- WHO, Guidelines for Drinking-water Quality, 4th edn., World Health Organization, Geneva, 2011a.

Standards

- SRPS ISO/IEC 17025:2006.
- Official Gazette of RS, No: 33/2016; 67/2011, 48/2012 1/2016; 50/2012; 24/2014; 74/2011.
- Official Gazette of SRS, No. 31/82.
- Official Gazette SRJ No: 42/1998, 44/1999, 28/2019; WHO 2011a.
- US EPA 1999a.
- US EPA 2012.
- SRPS EN ISO 5667-1:2008.
- SRPS EN ISO 5667-3:2017.
- SRPS EN ISO 5667-4:1997.
- SRPS EN ISO 5667-6:1997.
- SRPS EN ISO 5667-10:1997.
- SRPSH.Z1.106:1970.
- EN ISO 7027: 1999.
- EN ISO 10523: 2008.
- SRPS EN 27888:2009.
- SRPS ISO 9297/1:2007 revision 1.
- SRPSH.Z1.184:1974.
- SRPSH.Z1.106:1970.
- SRPS ISO 26777:2009.
- Standard methods for testing hygienic correctness "Drinking water" 1990.
- USEPA 375.4:1978.
- SRPS ISO 6332:2003.
- ISO 11083:1994(E).
- 2120C SMEWW 21.
- EN ISO 7027: 1999.

Green corrosion inhibitors in various corroding media

M. Thirumalaikumar*

Department of Applied Chemistry, Sri Venkateswara College of Engineering, Pennalur, Sriperumbudur – 602 117, TN, India

Received: April 24, 2020; Revised: February 27, 2021

Recently, development of green corrosion inhibitors is highly called for due to the increasing demands of green chemistry. Plant materials are ideal green candidates for toxic corrosion inhibitors. The review discusses the research work published on the use of different extracts such as leaf, root, stem, bark, pulp, fruit, etc. as corrosion inhibitors for metals in different corroding media. The inhibiting effect of these natural products as corrosion inhibitors for various metals has been evaluated by weight loss, hydrogen evolution, potentiodynamic polarization, electrochemical impedance spectroscopy and electrochemical frequency modulation techniques. The results revealed that most of the extracts act as mixed-type inhibitors. Thermodynamic parameters were calculated using adsorption isotherms. The surface morphology was studied by using scanning electron microscopy (SEM), energy dispersive X-ray spectroscopy (EDS), atomic force microscopy (AFM), X-ray photoelectron spectroscopy (XPS), FT-IR and X-ray diffraction (XRD). Quantum chemical calculations have been used to evaluate the structural, electronic and reactivity parameters of the inhibitors. Physisorption was reported as the probable mechanism for the adsorption of these extracts on the surface of metals. The inhibition action of these products was due to the formation of a protective film on the surface of metals.

Keywords: Corrosion, Biomaterials, Electrochemical Techniques, Inhibition

INTRODUCTION

All natural processes tend toward the lowest possible energy states. Since corrosion is a natural process, metals such as iron, steel, etc., have a natural tendency to combine with other chemical elements that are available in the environment to attain their lowest energy states. To get this lower energy states, iron and steel normally combine with oxygen and water, both of which are available in the environments, to form hydrated iron oxides (rust) that is similar in chemical composition with that of the original iron ore (Figure 1).

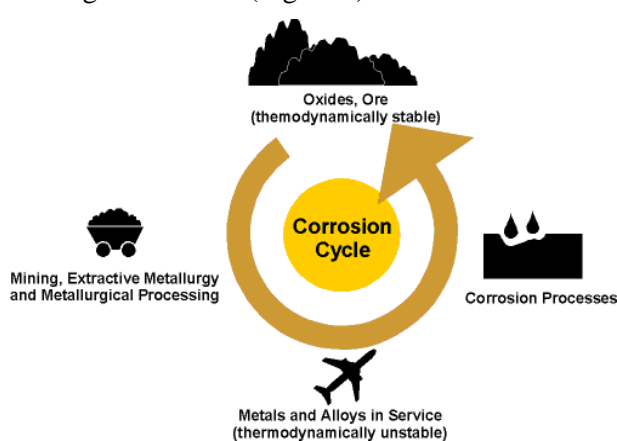


Fig. 1. Corrosion cycle of steel

The word “corrode” is derived from the Latin *corrodere* which means “to gnaw to pieces”.

Corrosion can be defined as a chemical or electrochemical reaction between a material, usually a metal, and its environment that produces a deterioration of the material and of its properties [1].

Corrosion occurs in different forms [1]. Classification is based on any one of three factors:

1. Nature of the corrodent: Corrosion may be classified as “wet” or “dry”.
2. Mechanism of corrosion: This involves either electrochemical or direct chemical reactions.
3. Appearance of the corroded metal: Corrosion is either uniform (the metal corrodes at the same rate over the entire surface) or it is localized (only small areas are affected).

Eight forms of wet corrosion can be identified based on the appearance of the corroded metal. These are a) Uniform (general) corrosion; b) Pitting corrosion; c) Crevice corrosion; d) Galvanic corrosion; e) Erosion corrosion; f) Inter-granular corrosion; g) De-alloying and h) Stress corrosion. This classification system is rather helpful in the study of corrosion problems.

The effects of corrosion in our daily lives are both direct and indirect. At home, corrosion is readily recognized on automobile body panels, charcoal grills, open-air furniture and metal tools. Painting such items will be one of the preventive maintenance approaches from corrosion [1]. Most

* To whom all correspondence should be sent:

E-mail: mtkumar@svce.ac.in

dangerous of all is corrosion that occurs in major industrial plants, such as electrical power plants or chemical processing plants. Plant shutdowns can and do occur as a result of corrosion. Some consequences are economic and cause the following: i) replacement of corroded equipment; ii) overdesign to allow for corrosion; iii) prevent maintenance (painting); iv) shutdown of equipment due to corrosion failure; v) contamination; vi) loss of efficiency; vii) loss of valuable product; viii) damage of equipment [1].

According to a recent report by the National Association of Corrosion Engineers (NACE), the annual worldwide cost of corrosion is over \$ 2.5 trillion which constitutes about 4.2% of Gross Domestic Product (GDP) [2]. In India, the annual cost of corrosion is over 5,000,000 million Indian rupees (i.e. about \$ 100 billion), while in South Africa, the direct cost of corrosion is estimated to be around R 130 billion (i.e. about \$ 9.6 billion) [3].

Other social consequences are i) safety, for example, sudden failure can cause fire, explosion, release of toxic product and construction collapse; ii) health, for example, pollution due to escaping product from corroded equipment or due to a corrosion product itself; iii) depletion of natural resources, including metals and the fuels used to manufacture them and iv) appearance as when corroded material is unpleasing to the eye [1]. There are five methods of corrosion control: a) material selection; b) coatings; c) inhibitors; d) cathodic protection and e) design. Each method is defined here.

a. *Material selection:* Materials that are used for this type of corrosion control are often called high performance alloys, special metals, exotic alloys or exotic metals. Some metals hold the properties to withstand corrosive environments, alongside issues of pitting, stress corrosion cracking and more. These metals are more expensive than a standard stainless steel but they can provide strength within environments with acids, alkali, salts and sea water [1]. The general relation between the rate of corrosion, the corrosivity of the environment and the corrosion resistance of a material is:

$$\frac{\text{Corrosivity of environment}}{\text{Corrosion resistance of metal}} = \text{Rate of corrosive attack}$$

b. *Coatings:* Coatings for corrosion protection can be divided into two broad groups – 1) metallic (applying a more noble metal coating on an active metal) and 2) nonmetallic (organic and inorganic) coatings. The aim of the coatings of the two types is

the same, that is, to isolate the underlying metal from corrosive media [1].

c. *Inhibitors:* Corrosion damage can be prevented by the use of corrosion inhibitors [4, 5], which is the best way to prevent destruction or degradation of metal surfaces in corrosive media. The use of corrosion inhibitors is the most economical and practical method in reducing corrosive attack on metals. Corrosion inhibitors are chemicals either synthetic or natural which, when added in small amounts to an environment, decrease the rate of attack by the environment on metals.

d. *Cathodic protection:* It suppresses the corrosion current which causes damage in a corrosion cell and forces the current to flow to the metal structure to be protected. Cathodic protection can be achieved by two application methods – 1) an impressed current system (uses a power source to force current from inert anodes to the structure to be protected) and 2) a sacrificial anode system (uses active metal anodes, for example, zinc or magnesium, which are connected to the structure) [1].

e. *Design:* Corrosion often occurs in dead spaces or crevices where the corrosive medium becomes more corrosive. These areas can be eliminated or minimized in the design process. Where stress corrosion cracking is possible, the components can be designed to operate at stress levels below the threshold stress for cracking [1].

Mechanism of corrosion

Literature survey revealed that many of the organic compounds (as well as the compounds extracted from plants) used as corrosion inhibitors are heterocyclic compounds that contain polar functional groups such as OH, OCH₃, Cl, NO₂, CN, CH₃, and NH₂, as well as unsaturated (double and triple) bonds that can serve as adsorption sites using a lone pair or π -electrons [3, 6]. These heterocyclic compounds adsorb on metallic surface through their active sites. The adsorbed inhibitor molecules shield the metal surface from direct attack by corrosive ions, and the organic compound is said to inhibit metallic corrosion [3, 6].

All metals exhibit the tendency to readily oxidize. A tabulation of the relative strength of this tendency is the galvanic series. The knowledge of a metal's position in this series helps in selecting an appropriate metal in structural and other applications. In a corrosion cell, the electron produced by the corrosion reaction will be consumed by a cathodic reaction. The electron and the hydrogen ions react to form atomic hydrogen and then molecular hydrogen gas. The formed hydrogen

gas tends to inhibit further corrosion by forming a very thin gaseous film at the surface of the metal. This film thus reduces the corrosion rate. Dissolved oxygen in water will react with the hydrogen, converting it to water thus destroying the film, which continues the corrosion. Other corrosion accelerating factors are pH value and temperature [7, 8].

It is often observed that the presence of electron-donating groups such as OH, NH₂, CH₃, and OCH₃ increases the inhibition performance, while presence of electron-withdrawing substituents such as NO₂, CN, COOH, COOC₂H₅ decreases the inhibition efficiency of organic molecules [9].

In order to reduce the threat caused by the corrosion of industrial installations, several steps have been adopted. However, one of the best options available for protecting metals against corrosion involves the use of corrosion inhibitors. Corrosion inhibitors are widely used in industry to reduce the corrosion rate of metals and alloys in contact with aggressive environments [10, 11]. These inhibitors can be adsorbed onto metal surfaces, block the active sites and decrease the corrosion rate. The adsorption ability of inhibitors onto the metal surface depends on the metal's nature and the chemical composition of electrolytes, as well as on the molecular structure and electronic characteristics of the inhibitor's molecules [12].

Inhibition efficiency of corrosion inhibitors increases with increase in concentration of active components as it is directly proportional to the number of electron-withdrawing or electron-donating groups present in the inhibitor [13]. Presence of heteroatoms, polar functional groups and π -electrons as active centers in a particular compound makes it an effective corrosion inhibitor [14, 15] because these heteroatoms or π -electrons facilitate electronic interactions between metal surface and inhibitor.

Corrosion inhibitor's safety and environmental issues arisen in industries have always been a global concern. These inhibitors may cause reversible (temporary) or irreversible (permanent) damage to the kidneys or liver of terrestrial and aquatic organisms or disturb their biochemical processes or enzyme systems [16]. Therefore, it is desirable to look for environmentally safe corrosion inhibitors.

Recently, a new type of corrosion inhibitors is being developed to meet the terms with the environmental regulations on industrial consumption and development; thus natural products, pharmaceutical ingredients and environment-friendly products have gained much attention as substances for green corrosion inhibitors

that have high inhibition efficiencies [17, 18]. The exploration of natural products of plant origin as inexpensive and eco-friendly corrosion inhibitors is an essential field of study. In addition, plant products are biodegradable, low-cost, readily available and renewable sources of materials. The most common natural substances used are plant extracts [19, 20].

Important parameters for extract preparation

Nowadays, development of green inhibitors is very much wanted because of the increasing demand of green chemistry. Because of natural and biological origin along with their ecofriendly isolation, plant extracts can be considered as green and sustainable materials as corrosion inhibitors for metals and alloys corrosion in aggressive media including HCl, H₂SO₄, H₃PO₄ and HNO₃ [21]. There are several methods available in literature for preparation of plant extracts. The parameters that should be considered during the preparation of plants extracts are described briefly.

Solvents for extraction: Choice of the suitable solvents for extraction is very important for effective extraction since the solvent diffused into plant tissue, solubilized and finally extracted the compounds (phytochemicals) present over there [22, 23]. Literature survey reveals that water is the best solvent owing to its simplicity, ready availability, non-toxic nature, non-flammable, non-hazardous and inexpensive properties [24-27]. However, preparation of some plant extracts requires organic solvents like ethanol and methanol.

Extraction temperature: Temperature has a very marked effect on the effective plant extract preparation. A very low temperature limits the effective solubility of the phytochemicals while very high temperature causes the decomposition of the active constituents (phytochemicals). Generally, extraction is carried out in the temperature range of 60 – 80 °C in order to find optimal extraction yield [28, 29].

Plant drying temperature: Plant materials are allowed to dry at room temperature in shade. This type of drying requires several days, weeks, even months; therefore, oven drying can also be used.

Advantages and limitations: Extracts of natural plants are environmentally friendly, nontoxic and relatively less expensive. They are easily biodegradable also. However, this biodegradability limits the storage and long-term usage of plant extracts. However, it is proposed that the decomposition of plant extracts by microorganisms can be prevented by addition of biocides such as sodium dodecyl sulfate and N-cetyl-N,N,N-trimethyl ammonium bromide. If plant materials are

used as corrosion inhibitors, to prevent the corrosion of metals, the plant kingdom will slowly diminish; metals will be protected at the cost of destruction of plant kingdom [30].

Mild steel

Mild steel, also known as plain-carbon steel, is the most common form of steel because of its relatively low price while it provides material properties that are acceptable for many applications such as different engineering applications for the production of some automobile components, structural shapes, pipelines, construction materials and transportation [31, 32]. Mild steel is known for its high carbon content of about 0.2% to 2.1%, manganese (1.65%), copper (0.6%), silicon (0.6%). It is produced from steel which is extracted from pig iron. It has outstanding ductility and toughness, high machinability and weldability which make its applications possible in engineering fields [20, 33, 34]. It can be hardened by heat treatment. It is used for the production of lightly stressed machine fittings, turbine motors, railways axels, pipes and drums. The mild steel is chosen as it is accessible and easily fabricated with high tensile strength [35].

Mild steel structures corrode as a result of electrochemical reaction with the environment. In most industries, maintenance operations such as pickling, cleaning and descaling are carried out to prolong the life span of the mild steel structures. But aggressive acidic media used for such operations often corrode the mild steel structures [36, 37]. Considering the viability of mild steel and its high cost of production and installation, several steps are taken to prolong its life period.

Extracts from *Pisidium guajava*, *Punica granatum*, *Ginko biloba*, *Tinospora crispa*, *Ficus carica*, *Uncaria gambir*, *Phyllanthus amarus*, *Murraya koenigii*, *Justicia gendarussa*, *Hibiscus sabdariffa* and *Zenthoxylum alatum* have been studied as corrosion inhibitors for mild steel in various acidic media [38-43].

The potential of *Tinospora crispa* as a corrosion inhibitor of mild steel in 1 M HCl has been determined [44]. Both water and acetone – water extracts of the plant were found to be good mild steel corrosion inhibitors in 1 M HCl. The maximum percentage of inhibition efficiency was obtained at the concentration of 800 ppm (water extract) and 1000 ppm (acetone-water extract). Based on a SEM photograph, it was found that the mild steel specimen in 1 M HCl has a rough surface due to localized attack of HCl thus forming a rust product on the surface. When a maximum concentration of the inhibitor is added, the mild steel surface becomes

significantly smooth and comparable to untreated mild steel surface.

Corrosion inhibition of mild steel in 1 M H₂SO₄ by leaves and stem extracts of *Sida acuta* was studied using chemical and spectroscopic techniques at 30 – 60 °C [45]. The inhibition efficiency increases with increasing extracts concentration and is more pronounced for the leaves compared to the stem extract. The corrosion inhibiting effect is attributed to phytochemical components such as saponins, flavonoids, alkaloids, organic acid and anthraquinones in the leaves and tannins, alkaloids and anthraquinones only in the stem extracts. Atomic absorption spectroscopy (AAS) was used to determine the amount of the iron from the bulk of the metal into the electrolyte in the absence and presence of the extracts of *Sida acuta*. The results obtained indicate that there was a decrease in the amount of dissolved iron in the presence of inhibitors.

The anticorrosion activity of *Citrus aurantifolia*, *Bitter leaf root*, *Piper nigrum*, *Musa paradisica* and *Nicotiana tabacum* was studied [46-48]. Corrosion inhibition has also been investigated for the extracts of *Swertia angustifolia*, *Ricinus communis* (Castor) leaves for mild steel in acidic media [49-51]. Herbs such as *Bread fruit*, *Ligularia fischeri*, *Phyllanthus amarus*, palm oil and aloe vera gel were used as a new type of green inhibitors for steel acidic corrosion [49-51]. The corrosion behavior of mild steel in 0.5 M HCl and 0.5 M H₂SO₄ solutions in presence of *Eriobotrya japonica* leaf extract was studied [52]. The inhibitive action of *Gundelia tournefortii* leaf extract on mild steel corrosion in 2 M HCl and 1 M H₂SO₄ solutions was studied [53]. Cathodic and anodic polarization curves show that this extract is a mixed-type inhibitor in both acidic media.

Use of *Amaranthus* extract, as mild steel corrosion inhibitor, in a pickling paste with H₂SO₄ has been investigated [54]. All measurements (corrosion current, polarization and cathodic polarization) showed that *Amaranthus* extract has excellent inhibition properties for mild steel corrosion in a 4 N H₂SO₄ solution. It is found that the *Amaranthus* leaves extract is uniformly adsorbed over the surface. The inhibition is due to the film formation onto the metal/acid solution interface. The extract polarizes the cathode and acts as a cathodic inhibitor. SEM micrographs prove that further corrosion is prevented due to the formation of protective layer. Inhibited pickling acid in the paste form can be conveniently applied on large structures, as well as on small tools to be pickled / cleaned. Corrosion inhibition of an extract of rice husk ash on mild steel in 1 M HCl and H₂SO₄ was investigated

[55]. Anticorrosion activity of *Tiliacora acuminata* leaf extract as a corrosion inhibitor in 1 M HCl has been investigated [56].

The inhibitive action of *Chromolaena odorata* stems extract, in various concentrations, against mild steel corrosion in a 1 M NaCl solution was studied using weight loss, potentiodynamic polarization methods and scanning electron microscopy [57]. Maximum inhibition efficiency of 99.83% was obtained, at 303 K, for an extract concentration of 3000 mg/L. Adsorption energies were lower with inhibited solutions than in uninhibited solutions, suggesting a decrease in mild steel corrosion rate, while Gibbs free energy, enthalpy and entropy of adsorption indicate that the adsorption process was spontaneous and endothermic in nature. The SEM and Langmuir adsorption isotherm studies suggested that the mechanism of corrosion inhibition occurred through an adsorption process. The inhibition action of lignin extract is due to the presence of hydroxyl and carbonyl groups.

Bitter leaves extract was studied as an inhibitive agent in HCl medium for the treatment of mild steel through pickling [58]. Thermometric, gravimetric and potentiodynamic polarization methods were employed in the study. The analysis of bitter leaves extract by gas chromatography revealed the presence of 96 g/mole of 2,4-hexadienal; 96 g/mole of 3,4-heptadiene; and 170 g/mole of 2-decenoic acid as the predominant chemical components. It is found that the activation energy for the corrosion inhibition process ranged from 39.831 to 77.533 kJ/mole, while the heat of adsorption ranged from 16.093 to 30.224 kJ/mole. These values showed that exothermic and spontaneous adsorption of the extract on the mild steel followed the physical adsorption mechanism. Maximum inhibition efficiency of 85.4% was obtained in this study. It was found that this extract is a suitable additive for pickling, cleaning and descaling operations.

The inhibitive action of *Piper guineense* (uzuza leaf) extract on the corrosion of mild steel in a 2 M H₂SO₄ medium has been studied using the weight loss method [59]. The gel extract, obtained by rigorous grinding and squeezing of the leaves, was used for the weight loss determination at various concentrations at temperatures of 303 K, 313 K and 323 K. The result showed that corrosion inhibition increases with increasing concentrations of the extract showing greater efficiency at higher temperatures of 313 K and 323 K. The methanolic extract of *Aquilaria malaccensis* leaf was confirmed to inhibit the corrosion of mild steel in 1 M HCl [60]. The leaf extract acted as a mixed-type cathodic inhibitor.

Inhibitive and adsorption properties of the ethanol extract of *Phyllanthus amarus* for the corrosion of mild steel in H₂SO₄ were investigated using gravimetric, thermometric and gasometric methods [61]. Thermodynamic consideration indicates that the adsorption of the extract is exothermic and spontaneous. A physical adsorption mechanism is proposed for the adsorption of the ethanol extract of *Phyllanthus amarus* on mild steel surface. The corrosion behavior of mild steel in 0.5 M H₂SO₄ solution in the presence of apple, *Malus domestica* and *Bonduc*, *Caesalpinia bonducella* leaf extracts was investigated [62]. The main components present in the extract are bonducellin and quercetin.

Lignin, a polyhydroxy compound, was extracted from the black liquor of pulp and paper industry and its inhibition efficiency on mild steel corrosion by sulfuric acid was investigated [63]. The corrosion inhibition efficiency increases with an increased concentration of lignin, up to 1000 ppm. The inhibitive effect of the aqueous extract of leaves of *Polyalthia longifolia* on the corrosion of mild steel was studied using the weight loss method at temperatures of 303 and 318 K [64]. The adsorption of the extract was spontaneous and occurs according to Flory-Huggins adsorption isotherm.

The effect of the extract of *Musa paradisiaca* on corrosion inhibition of mild steel in aqueous 0.5 M sulfuric acid was investigated [65]. Polarization measurement indicates that *Musa paradisiaca* acts as a mixed-type inhibitor and the inhibition efficiency decreases with rise in temperature. The stem extracts of *Bacopa monnieri* [66] and *Momordica charantia* fruit extract [67] were examined as corrosion inhibitors of mild steel in 1 M HCl medium.

To improve the corrosion inhibition potential of *Anogessius leocarpus* gum exudates for mild steel in acidic medium, corrosion inhibition efficiencies of the gum, KI, KCl and KBr were studied [68]. Aqueous extracts of the leaves of *Anthocleista djalonensis* have been investigated as nontoxic corrosion inhibitors for mild steel in acidic environments [69]. Polarization study indicates that the adsorbed organic matter extract inhibited the corrosion process via mixed-inhibition mechanism, affecting both the anodic metal dissolution reaction and the cathodic hydrogen evolution reaction. The use of *Grewa venusta* root extract as corrosion inhibitor with mild steel was investigated [70] using gravimetric and electrochemical techniques in 1.0 M hydrochloric acid. Chemical compounds identified in the ethanol distillate of *Grewa venusta* extract by GC-MS analysis is given in Table 1. The adsorption

of the extract molecules on the mild steel surface obeys Langmuir adsorption isotherm. The results showed that the inhibitor acted as a mixed-type inhibitor.

Essential oil of *Juniperus phoenicea* extracted by distillation has been tested as inhibitor for the corrosion of mild steel in 1 M acidic media [71]. The inhibition efficiency was found to increase with the oil content, attaining 83% at 1500 ppm. This oil acts as a mixed-type inhibitor. The inhibition performance and mechanism of *Houttuynia cordata* extract for the corrosion of mild steel in 0.5 M H₂SO₄ were investigated [72]. The extract of *Butea monosperma* has been examined to check the inhibitory effectiveness of mild steel corrosion in 0.5 M H₂SO₄ [73]. The *Butea monosperma* extract consists of stigmasterol β-D-glucopyranoside [74]. The corrosion inhibition of mild steel in HCl medium with pawpaw leaves extract as inhibitor has been reported [75]. *Cleome droserifolia* extract and

coffee husk were investigated for their capability to prevent mild steel corrosion in 1 M HCl [76, 77]. The *Mentha piperita* essential oil has been investigated as corrosion inhibitor for mild steel in 1 M HCl [78]. The oil has the following major compounds: 1-(p-fluorophenyl) anthraquinone, methenolone, selina-3,7(11)-diene and longifolene, as shown below.

The inhibition efficiency was modeled and optimized using response surface methodology. Annatto extract was investigated as a cheap and ecologically friendly corrosion inhibitor in acidic medium [79]. Thermodynamic models provided evidence of spontaneous physical and chemical adsorption mechanism with the evolution of heat. Phytochemical screening of this extract has revealed the presence of tannins, saponins, flavonoids, terpenoids, phenolics, anthraquinones, steroids, proteins and carbohydrates with no alkaloids [80]. Bixin and norbixin carotenoids (Figure 2) have been isolated from the extract [81, 82].

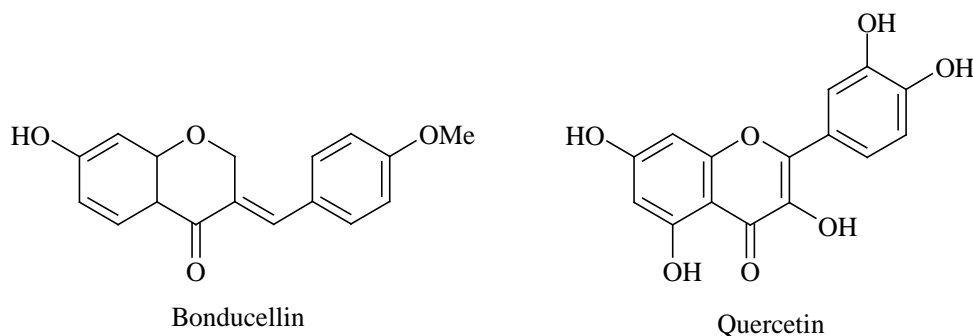
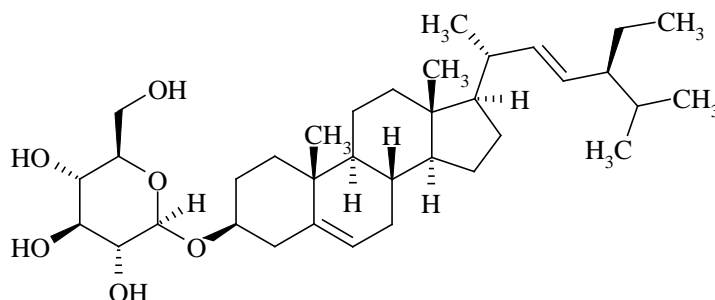


Table 1. Chemical compounds identified in the ethanol distillate of *Grewia venusta* extract

Peaks	Extract	Compound name	Molecular formula	Molecular weight g/mol
1	<i>Grewia venusta</i>	2-Pentanone, 4-methoxy-4-methyl	C ₇ H ₁₄ O ₂	130
2		4H-Pyran-4-one, 2,3-dihydro-3	C ₆ H ₈ O ₄	144
3		1,2,3-Propanetriol, mono acetate	C ₅ H ₁₀ O ₄	134
4		4H-Pyrazole, 3-t-butylsulfanyl-4	C ₉ H ₁₀ F ₆ N ₂ S	292
5		Dodecanoic acid, 3-hydroxy	C ₁₂ H ₂₄ O ₃	216
6		Hexadecanoic acid, 15-methyl	C ₁₈ H ₃₆ O ₂	284
7		Octadecanoic acid, stearic acid	C ₁₈ H ₃₆ O ₂	284
8		Cyclohexanol, 3,5-dimethyl	C ₈ H ₁₆ O	128
9		1,9-Nonanediol, dimethanesulfonate	C ₁₁ H ₂₄ O ₆ S ₂	316



Stigmasterol β -D-glucopyranoside

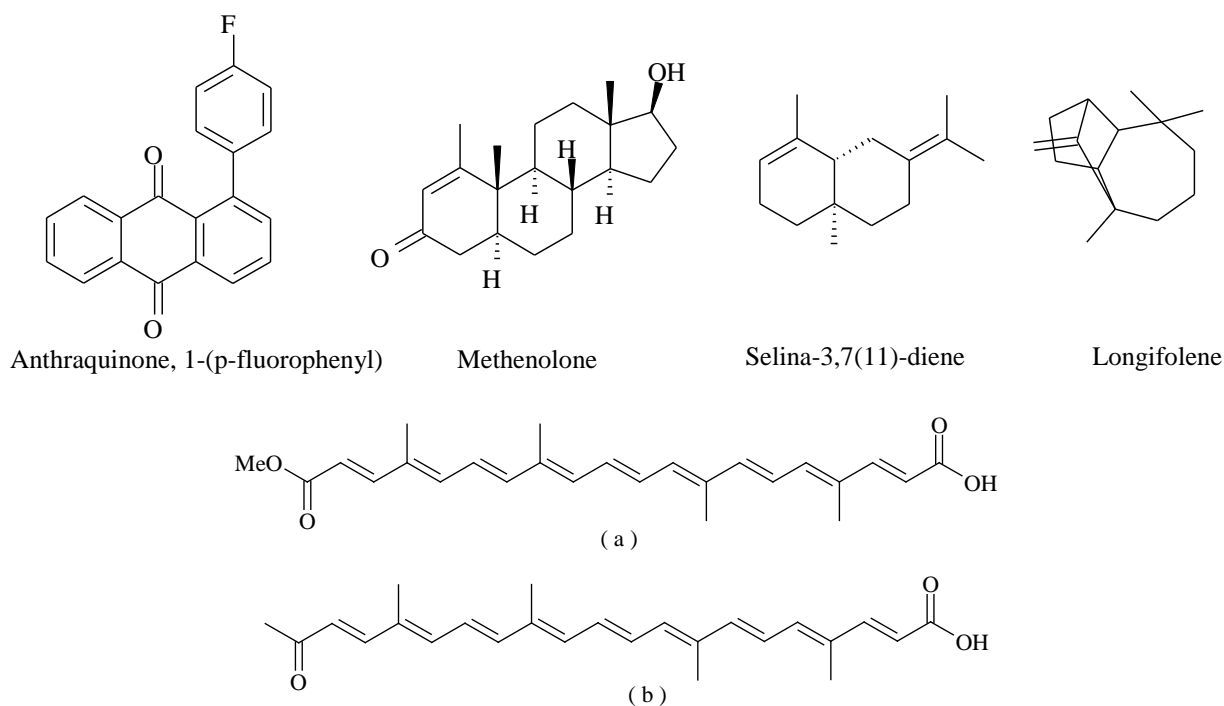


Fig. 2. Molecular structures of (a) bixin and (b) norbixin

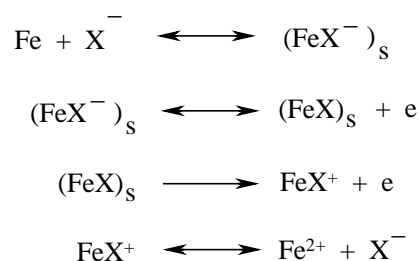
Thymus sahraouian essential oil [83] and *Viburnum sargentii* Koehne fruit extract [84] as new corrosion eco-friendly inhibitors have been used to protect mild steel in 1 M HCl. The methanol extracts from the leaves of *Pistacia terebinthus* L. [85] and extracts of *Acacia tortilis* leaf and bark [86] were tested as corrosion inhibitors for iron in a 3% NaCl solution and sea water, respectively. The influence of berberine extract (roots extract of *Coptis chinensis*) on corrosion of carbon steels in 3.5 wt.% NaCl solution saturated with CO₂ was evaluated [87].

The inhibition of the corrosion of mild steel in 1 M HCl and 1 M H₂SO₄ by *Spirulina platensis* has been studied at different temperatures such as 303 K, 313 K and 323 K by the weight loss method, potentiodynamic polarization method, electrochemical impedance spectroscopy measurements and SEM analysis [88]. From the results, the mode of adsorption is found to be physisorption.

It has been found that the leaves and stem extracts of *Sida acuta* inhibited the acid-induced corrosion of mild steel [89]. Addition of iodide ions enhances the inhibition efficiency to a considerable extent but decreases with rise in temperature. Adsorption of the extracts was found to obey Freundlich adsorption isotherm. Inhibition mechanism is deduced from the temperature dependence of the inhibition efficiency, as well as from assessment of kinetic and activation parameters that govern the processes.

The inhibitive action of ethanol extracts from leaves, bark and roots of *Nauclea latifolia* (NLE) on mild steel corrosion in H₂SO₄ solutions at 30 – 60 °C has been studied [90]. The mechanism of extracts action can be different, depending on metal, the medium and the structure of the inhibitor. One possible mechanism is the adsorption of the inhibitor, which blocks the metal surface and thus does not permit the corrosion process to take place [91].

The observed corrosion inhibition of mild steel in H₂SO₄ solutions can be explained by the adsorption of components of NLE on the metal surface [92]. Various mechanisms have been proposed for the inhibition of metallic corrosion in acid media [93, 94]. According to the mechanism, if a molecule or ion, X⁻, is adsorbed on the steel surface, a surface complex forms in the anodic process and the complex is then desorbed from the surface.



where s represents ion or compound at the surface. In general, if the adsorbed molecule / ion on the surface complex is stable, the corrosion of steel

is inhibited. Therefore, it can be concluded that the adsorption of the phytochemical components of the plant extract leads to the formation of a stable surface complex, which blocks the active sites on the surface of the metal thereby reducing the corrosion rate. Increase in the concentration of the phytochemicals increases the amount of the surface complex resulting in greater inhibition of the corrosion.

The *Jatropha curcas* seeds oil was tested as an iron corrosion inhibitor in an acidic medium [95]. The electrochemical measurements show that this seed oil is a mixed-type inhibitor. The inhibition efficiency increases with higher inhibitor concentrations to attain a maximum value of 97% at 250 ppm. The inhibition effect of *Mentha pulegium* extract on the acid corrosion of carbon steel in 1 M HCl solution was studied [96]. The inhibition action of *Salvia officinalis* [97], *Strychnos nux-vomica* [98], *Ilex paraguariensis* [99], *Cucumis sativus* [100], aqueous brown onion peel extract [101], *Eulychnia acida Phil.* [102], leaf extract of *Khaya senegalensis* [103] and *Salvia hispanica* [104] on carbon steel corrosion in acid media was investigated. Extract of *Juniperus procera* [105], both treated and untreated date palm tree waste [106], *Jasmine tea* [107], *Pulicaria undulate* [108], *Curcuma longa L.* [109], *Prunus persica* [110], *Lawsonia inermis* [111] and *Nerium oleander* [112] have been investigated as corrosion inhibitors for carbon steel in acidic media.

The alcoholic extracts of eight plants, namely *Lycium shawii*, *Teucrium oliverianum*, *Ochradenus baccatus*, *Anvillea garcinii*, *Cassia italica*, *Artemisia sieberi*, *Carthamus tinctorius* and *Tripleurospermum auriculatum*, were studied for their corrosion inhibitive effect on mild steel in 0.5 M HCl media using the open circuit potential (OCP), Tafel plots and A.C. impedance methods [4]. OCP values in the presence of plant extracts shifted to more positive potential with time compared to those of acid solution. This slight OCP displacement (~10 mV) in the presence of plant extracts suggests that all the plant extracts act as mixed-type corrosion inhibitors. The lowest I_{corr} values observed in the presence of extracts of *Artemisia sieberi* and *Tripleurospermum auriculatum* suggest that these two plant extracts possess stronger inhibitive properties in comparison to other studied plant extracts. The addition of alcoholic extracts of all the plants in aggressive media either shifts the corrosion potential (E_{corr}) values slightly toward positive side or remains constant but alters both anodic and cathodic Tafel slope values indicating that the presence of extracts inhibits both cathodic and

anodic reactions and the extracts can be classified as mixed corrosion inhibitors [113].

The corrosion rate of mild steel in 1 M H₂SO₄ in the absence and presence of different concentrations of *Lannea coromandelica* leaf extracts was determined [114]. Maximum inhibition efficiency was found to be 89% at 250 mg/L (308 K). The impedance parameters such as R_s , R_{ct} , C_{dl} and f_{max} derived from Nyquist plots are given in Table 2. The charge transfer resistance increased with an increase in the concentration of inhibitor in acid solution.

Table 2. Electrochemical impedance parameters for mild steel in 1 M H₂SO₄ in the absence and presence of *L. coromandelica* leaf extract

C_{inh} (mg/L)	R_s (Ωcm^2)	R_{ct} (Ωcm^2)	C_{dl} (F/cm ²)	% IE
0	2.2	3.7	2.9×10^{-2}	-
50	2.9	24.5	6.7×10^{-4}	84.9
100	4.3	38.1	2.4×10^{-4}	90.7
150	4.4	39.9	1.6×10^{-4}	92.2
200	4.8	47.3	1.1×10^{-4}	93.8
250	5.4	60.1	1.0×10^{-4}	93.8

FT-IR spectrum of the extract shows an absorption band at 3431 cm⁻¹ (associated hydroxyl) overlapped with the strong stretching mode of N-H. The 1635 cm⁻¹ band was due to stretching mode of C=O. The peaks at 2073 cm⁻¹ could be assigned to stretching mode of -C=N. The peaks at 1465 cm⁻¹ could be attributed to the stretching mode of aromatic substituted N=N. These observations confirmed that the leaf extract contains a mixture of natural products. The FT-IR spectrum of the adsorbed protective layer formed on mild steel surface indicates some additional peaks and some peaks shifted to the higher frequency region. This information provides that some interaction / adsorption had taken place over the metal surface. The N-H stretching shifted from 3431 to 3423 cm⁻¹ indicated the coordination of inhibitor with Fe²⁺ through the N atom of the N-H group. The shifting of C=O stretching from 1635 to 1734 cm⁻¹ confirms that there is a strong interaction between the extract and the mild steel surface. All these results confirmed the adsorption of inhibitor on the surface of the mild steel [115].

Peaks at $2\theta = 35.5^\circ, 59.9^\circ, 71.7^\circ$ in the XRD patterns suggested the presence of iron oxide and a very small amount of brown film of Fe₂O₃ for the mild steel immersed in H₂SO₄. In the XRD patterns of mild steel immersed in the test solution containing 250 mg/L of the leaf extract, the peaks due to iron appeared at $2\theta = 44.6^\circ$ and 65.5° which indicated the absence of oxides of iron (Fe₂O₃, Fe₃O₄ and FeOOH). This result was in good agreement with the observations made by Addoudi [116].

AFM surface examination reveals that the mild steel exposed to 1 M H₂SO₄ has a considerable porous structure with large and deep pores whereas in the presence of inhibitor the mild steel surface appears more flat, homogeneous and uniform which indicated that the extract provides an appreciable resistance to corrosion.

The phenolic (OOMW-Ph) and non-phenolic (OOMW-NPh) fractions of the extract of olive oil mill wastewaters were evaluated as a corrosion inhibitor of steel in molar hydrochloric acid [117]. Olive mill wastewater is a natural source with high amounts of bioactive substances with attractive properties [118] such as polyphenolic mixtures with different molecular weights [119]. In olive mill waste, hydroxytyrosol, tyrosol and oleuropein are the major phenolic components [119-121]. The inhibition efficiency of an aqueous extract of *Eclipta*

alba leaves in corrosion of carbon steel in sea water has been evaluated [122]. The active compound in an aqueous extract of *Eclipta alba* extract is wedelolactone (Figure 3). The inhibitive action of the argan press cake extract against corrosion of steel in a 1 M HCl solution was investigated [123]. Polarization studies showed that this extract was a mixed-type inhibitor with predominant cathodic effectiveness and its inhibition efficiency increased with the inhibitor concentration but decreased with rise in temperature. The inhibition of steel in hydrochloric acid and sodium chloride solutions by *Nicotiana* leaves extract was investigated [124]. The chemical constituents in *Nicotiana glauca* are anabasine, glutamic acid and 7-dehydrocholesterol [125].

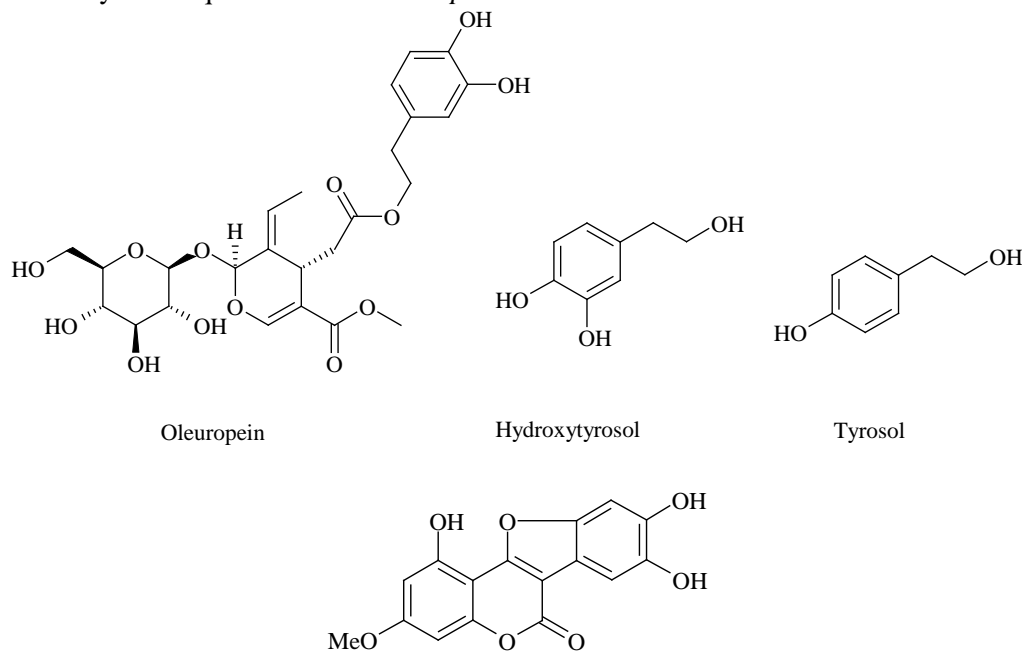
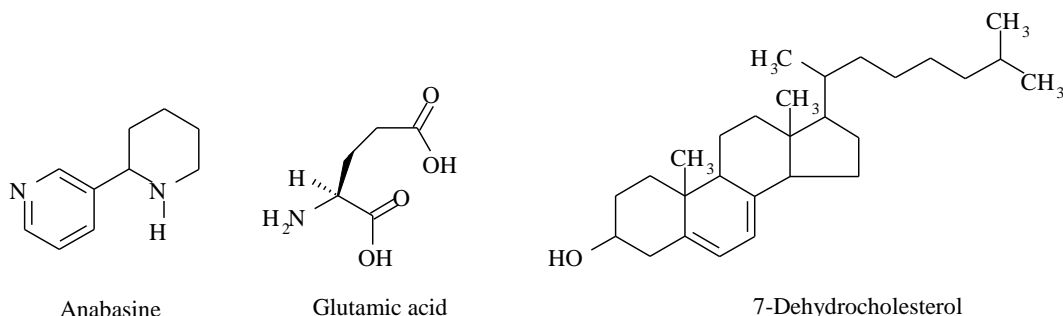


Fig. 3. Wedelolactone



The corrosion inhibition of mild steel in 0.5 M H₂SO₄ solution by the extract of *Litchi Chinensis* was studied by weight loss method, potentiodynamic polarization and electrochemical impedance spectroscopy [126]. The results show that the litchi

peels extract acts as mixed-type inhibitor. The extraction of *Zea mays hairs* (*Z. mays*) was carried out by Soxhlet and ultrasound techniques and through solvents. The extracts were rich in polyphenols. The inhibiting effect of the extracts on

mild steel corrosion in 1 M HCl solution was investigated by electrochemical measurements [127].

Essential oil from fennel (*Foeniculum vulgare*) was tested as inhibitor on carbon steel in 1 M HCl [128]. The main constituents are limonene and β -pinene (Figure 4).

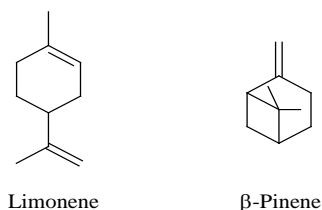
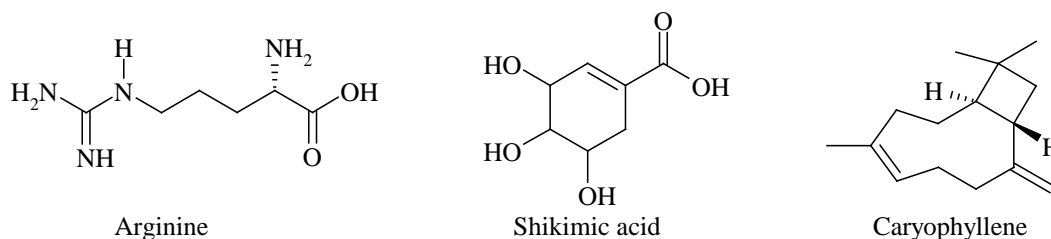


Fig. 4. Molecular structures of limonene and β -pinene

Corrosion inhibition of carbon steel in CO_2 -saturated chloride-carbonate solution by the olive leaf extract has been studied [129]. The olive leaf extract achieves high corrosion efficiency as a



Under normal conditions, reinforcement steel is protected by the formation of a passive film mainly composed of Fe(II) / Fe(III) oxides, due to the high alkalinity of the concrete pore solution (pH around 13) [140]. However, the passivity breakdown becomes easy when the chloride ions reach a threshold value in the pore solution and/ or the pore solution drops from its normal values to values approaching neutrality (pH around 9) due to the carbonation of concrete [141]. The effect of *Chamaerops humilis L.* extract on the behavior of reinforcement steel in a carbonated concrete pore solution (pH = 9) was studied [142]. The results show that the plant extract has a beneficial effect on the development of a passive layer. The corrosion mechanism of *Morinda lucida* leaf extract admixtures on concrete steel rebar in saline / marine simulating environment was investigated [143]. Two naturally derived Welan gum and Neem gum have been tested as corrosion inhibitors against the steel reinforced in concrete in NaCl media at different time intervals [144].

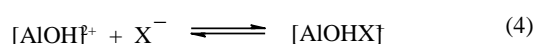
Aluminium

Aluminium is the third most abundant element and the most abundant metal in the earth's crust.

mixed-type inhibitor. The activity of the extract from the peel of fuji apples (*Malus domestica*) was studied as a potential corrosion inhibitor for carbon steel in a saline medium [130]. *Rose*, *Gardenia* and *Solanum violaceum* extracts were used as corrosion inhibitors of steel in acidic medium [131]. The corrosion inhibition characteristics of the extracts of *Salvadora persica* [132], Coconut leaf [133], *Tobacco rob* [134], Red onion seeds and peels [135], *Raphanus sativus L* [136], *Coleus forskohlii* leaf [137] and *Pinus massoniana* needle [138] on corrosion of steel in acidic medium were investigated. The extract of *Pinus massoniana* needle has arginine, shikimic acid and caryophyllene as major constituents.

Reinforcement steel corrosion in concrete has received considerable attention. It has been identified as the primary cause of deterioration in concrete structures [139].

Aluminium plays an essential role in automobiles, packaging, utensils, pipelines, etc. Aluminium is a reactive metal [145], aluminium and aluminium alloys are extensively used in industry in a variety of aggressive aqueous environments covering a wide range of pH. Aluminium is usually protected by a thin oxide film, whose solubility is negligible in neutral solutions (pH 4.0 – 8.5) at room temperature provided the solution does not contain activating anions whereas heavy corrosion is observed both in acidic and alkaline media [146]. Anodizing in sulphuric acid solution can produce a protective oxide layer [147]. According to Obot *et al.* [148], a general mechanism for the dissolution of Al metal would be given as in the following equations:



The controlling step in the metal dissolution is the complexation reaction between the hydrated cation

and the anion present, equation 3. In the presence of chloride ions, the reaction will correspond to equation 5 and the soluble complex ion formed increases the metal dissolution rate which depends on the chloride concentration:



The corrosion of Al [149] in alkaline solution has been studied in the presence of some plant extracts [150] such as *Gum Arabic* [151], *Pachylobus edulis* and *Raphia hookeri* [152], *Fenugreek* leaves [153], *Calendula officinalis* flower [154], *Sansevieria trifasciata* [155], *Mangrove tannins* [156], *Ocimum basilicum* [157], *Ocimum gratissimum* [158], lignin from wheat straw [159], *Neolamarkia cadamba* bark extract [160] and *Vigna unguiculata* [161].

The corrosion inhibition of *Ficus tricopoda* gum was investigated [162]. The gum was found to be a good adsorption inhibitor for the corrosion of Al in H_2SO_4 solution. The adsorption of the gum was

found to be endothermic at a critical concentration of 0.3 g/L and exothermic at concentrations above the critical limit. Corrosion behavior of Al in 0.1 M HCl, 0.1 M HClO_4 and 0.05 M H_2SO_4 solutions was studied using lupine extracts [163]. The results showed that the lupine extract is effective in the order $\text{HClO}_4 > \text{HCl} > \text{H}_2\text{SO}_4$. The chemical composition of lupine extract is represented in Figure 5. Corrosion inhibition of Al by the extract of *Trigonella foenum graecum L* was studied in 1 M HCl acid solution [164]. An inhibition efficiency of 88.6%, 84.41% and 75.77% was obtained by the addition of 1400 ppm of the extract using three solvents, DCM, ethanol and pentane, respectively. The potentiodynamic curves show that the decrease of Al corrosion in the presence of the extract mainly acts by a mixed process with an anodic tendency for both extracts with ethanol and with pentane while the extract with DCM showed a cathodic tendency.

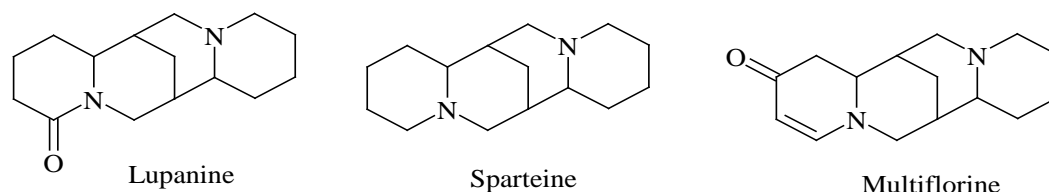


Fig. 5. Chemical composition of lupine.

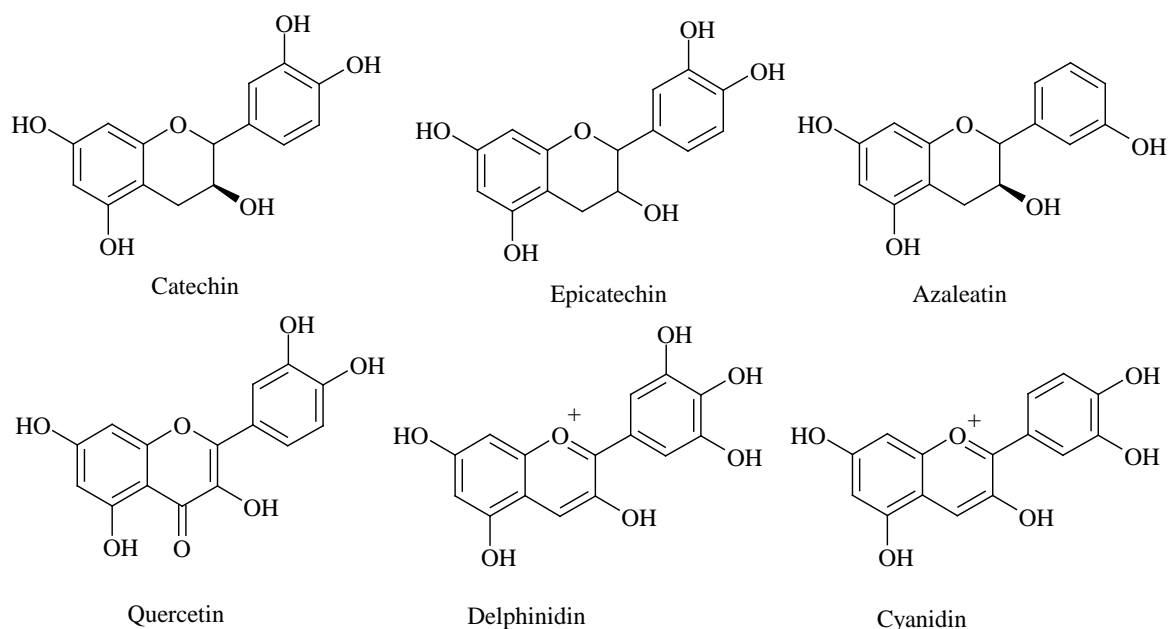


Fig. 6. Structures of *Cashew nut testa* tannin components

The inhibitive effects of *Treculia Africana* leaves extract [165], essential oil from *Mentha spicata* [166] and *Psidium guajava* [167] in the corrosion of Al in HCl solution were studied. The extract interaction with the metal surface was found to obey Freundlich and El-Awady adsorption isotherms.

Asparagus racemosus was used as a corrosion inhibitor of Al in acidic medium [168]. Steroidal saponin-shatavarin and sarsasapogenin are the active constituents of *Asparagus racemosus*. The thermometric and gravimetric analyses of Al corrosion control in HCl medium have been

performed using *Ricinus communis* extract [169]. The results showed that the extract contains phytochemicals such as alkaloids, cardiac glycosides, flavonoids, phenolics, phytates, saponins and tannins. *Cashew nut testa tannin* has been found to inhibit the corrosion of Al in HCl solutions [170]. It was found that *cashew nut testa tannin* is a cathodic inhibitor. The structures of the various components of this nut are given in Figure 6.

The *Psidium guajava* leaf extract was assessed as a corrosion inhibitor for a double thermally-aged Al-Si-Mg alloy in 3.5% weight NaCl solution [171]. Aluminium alloy corrosion behavior in 0.5 M HCl solution was studied using the ethanolic extract of *Cordia dichotoma* seeds [172]. The effect of the extract of *Lupinus varius L.* on the corrosion of Al in 1 M NaOH solution was investigated [173]. A first-order kinetic relationship with respect to Al was obtained with and without the extract from the kinetic treatment of the data. *Glycine max* extract was used as a corrosion inhibitor for Al alloy in 1 M HCl [174]. The corrosion inhibition of Al by *Ipomoea involcrata* (IP) in 1 M NaOH was studied [175]. The plant has been shown to contain mainly *d*-lysergic acid amide (Figure 7).

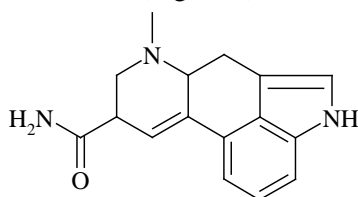


Fig. 7. Chemical structure of *d*-lysergic acid amide

The corrosion rate of aluminium was assessed by the H₂ evolution rate in the absence and presence of different concentrations of IP at 30 °C. The introduction of the plant extracts resulted in the reduction of the rate of H₂ gas evolution as compared to the blank. The study indicates a decrease in the protective nature of the inhibitive film formed on the metal surface at higher temperatures [176] which suggests a physical adsorption mechanism. Physical (electrostatic) adsorption takes place when inhibition efficiency decreases with increase in temperature [177]. The extracted compounds contain heteroatoms such as oxygen, nitrogen and aromatic rings with π -bonds in their molecules, which serve as adsorption sites onto the metal surface.

Increased activation energy in inhibited solutions compared to the blank suggests that the inhibitor is physically adsorbed on the corroding metal surface [178]. The negative Q_{ads} values ranging from (-11.09 to - 8.95 kJ/mol) indicate that the degree of surface coverage decreased with rise in temperature,

supporting the proposed physisorption mechanism [179].

Copper

Copper is a relatively noble metal, which is known to have attractive physical properties such as high electrical and thermal conductivities and mechanical workability [180, 181]. Copper metal is used in many industries like heat exchanger, condenser, electrical wiring, connectors and printed circuit boards. Many plant extracts have been reported as green corrosion inhibitors on copper in various corrosive media such as *Azadirachta* [182], *Cannabis* [183], *Zanthoxylum* [184], *Herba alba* [185] and *Calligonum comosum* [186]. *Capparis spinosa* extract is known to contain several organic compounds such as sterols, flavones, oxygenated heterocyclic constituents, alkaloids and isothiocyanate glycosides [187]. The corrosion inhibition efficiency of this extract on the corrosion of copper in 1 M NaOH solution was investigated [188]. Polarization measurements showed that the extract acts as a mixed-type inhibitor. Four different herbal compounds, *Pimpinella anisum*, *Carum carvi*, *Cuminum cyminum* and *Hibiscus sabdariffa* have been tested as green corrosion inhibitors for copper exposed to 0.5 M NaCl [189].

Corrosion inhibitive effects of *Withania somnifera* extract [190], *Chenopodium* extract [191], *Alchemilla vulgaris* extract [192], *Nerium oleander* extract [193] and *Myrrh* extract [194] were studied on copper in acidic environment. Extracts of *Ziziphus lotus* were experienced as a corrosion inhibitor of copper in sea water using polarization methods and weight loss measurements [195]. Majority of molecules in *Ziziphus lotus* extract are vitamin C, vitamin A, vitamin E and linoleic acid. Synergistic effect of barium chloride on the corrosion inhibition efficiency of aqueous lupine seed extract on copper in 2 M HNO₃ acid solution has been investigated [196].

Miscellaneous

The essential oil of *Artemisia herba alba* has been extracted and tested as an inhibitor of lead corrosion in 0.1 M Na₂CO₃ medium [197]. Zinc is one of the most important non-ferrous metals which find extensive use in metallic coating. Zinc corrodes in a solution with pH lower than 6 and higher than 12.5, but within this range the corrosion rate is very slow [198]. Under aggressive conditions, zinc metal undergoes corrosion, gaining white colored rust [199]. The inhibiting effect of *Ailanthus altissima* aqueous extract as a corrosion inhibitor for zinc in 0.5 M HCl, has been evaluated [120]. Results

revealed that this extract acted as a mixed-type inhibitor and adsorbed onto the zinc surface following Temkin isotherm. *Slanum nigrum* extract has been tested as an eco-friendly green inhibitor for zinc in 3.5% NaCl and 16 ppm Na₂S solution [121].

CONCLUSION

The research work on the corrosion inhibition of metals in various corroding media using a variety of natural compounds is presented in this review article. Plant extracts were the most studied natural products. A wide variety of solvents were used to prepare extracts of the leaves, seeds and stems of the respective plants. The inhibition efficiency of the green corrosion inhibitors tested increased with concentration. An increase in temperature resulted in the lower efficiency of the tested products. Although a number of plants and their phytochemical leads have been reported as anticorrosive agents, the vast majority of plants have not yet been properly studied for their anticorrosive activity. For example, of the nearly 3,00,000 plant species that exist on the earth, only a few (less than 1%) of these plants have been completely studied relative to their anticorrosive activity. Thus, enormous opportunities exist to find out novel, economical and eco-friendly corrosion inhibitors from these source of natural products.

Acknowledgements: The author wishes to express his gratitude to the Management and Head of the Department, Sri Venkateswara College of Engineering, Sriperumbudur for the continuous support.

REFERENCES

1. Corrosion: Understanding the Basics, Chapter 1, J. R. Davis (ed.), ASM International, 2000.
2. R. K. Gupta, M. Malviya, C. Verma, M. A. Quraishi, *Mater. Chem. Phys.*, **198**, 360 (2017).
3. C. Verma, E. E. Ebenso, *J. Mol. Liq.*, **233**, 403 (2017).
4. M. S. Al-Otaibi, A. M. Al-Mayouf, M. Khan, A. A. Mousa, S. A. Al-Mazroa, H. Z. Alkhatlan, *Arab. J. Chem.*, **7**, 340 (2014).
5. F. S. De Souza, A. Spinelli, *Corros. Sci.*, **51**, 642 (2009).
6. S. A. Umoren, O. Ogbobe, I. O. Igwe, E. E. Ebenso, *Corros. Sci.*, **50**, 1998 (2008).
7. S. A. Amadi, *Journal of School of Engineering RSUST*, **1**, 32 (2000).
8. E. C. Chinwuko, *Scoa Heritage System Awka*, 65 (2006).
9. C. Verma, L. O. Olasunkanmi, E. E. Ebenso, M. A. Quraishi, *J. Mol. Liq.*, **233**, 1 (2017).
10. A. Rajendran, C. Karthikeyan, *Int. J. Plant Res.* **2**, 9 (2012).
11. M. Thirumalaikumar, S. Jegannathan, *Port. Electrochim. Acta.*, **29**, 1 (2011).
12. T. I. Ismayil, M. A. Hany, M. A. Vagif, *Am. J. Appl. Chem.*, **1**, 79 (2013).
13. C. Verma, L. O. Olasunkanmi, E. E. Ebenso, *J. Phys. Chem. C*, **120**, 11598 (2016).
14. A. Bousskri, A. Anejjar, M. Messali, *J. Mol. Liq.*, **211**, 1000 (2015).
15. M. E. Belghiti, S. Tighadouini, Y. Karzazi, *J. Mater. Environ. Sci.*, **7**, 319 (2016).
16. A. Singh, M. A. Quraishi, *J. Chem. Pharm. Res.*, **4**, 322 (2012).
17. M. Abdallah, I. Zaaferany, J. Al-Fahemi, *Int. J. Electrochem. Soc.*, **7**, 6622 (2012).
18. B. Shylesha, T. V. Venkatesha, B. M. Praveen, *J. Chem. Pharm. Res.*, **3**, 501 (2011).
19. A. Kanchan, *J. Mater. Sci. Surf. Eng.*, **1**, 44 (2014).
20. C. E. Chuka, B. O. Odio, J. L. Chukwunke, J. E. Sinebe, *Int. J. Sci. & Tech. Res.*, **3(7)**, 306 (2014).
21. F. Chemat, M. A. Vian, G. Cravotto, *Int. J. Mol. Sci.*, **13**, 8615 (2012).
22. M. Nasrollahzadeh, S. M. Sajadi, M. Khalaj, *RSC Adv.*, **4**, 47313 (2014).
23. C. Capello, U. Fischer, K. Hungerbuhler, *Green Chem.*, **9**, 927 (2007).
24. H. Sharghi, R. Khalifeh, M. M. Doroodmand, *Adv. Synth. Catal.*, **351**, 207 (2009).
25. D. S. Bose, L. Fatima, H. B. Mereyala, *J. Organomet. Chem.*, **68**, 587 (2003).
26. R. S. Varma, *ACS Sustain. Chem. Eng.*, **4**, 5866 (2016).
27. H. Duan, D. Wang, Y. Li, *Chem. Soc. Rev.*, **44**, 5778 (2015).
28. J. Seo, S. Lee, M. L. Elam, S. A. Johnson, J. Kang, B. H. Arjmandi, *Food Sci. Nutr.*, **2**, 174 (2014).
29. N. A. N. Mohamad, N. A. Arham, J. Jai, A. Hadi, *Adv. Mater. Res. Trans. Tech. Publ.*, **832**, 350 (2014).
30. M. Sangeetha, S. Rajendran, T. S. Muthumegala, A. Krishnaveni, *Zastita Materijala*, **52**, 1 (2011).
31. D. K. Singh, S. Kumar, G. Udayabhanu, R. P. John, *J. Molecu. Liq.*, 216, 738 (2016).
32. W. D. Callister, *Material Science and Engineering and Introduction*, John Willey and Sons Inc., 4th edn., 1997, p. 550.
33. O. P. Aggrawal, *Engineering Chemistry*, Khanna Publications, New Delhi, 2010.
34. P. Bothi Raja, M. G. Sethuraman, *Mater. Corros.*, **59**, 22 (2009).
35. M. Yadav, U. Sharma, *J. Mater. Environ. Sci.*, **2**, 407 (2011).
36. K. K. Alaneme, S. J. Olusegun, O. T. Adelowo, *Alexandria Engineering Journal*, **55(1)**, 673 (2016).
37. P. K. Jaseela, M. Kuruvilla, L. Williams, C. Jacob, K. O. Shamsheera, A. Joseph, *Arab. J. Chem.*, **13**, 6921 (2020).
38. K. K. Anupama, J. Abraham, *Res. Chem. Intermed.*, **39**, 4067 (2013).
39. M. Behpour, S. M. Ghoreishi, M. Khayatkashani, N. Soltani, *Mater. Chem. Phys.*, **131**, 621 (2012).
40. S. Deng, X. Li, *Corros. Sci.*, **55**, 407 (2012).
41. M. H. Hussin, M. J. Kassim, N. N. Razali, N. H. Dahon, D. Nasshorudin, *Arab. J. Chem.*, **7**, 2 (2011).

42. A. Singh, I. Ahamad, V. K. Singh, M. A. Quraishi, *J. Solid State Electrochem.*, **15**, 1087 (2011).
43. G. Gunasekaran, L. R. Chauhan, *Electrochim. Acta*, **49**, 4387 (2004).
44. M. Hazwan Hussin, M. Jain Kassim, N. N. Razali, N. H. Dahon, D. Nasshorudin, *Arab. J. Chem.*, **9**, S616 (2016).
45. S. A. Umoren, U. M. Eduok, M. M. Solomon, A. P. Udoh, *Arab. J. Chem.*, **9**, S209 (2016).
46. A. I. Caroline, A. S. Abdulrahman, I. H. Kobe, *Am. J. Mater. Eng. Technol.*, **3**, 35 (2015).
47. G. Ji, S. Anjum, S. Sundaram, *Corros. Sci.*, **90**, 107 (2015).
48. J. Bhawsar, P. K. Jain, P. Jain, *Alexandria Eng. J.*, **54**, 769 (2015).
49. P. M. Ejikeme, S. G. Umana, M. C. Menkiti, *Int. J. Mater. Chem.*, **5**, 14 (2015).
50. K. K. Anupama, K. Ramya, A. Joseph, *J. Mol. Liq.*, **216**, 146 (2016).
51. A. K. Singh, S. Mohapatra, B. Pani, *J. Ind Eng. Chem.*, **33**, 288 (2016).
52. K. M. Hijazi, A. M. Abdel-Gaber, G. O. Younes, *Int. J. Electrochem. Sci.*, **10**, 4366 (2015).
53. N. Soltani, M. Khayatkashani, *Int. J. Electrochem. Sci.*, **10**, 46 (2015).
54. M. Srivastava, *Port. Electrochim. Acta*, **38**, 99 (2020).
55. K. K. Alaneme, Y. S. Daramola, S. J. Olusegun, A. S. Afolabi, *Int. J. Electrochem. Sci.*, **10**, 3553 (2015).
56. R. Karthik, P. Muthukrishnan, S.-M. Chen, B. Jeyaprabha, P. Prakash, *Int. J. Electrochem. Sci.*, **10**, 3707 (2015).
57. M. M. Muzakir, F. O. Nwosu, S. O. Amusat, *Port. Electrochim. Acta*, **37**, 359 (2019).
58. O. D. Onukwuli, M. Omotioma, *Port. Electrochim. Acta*, **37**, 115 (2019).
59. S. O. Anuchi, N. C. Ngobiri, *Port. Electrochim. Acta*, **36**, 285 (2018).
60. H. L. Y. Sin, M. Umeda, S. Shironita, A. A. Rahim, B. Saad, *Int. J. Electrochem. Sci.*, **11**, 7562 (2016).
61. N. O. Eddy, *Port. Electrochim. Acta*, **27**, 579 (2009).
62. K. M. Hijazi, A. M. Abdel-Gaber, G. O. Younes, *Int. J. Electrochem. Sci.*, **10**, 4779 (2015).
63. M. Shivakumar, M. S. Dharmaparakash, S. Manjappa, K. L. Nagashree, *Port. Electrochim. Acta*, **35**, 351 (2017).
64. O. Chinyeum, D. E. Ogbeifun, M. O. Edema, *Port. Electrochim. Acta*, **32**, 315 (2014).
65. R. S. Mayangalmbam, V. Sharma, G. Singh, *Port. Electrochim. Acta*, **29**, 405 (2011).
66. C. Wang, P. Liu, P. Liu, L. Li, J. Liu, *Int. J. Electrochem. Sci.*, **14**, 9415 (2019).
67. A. Zhao, H. Sun, L. Chen, Y. Huang, X. Lu, N. Mu, H. Gao, S. Wang, A. Singh, *Int. J. Electrochem. Sci.*, **14**, 6814 (2019).
68. P. O. Ameh, A. O. Odiongenyi, N. O. Eddy, *Port. Electrochim. Acta*, **30**, 235 (2012).
69. C. E. Ogukwe, C. O. Akalezi, M. A. Chidiebere, K. L. Oguzie, Z. O. Iheabunike, E. E. Oguzie, *Port. Electrochim. Acta*, **30**, 189 (2012).
70. I. Y. Suleiman, S. A. Salihu, O. S. Emokpaire, O. C. Ogheneme, L. Shuaibu, *Port. Electrochim. Acta*, **35**, 143 (2017).
71. Y. Elkhofji, I. Forsal, E. M. Rakib, B. Mernari, *Port. Electrochim. Acta*, **36**, 77 (2018).
72. X. Zheng, M. Gong, Q. Li, *Int. J. Electrochem. Sci.*, **12**, 6232 (2017).
73. A. Saxena, D. Prasad, R. Haldhar, *Int. J. Electrochem. Sci.*, **12**, 8793 (2017).
74. M. Mishra, Y. Shukla, S. Kumar, *Phytochem.*, **54**, 835 (2000).
75. M. Omotioma, O. D. Onukwuli, *Port. Electrochim. Acta*, **34**, 287 (2016).
76. A. S. Fouda, R. M. Abou Shaba, A. E. El-Shenawy, T. J. A. Seyam, *Int. J. Electrochem. Sci.*, **13**, 7057 (2018).
77. R. F. B. Cordeiro, A. J. S. Belati, D. Perrone, E. D. Elia, *Int. J. Electrochem. Sci.*, **13**, 12188 (2018).
78. Z. Bensouda, M. Driouch, M. Sfaira, A. Farah, M. Ebn Touhami, B. Hmouti, *Int. J. Electrochem. Sci.*, **13**, 8198 (2018).
79. E. Ituen, I. S. Umoren, *Port. Electrochim. Acta*, **35**, 27 (2017).
80. K. Ganju, E. Ganju, *J. Medic. Pharm. Innov.*, **1**, 21 (2014).
81. J. F. Reith, J. W. Gielen, *J. Food Sci.*, **36**, 861 (1971).
82. G. F. Silva, F. M. Gamarra, A. L. Oliceira, *Brazil J. Chem. Eng.*, **25**, 419 (2008).
83. Z. Bensouda, M. Driouch, R. A. Belakhmima, M. Sfaira, M. Ebn Touhami, A. Farah, *Port. Electrochim. Acta*, **36**, 339 (2018).
84. X. Wang, Y. Wang, Q. Wang, Y. Wan, X. Huang, C. Jing, *Int. J. Electrochem. Sci.*, **13**, 5228 (2018).
85. M. Barbouchi, B. Benzidiia, M. El Idrissi, M. Choukrad, *Port. Electrochim. Acta*, **38**, 175 (2020).
86. I. H. Ali, A. M. Idris, M. H. A. Suliman, *Int. J. Electrochem. Sci.*, **14**, 6406 (2019).
87. Y. Lin, A. Singh, E. E. Ebenso, M. A. Quraishi, Y. Zhou, Y. Huang, *Int. J. Electrochem. Sci.*, **10**, 194 (2015).
88. C. Kamal, M. G. Sethuraman, *Arab. J. Chem.*, **5**, 155 (2012).
89. U. M. Eduok, S. A. Umoren, A. P. Udoh, *Arab. J. Chem.*, **5**, 325 (2012).
90. I. E. Uwas, P. C. Okafor, V. E. Ebiekpe, *Arab. J. Chem.*, **6**, 285 (2013).
91. M. Christov, A. Popova, *Corros. Sci.*, **46**, 1613 (2004).
92. P. C. Okafor, E. E. Ebenso, *Pigm. Res. Tech.*, **36(3)**, 134 (2007).
93. P. C. Okafor, M. E. Ikpi, I. E. Uwah, E. E. Ebenso, U. J. Ekpe, S. A. Umoren, *Corros. Sci.*, **50**, 2310 (2008).
94. A. M. Abdel-Gaber, B. A. Abd-El-Nabey, I. M. Sidahmed, A. M. El-Zayady, M. Saadway, *Corros. Sci.*, **48(9)**, 2765 (2006).
95. M. Zouarhi, M. Chellouli, S. Abbout, H. Hammouch, A. Dermaj, S.O. Said Hassane, P. Decaro, N. Bettach, N. Hajjaji, A. Srhiri, *Port. Electrochim. Acta*, **36**, 179 (2018).

96. A. Khadraoui, A. Khelifa, H. Boutoumi, B. Mettai, Y. Karzazi, B. Hammouti, *Port. Electrochim. Acta*, **32**, 271 (2014).
97. A. Rodriguez-Torres, M. G. Valladares-Cisneros, J. G. Gonzalez-Rodriguez, *Int. J. Electrochem. Sci.*, **10**, 4053 (2015).
98. N. Soltani, N. Tavakkoli, M. Ghasemi, *Int. J. Electrochem. Sci.*, **11**, 8827 (2016).
99. T. F. Souza, M. Magalhaes, V. V. Torres, E. D'Elia, *Int. J. Electrochem. Sci.*, **10**, 22 (2015).
100. G. M. Al-Senani, *Int. J. Electrochem. Sci.*, **11**, 291 (2016).
101. K. C. R. Ferreira, R. F. B. Cordeiro, J. C. Nunes, H. Orofino, M. Magalhaes, A. G. Torres, E. D'Elia, *Int. J. Electrochem. Sci.*, **11**, 406 (2016).
102. R. Venegas, F. Figueredo, G. Carvallo, A. Molinari, R. Vera, *Int. J. Electrochem. Sci.*, **11**, 3651 (2016).
103. I. H. Ali, *Int. J. Electrochem. Sci.*, **11**, 2130 (2016).
104. E. A. Flores-Frias, J. Porcayo-Calderon, M. A. Lucio-Garcia, J. G. Gonzalez-Rodriguez, L. Martinez-Gomez, *Int. J. Electrochem. Sci.*, **12**, 8227 (2017).
105. I. H. Ali, M. H. A. Suleiman, *Int. J. Electrochem. Sci.*, **13**, 3910 (2018).
106. G. M. Al-Senani, M. Alshabanat, *Int. J. Electrochem. Sci.*, **13**, 3777 (2018).
107. J. Tang, H. Wang, X. Jiang, Z. Zhu, J. Xie, J. Tang, Y. Wang, M. Chamas, Y. Zhu, H. Tian, *Int. J. Electrochem. Sci.*, **13**, 3625 (2018).
108. A. S. Fouda, M. Eissa, G. Y. Elewady, W. T. El-Beairy, *Int. J. Electrochem. Sci.*, **12**, 9212 (2017).
109. E. A. Flores-Frias, V. Barba, M. A. Lucio-Carcia, R. Lopez-Cecenes, J. Procayo-Calderon, *Int. J. Electrochem. Sci.*, **14**, 5026 (2019).
110. A. Rodriguez-Torres, O. Olivares-Xometl, M. G. Valladares-Cisneros, *Int. J. Electrochem. Sci.*, **13**, 3023 (2018).
111. A. S. Fouda, M. M. Hegazi, A. El-Azaly, *Int. J. Electrochem. Sci.*, **14**, 4668 (2019).
112. A.S. Fouda, M. Abdel Azeem, S. A. Mohamed, A. El-Hossiany, E. El-Desouky, *Int. J. Electrochem. Sci.*, **14**, 3932 (2019).
113. W. Huilong, Z. Fiashen, L. Fing, *Anti-Corros. Meth. Mater.*, **49**, 127 (2002).
114. P. Muthukrishnan, B. Jeyaprabha, P. Prakash, *Arab. J. Chem.*, **10**, S2343 (2017).
115. E. E. Ebenso, N. O. Eddy, A. O. Odiongenyi, *Afr. J. Pure Appl. Chem.*, **2**, 107 (2008).
116. Y. Abboudi, B. Hammouti, A. Abourrichel, B. Ihssanel, A. Bennamari, M. Charroufi, S. S. Al-Deyab, *Int. J. Electrochem. Sci.*, **7**, 2543 (2012).
117. D. Bouknana, B. Hammouti, M. Messali, A. Aouniti, M. Sbaa, *Port. Electrochim. Acta*, **32**, 1 (2014).
118. H. K. Obied, M. S. Allen, D. R. Bedgood, *J. Agric. Food Chem.*, **53**, 823 (2005).
119. M. Hamdi, *Appl. Biochem. Biotech.*, **37**, 155 (1992).
120. A. De Leonardis, V. Macciola, G. Lembo, *Food Chem.*, **100**, 998 (2007).
121. S. Khoufi, F. Aloui, S. Sayadi, *J. Hazard. Mater.*, **151**, 531 (2008).
122. V. Johnsirani, J. Sathiyabama, S. Rajendran, S. M. Lydia Christy, J. Jeyasundari, *Port. Electrochim. Acta*, **31**, 95 (2013).
123. L. Afia, R. Salghi, A. Zarrouk, H. Zarrok, O. Benali, B. Hammouti, S. S. Al-Deyab, A. Chakir, L. Bazzi, *Port. Electrochim. Acta*, **30**, 267 (2012).
124. D. E. Abd-El-Khalek, B. A. Abd-El-Nabey, A. M. Abdel-Gaber, *Port. Electrochim. Acta*, **30**, 247 (2012).
125. T. C. Tso, L. G. Burk, T. P. Sorokin, M. E. Engelhaupt, *Plant Physiol.*, **37**, 257 (1962).
126. M. Ramananda Singh, P. Gupta, K. Gupta, *Arab. J. Chem.*, **12**, 1035 (2019).
127. S. Aourabi, M. Driouch, M. Kadiri, F. Mahjoubi, M. Sfaira, B. Hammouti, *Arab. J. Chem.*, **13**, 7183 (2020).
128. N. Lahhit, A. Bouyanzer, J.-M. Desjobert, B. Hammouti, R. Salghi, J. Costa, C. Jama, F. Bentiss, L. Majidi, *Port. Electrochim. Acta*, **29**, 127 (2011).
129. G. Pustaj, F. Kapor, Z. Veinovic, *Int. J. Electrochem. Sci.*, **11**, 7811 (2016).
130. R. Vera, F. Figueredo, A. Diaz-Gomez, A. Molinari, *Int. J. Electrochem. Sci.*, **13**, 4139 (2018).
131. X. Wang, Y. Gu, Q. Zhang, L. Xu, X. Li, *Int. J. Electrochem. Sci.*, **14**, 8405 (2019).
132. A. A. M. Hassan, H. T. M. Abdel-Fatah, *Int. J. Electrochem. Sci.*, **11**, 6959 (2016).
133. S. Chen, B. Zhu, X. Liang, *Int. J. Electrochem. Sci.*, **15**, 1 (2020).
134. Y. Guo, M. Gao, H. Wang, Z. Liu, *Int. J. Electrochem. Sci.*, **12**, 1401 (2017).
135. E. A. Noor, A. Al-Moubaraki, A. H. Al-Zhrani, M. H. Hubani, *Int. J. Electrochem. Sci.*, **11**, 6523 (2016).
136. X. Jiang, C. Lai, Z. Xiang, Y. Yang, Bang-long Tan, Zhong-qiu Long, Lin-peng Liu, Yun-tian Gu, Wen-jian Yang, X. Chen, *Int. J. Electrochem. Sci.*, **13**, 3224 (2018).
137. I. H. Ali, R. Marzouki, Y. Ben Smida, A. Brahmia, M. F. Zid, *Int. J. Electrochem. Sci.*, **13**, 11580 (2018).
138. X. Wang, S.-fei Ren, D.-X. Zhang, H. Jiang, Y. Gu, *Int. J. Electrochem. Sci.*, **13**, 9888 (2018).
139. Y. Zhao, W. Jin, *Steel Corrosion Induced Concrete Cracking*, 1st edn., Heinemann, Butterworth, 2016.
140. P. Ghods, O. B. Isgor, F. Bensebaa, *Corrosion Sci.*, **58**, 159 (2012).
141. L. Bertolini, B. Elsener, P. Pedferri, *Corrosion of Steel in Concrete: Prevention, Diagnosis, Repair*, Weinheim, Wiley-VCH, 2013.
142. D. Benmessaoud Left, M. Zertoubi, S. Khoudali, M. Azzi, *Port. Electrochim. Acta*, **36**, 249 (2018).
143. J. O. Okeniyi, C. A. Loto, A. P. I. Popoola, *Int. J. Electrochem. Sci.*, **10**, 9893 (2015).
144. M. G. L. Annaamalai, G. Maheswaran, N. Ramesh, C. Kamal, G. Venkatesh, P. Vennila, *Int. J. Electrochem. Sci.*, **13**, 9981 (2018).
145. M. Metikos-Hucovic, *J Appl. Electrochem.*, **32**, 35 (2002).
146. M. Pourbaix, *Atlas of Electrochemical Equilibria in Aqueous Solutions*, Pergamon Press, London, 1966.
147. S. Wernick, R. Pinner P. G. Sheasby, *The Surface Treatment of Aluminum and its Alloys*, ASN

- International Finishing Publications Ltd., Teddington, 1987.
148. I. B. Obot, N. O. Obi-Egbedi, S. A. Umoren, *Int. J. Electrochem. Sci.*, **4**, 863 (2009).
 149. K. Khanari, M. Finsgar, M. K. Hrcic, U. Maver, Z. Knez, B. Seiti, *RSC Adv.*, **7**, 2299 (2017).
 150. M. Sangeetha, S. Rajendran, J. Sathiyabama, A. Krishnaveni, *Port. Electrochim. Acta*, **31**, 41 (2013).
 151. S. A. Umoren, I. B. Obot, E. E. Ebenso, P. C. Okafor, O. Ogbobe, E. E. Oguzie, *Anti-Corros. Methods Mater.*, **53**, 277 (2006).
 152. S. A. Umoren, I. B. Obot, E. E. Ebenso, P. C. Okafor, *Port. Electrochim. Acta*, **26**, 267 (2008).
 153. E. A. Noor, *Int. J. Electrochem. Sci.*, **2**, 996 (2007).
 154. R. Subha, R. Saratha, *J. Corr. Sci. Eng.*, **10**, 1 (2006).
 155. E. E. Oguzie, *Corrosion Sci.*, **49**, 1527 (2007).
 156. A. A. Rahim, E. Rocca, J. Steinmetz, M. J. Kassim, R. Adnan, S. M. Ibrahim, *Corrosion Sci.*, **49**, 402 (2007).
 157. E. E. Oguzie, A. I. Onuchukwu, P. C. Okafor, E. E. Ebenso, *Pig. Resin Technol.*, **35**, 63 (2006).
 158. M. O. Nkiko, J. T. Bamgnose, *Port. Electrochim. Acta*, **29**, 419 (2011).
 159. M. M. El-Deeb, E. N. Ads, J. R. Humaidi, *Int. J. Electrochem. Sci.*, **13**, 4123 (2018).
 160. N. Chaubey, V. K. Singh, M. A. Quraishi, E. E. Ebenso, *Int. J. Electrochem. Sci.*, **10**, 504 (2015).
 161. S. A. Umoren, I. B. Obot, L. E. Akpabio, S. E. Etuk, *Pig. Resin Technol.*, **37**, 98 (2008).
 162. N. O. Eddy, P. O. Ameh, M. Y. Gwarzo, I. J. Okop, S. N. Dodo, *Port. Electrochim. Acta*, **31**, 79 (2013).
 163. B. A. Abd-El-Naby, O. A. Abdullatef, H. M. El-Kshlan, E. Khamis, M. A. Abd-El-Fatah, *Port. Electrochim. Acta*, **33**, 265 (2015).
 164. A. Ennouri, A. Lamiri, M. Essahli, *Port. Electrochim. Acta*, **35**, 279 (2017).
 165. P. M. Ejikeme, S. G. Umana, O. D. Onukwuli, *Port. Electrochim. Acta*, **30**, 317 (2012).
 166. F. Bensabah, S. Houbairi, M. Essahli, A. Lamiri, J. Naja, *Port. Electrochim. Acta*, **31**, 195 (2013).
 167. Y. C. Sharma, S. Sharma, *Port. Electrochim. Acta*, **34**, 365 (2016).
 168. S. Bashir, G. Singh, A. Kumar, *Port. Electrochim. Acta*, **37**, 83 (2019).
 169. O. D. Onukwuli, M. Omotoma, I. Obiora-Okafo, *Port. Electrochim. Acta*, **38**, 19 (2020).
 170. N. J. N. Nnaji, N. O. Obi-Egbedi, C. O. B. Okoye, *Port. Electrochim. Acta*, **32**, 157 (2014).
 171. L. M. Sani, M. Abdulwahab, S. A. Yaro, F. O. Kolawole, *Port. Electrochim. Acta*, **34**, 119 (2016).
 172. S. Sharma, Y. C. Sharma, *Port. Electrochim. Acta*, **37**, 1 (2019).
 173. M. K. Irshadat, E. M. Nawafleh, T. T. Bataineh, R. Muhaidat, M. A. Al-Qudah, A. A. Alomary, *Port. Electrochim. Acta*, **31**, 1 (2013).
 174. A. M. El-Azaly, *Int. J. Electrochem. Sci.*, **14**, 2714 (2019).
 175. I. B. Obot, N. O. Obi-Egbedi, *Port. Electrochim. Acta*, **27**, 517 (2009).
 176. I. B. Obot, N. O. Obi-Egbedi, S. A. Umoren, *Corros. Sci.*, **51**, 276 (2009).
 177. S. A. Umoren, I. B. Obot, E. E. Ebenso, P. C. Okafor, O. Ogbobe, E. E. Oguzie, *Anti-Corros. Methods and Mater.* **53(5)**, 277 (2006).
 178. S. A. Umoren, I. B. Obot, N. O. Obi-Egbedi, *Mater. Sci.*, **44(1)**, 274 (2009).
 179. S. A. Umoren, I. B. Obot, E. E. Ebenso, *E-J. Chem.*, **5(2)**, 355 (2008).
 180. M. G. Fontana, *Corrosion Engineering*, 3rd edn., McGraw-Hill, Singapore, 1986.
 181. M. Hourani, F. Wedian, *Corros. Sci.*, **42**, 2131 (2000).
 182. L. Valek, S. Martinez, *Mater. Lett.*, **61**, 148 (2007).
 183. B. A. Abd-El-Nabey, A. M. Abdel-Gaber, *Int. J. Electrochem. Sci.*, **8**, 7124 (2013).
 184. J. S. Chauhan, *Asian J. Chem.*, **21**, 1975 (2009).
 185. M. B. Mihajlovic, M. M. Antonijevic, *Int. J. Electrochem. Sci.*, **10**, 1027 (2015).
 186. M. S. Nooshabadi, F. S. Hoseiny, *Metall. Mater. Trans. A*, **46**, 293 (2015).
 187. M. A. Khanfer, S. S. Sabri, *Nat. Prod. Res.*, **17**, 9 (2003).
 188. F. Wedian, M. A. Al-Qudah, A. N. Abu-Baker, *Port. Electrochim. Acta*, **34**, 39 (2016).
 189. A. M. Nagiub, *Port. Electrochim. Acta*, **35**, 201 (2017).
 190. H. M. Elabbasy, *Int. J. Electrochem. Sci.*, **14**, 5355 (2019).
 191. M. M. Motawea, A. El-Hossiany, A. S. Fouda, *Int. J. Electrochem. Sci.*, **14**, 1372 (2019).
 192. R. K. Ahmed, S. Zhang, *Int. J. Electrochem. Sci.*, **14**, 10657 (2019).
 193. A. S. Fouda, H. M. Elabbasy, *Int. J. Electrochem. Sci.*, **14**, 6884 (2019).
 194. S. Y. Al-Nami, A. S. Fouda, *Int. J. Electrochem. Sci.*, **15**, 1187 (2020).
 195. R. Oukhrib, E. I. Issami, B. El Ibrahim, K. El Mouaden, L. Bazzi, L. Bammou, A. Chaouay, R. Salghi, S. Jodeh, B. Hammouti, A. Amin-Alami, *Port. Electrochim. Acta*, **35**, 187 (2017).
 196. A. S. Fouda, S. H. Etaiw, D. M. Abd El-Aziz, O. A. Elbaz, *Int. J. Electrochem. Sci.*, **12**, 5934 (2017).
 197. EI-M. Inaam, H. Sara, E. Mohamed, L. Saadia, L. Abdeslam, *Port. Electrochim. Acta*, **33**, 305 (2015).
 198. R. T. Vashi, K. Desai, *Der. Pharma Chemica*, **4**, 2117 (2012).
 199. A. S. Fouda, A. Abdel Nazeer, A. Saber, *J. Korean Chem. Soc.*, **58**, 160 (2014).
 200. A. S. Fouda, S. M. Rashwan, M. M. K. Darwish, N. M. Arman, *Port. Electrochim. Acta*, **36**, 309 (2018).
 201. A. S. Fouda, E. E. El-Katori, S. Al-Mhyawi, *Int. J. Electrochem. Sci.*, **12**, 9104 (2017).

Fabrication and characterization of CdS-Cu₂S thin film heterojunction diode using chemical bath deposition technique

M. K. Dutta*, R. K. Sarkar, S. Karmakar

Department of Physics, Birla Institute of Technology, Mesra, Off-Campus Deoghar, Jasidih, Deoghar - 814142, India

Received: June 14, 2020; Revised: December 19, 2020

Various methods have so far been used to fabricate and characterize CdS-Cu₂S heterojunction thin film devices. In this paper a chemical bath deposition technique was used to synthesize the same on a non-conducting glass substrate. In this fabrication process a cadmium sulfide (CdS) layer was formed by depositing a chemical compound consisting of cadmium chloride, ammonium acetate, thiourea and ammonium hydroxide solution on the glass surface. The copper sulfide (Cu₂S) layer was grown by dipping a small portion of the CdS sample into a cuprous chloride solution. Different doping concentrations of the heterojunction diode were achieved by using boric acid solutions of different molarity. Aluminium dots were deposited on the samples by using a vacuum coating system for measurement of different characteristics through computer interfacing. Both forward and reverse bias I-V and C-V characteristics of the resultant n-CdS and p-Cu₂S heterojunction diode were measured and analyzed for various doping concentrations.

Keywords: Semiconductor devices; heterojunction; chemical bath deposition technique; doping concentration; diode characteristics.

INTRODUCTION

Fabrication and characterization of thin film heterojunction devices has become a subject of interest by the researchers [1, 2]. Among various thin film devices CdS-Cu₂S heterojunction is one of the most interesting devices [3, 4]. Cadmium sulfide (CdS) is a material with a large absorption coefficient and copper sulfide (Cu₂S) is suitable for generating a large amount of photocurrent. Cu₂S is also a very promising agent for different photovoltaic applications because of its unique structure and stoichiometric composition. Thin layer of Cu₂S (0.1 μm to 0.3 μm) has a bandgap of 1.2 eV which is suitable to exhibit high luminescence efficiency [5]. It is a very useful material to act as a p-type semiconductor for solar cells. On the other hand, cadmium sulfide (CdS) is a suitable material for acting as a n-type semiconductor [5]. CdS is a direct bandgap semiconductor having a band gap of 2.4 eV in the visible region [5-8]. CdS is a potential absorber for thin film photovoltaic cells and also acts as an efficient window material which can form a heterojunction with a bandgap material like Cu₂S. CdS thin film (8 μm to 20 μm) was deposited by various research groups [9, 10] using different techniques, namely, vacuum evaporation, spray pyrolysis, electro deposition technique, etc. In this work a CdS-Cu₂S thin film heterojunction was formed by using chemical bath deposition technique (CBDT). CBDT is a very useful method

for growing thin film compound semiconductors using different chemical solutions [2]. Using this method different deposition characteristics such as film thickness, deposition rate, etc. could be controlled easily by varying solution molarity, pH, temperature, etc. This technique is simple and not too expensive also.

THEORY

When two semiconductors of different band gaps are joined together, the atoms of the heterojunction form chemical bonds at the interface. Due to mismatch of lattice constants across the hetero interface there exists a region of crystal dislocation and crystal imperfections which spans over many crystalline layers. This dislocation acts as a scattering center and recombination center for electrons and holes, limiting their mobilities and recombination life time as well. These effects may result in a poor-quality device formation. Device performance can significantly be improved by (a) using materials with nearly equal lattice constants, (b) using alternative layers of semiconducting material, producing a structure called superlattice which reduces the number of dislocations, and (c) choosing the substrate crystal plane that is slightly offset from the major crystal plane so that the distance between the atoms on the substrate surface approximates the distance between the atoms in the deposited film of another semiconductor material [11].

* To whom all correspondence should be sent:

E-mail: manoj@bitmesra.ac.in

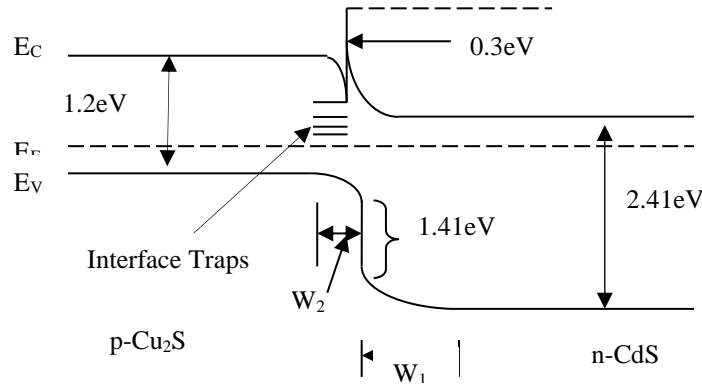


Fig. 1. Energy band diagram of Cu₂S-CdS heterojunction

Fig. 1 shows the energy band diagram of Cu₂S-CdS heterojunction [12]. The built-in barrier potential is shown in Eqn. (1):

$$V_{bi} = \frac{qN_{dn}W_1^2}{2\varepsilon_n} + \frac{qN_{ap}W_2^2}{2\varepsilon_p} \quad (1)$$

where ε_n and ε_p are permittivities, N_{dn} and N_{ap} are the carrier concentrations of CdS and Cu₂S materials, respectively, W_1 and W_2 are widths of the depletion regions, q is the electronic charge, V_{bi} is the built-in potential. Here it is assumed that ε_n and ε_p have the same order of magnitude.

Total depletion width shown in Eqn. (2) is equal to:

$$W = W_1 + W_2 = \left\{ \frac{2\varepsilon_n\varepsilon_p(N_{dn} + N_{ap})^2 V_{bi}}{qN_{dn}N_{ap}(\varepsilon_n N_{dn} + \varepsilon_p N_{ap})} \right\}^{1/2} \quad (2)$$

The junction capacitance shown in Eqn. (3) is equal to:

$$C_j = \left\{ \frac{qN_{dn}N_{ap}\varepsilon_n\varepsilon_p}{2(\varepsilon_n N_{dn} + \varepsilon_p N_{ap})(V_{bi} + V)} \right\}^{1/2} \quad (3)$$

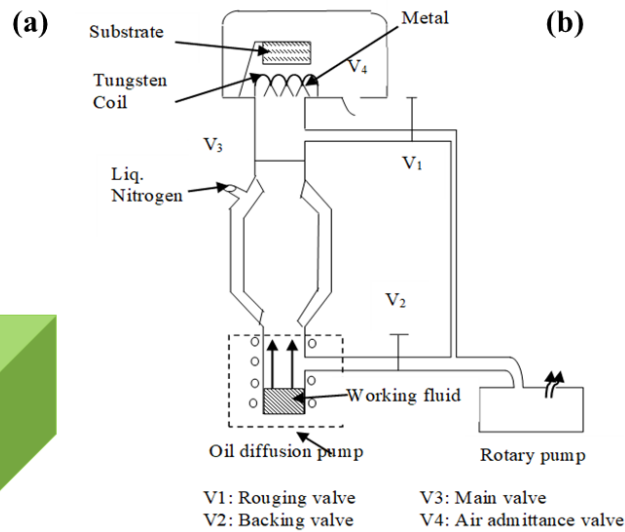
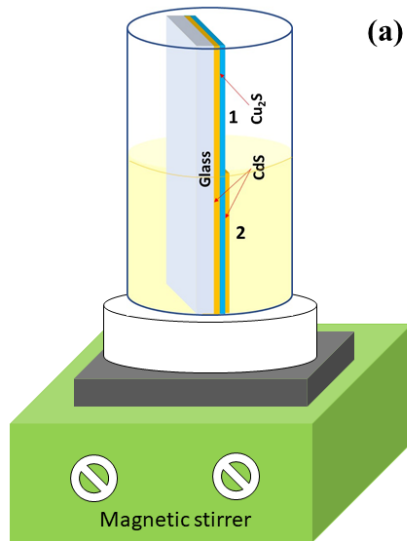


Fig. 2. Schematic illustrations of (a) CBDT setup and (b) vacuum coating unit

where V is the total applied voltage. Since the barrier heights seen by electrons and holes are not the same in case of heterojunction so their current-voltage characteristics are derived on the basis of thermionic emission of carriers over the barrier shown in Eqn. (4):

$$J = A^* T^2 \exp\left(\frac{-\Phi}{kT}\right) \quad (4)$$

where A^* is the effective Richardson constant and Φ is the effective barrier height [8, 11, 12].

EXPERIMENTAL

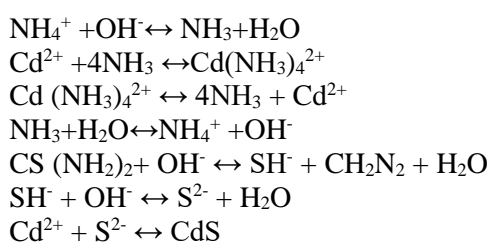
All chemicals used in this study were of 99.99% spectroscopic purity, manufactured by Aldrich.

Cleaning of glass samples

Glass samples were cleaned with trichloroethylene (TCE), acetone and methanol before they were used for deposition.

Deposition of CdS thin film on glass surface

(a) *Synthesis of CdS thin film.* A mixture of 0.5 cm³ of 10⁻³ M CdCl₂ solution, 9.5 cm³ of 0.005M (NH₂)₂CS (thiourea) solution, 0.8 cm³ of 0.01M NH₄Ac (ammonium acetate) solution, 5.6 cm³ of 0.25M NH₄OH solution was prepared. The solution was taken in a glass beaker and placed on the pad of a magnetic stirrer. The schematic of the deposition setup is illustrated in Fig. 2(a). The heater was switched on and the temperature was fixed at 75-80°C. The glass samples were immersed in the solution on stirring for 1.5 h until the solution became deep yellow. CdS was formed by the chemical reaction of CdCl₂ with (NH₂)₂CS buffered by NH₄OH and NH₄Ac. The chemical reactions for the formation of CdS layer are as follows [13, 14]:



(b) *Deposition of Cu₂S thin film.* The Cu₂S film was grown by conversion of the CdS film by chemical reaction with cuprous chloride (Cu₂Cl₂). A Cu₂Cl₂ solution was prepared by mixing Cu₂Cl₂ powder in distilled water. Now by dipping the whole slide in the solution for 2 min the CdS film was converted into Cu₂S film following the reaction shown below [15]:



A topotaxial layer of copper sulfide was formed by mutual exchange of two Cu⁺ ions for each Cd²⁺ ion from the CdS layer. The excess amount of Cu₂Cl₂ was removed from the samples by rinsing repeatedly with distilled water.

Formation of the CdS-Cu₂S junction

A second layer of CdS was grown on a selected portion of the Cu₂S film for the formation of the CdS-Cu₂S heterojunction. Initially some composite mixture prepared for synthesis of CdS thin film was taken in a glass beaker and a half portion of the sample was immersed in the solution. The beaker was placed on a magnetic stirrer and the solution was stirred in such a way that the solution could not wet the whole slide. In this way CdS thin film could be deposited on the half portion of the slide. This selected deposition step was repeated thrice. At this step proper masking arrangement was made to cover the upper portion of the Cu₂S film. Such an arrangement led to a clean well-defined junction at

the half portion of the sample. The samples thus prepared were kept at room temperature for a day for proper drying.

Metallization

To deposit metal dots on the as-prepared samples a vacuum coating system was used. Al metal wire (99.999% pure) was cut into small pieces which were bent according to the shape ‘^’ and a metal mask with circular aperture was used. The mask and the metal wires were ultrasonically cleaned with trichloroethylene, acetone, methanol and distilled water. Air admittance valve (V₄) was opened for loading of samples. Metal pieces were loaded on the heating filament. The mask was loaded on the top of the sample and the chamber was closed. For the deposition of metal dots, the required chamber pressure was of the order of 10⁻⁶ bar. This was achieved by joining the deposition chamber to the vacuum line consisting of a rotary pump and an oil diffusion pump. In addition to this, as p = nKT (where the terms have their usual significance), in order to achieve the operating pressure, the chamber was covered externally by flowing boiling liquid nitrogen through the outer jacket of the chamber. The whole process of metal dot deposition is conceptually depicted in Fig. 2(b) [16].

Preparation of doping solution

Boron was doped into the CdS-Cu₂S heterojunction with different concentrations by dipping region 2 of the as-prepared diodes (as indicated in Fig. 2(a)) in a solution that was prepared by adding aqueous solutions of H₃BO₃ of different molarity to the CdCl₂ solution. During this process, region 1 was masked properly to avoid Cd contamination in this layer. The pH of the resultant solution was measured by using Global digital pH meter of type DpH-500. The pH values of the different solutions were calibrated noting that pH=10.68, 10.58 and 10.56 corresponded to 0 M, 10⁻⁴ M, and 10⁻² M H₃BO₃ solution, respectively. Thus, lowering of the pH value of the above-mentioned solution is indicative of constant enhancement in the B³⁺ ion concentration in the solution, and hence, of a higher probability of doping. This process enabled us to dope the CdS layer with boron directly and the Cu₂S layer indirectly through diffusion, thereby forming a boron-doped n-CdS and p-Cu₂S heterojunction diode.

X-ray diffraction (XRD)

The as-prepared diodes were examined by XRD using CuKα radiation. To accomplish this, the two halves of the diodes were exposed to X-rays

separately in a Rigaku made SmartLab SE diffractometer. Before recording the XRD spectra, the instrument was calibrated by using the (422) diffraction peak of a standard silicon sample.

Electrical measurements

The current-voltage characteristics of the fabricated devices were studied using an HP multimeter of microvolt resolution and current sensitivity of $\pm 1\%$ of the actual value. The RS-232 port was used for computer interfacing. The capacitance of the device was measured with the help of an HP LCR meter. In order to apply a bias voltage, a triple output HP power supply was used.

RESULTS AND DISCUSSION

In this work, the crystalline compositions of the two halves of the as-prepared CdS-Cu₂S heterojunction diodes, and their I-V and C-V characteristics, were determined.

Fig. 3 shows the typical XRD spectra recorded corresponding to the portions marked as 1 and 2 in Fig. 2(a) for one of the as-prepared undoped samples.

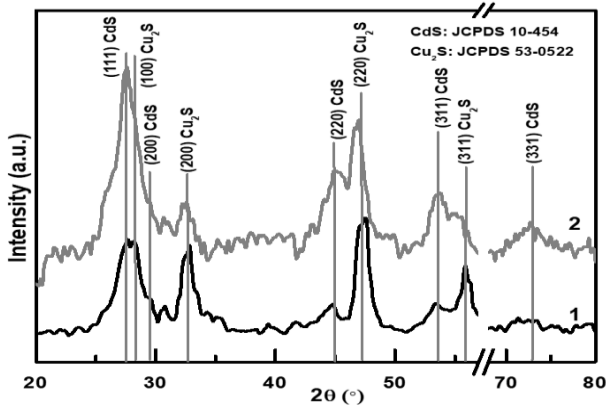


Fig. 3. Typical XRD spectra of the two halves of one of the undoped diodes, as indicated in Fig. 2(a).

Both spectra are found to contain some well-defined peaks signifying the presence of crystalline species within the sample. However, a significant amount of noise, which is characteristic of defects within a sample, is also seen in both spectra. This noise is consistent with the chemical synthesis processes that are quite different from the high-temperature routes. Comparing the XRD spectra of the sample with the standard XRD data, (the JCPDS card numbers are mentioned in Fig. 3), it was found that both portions 1 and 2 of the sample contain mixtures of crystalline CdS and Cu₂S, however with different mass fractions. In the XRD spectrum corresponding to region 1, the (220) peak of Cu₂S is the most intense one. On the other hand, the intensity of the (111) peak corresponding to CdS (the most intense peak for CdS) is higher than that of the (220)

peak of Cu₂S. The XRD spectra are thus consistent with the structure of the diode, as is schematically demonstrated in Fig. 2(a). No noticeable changes were detected in the XRD spectra for the doped diodes, possibly because boron did not take part in the formation of the crystallites; rather, it took place in the interstitial sites.

I-V and C-V characteristics were measured for a number of CdS-Cu₂S thin film heterojunction diodes, which were fabricated by repeating the whole experimental procedure (Figs. 4 and 5). The qualitative behavior of the undoped and the doped diodes was almost the same with a quantitative difference. The cut-in voltage (V_γ) was approximately 0.3 V for the undoped case (Fig. 4). For the doped diodes, the value of V_γ was found to vary between 2-3 V (for the diodes doped with 10^{-4} M H₃BO₃ solution), and between 3-4 V (for the diodes doped with 10^{-2} M H₃BO₃ solution). The change in V_γ for different doping cases could be attributed to a change in barrier height or built-in potential. From the expression of current density (J) the following expression (Eqn. 5) can be obtained [11]:

$$\frac{J_1}{J_2} = \frac{(V_{bi})_1}{(V_{bi})_2} \exp(-38\Delta V_{bi}) \quad (5)$$

where ΔV_{bi} is the change in barrier height. This expression shows that a slight change in barrier height drastically changes the current density. The change in barrier height can be explained as follows: CdS is an n-type material and the associated Fermi level is closer towards the conduction band whereas Cu₂S is a p-type material with Fermi level closer to the valence band. Boron is an n-type dopant to CdS and a p-type to Cu₂S. Boron is doped in the form of B³⁺ ions derived from H₃BO₃ which was mixed in the solution that was already prepared for depositing CdS in the second phase. As the Cu₂S thin film was dipped in the doping solution the B³⁺ ions penetrated inside the material and introduced p-type impurity. But as the CdS film was earlier deposited on the whole substrate so the effect of doping on the converted Cu₂S layer will be less as compared to the single CdS layer. Therefore, the doped CdS will create a larger barrier height with the doped or undoped Cu₂S as compared to undoped CdS layer [5]. Slight change of barrier height causes a large change in the values of J and V_γ [11, 17]. The C-V characteristic shows that the forward capacitance increases with voltage for doped and undoped diodes (Fig. 5). Increase in the forward capacitance may be due to charge storage at the semiconductor junction [8, 17]. Charge storage is caused by the charges that cannot follow up the change in signal voltage. All measurements were performed at a frequency of 100 kHz because at this

frequency the energy levels are properly populated and therefore a significant accumulation of charges was obtained. The reverse capacitance changes very slowly with the voltage for the undoped case and remains almost constant for doped diodes (Fig. 5). This result may be due to non-uniform film structures along with other nonidealities such as interface traps, etc. [8, 17].

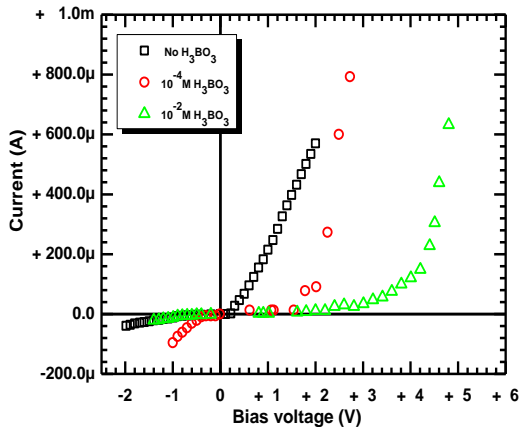


Fig. 4. I-V characteristics of the as-prepared diodes.

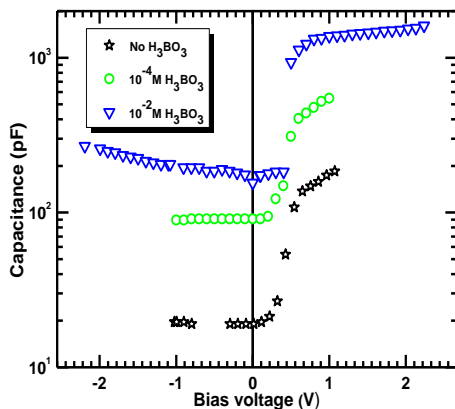


Fig. 5. C-V characteristics of the as-prepared diodes.

CONCLUSIONS

In this paper a low-cost CdS-Cu₂S heterojunction fabrication by using chemical bath deposition technique was discussed. I-V, C-V characteristics of the fabricated heterojunction diode were measured by computer interfacing measurement technique.

I-V characteristics showed that, as the doping concentration changes, the cut-in voltage of the heterojunction diode also changes due to a change in the barrier height. Both the forward and reverse bias currents were also found changing with doping concentration. C-V characteristics showed the known characteristic changes due to the change in doping concentration.

Acknowledgement: The authors would like to thank Prof. R. C. Jha, Director, and all other authorities of Birla Institute of Technology, Mesra Off-Campus Deoghar, for their cooperation and support to carry out this work.

REFERENCES

1. E. Gaubaev, I. Brytavskiy, T. Ceponis, J. Kusakovskij, G. Tamulaitis, *Thin Solid Films*, **531**, 131 (2013).
2. A. E. Rakhshani, A. S. Al-Azab, *J. Phys.: Condens. Matter*, **12**, 8745 (2000).
3. L. Mahdjoubi, M. Derdouri, M. Benmalek, *Solar Cells*, **5**, 205 (1982).
4. Shrotriya, V. Rajaram, Advanced Materials and Radiation Physics, AIP Conference Proceedings 1675, M. M. Sinha et al. (eds.), 0300561, 2015.
5. K. L. Chopra, S. R. Das, *Thin Film Solar Cells*, Springer US, 1983, ISBN: 978-1-4899-0418-8.
6. H. S. Solimena, A. A. M. Farag, M. M. Saadeldinc, K. Swaby, *Acta Physica Polonica A*, **127** (2015).
7. A. Ashour, *Journal of Optoelectronics and Advanced Materials*, **8**, 1447 (2006).
8. S. M. Sze, K. K. Ng, *Physics of Semiconductor Devices*, 3rd edn., Wiley, 2008.
9. S. Rohit, *IOSR Journal of Electrical and Electronic Engineering*, **2**, 47 (2012), ISSN: 2278-1676.
10. M. Ray, P. Chattopadhtay, *Indian Journal of Pure and Applied Physics*, **35** (1997).
11. B. G. Streetman, S. K. Banerjee, *Solid State Electronic Devices*, 6th edn., PHI Learning Pvt. Ltd. New Delhi, 2009.
12. V. Jayaraman, Master's Thesis. University of Kentucky, Paper 267, 2005.
13. O. Isaiah Oladeji, L. Chow, *J. Electrochem. Soc.*, **144** (1997).
14. M. M. El Nahass, A. M. A. El Barry, *Indian Journal of Pure & Applied Physics*, **45**, 465 (2007).
15. E. R. Hill, B. G. Keramidas, *Revue de Physique Appliquée*, **1**(3), 189 (1966).
16. D. M. Mattox, *The Foundations of Vacuum Coating Technology*, Noyes Publications, 2003, ISBN 0-8155-1495-6.
17. D. Neamen, Dh. Biswas, *Semiconductor Physics and Devices (SIE)*, 4th edn., McGraw Hill Education, 2017.

Modeling and simulating of heat transfer for three-layer skin using an external thermal pulse

R. K. Yaghoobi¹, Masoud Khajenoori^{2*}, Maryam Khajenoori²

¹Association of Freelance Researchers, Ferdows, Iran

²Faculty of Chemical, Gas and Petroleum Engineering, Semnan University, Semnan, Iran

Received: June 29, 2020; Revised: December 23, 2020

The skin heat transfer models have attracted many researchers in recent years for improving the hyperthermia techniques and for evaluating burn injuries. Nevertheless, many of these researchers, which used the one-layer skin heat transfer model, could not provide useful information about the heat transfer in the laminar structure of skin tissue. Some researchers, which used the multi-layer skin heat transfer model, have questionable results in some cases. Therefore, in this study, we first developed a one-dimensional heat transfer model for a three-layer skin. Then, we investigated the effect of blood perfusion in this heat transfer model under the conditions of thermal equilibrium and the conditions of applying the external thermal pulse to the skin surface. For this work, we provided a direct solution for the conditions of thermal equilibrium and an approximate solution using a finite-difference method (FDM) for the conditions of applying an external thermal pulse. Finally, we evaluated the amount of thermal expansion and damage resulted from different thermal pulses and blood perfusion rates. Generally, the results of this study revealed that the blood perfusion rate has a large influence on the temperature distribution, thermal expansion and thermal damage, so that it significantly can lessen the burn degree, especially of the dermis and subcutaneous fat layers. Nevertheless, skin surface temperature according to the arterial blood temperature can completely reverse the effects of the blood perfusion rate in the temperature distribution of skin tissue. These results also showed that different structural and thermal properties of skin layers, especially thickness and thermal conductivity along with the blood vessels penetrated in the skin layers, can turn the skin tissue into a special thermal insulator, which well disagrees with any change in temperature in the skin surface.

Keywords: Three-layer skin model, Heat transfer, Pennes model, Thermal damage

INTRODUCTION

Skin is one of the most important thermoregulation organs in the human body that continuously regulates the temperature of internal tissues by using different modes of heat transfer such as conduction, convection, radiation and perspiration [1]. Hence, understanding the heat transfer process in the skin is a major challenge in the thermodynamic studies to improve local hyperthermia techniques [2-7] and also evaluate the burn injuries [8].

The main objective of local hyperthermia techniques is also to raise the temperature of the diseased tissue to a therapeutic value above the core temperature, and then thermally destroy it [9-11]. Accordingly, the therapeutic value is a very important factor in this therapy. However, there is no consensus as to what is the safest or most effective target temperature for hyperthermia. For example, some researchers defined this value for the local hyperthermia between 39.5 and 40.5°C [12] and some others defined it between 41.8 and 42°C (Europe, USA) to near 44°C (Japan, Russia) [13]. Furthermore, current studies have confirmed that the heat transfer within the skin is a heat conduction process coupled with physiological processes such as

blood perfusion, gland activity, tissue metabolism and sometimes heat losses of the hair [1, 14, 15], so that these physiological processes can create different self-regulation activities by changing the characteristics of each of the skin layers. Therefore, finding an optimal thermal pattern for local hyperthermia techniques and evaluating burn injuries request comprehensive information for the heat transfer mechanism of skin tissue.

Currently, various histological studies have been done on body tissues, especially skin tissues. Nevertheless, although these studies have provided remarkable results about macroscopic parameters such as the core temperature, these studies, due to laboratory and technical limitations, could not usually provide useful information about the temperature distribution of skin layers. Hence, researchers have often focused on mathematical models based on Fourier's heat transfer law for understanding the heat transfer mechanism of skin layers. In this regard, Pennes [16], who proposed a bio-heat transfer equation based on this law, is one of the researchers that have provided a general model for evaluating heat transfer in different body tissues. It is remarkable that this bio-heat transfer equation is currently the basis of many studies in thermal

* To whom all correspondence should be sent:
E-mail: khajenoori1390@gmail.com

diagnostics [17], thermal parameter estimation [18-20] and burn injury evaluation [8, 21, 22] for evaluating different modes such as different boundary conditions and blood perfusion rates. For example, Vyas and Rustgi [23] obtained an analytical solution based on a cylindrically symmetric model (in which the laser beam is traveling only in the z -direction) to study the laser-tissue interaction. Newman [24] investigated the thermal washout in biological tissues by using Green's function method. Zhu and Weinbaum [25] applied the Green's function method to solve a series of steady-status bio-heat transfer problems in which the Pennes' perfusion term was not included. Durkee and Antich [26, 27] addressed the time-dependent Pennes' equation in 1-D multi-region Cartesian and spherical geometry. Legendijk *et al.* [28] also contributed to understanding some specific heat transfer problems during a tumor hyperthermia process. Kengne [29] investigated the effect of the temperature-dependent thermal conductivity on the nonlinear temperature distribution by using the Taylor expansion method. Deng [30] analyzed the Pennes bio-heat transfer equation for one-layer skin influenced by various heat sources. In [1, 14, 15] Xu *et al.* analytically examined the biothermomechanic behavior of skin tissue under various boundary conditions by using the one-layer Pennes bio-heat transfer equation. They also examined the biothermomechanic behavior in the multi-layer Pennes by the bio-heat transfer equation using the finite-difference method. Lin and Chou [31] proposed a numerical scheme combined with differential transform and finite-difference methods for solving the Pennes bio-heat transfer equation. They examined the one-layer skin heat transfer model in the constant temperature surface. Lai and Chan [32] developed a two-dimensional heat transfer model for a 12-segment human body. They stated that their model was validated for predicting skin and body core temperatures under a wide range of thermal conditions. Strakowska *et al.* also evaluated the Pennes bio-heat transfer equation for a skin tissue, in which each of the three layers had different thermal parameters. These researchers finally reported that there was a rate of significant fitting between the temperature of the skin surface estimated by the Pennes equation and temperature recorded by a thermal camera from the skin surface in a certain time interval [33].

Generally, although these studies provided interesting results in some cases for improving the therapeutic applications, their results were questionable in some cases. For example, some of these researchers [1, 14, 15] reported that an external heat source in addition to the strain caused by thermal expansion generates a mechanical strain, while a thermal loading (external heat source) based on the solid mechanics only generates thermal strain in the

solid material. Some other researchers [1, 30], which investigated the influence of blood perfusion rate on the temperature distribution of skin tissue, also considered that increasing the blood perfusion rate generally decreases the temperature distribution of skin tissue, while the temperature of skin tissue in addition to the blood perfusion rate depend on air temperature adjacent to skin surface. On the other hand, the human skin consists of three layers: the epidermis, the dermis and the subcutaneous layer. The two internal layers, especially the subcutaneous layer is primarily made up of fat and connective tissue [34]. It is remarkable that the fat insulates the body against both heat and cold. Therefore, the thermal response of these layers to an external heat source can turn from a conductor to an insulator and conversely [34], because the fat layers act as a thermal inductor against heat. This means that the temperature distribution resulted from an external heat source has special dynamics. Nonetheless, some of these researchers [1, 14, 15], who examined the heat transfer in the three skin layers, did not report such dynamics. Furthermore, it is also amazing that other researchers have reported their outcomes at temperatures above 45°C regardless of the fact that at temperatures above 45°C the skin changes due to the burn. This is another questionable result of these researches.

Therefore, in this study, we provided a one-dimensional bio-heat transfer model based on the Pennes equation that presented interesting results about the dynamics of skin heat transfer and also the thermal expansion and damage caused by an external heat source on the three skin layers. The remainder of this paper is organized as follows: Sections 2 and 3 present the heat transfer equations and boundary conditions of the proposed model for three skin layers. Section 4 provides equilibrium temperature distribution in the three skin layers by solving the equations of the proposed model under the condition of thermal equilibrium of skin tissue. Section 5 shows the total temperature distribution resulted from a thermal pulse applied on the skin surface which obtained from the solution the equations of the proposed model by using the backward finite-difference method (BFDM), which is also known as the backward Euler method. Sections 6 and 7 provide the thermal expansion and damage created by different thermal pulses and blood perfusion rates. Finally, section 8 presents a brief conclusion about the results obtained in this research.

Heat transfer equations of a three-layer skin

As stated, the heat transfer in the skin layers is a heat conduction process coupled with blood perfusion. Hence, this process is also dependent on the size of the blood vessels. In addition, since the thermal equilibration length of blood vessels (L_{eq})

[35, 36] in the skin tissue is significantly shorter than the length of the blood vessel in this tissue, i.e. about 2×10^{-5} to 3×10^{-5} mm [1, 37], the temperature of ejected blood through the vessels is approximately equal to the temperature of the skin tissue. These conditions also confirm that the Pennes bio-heat transfer equation suffices to model the heat transfer in the two internal layers of the skin [1, 38]. It is also suitable to model the heat transfer in the outer layer of the skin.

The Pennes equation is a derivation of Fourier's heat transfer equation and general bio-heat transfer equation [16]. This equation is defined as follows:

$$\rho c \frac{\partial T}{\partial t} = k \frac{\partial^2 T}{\partial z^2} + Q_{met} + Q_b(T) \quad (1)$$

where ρ , c and k are the density, specific heat and thermal conductivity of the skin tissue, respectively. Q_{met} is the metabolic heat generation in the skin tissue and Q_b is the heat generated by vessels and is expressed as follows:

$$Q_b(T) = \omega_b \rho_b c_b (1 - \mu)(T_a - T) \quad (2)$$

where ρ_b and c_b refer to blood. ω_b is the blood perfusion rate. T_a and T are the temperature of arterial blood and skin tissue, respectively. μ has been usually considered equal to zero [1, 16, 31]. It also seems that this parameter is a thermal friction coefficient, which Pennes added to its equation and considered that its value can be between 0 and 1.

Proposed model for three skin layers

In this work, we investigated the heat transfer in one-dimension for three layers of the skin (see Fig. 1). This approximation is good when the heat is propagated in the direction perpendicular to the skin surface (e.g. during laser heating). As shown in Fig. 1, we assumed the skin tissue as three cubes with infinite length and width, and finite depth. Therefore, we simplified the Laplace operator in equation (1) for each of the skin layers as equation (3). In other words, we actually used a one-dimensional model as outlined at the beginning of the next subsection.

$$\nabla^2 T = \frac{\partial^2 T}{\partial z^2} \quad (3)$$

Accordingly, by using equations (1) and (3) we rewrote the heat transfer equations for each of the three skin layers as follows:

$$\begin{cases} \rho_e c_e \frac{\partial T_e}{\partial t} = k_e \frac{\partial^2 T_e}{\partial z^2} + Q_{e,met} \\ \rho_d c_d \frac{\partial T_d}{\partial t} = k_d \frac{\partial^2 T_d}{\partial z^2} + Q_b(T_d) + Q_{d,met} \\ \rho_f c_f \frac{\partial T_f}{\partial t} = k_d \frac{\partial^2 T_f}{\partial z^2} + Q_b(T_f) + Q_{f,met} \end{cases} \quad (4)$$

Notations e , d and f represent the epidermis, dermis and subcutaneous fat layers, respectively. As seen in the equation relevant to the epidermis layer, we do not consider the blood perfusion term for this layer, because the blood perfusion of this layer is negligible. We also assumed that the heat wasted through sweat glands and hairs is negligible and the thermal properties of skin layers are homogeneous. In the next section, we provided the boundary conditions for each of the skin layers.

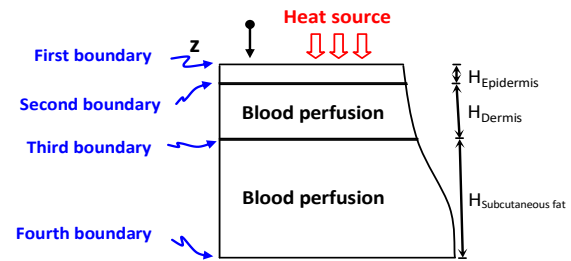


Fig. 1. The corresponding idealized skin model

Boundary conditions of three-layer skin

As shown in Fig. 1, there are four boundaries in the one-dimensional heat transfer model for three-layer skin. The first boundary is related to the temperature of the skin surface that is equivalent to the temperature generated by the external heat source on this surface. The second boundary is located between the epidermis and dermis layers. Similarly, the third boundary is located between the dermis and the subcutaneous fat layer. Second and third boundaries have the same temperature and heat flux profiles. The last boundary is between the subcutaneous fat layer and the internal layer (fat layer). The temperature of this boundary is approximately equal to the core temperature, i.e. $\sim 37^\circ\text{C}$ [39]. Therefore, we defined the boundary conditions of the three skin layers as follows:

$$\left\{ \begin{array}{l} C_1: T_e(0,t) = Q_{ext}(t) \\ C_2: T_e(H_e,t) = T_d(0,t) \\ C_3: k_e \frac{\partial T_e(H_e,t)}{\partial z} = k_d \frac{\partial T_d(0,t)}{\partial z} \\ C_4: T_d(H_d,t) = T_f(0,t) \\ C_5: k_d \frac{\partial T_d(H_d,t)}{\partial z} = k_f \frac{\partial T_f(0,t)}{\partial z} \\ C_6: T_f(H_f,t) = T_c \end{array} \right. \quad (5)$$

where T_c is the core temperature. In the next section, we solved the equations of the proposed model under the conditions of thermal equilibrium of skin tissue.

Equilibrium temperature distribution

As we know, the equilibrium temperature distribution in the three skin layers can be obtained through solving equations (4) at time $t = 0$. Therefore, we can rewrite the heat transfer equations of the three skin layers under the conditions of thermal equilibrium as:

$$\left\{ \begin{array}{l} a: k_e \frac{\partial^2 T_e(z_e,0)}{\partial z_e^2} + Q_{e,met} = 0 \\ b: k_d \frac{\partial^2 T_d(z_d,0)}{\partial z_d^2} + \omega_b \rho_b c_b (1-\mu)(T_a - T_d(z_d,0)) + Q_{d,met} = 0 \\ c: k_f \frac{\partial^2 T_f(z_f,0)}{\partial z_f^2} + \omega_b \rho_b c_b (1-\mu)(T_a - T_f(z_f,0)) + Q_{f,met} = 0 \end{array} \right. \quad (6)$$

Similarly, we rewrote the boundary conditions in $t = 0$ as equations (7), with the exception that we replaced the first boundary condition (C_1 in equations (5)) with a new boundary condition (C_1 in equations (7)), because this boundary, due to $Q_{ext}(0) = 0$ exchanges the heat of skin surface as the convective. Therefore, this new boundary condition is equivalent to heat flows exchanged between the skin surface and the air. In these equations, T_{air} is the air temperature in adjacent to the skin surface. h_{air} is also the heat convection coefficient between the skin surface and the surrounding air.

$$\left\{ \begin{array}{l} C_1: -k_e \frac{\partial T_e(0,0)}{\partial z_e} = h_{air}[T_{air} - T_e(0,0)] \\ C_2: T_e(H_e,0) = T_d(0,0) \\ C_3: k_e \frac{\partial T_e(H_e,0)}{\partial z_e} = k_d \frac{\partial T_d(0,0)}{\partial z_d} \\ C_5: T_d(H_d,0) = T_f(0,0) \\ C_4: k_d \frac{\partial T_d(H_d,0)}{\partial z_d} = k_f \frac{\partial T_f(0,0)}{\partial z_f} \\ C_6: T_f(H_f,0) = T_c \end{array} \right. \quad (7)$$

Table 1. Values employed for the parameters of the proposed model

Variant	Value	Unit
Blood density	1060	Kg/m ³
Blood specific heat	3770	J/Kg.°C
Density		
Epidermis	1190	Kg/m ³
Dermis	1116	
Subcutaneous fat	971	
Skin specific heat		
Epidermis	3600	J/Kg°C
Dermis	3300	
Subcutaneous fat	2700	
Thermal conductivity		
Epidermis	0.235	W/m°C
Dermis	0.445	
Subcutaneous fat	0.185	
Thickness		
Epidermis (H _e)	0.1	mm
Dermis (H _d)	1.5	
Subcutaneous fat (H _f)	4.4	
Metabolic heat generation		
Epidermis	368.1	W/ m ³
Dermis	368.1	
Subcutaneous fat	368.1	
Thermal expansion coefficient		
Epidermis	1e-4	1/°C
Dermis	1e-4	
Subcutaneous fat	1e-4	
Body core temperature (T _c)	37	°C
Arterial blood temperature (T _a)	37	°C
Air temperature (T _{air})	25	°C

Table 1 provides the values employed for the parameters of the proposed model. According to these values, the characteristic equation obtained from the differential equations (6b) and (6c) have a delta greater than zero ($\Delta > 0$). Therefore, the general solution of these differential equations is as follows:

$$\begin{cases} T_e(z_e,0) = \frac{-Q_{e,met}}{2k_e} z_e^2 + Az_e + B \\ T_d(z_d,0) = Ce^{x_d z_d} + De^{-x_d z_d} + y_d \\ T_f(z_f,0) = Ee^{x_f z_f} + Fe^{-x_f z_f} + y_f \end{cases} \quad (8)$$

$$W = \begin{bmatrix} A \\ B \\ C \\ D \\ E \\ F \end{bmatrix}, \quad P = \begin{bmatrix} -h_{co}T_{air} \\ y_d + \frac{Q_{e,met}H_e^2}{2k_e} \\ Q_{e,met}H_e \\ y_f - y_d \\ 0 \\ T_c - y_f \end{bmatrix}$$

$$\begin{cases} x_d = \sqrt{\frac{\omega_b \rho_b c_b (1-\mu)}{k_d}} \\ x_f = \sqrt{\frac{\omega_b \rho_b c_b (1-\mu)}{k_f}} \\ y_d = T_a + \frac{Q_{d,met}}{\omega_b \rho_b c_b (1-\mu)} \\ y_f = T_a + \frac{Q_{f,met}}{\omega_b \rho_b c_b (1-\mu)} \end{cases}$$

The particular solution of these equations by using the boundary conditions provided in equations (7) creates a system of linear equations as follows:

$$M.W = P \quad (9)$$

$$M = \begin{bmatrix} k_e & -h_{co} & 0 & 0 & 0 & 0 \\ H_e & 1 & -1 & -1 & 0 & 0 \\ k_e & 0 & -k_d x_d & k_d x_d & 0 & 0 \\ 0 & 0 & e^{x_d H_d} & e^{-x_d H_d} & -1 & -1 \\ 0 & 0 & k_d x_d e^{x_d H_d} & -k_d x_d e^{-x_d H_d} & -k_f x_f & k_f x_f \\ 0 & 0 & 0 & 0 & e^{x_f H_f} & e^{-x_f H_f} \end{bmatrix}$$

Solving this system of linear equations by using the Gauss-Jordan elimination method [40] gets the coefficients (A-F) of equations (8). Table 2 summarizes these coefficients for three different blood perfusion rates at air temperature of 25°C and 40°C, which we calculated by the Gauss-Jordan elimination method.

Fig. 2 shows the simulation results of equations (8) by using these coefficients. As shown in Fig. 2, the equilibrium temperature distribution in the three skin layers depends on the blood perfusion rate (ω_b) and the air temperature in the adjacent to the skin surface (T_{air}), so that if the air temperature is lower than the arterial blood temperature, increasing the blood perfusion rate exponentially enhances the temperature of the three skin layers (Fig. 2a) and if the air temperature is higher than the arterial blood temperature, increasing the blood perfusion rate exponentially reduces the temperature of three skin layers (Fig. 2b). Therefore, the blood perfusion rate is one of the effective self-regulatory activities in the skin tissues for returning the skin temperature to the arterial blood temperature. The air temperature also plays an important role in this distribution, because self-regulatory activities (brain and heart activities) in the human body always try to hold 37°C for the core temperature by changing the blood perfusion rate.

Table 2. Coefficients of equations (8) under three different blood perfusions

T_{air}	ω_b	A	B	C	D	E	F
25 °C	0.01	862.38	35.13	-0.14	-1.65	0.02	-1.29
	0.001	710.54	33.35	0.14	-3.82	1.12	-4.27
	0.0001	666.05	32.83	3.35	-8.38	6.68	-11.19
40 °C	0.01	-214.86	37.48	0.03	0.41	-0.01	0.32
	0.001	-175.70	37.94	-0.08	0.90	-0.33	1.02
	0.0001	-164.21	38.07	-1.38	1.51	-2.24	2.25

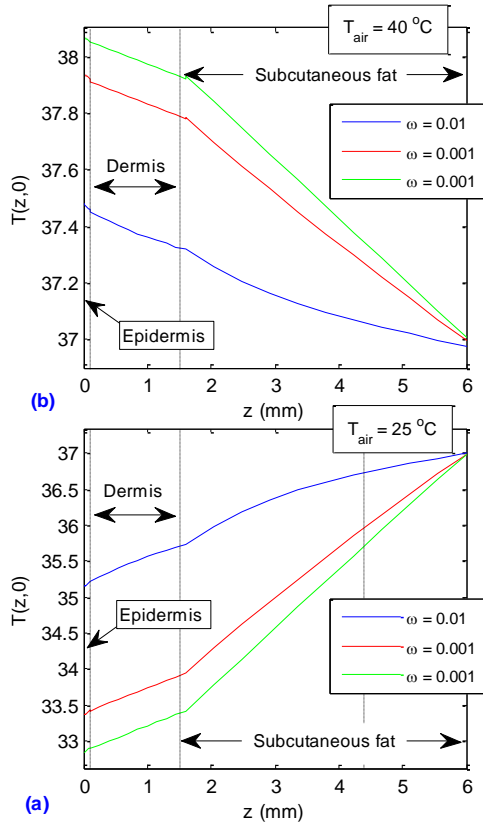


Fig. 2. Effect of blood perfusion rate and air temperature on the equilibrium temperature distribution of the skin layers: a) $T_{air} = 25^{\circ}C$, b) $T_{air} = 40^{\circ}C$

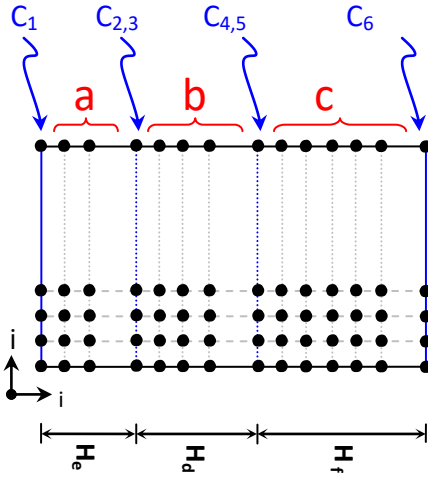


Fig. 3. Finite-difference mesh used for three skin layers

Temperature distribution resulted from an external heat source

Temperature distribution in the three skin layers generally consists of the equilibrium temperature distribution and the temperature distribution resulted from an external heat source. Therefore, this distribution can be calculated by solving the bio-heat transfer equations (4) under the boundary conditions provided in equations (5). Nevertheless, although the general solution of these partial differential

equations is available, the particular solution of these equations by using the boundary conditions provided in equations (5) is inaccessible with the current science. We accordingly solved these partial differential equations by using the backward finite-difference method (BFDM) [41, 42], which is usually known as the backward Euler method. The following equations present the approximate differential equations obtained from equations (4) and (5) by using the BFDM:

$$\left. \begin{aligned}
 a: & \left[\frac{\rho_e c_e}{\Delta t} + \frac{2k_e}{\Delta z_e^2} \right] T_{ei,j} - \frac{\rho_e c_e}{\Delta t} T_{ei,j-1} - \frac{k_e}{\Delta z_e^2} [T_{ei+1,j} + T_{ei-1,j}] = Q_{e,met} \\
 b: & \left[\frac{\rho_d c_d}{\Delta t} + \frac{2k_d}{\Delta z_d^2} - \omega_b \rho_b c_b (1-\mu) \right] T_{di,j} - \frac{\rho_d c_d}{\Delta t} T_{di,j-1} - \frac{k_d}{\Delta z_d^2} [T_{di+1,j} + T_{di-1,j}] \\
 & = Q_{d,met} - \omega_b \rho_b c_b (1-\mu) T_a \\
 c: & \left[\frac{\rho_f c_f}{\Delta t} + \frac{2k_f}{\Delta z_f^2} - \omega_b \rho_b c_b (1-\mu) \right] T_{fi,j} - \frac{\rho_f c_f}{\Delta t} T_{fi,j-1} - \frac{k_f}{\Delta z_f^2} [T_{fi+1,j} + T_{fi-1,j}] \\
 & = Q_{d,met} - \omega_b \rho_b c_b (1-\mu) T_a
 \end{aligned} \right\} \quad (10)$$

$$\begin{aligned}
 C_1: & T_{e1,j} = Q_{ext} \\
 C_{2,3}: & T_{d1,j} = T_{eend-1,j} \\
 C_{4,5}: & T_{f1,j} = T_{dend-1,j} \\
 C_6: & T_{fend,j} = T_c
 \end{aligned}$$

where i and j are the unit vectors of the z -axis and the t -axis in finite-difference mesh, respectively. Fig. 3 provides the finite-difference mesh employed in this study. As shown in the figure, we used the approximate bio-heat transfer equations (a-c) for points located into the skin layers, and the approximate equations of boundary conditions for points located on boundaries. In other words, we computed an equation for each of the points located on the finite-difference mesh by using equations (10). Finally, we solved the system of linear equations generated by these equations by using the Gauss-Jordan elimination method, and got the temperature of each of the mesh points.

Fig. 4 indicates the effect of two different blood perfusion rates on the temperature distribution resulted from a thermal pulse of 0.25 s ($Q(t)$) applied on the skin surface. As seen in this figure, comparing the patterns together generally shows that increasing the blood perfusion rate in the internal layers amplifies the amount of heat absorption, because the temperature of the thermal pulse is higher than that of arterial blood (Fig. 2). Lower temperature distribution in inner layers, especially the subcutaneous fat layers, confirms this issue. These distributions also show that two internal layers, especially the subcutaneous fat layers, like a thermal inductor always disagree with any change in the thermal flow. Areas marked with the red and yellow

arrows in these patterns confirm this issue that the internal layers recoil the heat at the beginning of the thermal pulse and absorb the heat after removing the thermal pulse. In other words, since thermal flow is increased and decreased in the rising and falling edges of the thermal pulse, the internal layers, especially the subcutaneous fat layers, as a thermal inductor disagree with it in these times. Therefore, this means that the thermal response in the skin tissue against an external heat source can become from a conductor an insulator and conversely, due to changing the heat flow. This property of internal layers, in addition to reducing the amount of stress entered on internal tissues, also leads to the gradual expansion and contraction of skin tissue, which are effective processes for reducing thermal damage, especially at low temperatures. In other words, the gradual expansion and contraction slowly convert thermal energy into kinetic energy, which result in less thermal damage. In the next section, we calculated the thermal expansion of the skin.

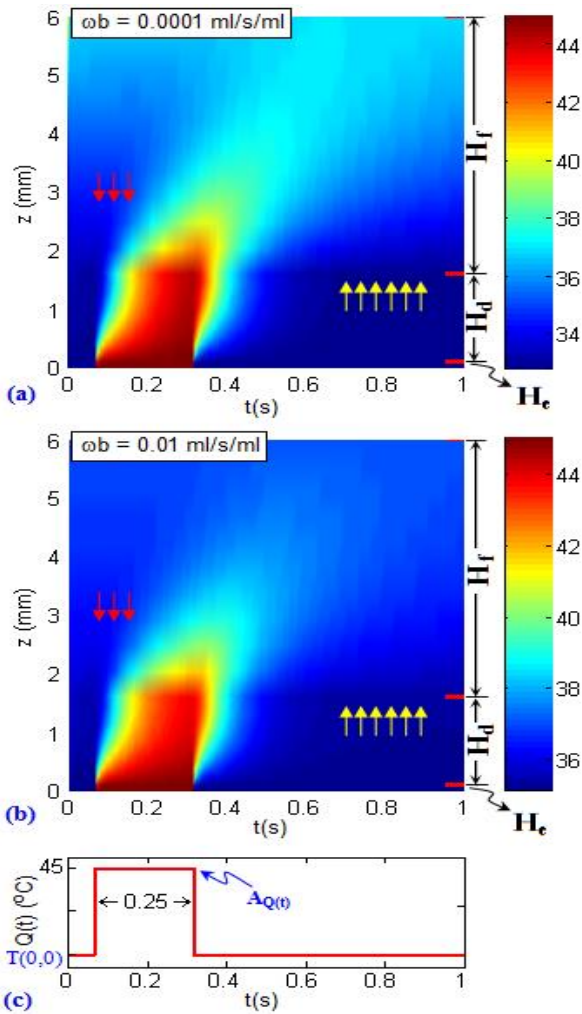


Fig. 4. Effect of two different blood perfusion rates on temperature distribution resulted from a thermal pulse: a) 0.0001 ml/s/ml, b) 0.01 ml/s/ml, c) the thermal pulse.

Thermal expansion in three skin layers

Strain according to Hooke's Law in 1D is defined as follows [43]:

$$\varepsilon = \varepsilon_M + \varepsilon_T \quad (11)$$

where ε_M and ε_T are strains resulted from the mechanical and thermal loading. Since we have only a thermal loading on the skin tissue (ΔT), the term relevant to mechanical strain was zero. Therefore, the strain is:

$$\varepsilon(t) = \varepsilon_T(t) = \alpha_s \Delta T(t) = \frac{\Delta \delta(t)}{\Delta x} \quad (12)$$

where α_s is the linear coefficient of thermal expansion and δ is thermal expansion. According to this equation, we can calculate total thermal expansion as follows:

$$\delta(t) \approx \sum_i \alpha_s \Delta T_i(t) \Delta x_i(t) \quad (13)$$

Fig. 5 provides a part of finite-difference mesh in Fig. 3 that visually describes equation (13). Since we considered the temperature of internal tissue equal to the core temperature (T_c) and also, since α_{air} is much larger than α_s , equation (13) is an acceptable estimation for thermal expansion created in the skin.

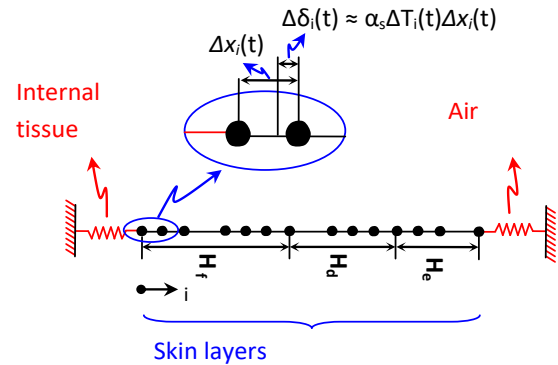


Fig. 5. A part of finite-difference mesh in Fig. 3 employed for calculating the thermal expansion of skin layers.

Fig. 6 illustrates the thermal expansion resulted from the temperature distribution in Fig. 4a. As shown in this figure, total thermal expansion has a gradual increase during applying the thermal pulse, and a gradual decrease after removing the thermal pulse, so that the time constant of the contraction phase is larger than that of the expansion phase in the skin layers. Comparing the thermal expansion of the two internal layers with total thermal expansion generally shows that the cause of a larger time constant in the contraction phase is the subcutaneous fat layer. The cause of the smaller time constant in the expansion phase is the dermis layer.

Besides, although the amount of total thermal expansion is negligible at low temperatures and the

kinetic energy generated by these temperatures cannot disrupt the molecular bonds of proteins, the amount of total thermal expansion at high temperatures due to the excessive kinetic energy can disrupt the molecular bonds of proteins. Fig. 7 shows the total thermal expansion resulted from the thermal pulses of 0.25 s with different amplitudes ($A_{Q(t)}$). As seen in this figure, increasing the temperatures exponentially increases the amount of thermal expansion. Therefore, this amount of thermal expansion coupled with its equivalent kinetic energy at high temperatures can simply disrupt the molecular bonds of protein. This discontinuity changes the nature of materials, and its result is thermal damage. In the following section, we investigated the thermal damage generated by a temperature distribution in the skin.

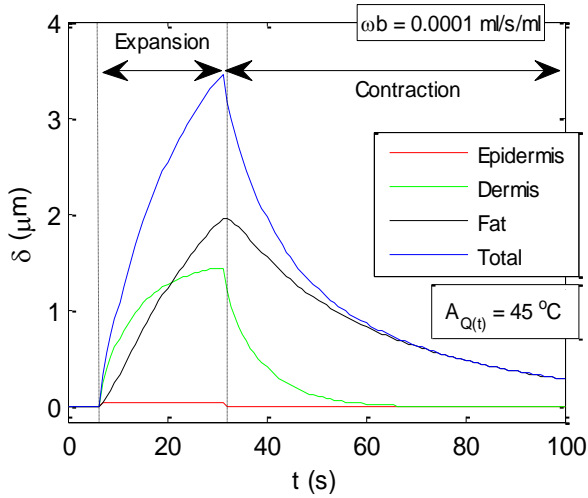


Fig. 6. Thermal expansion in the skin layers

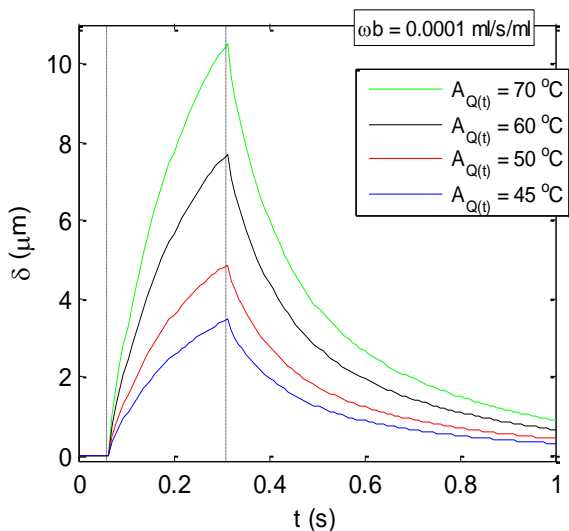


Fig. 7. Thermal damage resulting from thermal pulses of 0.25 s with different amplitudes (see $A_{Q(t)}$ in Fig. 4) in three skin layers.

Total thermal expansion resulted from the thermal pulses of 0.25 s with different amplitudes ($\alpha_s = 0.0001$).

Thermal damage in three skin layers

It is obvious that the temperature is a very important factor to enhance the rate of successful collisions between the particles of a reactant. Therefore, increasing the temperature in the skin tissue amplifies the kinetic energy and causes that the molecules vibrate rapidly and violently. This vibration in the molecules also increases the rate of protein denaturation, which outcome at long term is the thermal damage. So, the thermal damage (Ω) in the skin tissue generally depends on the rate of protein denaturation (k) and exposure time (t) at a given temperature. Henriques and Moritz [44, 45] have accordingly proposed that the thermal damage in a tissue can be measured by the Arrhenius equation [46] as follows:

$$k(T(z)) = \frac{d\Omega(z)}{dt} = Ae^{-\frac{E_a}{R[T(z)+273.15]}} \quad (14)$$

or, equivalently:

$$\Omega(z) = \int_0^t Ae^{-\frac{E_a}{R[T(z)+273.15]}} dt \quad (15)$$

where $R = 8.314 \text{ J}\cdot\text{mol}^{-1}\cdot\text{K}^{-1}$ is the universal gas constant. A is collision frequency, which has a non-linear relationship with activation energy (E_a) [47]. $E_a = 21149.324 + 2688.367 \ln(A)$.

In the present study, the burn injury in the skin is calculated by using the burn integration of 15, with the collision frequency $A = 2.1 \times 10^{98}$ ($E_a = 75005 \text{ J}\cdot\text{mol}^{-1}$). Note that it is now widely accepted that $\Omega = 0.53$, first degree burn; $\Omega = 1$, second degree burn; $\Omega = 10^4$, third degree burn [15].

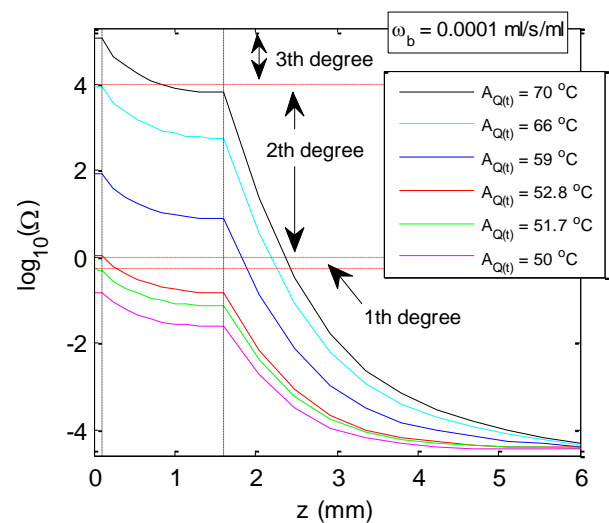


Fig. 8. Thermal damage resulting from thermal pulses of 0.25 s with different amplitudes (see $A_{Q(t)}$ in Fig 4) in three skin layers.

Fig. 8 presents the thermal damage resulted from thermal pulses of 0.25 s with different amplitudes for three skin layers. To better display the status of thermal damage in each of the skin layers, we reported its logarithmic values. The curves of Fig 8 actually indicate that a thermal pulse of 0.25 s in a narrow temperature band (51.8°C to 52.8°C) can create a first-degree burn on the two external layers of skin, especially the epidermis layers. Interestingly, the most severe type of this burn, which occurs in $\Omega \approx 1$ ($T \approx 52.8^\circ\text{C}$), only involves a very small part of dermis layers, while the second-degree burn, which is generated by a thermal pulse of 0.25 s in a wider temperature band (52.8°C to 66.8°C), involves a significant part of dermis layers. Hence, the symptoms of this burn often are blisters and severe pain. But the most serious type of skin burn, i.e. the third-degree burn, which is generated by thermal pulses above 66°C, burns the epidermis and dermis layers and a significant part of the subcutaneous fat layer. Hence, this burn leads to the destruction of the sensory nerve endings of the outer layers. Nevertheless, although the results of Fig. 8 reported a critical condition for skin at high temperatures, the blood vessels in the two internal layers can reduce the amount of thermal damage by regulating the blood perfusion rates. Fig. 9 shows the effect of different blood perfusion rates on the thermal damage resulted from thermal pulses of 0.25 s.

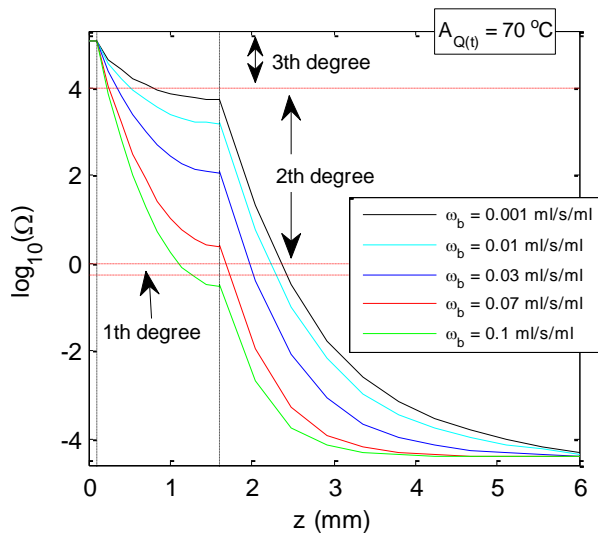


Fig. 9. Effect of different blood perfusion rates on the thermal damage led by thermal pulses of 0.25 s in the three skin layers.

As shown in this figure, increasing the blood perfusion rate significantly decreases the thermal damage in the dermis and subcutaneous fat layers. In other words, the blood vessels with more heat absorption in the higher blood perfusion rate try to hold the skin temperature at the blood temperature (37°C). This process in the vessels leads to reduction

of the thermal damage at 0.25 s. In the next section, we presented a brief conclusion about the results obtained in this research.

DISCUSSION AND CONCLUSION

As stated, some of the researchers [1, 30] generally reported that increasing the blood perfusion rate only reduces the temperature of skin layers, while analytical studying the one-dimensional heat transfer model developed in this work for three-layer skin showed that the thermomechanical responses generated by the laminar structure of skin tissue coupled with the blood vessels penetrated in skin layers extremely depend on the skin surface temperature (Fig. 2). In fact, this temperature can completely reverse the effects of the blood perfusion rate, so that if the skin surface temperature is lower than the arterial blood temperature, increasing the blood perfusion rate exponentially enhances the temperature of skin layers (Fig. 2a). Conversely, if the skin surface temperature is higher than the arterial blood temperature, increasing the blood perfusion rate exponentially reduces the temperature of three skin layers (Fig. 2b). This means that the heat adsorption and desorption performed by the blood vessels depend on the temperature gradient between the arterial blood temperature and the temperature of each point from the skin tissue. Furthermore, the temperature of each point from the skin tissue is proportional to the boundary conditions, especially the skin surface temperature. Therefore, the blood perfusion rate has not the same effect on all the points of skin tissue. The temperature distributions of the three skin layers for two different blood perfusion rates in Fig 4 confirm this issue. These temperature distributions also confirm that thermal and structural properties (Table 1) due to their special arrangement in different skin layers give special flexibility to the skin against heat. For example, as shown in Table 1, the thermal conductivity of the subcutaneous fat layer (0.185 W/m°C) is less than that of the dermis layer (0.445 W/m°C). This difference in the thermal conductivity of the two layers leads to gradual spreading of the heat in the subcutaneous fat layer and quick spreading of the heat in the dermis layer. This heat transfer process has a direct effect on the amount of heat absorbed by the blood vessels. In other words, the subcutaneous fat layer, due to its greater thickness (4.4 mm) absorbs more heat than the dermis layer. Therefore, the dermis layer experiences a higher temperature than the subcutaneous fat layer (Fig. 4). This means that the dermis layer converts more thermal energy into kinetic energy. Consequently, the thermal expansion of the dermis layer exceeds that of the subcutaneous fat layer (Fig. 6). This thermal expansion along with

its equivalent kinetic energy at low temperatures can be eliminated by the blood vessels, but the kinetic energy generated by the high temperatures cannot be eliminated by the blood vessels. Hence, the unabsorbed kinetic energy exponentially increases the distance (and motion) between constituents of matter, whose outcome is a thermal expansion (Fig. 7). This critical status disrupts bonds between the constituents of materials and changes the nature of materials. The result of this change in the tissue is thermal damage, which usually appears as an injury (Fig. 8).

Interestingly, the epidermis layer, despite having a lower thermal conductivity ($0.235 \text{ W/m}^{\circ}\text{C}$) than the dermis layer, tolerates high temperature due to the low thickness and proximity to the skin surface (Fig. 4). This high temperature in the epidermis layer creates thermal expansion, which is relatively less than that of other layers. Nevertheless, this expansion compared with the thickness of the epidermis layer (0.1 mm) is remarkable, so that usually creates the most damage in the burning conditions, i.e. high temperature and exposure time at this temperature. Fig. 8 well confirms this issue. This figure also confirms that the burn degree in all of the skin layers is directly proportional to the temperature applied to the skin surface and can be reduced by increasing the blood perfusion rate (Fig. 9). Some of the researchers [1, 14, 15] nonetheless reported that the blood perfusion rate has little influence on burn damage; while they considered that this rate has a high influence on the temperature distribution in the skin. It is remarkable that these researchers used equation (13) for calculating the burn damage, in which there is a direct proportion between the temperature and the thermal damage. Therefore, this direct proportion does not confirm the outcome reported by these researchers.

There are also limitations in our paper. First, we have assumed constant properties for each of the skin layers, while these properties are usually non-constant, especially at the boundary of layers. Second, we have considered the present model as one-dimensional one, but the skin is a spatial object. Third, our model includes three layers. Accordingly, we assumed the boundary condition between the subcutaneous fat layer and the fat layer equal to the core temperature, while the internal layers (fat, muscle and bone) have a non-stationary temperature distribution.

Nevertheless, although the elimination of each of the limitations will be an interesting start point for future works, the results reported in the previous section show that the present model has an adequate ability to model the heat transfer and to evaluate the burn injuries in multi-layer skin. Therefore, this model can be very interesting for improving medical applications such as the local hyperthermia

techniques and for evaluating the burn injuries. The outcomes obtained from this model can be also validated and employed in laminar insulations used in building facilities, in which heating installations usually penetrate in some layers.

REFERENCES

1. F. Xu, T.J. Lu, K. A. Seffen, *Journal of the Mechanics and Physics of Solids*, **56**(5), 1852 (2008).
2. D. A. Stewart, T. R. Gowrishankar, J. C. Weaver, *IEEE Transactions on Plasma Science*, **34**(4), 1480 (2006).
3. B. Stec, A. Dobrowolski, W. Susek, *IEEE Transactions on Biomedical Engineering*, **51**(3), 548 (2004).
4. N. S. Sadick, J. Shaoul, *Journal of Cosmetic and Laser Therapy*, **6**(1), 21 (2004).
5. R. A. Weiss, M. A. Weiss, G. Munavalli, K. L. Beasley, *Journal of Drugs in Dermatology JDD*, **5**(8), 707 (2006).
6. Y.-K. Tay, C. Kwok, E. Tan, *Lasers in Surgery and Medicine*, **38**(3), 196 (2006).
7. D. J. Goldberg, *Expert Review of Medical Devices*, **4**(2), 253 (2007).
8. K. R. Diller, I. C. Young, Modeling of Bioheat Transfer Processes at High and Low Temperatures, in: *Advances in Heat Transfer*, Elsevier, 1992, p. 157.
9. J. van der Zee, *Annals of Oncology*, **13**(8), 1173 (2002).
10. P. Wust, B. Hildebrandt, G. Sreenivasa, B. Rau, J. Gellermann, H. Riess, R. Felix, P. M. Schlag, *The Lancet Oncology*, **3**(8), 487 (2002).
11. M. R. Habib, D. L. Morris, Local and Regional Hyperthermia, in: *Induction Chemotherapy: Systemic and Locoregional*, K. R. Aigner, F. O. Stephens (eds.) Springer International Publishing: Cham., p. 53.
12. P. Wolf, *Innovations 2016 in biological cancer therapy, a guide for patients and their relatives*, Naturasanitas, 2008, p. 31.
13. G. F. Baronzio, E. D. Hager, *Hyperthermia in Cancer Treatment: A Primer*, Springer US, 2008.
14. F. Xu, *Applied Mechanics Reviews*, **62**(5), 050801 (2009).
15. F. Xu, T. Wen, T. J. Lu, K. A. Seffen, *Journal of the Mechanical Behavior of Biomedical Materials*, **1**(2), 172 (2008).
16. E. H. Wissler, *Journal of Applied Physiology*, **85**(1), 35 (1998).
17. J. Liu, L. X. Xu, *International Journal of Heat and Mass Transfer*, **43**(16), 2827 (2000).
18. T. A. Balasubramaniam, H. F. Bowman, *Journal of Heat Transfer*, **96**(3), 296 (1974).
19. M. M. Chen, K. R. Holmes, V. Rupinskis, *Journal of Biomechanical Engineering*, **103**(4), 253 (1981).
20. R. C. Eberhart, A. Shitzer, E. J. Hernandez, *Annals of the New York Academy of Sciences*, **335**, 107 (1980).
21. D. A. Torvi, J. D. Dale, *Journal of Biomechanical Engineering*, **116**(3), 250 (1994).

22. C. J. Andrews, L. Cuttle, M. J. Simpson, *International Journal of Heat and Mass Transfer*, **101**, 542 (2016).
23. R. Vyas, M. L. Rustgi, *Medical Physics*, **19**(5), 1319 (1992).
24. W. H. Newman, P. P. Lele, H. F. Bowman, *International Journal of Hyperthermia: The Official Journal of European Society for Hyperthermic Oncology, North American Hyperthermia Group*, **6**(4), 771 (1990).
25. L. Zhu, S. Weinbaum, *Journal of Biomechanical Engineering*, **117**(1), 64 (1995).
26. J. W. Durkee, P. P. Antich, C. E. Lee, *Physics in Medicine and Biology*, **35**(7), 847 (1990).
27. J. W. Durkee, P. P. Antich, C. E. Lee, *Physics in Medicine and Biology*, **35**(7), 869 (1990).
28. J. J. W. Lagendijk, *Physics in Medicine and Biology*, **45**(5), R61 (2000).
29. E. Kengne, I. Mellal, A. Lakhssassi, Bioheat transfer problems with spatial or transient heating on skin surface or inside biological bodies, in: 7th International Conference on Biomedical Engineering and Informatics, 2014.
30. Z.-S. Deng, J. Liu, *Journal of Biomechanical Engineering*, **124**(6), 638 (2002).
31. S. Y. Lin, T. M. Chou, Numerical Analysis of the Pennes Bioheat Transfer Equation on Skin Surface, in: Third International Conference on Robot, Vision and Signal Processing (RVSP), 2015.
32. D. Lai, Q. Chen, *Energy and Buildings*, **118**, 114 (2016).
33. M. Strakowska, G. de Mey, B. Vitzek, M. Strzelecki, *Journal of Mechanics in Medicine and Biology*, **15**(4), 1550044 (2015).
34. M. Geerligs, *Journal of Philips Research*, 1 (2006).
35. J. C. Chato, *Journal of Biomechanical Engineering*, **102**(2), 110 (1980).
36. M. M. Chen, K. R. Holmes, *Annals of the New York Academy of Sciences*, **335**, 137 (1980).
37. J. Crezee, J. J. W. Lagendijk, *Physics in Medicine and Biology*, **37**(6), 1321 (1992).
38. H. H. Pennes, *Journal of Applied Physiology*, **85**(1), 5 (1998).
39. J. S. Hutchison, *The New England Journal of Medicine*, **358**(23), 2447 (2008).
40. Xin Gui, F. H. George, Proc. International symposium on symbolic and algebraic computation. 1997, ACM, Kihei, Maui, Hawaii, USA.
41. D. G. Zill, M. R. Cullen, *Advanced Engineering Mathematics*, Jones and Bartlett Publishers, 2006.
42. N. O. a. S. Matthew, *Numerical Techniques in Electromagnetics*, CRC Press, 2001.
43. L. P. Kollar, *Mechanics of Composite Structure*. Cambridge University Press, Cambridge, 2003.
44. F. C. Henriques, A. R. Moritz, *The American Journal of Pathology*, **23**(4), 530 (1947).
45. A. R. Moritz, F. C. Henriques, *The American Journal of Pathology*, **23**(5), 695 (1947).
46. K. J. Laidler, *Chemical Kinetics*, Pearson Education, 1987.
47. N. T. Wright, *Journal of Biomechanical Engineering*, **125**(2), 300 (2003).

Design of sodium carbonate functionalized TiO₂-coated Fe₃O₄ nanoparticles as a new heterogeneous catalyst for pyrrole synthesis

K. Fattahi, M. Farahi*, B. Karami, R. Keshavarz

Department of Chemistry, Yasouj University, Yasouj 75918-74831, Iran

Received: July 07, 2020; Revised: December 03, 2021

The novel Fe₃O₄@TiO₂ supported sodium carbonate (Fe₃O₄@TiO₂@(CH₂)₃OCO₂Na) is reported with a view to introduce new synthetic routes under green and mild conditions. Additionally, it is shown this base-functionalized magnetic catalyst exhibits excellent activity for the synthesis of pyrroles *via* Paal-Knorr reaction. The structure of this catalyst was studied by FT-IR, XRD, SEM, EDS and VSM analysis. The separation of this catalyst is done in a facile manner by an external magnetic field and its use without reducing catalytic activity is possible for five times.

Keywords: pyrrole, Paal-Knorr reaction, nanocatalyst, Fe₃O₄, TiO₂

INTRODUCTION

Due to increasing environmental regulations, global safety of nature is the most important factor in modern science and technology, in particular, in the organic synthesis area. High activity and selectivity, and desired resilience of nanocatalysts make them to be recognized as pioneers of green chemistry. The important advantage of nanoparticles is their high specific surface area to volume ratio leading to increased contact with the reactants. Despite the several mentioned benefits of nanomaterials, they are difficult to separate. Therefore, it is important to design recoverable and green nanocatalysts [1, 2]. Heterogeneous catalysis using nanomaterials as recyclable catalysts for organic transformations has attracted the attention. Magnetic nanoparticles (MNPs) have been intensively investigated in recent years. Owing to the facility of isolation from the reaction mixture using an external magnet, as well as to the fact that such types of systems possess high-potential active sites for loading of other functional groups, it would be reasonable to use magnetic nanoparticles. Among them, nano-Fe₃O₄ is most commonly used due to its unique physical properties including high surface area, superparamagnetism, low toxicity and their potential applications [3]. One of the inherent disadvantages of iron oxide nanoparticles is aggregation/oxidation and coating by metal oxides reduces this problem [4]. Titanium dioxide is a suitable substance for this purpose and can improve the catalytic activity of the magnetite nanoparticles. More attention is being paid to titania layer as coating of magnetic nanoparticles for increasing the surface area and simplifying the surface functionalization [5-7].

Pyrroles as an important class of heterocyclic compounds find widespread use in the pharmaceutical and agrochemical industries [8]. They are also widely applied in synthetic organic chemistry and material science. Pyrrole and its derivatives are also often seen as building blocks in naturally occurring and biologically active compounds. These heterocycles are prevalent in many drugs thus chemists are increasingly interested to discover new methods for rapid construction of pharmacologically important drug-like compounds [9]. So, it is not surprising that many synthetic approaches have been reported for the synthesis of pyrroles. The most widely used method is the Paal-Knorr synthesis, which consists of condensation of primary amines with 1,4-dicarbonyl compounds to obtain substituted pyrroles [10-12]. Numerous catalysts such as zeolite, Bi(NO₃)₃·5H₂O, HCl, Ti(OPri)₄, Al₂O₃, *p*-TSA, layered zirconium phosphate and zirconium sulfophenyl phosphonate have been applied in the Paal-Knorr reaction [13].

Synthesis of surface-modified magnetite nanoparticles is one of the major areas of our current research. In connection with our previous studies [14-20], we decided to introduce Fe₃O₄@TiO₂@(CH₂)₃OCO₂Na as a magnetically recoverable solid base catalyst.

EXPERIMENTAL

All chemicals used in this research were purchased from Fluka and Merck chemical companies. Melting points were determined by an electrothermal KSB1N apparatus and are uncorrected. Fourier transform infrared (FT-IR) spectra were recorded on a Shimadzu-470 spectrometer using KBr pellets. X-ray powder diffraction (XRD) patterns were recorded using a

* To whom all correspondence should be sent:

E-mail: farahimb@yu.ac.ir

Bruker AXS (D8 Advance) X-ray diffractometer with Cu K α radiation ($\lambda = 0.15418$ nm). The measurement was made in 2θ ranging from 10° to 80° at the speed of 0.05° min⁻¹. Energy dispersive spectroscopy (EDS) was performed using a TESCAN Vega model instrument. The morphology of the particles was observed by scanning electron microscopy (SEM) under an acceleration voltage of 26 kV. The magnetic measurement was carried out in a vibrating sample magnetometer (VSM) Kashan University, Kashan, Iran) at room temperature.

Synthesis of Fe₃O₄ MNPs

FeCl₃·6H₂O (2.7 g, 10 mmol) and FeCl₂·4H₂O (1 g, 5 mmol) were dissolved in distilled water (45 mL) and stirred for 15 min under argon atmosphere at 80 °C. Sodium hydroxide solution (5 mL, 10 M) was then added dropwise to the solution as long as the color of solution was black. After about 1 h, the generated iron oxide nanoparticles were collected with a magnet and rinsed thoroughly with distilled water two or three times. MNPs Fe₃O₄ was dried at 60 °C [21].

Preparation of Fe₃O₄@TiO₂

Nano-Fe₃O₄ was initially diluted in a mixture of ethanol and acetonitrile (125:45 mL). The resulting dispersion was then homogenized by ultrasonic vibration in a water bath. Then followed the addition of ammonia aqueous solution (0.75 mL, 25%) while stirred vigorously by a mechanical stirrer at room temperature for 30 min. Tetraethyl orthotitanate (TEOT) (1.5 mL) in absolute ethanol (20 mL) was then added dropwise to the solution under continuous mechanical stirring at 30 °C for 2 h. Fe₃O₄@-TiO₂ was separated by a magnet, washed several times with ethanol, and dried at room-temperature [22].

Procedure for the synthesis of Fe₃O₄@TiO₂@(CH₂)₃Cl

Fe₃O₄@TiO₂ (0.5 g) was ultrasonically dispersed in dry toluene (80 mL) for 15 min. Next, 3-chloropropyltriethoxysilan (0.121 g, 0.5 mmol) was added to the mixture and stirred with argon gas under reflux conditions for 12 h. Next, Fe₃O₄@TiO₂@(CH₂)₃Cl was obtained by magnetic separation and washed with deionized water and ethanol [18].

Synthesis of Fe₃O₄@TiO₂@(CH₂)₃OCO₂Na (1)

In the final step, the prepared Fe₃O₄@TiO₂@(CH₂)₃Cl (0.5 g) was dissolved in DMSO (50 mL) and ultrasonicated for 15 min. Then Na₂CO₃ (1 g) was added and the reaction mixture was heated at 90 °C for 24 h. The final product was separated from the solution with a magnet and then washed several times with water and ethanol followed by drying at 60 °C under vacuum.

General procedure for the synthesis of pyrrole derivatives (4)

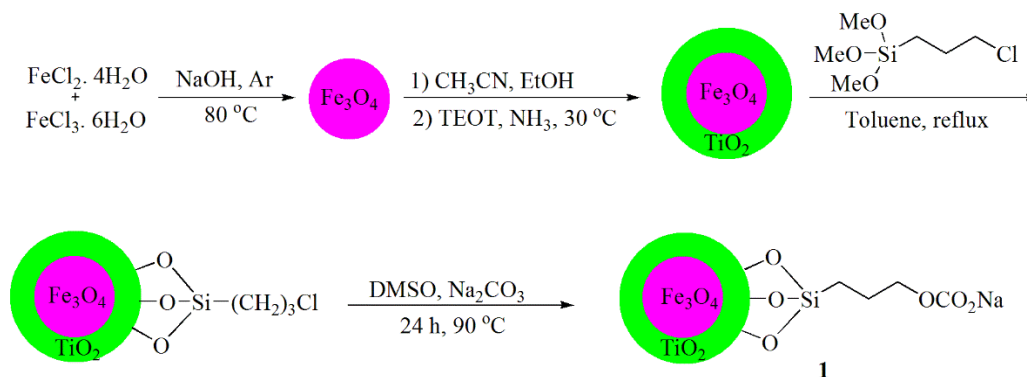
Fe₃O₄@TiO₂@(CH₂)₃OCO₂Na (0.003 g) was added to a mixture of 2,5-hexadione (1 mmol) and aniline derivatives (1 mmol) at 80 °C. The mixture was stirred under solvent-free conditions for 15-25 min and the reaction process was followed by thin-layer chromatography. After completion, the reaction mixture was dissolved in hot EtOH (5 mL). The catalyst was removed from the reaction mixture using an external magnet. The solvent was then removed and the crude products were purified by crystallization from *n*-hexane.

Catalyst recovery instructions

2,5-Hexadione (1 mmol), aniline (1 mmol), and Fe₃O₄@TiO₂@(CH₂)₃OCO₂Na (0.003 g) were stirred under free-solvent condition at 80 °C for 20 min. After completion of the reaction, hot ethanol (5 mL) was added to the reaction and the mixture was subjected to separation using a permanent magnet. It was repeatedly washed with distilled water (10 mL each), three times with methanol (10 mL each) and then dried at 80 °C. Finally, it was reused in subsequent runs.

RESULTS AND DISCUSSION

The magnetic nanocatalyst Fe₃O₄@TiO₂@(CH₂)₃OCO₂Na (**1**) was prepared following the procedure shown in Scheme 1. Firstly, the chemical coprecipitation of Fe²⁺ and Fe³⁺ ions in basic solution led to the formation of nano-Fe₃O₄. Then, in order to avoid possible aggregation or oxidation of the iron oxide nanoparticles, the obtained MNPs were coated with TiO₂ using tetraethyl orthotitanate (TEOT). Nanoparticles Fe₃O₄@TiO₂ can be functionalized with 3-chloropropyltriethoxysilan molecule. Finally, the surface of Fe₃O₄@TiO₂@(CH₂)₃Cl was functionalized with Na₂CO₃ to give nanocatalyst **1**. The prepared catalyst was characterized by FT-IR, XRD, SEM, EDS and VSM analysis.



Scheme 1. Synthesis of Fe₃O₄@TiO₂@(CH₂)₃OCO₂Na (**1**).

Fig. 1 shows the XRD patterns of Fe₃O₄, Fe₃O₄@TiO₂ and Fe₃O₄@TiO₂@(CH₂)₃OCO₂Na. In Fig. 1c the peaks at $2\theta = 30.2, 35.6, 43.4, 53.9, 57.4$ and 63.0 are related to (220), (311), (400), (422), (511) and (440) showing the cubic spinel structure of Fe₃O₄ [23]. Also, the mentioned indices revealed that the new catalyst in Fig. 1c has a similar structure to Fe₃O₄ nanoparticles in Fig. 1a, and this shows that no phase change was observed after surface modification of the magnetite nanoparticles. The characteristic peaks confirming the presence of -OCO₂Na appeared around 10, 34, 36 and 43 (2θ), some of which were overlapped by Fe₃O₄ peaks [24].

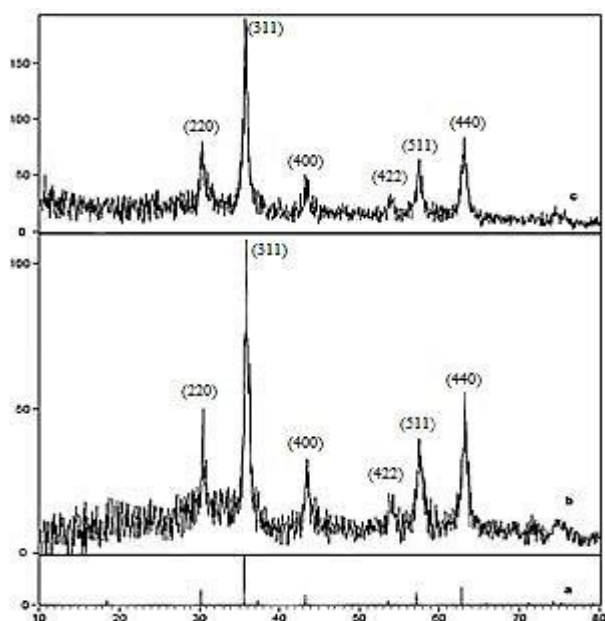


Fig. 1. XRD patterns of (a) Fe₃O₄, (b) Fe₃O₄@TiO₂, and (c) Fe₃O₄@TiO₂@(CH₂)₃OCO₂Na.

The FT-IR spectra of Fe₃O₄, Fe₃O₄@TiO₂, Fe₃O₄@-TiO₂@(CH₂)₃Cl and Fe₃O₄@TiO₂@(CH₂)₃OCO₂Na were compared to analyze the progress of the designed catalyst (Fig. 2). The presence of characteristic peaks corresponding to Fe-O stretching vibration near 586 cm⁻¹ in all compared spectra is a confirmation of the

preservation of the nanostructure of Fe₃O₄ throughout the process. The broad band between 400-700 and 1400 cm⁻¹ seen in Fig. 2b may be assigned to the Ti-O-Ti stretching modes and Fe-O-Ti bonds, respectively [25, 18]. In Fig. 2c, CH₂ bending, as a broad band and symmetric CH₂ and asymmetric CH₂ of the alkyl chains appeared at 1480 cm⁻¹ and 2860 to 2923 cm⁻¹ [23]. In Fig. 2d the peak related to -OCO₂Na group appeared at 1407 and 1636 cm⁻¹ [24].

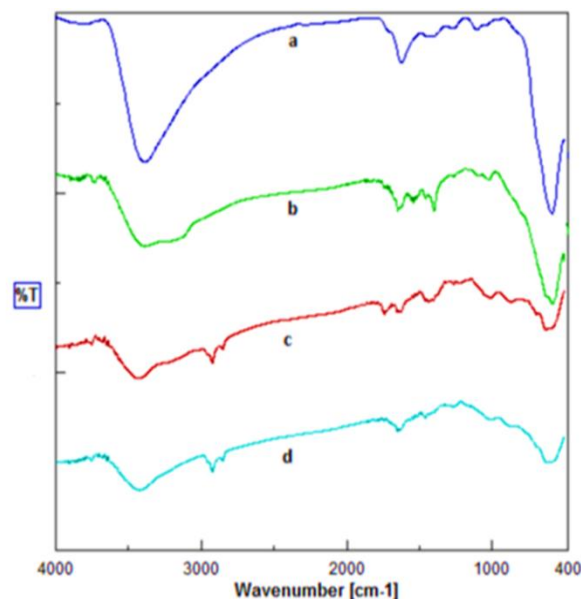


Fig. 2. The FT-IR spectra of (a) Fe₃O₄ MNPs, (b) Fe₃O₄@TiO₂, (c) Fe₃O₄@TiO₂@(CH₂)₃Cl, and (d) Fe₃O₄@TiO₂@(CH₂)₃OCO₂Na.

The EDS pattern of the synthesized nanocatalyst **1** is shown in Fig. 3. It is seen that Fe₃O₄@TiO₂@(CH₂)₃OCO₂Na contains all expected elemental cases including Ti, O, Fe, C, Si and Na.

The SEM image of Fe₃O₄@TiO₂@(CH₂)₃OCO₂Na was recorded to show the morphology of the catalyst **1** (Fig. 4). This image shows the proper size of nanoparticles and their spherical shapes.

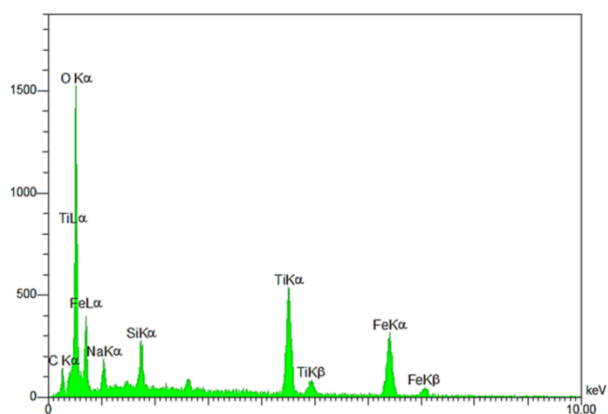


Fig. 3. EDS analysis of Fe₃O₄@TiO₂@(CH₂)₃OCO₂Na.

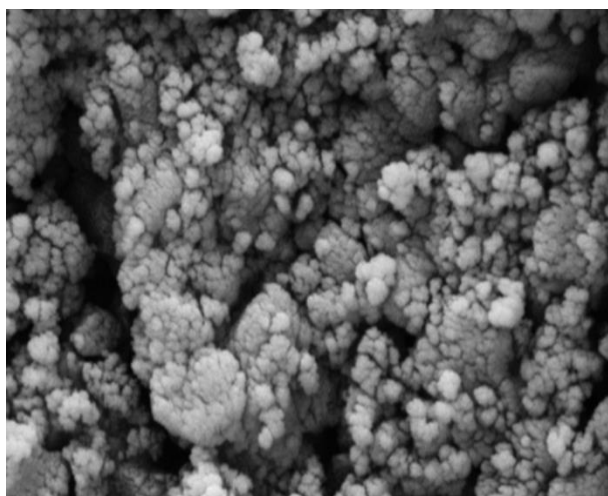


Fig. 4. SEM image of catalyst **1**.

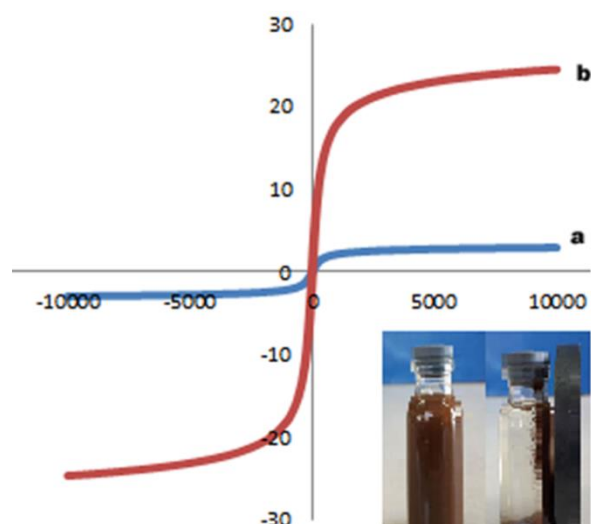
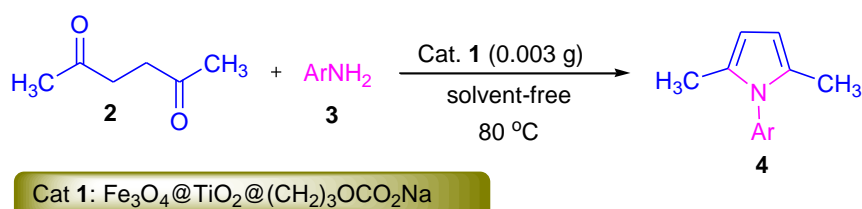


Fig. 5. Room-temperature magnetization curves of (a) Fe₃O₄@TiO₂@(CH₂)₃OCO₂Na and (b) recycled catalyst from the model reaction.

Fig. 5 shows the magnetization *versus* applied field of the catalyst obtained by VSM. Comparison of two curves is shown, which proves that the magnetic property is retained after the catalyst being used in the reaction.

Having successfully prepared the new nanocatalyst, we investigated the use of Fe₃O₄@TiO₂@(CH₂)₃OCO₂Na (**1**) as a novel reusable nanocatalyst in the synthesis of pyrrole derivatives *via* the reaction of 2,5-hexanedione (**2**) and amines (**3**) (Scheme 2).



Scheme 2. Fe₃O₄@TiO₂@(CH₂)₃OCO₂Na-catalyzed synthesis of pyrrole **4**.

Firstly, in order to optimize the reaction conditions, the reaction of 2,5-hexanedione and aniline was selected as a model reaction. The model reaction was performed using Fe₃O₄@TiO₂@(CH₂)₃OCO₂Na at various conditions. On the basis of the results obtained, we found that this reaction was efficiently performed in the presence of 0.003 g of nanocatalyst **1** at 80 °C under solvent-free conditions (Table 1). A series of the product with different substituents was prepared from different aromatic amines bearing electron-withdrawing and electron-donating groups (Table 2). The structures of the obtained products were deduced from their FT-IR spectra and they were compared with authentic samples [26-28]. The synthesis of various pyrrole

derivatives has also been performed using other catalysts. Table 3 compares the production efficiency of product **4a** in the presence of different catalysts. According to this table, the nanocatalyst synthesized by us (Fe₃O₄@TiO₂@(CH₂)₃OCO₂Na), gives better efficiency in the shortest time using small amounts of catalyst. According to the nature of the substrate, catalyst and condition of the experiment, a most reasonable mechanism was advanced (Scheme 3). Initially, intermediate **5** is formed *via* condensation of the 1,4-dicarbonyl compound with amine in the presence of the catalyst. The compound **5** can lead to pyrroles following a cyclization and subsequent dehydration-aromatization route.

Table 1. Evaluating reaction conditions on model reaction.

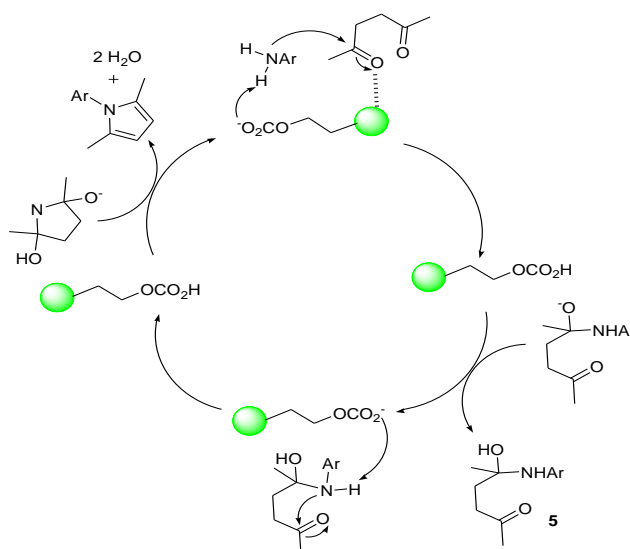
Entry	Catalyst 1/g	Solvent	Temp./°C	Yield ^a /%
1	0.001	None	25	5
2	0.001	None	60	30
3	0.001	CH ₃ OH	Reflux	10
4	0.001	CHCl ₃	reflux	15
5	0.001	H ₂ O	reflux	10
6	0.002	None	60	50
7	0.003	None	60	83
8	0.004	None	60	80
9	0.003	None	80	90
10	0.003	None	100	85
11	0.003	Toluene	reflux	75
12	0.003	CHCl ₃	reflux	77
13	0.003	CH ₃ OH	Reflux	70
14	0.003	H ₂ O	reflux	70

^a Isolated yield.**Table 2.** Synthesis of pyrroles **4** in the presence of Fe₃O₄@TiO₂@(CH₂)₃OCO₂Na.

Entry	Ar	Time/min	M.p./°C	Yield ^a /%
4a	C ₆ H ₅	20	49-51 [26]	96
4b	4-OCH ₃ C ₆ H ₄	15	58-60 [26]	81
4c	4-CH ₃ C ₆ H ₄	15	44-46 [27]	91
4d	4-NO ₂ C ₆ H ₄	20	142-144 [27]	90
4e	3-BrC ₆ H ₄	25	73-75 [26]	87
4f	4-ClC ₆ H ₄	25	75-77 [27]	92
4g	4-NH ₂ C ₆ H ₄	20	243-245 [26]	90
4h	2-CH ₃ C ₆ H ₄	20	57-60 [28]	80
4i	2-Naphthyl	20	118-120 [26]	83

^a Isolated yield.**Table 3.** Comparison of the efficiency of the Fe₃O₄@TiO₂@(CH₂)₃OCO₂Na nanocatalyst with other catalysts for the synthesis of **4a**.

Catalyst	Time (min)	Yield ^a (%)
Fe ₃ O ₄ @TiO ₂ @(CH ₂) ₃ OCO ₂ Na	20	96
UO ₂ (NO ₃) ₂ .6H ₂ O	30	94 [26]
BiCl ₃ /SiO ₂	60	92 [28]
Sc(OTf) ₃	25	93 [8]
Ionic liquid	180	96 [13]

^a Isolated yield.**Scheme 3.** Proposed mechanism for the synthesis of pyrroles by nanocatalyst **1**.

The main drawback of some reported methods for Paal-Knorr synthesis of pyrroles is that the catalysts cannot be recovered or reused. In this work, to examine the reusability of the prepared nanocatalyst, after completion of the model reaction, the reaction mixture was diluted with ethanol and the catalyst was magnetically removed from it. Afterwards, the isolated catalyst was washed by distilled water and methanol and dried. The separated catalyst was directly used for the next run under the same conditions. The results showed that the catalyst can be reused without deactivation even after five cycles (Fig. 6).

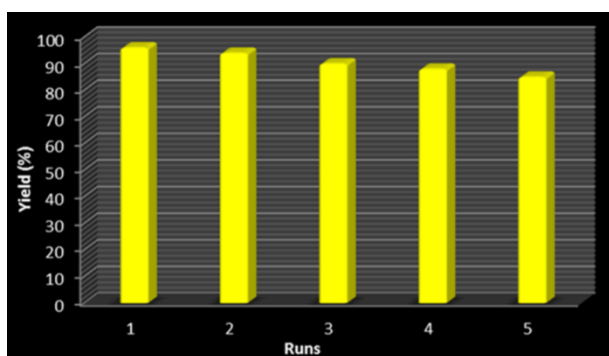


Fig. 6. Reusability study of nanocatalyst **1** in the synthesis of **4a** at 80 °C under solvent-free conditions.

CONCLUSIONS

In summary, we introduced for the first time the preparation, characterization, and application of sodium carbonate immobilized on TiO₂-coated Fe₃O₄ nanoparticles (**1**). Fe₃O₄@TiO₂@(CH₂)₃OCO₂Na was characterized using FT-IR, XRD, SEM, EDS and VSM analysis. Some pyrrole derivatives as useful heterocycles were synthesized via the Paal-Knorr reaction using this catalyst. It can be stored for long times without significant loss in activity. The catalyst recyclability, mild conditions, high yield, short reacting times and long storage, are the main promising points of this work.

Acknowledgement: We gratefully acknowledge the partial support of this work by Yasouj University, Iran.

REFERENCES

- M. A. Zolfigol, A. R. Moosavi-Zare, P. Moosavi, V. Khakyzadeh, A. Zare, *C. R. Chimie*, **16**, 962 (2013).
- A. Amoozadeh, S. Golian, S. Rahmani, *RSC Adv.*, **5**, 45974 (2015).
- M. Tajbakhsh, M. Farhang, R. Hosseinzadeh, Y. Sarrafi, *RSC Adv.*, **4**, 23116 (2014).
- R. B. Nasir Baig, R. S. Varma, *Chem. Commun.*, **49**, 752 (2013).
- W. Zhang, Y. Li, C. Wang, P. Wang, *Desalination*, **266**, 40 (2011).
- K. Koci, V. Matejka, P. Kovar, Z. Lacny, L. Obalova, *Catal. Today*, **161**, 105 (2011).
- K. Shimura, T. Miyazawa, T. Hanaoka, S. Hirata, *Appl. Catal. A*, **8**, 460 (2013).
- J. Chen, H. Wu, Z. Zheng, C. Jin, X. Zhang, W. Su, *Tetrahedron Lett.*, **47**, 5383 (2006).
- Y. H. He, G. Q. Wang, Z. Guan, *J. Heterocycl. Chem.*, **47**, 486 (2010).
- V. Amarnath, D. C. Anthony, K. Amarnath, W. M. Valentine, L. A. Wetterau, D. G. Graham, *J. Org. Chem.*, **56**, 6924 (1991).
- R. U. Braun, K. Zeitler, T. J. Muller, *J. Org. Lett.*, **3**, 3297 (2001).
- K. H. Lui, M. P. Sammes, *J. Chem. Soc. Perkin Trans.*, **1**, 457 (1990).
- B. Wang, Y. Gu, C. Luo, T. Yang, L. Yang, J. Suo, *Tetrahedron Lett.*, **45**, 3417 (2004).
- M. Farahi, B. Karami, R. Keshavarz, F. Khosravian, *RSC Adv.*, **7**, 46644 (2017).
- H. Mohamadi Tanuraghaj, M. Farahi, *RSC Adv.*, **8**, 27818 (2018).
- H. Mohamadi Tanuraghaj, M. Farahi, *New J. Chem.*, **43**, 4823 (2018).
- M. Farahi, F. Tamaddon, B. Karami, S. Pasdar, *Tetrahedron Lett.*, **56**, 1887 (2015).
- J. Etemad Gholtash, M. Farahi, *RSC Adv.*, **8**, 40962 (2018).
- F. Khosravian, B. Karami, M. Farahi, *New J. Chem.*, **41**, 11584 (2017).
- M. Farahi, B. Karami, Z. Rajabi Behesht Abad, S. Akrami, *Lett. Org. Chem.*, **14**, 612 (2017).
- F. Nemati, M. Heravi, D. Elhampour, *RSC Adv.*, **5**, 45775 (2015).
- M. A. Zolfigol, R. Ayazi-Nasrabadi, *RSC Adv.*, **6**, 69595 (2016).
- Z. Rashid, H. Naeimi, A. H. Zarnani, M. Nazari, M. Nejadmoghaddam, R. Ghahremanzadeh, *RSC Adv.*, **6**, 36840 (2016).
- K. Eskandari, B. Karami, S. Khodabakhshi, *Catal. Commun.*, **54**, 124 (2014).
- R. Chalasani, S. Vasudevan, *ACS Nano*, **7**, 4093 (2013).
- V. S. V. Satyanarayana, A. Sivakumar, *Ultrason. Sonochem.*, **18**, 917 (2011).
- O. Marvi, H. T. Nahzomi, *Bull. Chem. Soc. Ethiop.*, **32**, 139 (2018).
- K. Aghapoor, L. Ebadi-Nia, F. Mohsenzadeh, M. Mohebi Morad, Y. Balavar, H. R. Darabi, *J. Organomet. Chem.*, **708**, 25 (2012).

Potential of municipal solid waste generated in Bulgaria for energy production

M. K. Mladenov

Department of Environmental Engineering, University of Chemical Technology and Metallurgy, 8, Boul. "St. Kliment Ohridski", Sofia 1756, Bulgaria

Received: July 09, 2020; Revised: March 08, 2021

In order to achieve the goals of the circular economy, energy is seen as a key element, especially when it is extracted from clean and accessible renewable sources, such as various types of wastes. Incineration is one of the possible methods for wastes treatment, which is increasingly used to utilize their energy potential. In this regard, the current article presents calculations on the energy potential of municipal solid wastes (MSW) generated in Bulgaria, in order to determine their suitability to produce energy and satisfy the energy needs of the population. The results of the calculations determine the possibility of burning of municipal solid wastes in order to utilize their energy value.

The data from the calculations show that the solid waste generated by small settlements with inhabitants under 3 001 people have the highest energy value and their combustion can lead to energy savings for the needs of 218 828 households with an average monthly electricity consumption of about 350 kWh. However, due to the current technological, economic and environmental prerequisites in the country, it is recommended that the main efforts for building of combustion plants for waste incineration should be focused primarily on the recovery of the huge amount of waste generated by settlements with inhabitants over 50 000 people.

Keywords: municipal solid wastes (MSW); incineration/combustion; waste to energy; utilization of wastes; energy value

INTRODUCTION

MSW are generated from various sources of human activity. Miezah *et al.* [1] report that in developing countries, 55-80% of the MSW are generated from households, followed by commercial or market areas (10-30%). Lebersorger and Beigl [2] describe in detail the social and other factors on which the generated amounts of MSW depend – demographics, population density, age and education of the population, etc. Erasu *et al.* [3] also give a connection between the level of economic development of the respective country and the amount of generated household waste due to a change in consumer behavior and lifestyle of the people. According to Palanivel and Sulaiman [4], the characteristics and composition of MSW depend on the topography of the area, food habits and commercial status of the city, seasons, etc. Karak *et al.* [5] forecast the amount of solid waste generated and expect increasing of the total solid waste to 27 billion tonnes worldwide in 2050, compared to 13 billion tonnes in 1990.

According to data published by Kawai and Tasaki [6], the amount of MSW generated per capita for Bulgaria is 1.26 kg.person⁻¹.day⁻¹. This quantity is slightly below the average for the member states of the European Union (EU), where the values are in the range of 0.85–1.83 kg.person⁻¹.day⁻¹. The data of the Ministry of environment and waters of Bulgaria (MOEW) published in an official report [7] also show that the generation of household waste per

capita per year in Bulgaria, compared to the EU-28 is below average and that the country has positive trends for this indicator. The same report finds that there are significant differences between the municipalities in the country in terms of the indicator of generated MSW per capita per year.

Currently, there is a general consensus in the world that much of the generated wastes, including MSW, can be applied as raw materials into a circular process, recovering their energetic and chemical content and avoiding the environmental and human-health issues related to the incorrect disposal. Many authors point out that the kind of wastes should be considered as such a potential material and energy resource [8-13] and that efforts are needed, both at institutional and state level, to increase the rate of their utilization [14, 15].

Incineration is one of the possible methods for treatment of household wastes, which is increasingly applied to utilize their energy potential. The problem with wastes is that they usually contain 2 to 4 times less heat energy than conventional fuels. This is due to the heterogeneity in their composition, the presence of high moisture and ash substances, the differences in physicochemical properties and other reasons [1]. High humidity of wastes can lead to partial or complete impossibility of their use, from a technological point of view, and high ash content

* To whom all correspondence should be sent:
E-mail: mladenov@uctm.edu

can lead to economic inexpedience. Both components reduce the proportion of the other useful components and lead to increases in heat loss, needed to evaporate moisture and to the removal of fuel particles mechanically entrained by the ash [16].

The aim of this article is to present the results of the calculations performed on the combustion air, flue gases composition and energy values from the incineration process of different groups of mixed solid wastes generated in Bulgaria and to assess their potential for energy production.

EXPERIMENTAL

Statistical and morphological data on the generated MSW and energy consumption in Bulgaria

According to official data of the MOEW [17], the total amount of MSW generated in Bulgaria in 2014 was 3 193 kt (17% of the total amount of generated non-hazardous waste in the country) and in comparison to 2008, there is a decrease in the generated quantities. In 2014, the generated household waste per capita was 442 kg.person⁻¹.year⁻¹, and the waste accumulation rate was close to the EU-28 average for 2013 (481 kg.person⁻¹.year⁻¹) and about 1/3 of the generated MSW were handed over

for utilization. At the same time, the norm for recycling of MSW per person for 2014, for Bulgaria is 108 kg.person⁻¹.year⁻¹ and is lower than the average European norm (EU-28) equal to 130 kg.person⁻¹.year⁻¹.

In a subsequent Report on the state and protection of the environment for 2017 [18], it is noted that “from 2009 to 2013 there is a decreasing trend and for the period from 2013 to 2017 the quantities of generated MSW remain relatively constant” (see Fig. 1). It is also noted that “for the reporting year 2017 the national target of 40% for recycling of the household waste, set in the legislation, has not been reached”, and the generated MSW for 2017 are 3 080 kt. The norm for recycling of MSW for 2017, for Bulgaria is 117 kg.person⁻¹.year⁻¹, compared to the average for European countries (EU-28) equal to 144 kg.person⁻¹.year⁻¹ [18]. Comparing with the data from 2014, it is seen that this indicator has made some progress in the degree of recycling, but is still below the EU average value.

Table 1 shows the distribution of energy consumption in the country for the period 2013-2017 by sectors, by data from the MOEW published in the National report on the state and protection of the environment for 2017 [18].

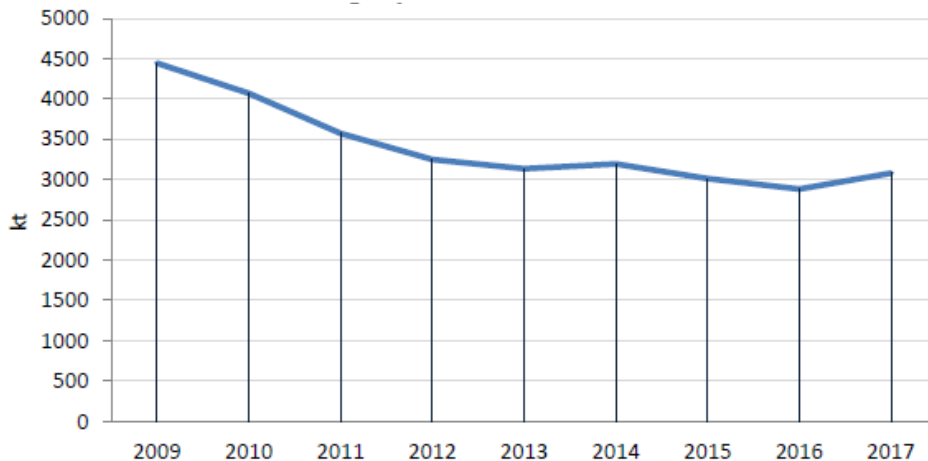


Figure 1. Quantities of generated MSW (kt) in Bulgaria during the period 2009-2017 [18]

Table 1. Total energy consumption by economic sectors, ktOE [18]

Sector	Year				
	2013	2014	2015	2016	2017
Industry	2 586	2 620	2 713	2 642	2 721
Transport	2 620	2 917	3 212	3 267	3 325
Household	2 241	2 165	2 193	2 252	2 319
Agriculture	194	190	186	185	173
Services	1 030	992	1 086	1 172	1 200
Total energy consumption	8 671	8 884	9 390	9 518	9 738

The report notes that in 2017, compared to the previous year, the most significant growth was observed in industry and households – 2.9%, followed by services and transport – 1.8%, and also a long-term downward trend in agricultural consumption – 7.0%.

The table shows that in this period, the total energy consumption in the country increased by about 12% and reached 9 738.0 ktoe. Official data also show that the share of energy produced from renewable sources is increasing, reaching 2 041.0 ktoe in 2017, compared to 2010 (1 396.6 ktoe). There is also an increase in the total consumption of electricity from renewable sources for 2017, reaching a value of 648.8 ktoe, compared to 2016 with a value of 633.3 ktoe. The contribution of the various sources is also noted: 57.2% from hydroelectric power plants, 18.9% from wind power plants, 18.6% from photovoltaics and 5.3% from biomass power plants [18].

The National action plan for renewable energy [19] notes that the country has significant forest resources and developed agriculture – sources of both solid biomass and raw materials for the production of biogas and liquid fuels from biomass, which could be used for energy production. According to this plan, by 2020 a mandatory national target of 16% share of the energy from renewable sources in gross total consumption of electricity has been set, which goal was achieved and reported in 2013, in the Second national report for progress of Bulgaria for the promotion and use of energy from renewable sources [20].

The previously cited National action plan [19] for 2020 provides an estimate of the amount of primary energy derived from 550 kt of the biodegradable part of municipal solid waste and landfill gas, amounting to 110 ktoe, and predicts that the amount of electricity produced from biomass will reach 865 GWh. Also it is noted that, despite the available international estimates of the rich potential of biomass for electricity production in the country, the opinion of Bulgarian experts is that biomass can be directed to electricity generation only through plants

for combined production of heat and power. Directing it to condensing plants is considered unprofitable from every point of view: environmental, economic and technological. Also, in that plan is noted that biomass is the renewable source with the greatest potential in Bulgaria and at the same time with a variety of applications – as a raw material for the production of briquettes, pellets and other solid fuels, such as fuel for cogeneration and direct combustion for heating and producing hot water for the population. Unfortunately, that plan mainly examines the possibilities for application of plant biomass in households and small installations, which, however, do not allow for the combustion of large quantities of municipal solid waste and energy production from them.

The data from the National waste management program 2014-2020 [7] mention that over 50% of the municipal waste is biodegradable and according to the size of the settlements the morphology is different and includes garden and green waste, food waste, paper, cardboard and other biodegradable wastes. At the same time that waste goes to different landfills, due to which it is not possible to introduce an average morphological composition for the country. Precisely for these and a number of other reasons, it is necessary to focus efforts on their utilization through their processing for energy production near the places of their generation and disposition.

Parameters of MSW, in view of their use for energy production

Before being subjected to incineration, the MSW must undergo a pre-sorting stage in which the biodegradable garden and non-combustible components and the hazardous and inert materials, contained in them to be removed. According to the Methodology for determining the morphological composition of municipal waste [21] the data for the formed different combustible fractions at certain types of generators, in kg.person⁻¹.year⁻¹ are shown in Table 2.

Table 2. Formed different fractions of wastes at certain types of generators

Waste fraction, %	Size of the settlement, by number of inhabitants				
	less than 3001	3 001 – 25 000	25 001 – 50 000	50 001 – 150 000	over 150 000
Kitchen/food	15.60	23.20	28.00	30.60	28.90
Paper and cardboard	10.10	14.00	15.00	17.60	20.80
Textile	2.00	3.70	2.90	2.90	2.80
Wood	2.90	2.00	2.90	2.10	2.00
Rubber and leather	2.00	1.80	2.00	2.00	1.80
Plastic	10.30	10.10	12.80	15.40	11.30

For the purpose of calculating energy production during the combustion process, the "work mass" of the waste fraction is taken into account, which includes the individual content of the elements carbon (C^w), hydrogen (H^w), oxygen (O^w), nitrogen (N^w), sulfur (S^w), ash (A^w) and moisture (humidity) (W^w). The sum of all of them must be equal to 100% [22, 23], according to the equation:

$$C^w + H^w + O^w + N^w + S^w + A^w + W^w = 100 \% \quad (1)$$

Also, when calculating the energy potential of wastes, it is necessary to use thermal properties data, which for some "pure" fractions of the waste have long been known in the literature [22] – see Table 3.

In order to determine the possibility of energy production from the wastes, it is necessary to know their composition in relation to the above-mentioned elements with a calorific value by incineration. Practical determination through analysis by each element of each batch of waste, in this case is an expensive, laborious and slow process. That can be avoided by applying alternative calculation procedures based on the morphological composition, which can give a

sufficiently accurate composition of the waste intended for incineration. Thus, e.g. using equations (2) and (3) proposed by Totev [22], the content of each element in the mixed MSW can be calculated based on its morphological composition and the total contribution for each element based on its individual content in each fraction of the mixed waste.

$$X_E = a_E * \frac{Y_E}{100} [\%] \quad (2)$$

$$X_{total} = X_{E1} + X_{E2} + \dots + X_{En} \quad (3)$$

where: X_E – individual content of the specific element in the mixed waste, contained in the respective fraction of the morphological composition, %; Y_E – content of the specific element in the respective waste fraction, %; a_E – content of the respective fraction in the total amount of waste, %; X_{total} – total work mass of the respective element in the mixed waste, %; X_{E1} to X_{En} – individual contents of the element in each fraction of the waste, %.

Here, calculations were performed for the composition of mixed MSW according to [22], which was recalculated in working mass – see Table 4.

Table 3. Thermal properties of some fractions of wastes, in work mass [22]

Type of "pure" waste	Combustible element						
	S ^w , %	O ^w , %	W ^w , %	A ^w , %	C ^w , %	H ^w , %	N ^w , %
Papper/cardboard	0.18	39.80	10.24	5.38	38.95	5.23	0.22
Textile	0.12	28.30	10.00	2.20	49.28	5.94	4.16
Wood	0.04	33.80	20.00	0.80	40.46	4.78	0.12
Rubber	1.98	0	1.20	9.88	76.69	11.25	0
Plastic and other particles	0.05	17.62	4.00	60.00	15.93	2.35	0.05

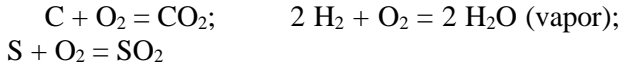
Table 4. Thermal properties, based on the morphological composition of municipal solid waste in Bulgaria, depending on the settlements of generation

MSW generated by settlements with a population of:	Combustible element						
	S ^w , %	O ^w , %	W ^w , %	A ^w , %	C ^w , %	H ^w , %	N ^w , %
less than 3001	0.21	20.12	31.43	17.91	26.17	3.56	0.60
3 001 – 25 000	0.19	19.95	35.27	14.83	25.53	3.48	0.75
25 001 – 50 000	0.19	19.3	36.31	15.75	24.43	3.34	0.68
50 001 – 150 000	0.18	19.41	35.66	16.76	24.04	3.30	0.65
over 150 000	0.19	20.79	35.62	13.98	25.30	3.46	0.66

Calculation of the combustion process and the energy value of the MSW

In order to ensure the comparability of the results obtained, calculations were carried out per kilogram of the waste mass, subject to the following prerequisites:

- the combustion reactions involved in the actual combusting process are:



- dry atmospheric air in proportion k ($k = \%N_2/\%O_2 = 3.76$), is used;

- stoichiometric calculations are converted to normal conditions ($P = 1$ at, $t = 0$ °C, $V = 22.4$ m³);

- a calculation of theoretical (stoichiometric) combustion, before calculating the actual combustion, must be done. Some of the used equations are described in [23];

- the air flow rate value (α) for calculating actual combustion is assumed to be the maximum possible [23] – $\alpha = 1.7$;

- the absolute humidity value is assumed to be 12 [23] – $g_{H_2O} = 12 [g.water / m^3 dry.air]$

In the process of calculating the actual combustion, it is necessary to calculate the parameters: amount of oxygen; quantity of dry and humid air; excess air. The equations used are described in detail below.

- amount of oxygen required:

$$V_{O_2} = 0,01 * (1,867 * C^w + 5,6 * H^w + 0,7 * S^w - 0,7 * O^w), \frac{m^3 O_2}{kg.fuel} \quad (4.1)$$

- required amount of dry air (DA):

$$L_{\alpha}^{DA} = \alpha * L_0^{DA} - L_0^{DA} = (\alpha - 1) * L_0^{DA} [m^3 DA / kg.fuel] \quad (4.2)$$

where L_0^{DA} is the required DA for the theoretical combustion.

- required amount of wet air (WA):

$$L_{\alpha}^{WA} = (1 + 0,001244 * g_{H_2O}) * \alpha * L_0^{DA} [m^3 WA / kg.fuel] \quad (4.3)$$

- excess air required (EA):

$$L' = L_{\alpha}^{WA} - L_0^{WA} [m^3 EA / kg.fuel] \quad (4.4)$$

where L_0^{WA} is the required WA for the *theoretical combustion.

The products of actual combustion are: carbon dioxide (CO₂), water vapor (H₂O_v), sulfur dioxide (SO₂), nitrogen (N₂), oxygen from combustion products (O₂) and total flue gas (wet smoke (WS)). The equations used to calculate them are given below:

$$- CO_2: V_{CO_2}^{\alpha} = 0,01 * 1,867 C^w, \frac{m^3 CO_2}{kg.fuel} \quad (5.1)$$

- H₂O_v:

$$V_{H_2O}^{\alpha} = V_{H_2O} + 0,001244 * g_{H_2O} * (\alpha - 1) * L_0^{DA}, \frac{m^3 H_2O}{kg.fuel} \quad (5.2)$$

where V_{H_2O} is the quantity of water vapour calculated in theoretical combustion.

$$- SO_2: V_{SO_2}^{\alpha} = 0,01 * 0,7 S^w, \frac{m^3 SO_2}{kg.fuel} \quad (5.3)$$

$$- N_2: V_{N_2}^{\alpha} = V_{O_2} + \alpha * k * V_{O_2}, \frac{m^3 N_2}{kg.fuel} \quad (5.4)$$

- Excess O₂:

$$V_{O_2}' = (\alpha - 1) * V_{O_2}, \frac{m^3 excess O_2}{kg.fuel} \quad (5.5)$$

- WS:

$$V_{\alpha}^{WS} = V_{CO_2} + V_{H_2O}^{\alpha} + V_{SO_2} + V_{N_2}^{\alpha} + V_{O_2}', \frac{m^3 WS}{kg.fuel} \quad (5.6)$$

On the basis of the calculated quantities for the combustion products (according to equations 5.1-5.6), the composition of the flue gas is determined by calculating the percentages of the individual components (X). Each component of the flue gas is a ratio of its volume (V_X) to the total amount of flue gas (V_α^{WS}), expressed as a percentage and calculated by the following equation:

$$\% X = \frac{V_X}{V_{\alpha}^{WS}} * 100 \quad (6)$$

The sum of the individual values of each component of the flue gas must be equal to 100%.

In the present study, for the calculation of the heat of combustion (heating value) the equation (7) proposed by M. Ioelovich [24] was used. He proposed that equation as the most promising approach to improve the calculation of combustion heat, for application in the calculation of the energy of solid fuels based on natural materials, such as peat, lignite, firewood and other plant-based wastes.

$$q \text{ (MJ/kg)} = 0.344 * C + H + 0.105 * S - 0.110 * O - 0.015 * N \quad (7)$$

where: C, H, S, O and N are the percentages of the corresponding elements in the burned material.

According to Ioelovich, that equation provides a decrease in the deviation of the calculated from the experimental results to 1-2%, and the obtained results are more accurate than those obtained in the calculation with the well-known Mendeleev equation.

Based on the values obtained for the combustion heat of the material, given that 1 kWh is equal to 3.6 MJ, it is easy to calculate the energy value that it will generate upon complete combustion of 1 kg and 1 ton of combustible material, respectively. The calculation of the saved energy for households is

made on the basis of an assumption for average monthly electricity consumption for a family of four in Bulgaria, equal to 350 kWh, and assuming that the combustion rate it reaches is 1/10 of the generated total annual amount of municipal solid waste in the country.

RESULTS AND DISCUSSION

The results from the calculations done for the parameters of the combustion process of the various municipal wastes are given in Table 5, and for the combustion products and the composition of the expected generated flue gases – in Tables 6 and 7.

Table 5. Results of calculations for the amounts of oxygen, wet and dry air, and excess air required for combustion

MSW for combustion, generated by settlements with a population of:	Parameter calculated according to equation			
	(4.1)	(4.2)	(4.3)	(4.4)
less than 3001	0.55	4.51	1.83	1.86
3 001 – 25 000	0.53	4.38	1.78	1.80
25 001 – 50 000	0.51	4.18	1.70	1.72
50 001 – 150 000	0.50	4.10	1.66	1.69
over 150 000	0.52	4.29	1.74	1.77

Table 6. Results of calculations for combustion products (units of measurement are according to calculation formulas)

MSW for combustion, generated by settlements with a population of:	Parameter calculated according to equation					
	(5.1)	(5.2)	(5.3)	(5.4)	(5.5)	(5.6)
less than 3001	0.49	0.86	0.0015	4.05	0.38	5.79
3 001 – 25 000	0.48	0.89	0.0013	3.94	0.37	5.69
25 001 – 50 000	0.46	0.89	0.0013	3.77	0.36	5.47
50 001 – 150 000	0.45	0.87	0.0013	3.69	0.35	5.36
over 150 000	0.47	0.89	0.0013	3.86	0.36	5.59

Table 7. Results of flue gas composition calculations, in %

MSW for combustion, generated by settlements with a population of:	CO ₂	H ₂ O _v	SO ₂	N ₂	O ₂
less than 3001	8.45	14.79	0.025	70.09	6.64
3 001 – 25 000	8.38	15.71	0.023	69.32	6.56
25 001 – 50 000	8.34	16.23	0.024	68.88	6.52
50 001 – 150 000	8.37	16.29	0.024	68.79	6.51
over 150 000	8.45	15.99	0.024	69.01	6.53

Table 8. Results for heating values, electricity and economized electricity

MSW for combustion, generated by settlements with a population of:	Heating value, MJ/kg	Electricity, kWh/ton	Electricity*, GW/year	Economized electricity from conventional sources for household, count/year
less than 3001	10.36	2878.4	919.1	218 828
3 001 – 25 000	10.08	2799.0	893.7	212 793
25 001 – 50 000	9.63	2675.2	854.2	203 378
50 001 – 150 000	9.44	2633.3	837.6	199 432
over 150 000	9.89	2746.2	876.9	208 777

* At combusting of 1/10 of the annual amount of generated MSW

The initial composition of the mixed MSW (see Table 4) shows insignificant differences in the fractional composition. This logically assumes that no significant difference should be expected in the results obtained from the calculations for the required amounts of oxygen, wet and dry air and excess air for the combustion process, and for the composition of the flue gases and the amount of combustion products. The results presented in Tables 5-7 confirm this expectation. For example, the difference between the minimum and maximum required quantities of excess air for the combustion process is insignificant, 1.69 (for MSW from settlements with inhabitants between 50 001 and 150 000) and 1.86 (for MSW from settlements with less than 3 001 inhabitants), respectively. The results for the type of combustion products and their quantities also do not differ significantly. The differences in the percentage distribution of the generated gases are significant, albeit to a minimal extent, only in terms of the distribution between the fractions of generated water vapor and nitrogen. Significant differences are expected in terms of the economic effect of saving transport costs for transporting waste to regulated landfills and saving energy from conventional sources, in case they are incinerated as close as possible to the place of their generation.

The calculations for the energy value, the amount of produced energy and the possible amount of saved energy produced from conventional fuels, given in Table 8, are performed without taking into account the heat losses of the heat generator due to incomplete combustion of the fuel due to chemical or mechanical reasons. These calculations give a satisfactory idea of the potential of the different groups of MSW generated in the country, in view of their use for energy production.

Again, as with the parameters of the combustion process, insignificant differences are observed between the values obtained for the heating value and the electricity obtained from the combustion of a ton of waste, as the average values for both indicators are 9.88 MJ/kg and 2 746.4 kWh/t, respectively. It is interesting to note that the calculated values show that the MSW generated by small settlements with inhabitants under 3 001 people, display the highest energy value and their combustion can lead to energy savings for the needs of 218 828 households. However, the problems at the incineration of that waste are related to technological capabilities for their collection and landfilling, ensuring of continuous operation of the combustion plants and the high cost of building and maintaining the necessary infrastructure related to their possible

incineration on site and realization of the produced electricity, which is often unaffordable for small municipalities. On the other hand, the largest amounts of generated waste – from settlements with inhabitants over 150 000 people, have an energy value as maximum close to the average and the generated electricity and the energy saved for households are closest to the average compared to the different types of MSW. For that reason, it is recommended that the initial efforts to build combustion plants for waste combustion in the country should be focused mainly on the recovery of these amounts of waste in order to achieve the fastest and most significant effect, both in terms of environmental protection and achieving higher economic efficiency.

CONCLUSIONS

The results obtained from the calculations for the required amounts of oxygen, wet and dry air and excess air for the combustion process and for the composition of the flue gases and the amount of combustion products of MSW generated by settlements with different populations based on the initial morphological composition, do not logically show a significant difference.

The calculations of the energy value, the amount of produced energy and the possible amount of saved energy produced from conventional sources for households, give a satisfactory idea of the potential of the different groups of municipal solid waste generated in the country and prove their possible application for energy production.

The highest energy value can be produced by the solid wastes generated by small settlements with inhabitants under 3 001 people –10.36 MJ/kg. Their combustion can lead to savings in electricity produced from conventional fuels for 218 828 households with an average monthly electricity consumption of 350 kWh.

Based on the various technological, economic and environmental prerequisites, at present it is recommended that the main efforts to build combustion plants for waste combustion in the country should be aimed primarily at recovering the huge amount of waste generated by settlements with inhabitants over 50 000 people.

Acknowledgement: *The author would like to thank for the support of Science and Research Programme (SRC) of the UCTM – Sofia (Contract № 12 080/2021).*

REFERENCES

1. K. Miezah, K. Obiri-Danso, Z. Kádár, B. Fei-Baffoe, M. Y. Mensah, *Waste Management*, **46**, 15 (2015).
2. S. Lebersorger, P. Beigl, *Waste Management*, **31**, 1907 (2011).
3. D. Erasu, T. Feye, A. Kiros, A. Balew, *J. of the Air and Waste Management Association*, **68(12)**, 1391 (2018).
4. Th. M. Palanivel, H. Sulaiman, *APCBEE Procedia*, **10**, 96 (2014).
5. T. Karak, R. M. Bhagat, Pr. Bhattacharyya, *Critical Reviews in Environmental Science and Technology*, **42(15)**, 1509 (2012).
6. K. Kawai, T. Tasaki, *J. Mater Cycles Waste Manag.*, **18**, 1 (2016).
7. Ministry of Environment and Water (MOEW), National waste management program 2014-2020, Sofia, 2014, (in Bulgarian).
8. J. Qin, R. Zhao, T. Chen, Zh. Zi, J. Wu, *Int. J. Coal. Sci. Technol.*, **12**, 1 (2018).
9. M. K. Awasthi, S. Sarsaiya, H. Chen, Q. Wang, M. Wang, S. K. Awasthi, J. Li, T. Liu, A. Pandey, Z., Chapter 3: *Global Status of Waste-to-Energy Technology*, in: *Current Developments in Biotechnology and Bioengineering*, Elsevier, 2017, p. 31.
10. I. Chamurova, R. Stanev, N. Deliyski, *J. Chem. Tech. Met.*, **52(2)**, 355 (2017).
11. H. Manninen, K. Peltola, J. Ruuskanen, *Waste Management & Research*, **15**, 137 (1997)
12. A. Johari, R. Mat, H. Alians, H. Hashim, M.H. Hassim, Z.Y. Zakaria, M. Rozainee, *Sains Malaysiana*, **43(1)**, 103 (2014).
13. B. Vaish, V. Srivastava, P. Singh, A. Singh, Pr. K. Singh, R. Pr. Singh, *Energ. Ecol. Environ.*, **1(5)**, 323 (2016).
14. S. G. Barnabas, G. D. Sivakumar, G. S. Pandian, K. A. Geethan, S. Pr. Kumar, P. Pr. Rajeevan, P. Dh. Kumar, *Eco. Env. & Cons.*, **23**, 339 (2017).
15. H. Abdel-Shafy, M. Mansour, *Egyptian Journal of Petroleum*, **27(4)**, 1275 (2018).
16. K. Skanderova, J. Malaťak, J. Bradna, *Agronomy Research*, **13(2)**, 413 (2015).
17. MOEW, National report on the state and protection of the environment for 2014, 2016, p. 169 (in Bulgarian).
18. MOEW, National report on the state and protection of the environment for 2017, 2019, p. 220 (in Bulgarian).
19. Ministry of Economy, Energetics and Tourism (MEET), National action plan for renewable energy, 2012 (in Bulgarian).
20. MEET, Second national report for progress of Bulgaria for the promotion and use of energy from renewable sources, 2013. (in Bulgarian).
21. MOEW, Methodology for determining the morphological composition of municipal waste, 2012, (in Bulgarian).
22. I. Totev, Treatment of MSW, UASG, Sofia, 1998.
23. L. S. Paraschiva, Al. Serban, Sp. Paraschiv, *Energy Reports*, **6**, 36 (2020).
24. M. Ioelovich, Short Overview of Methods for Calculation of Combustion Heat, 2017. DOI:10.13140/RG.2.2.16303.94884.

Experimental and modelling studies of hydrogen generation from NaBH₄/Al₂O₃ nanoparticles/H₂O system with CoCl₂ as a catalyst

A. Sudan, A. Kaur*, D. Gangacharyulu, R. K. Gupta

Department of Chemical Engineering, Thapar Institute of Engineering and Technology, Patiala, India

Received: August 24, 2020; Revised: December 13, 2020

Sodium borohydride is extensively used for solid-state hydrogen storage & generation and considered as the most prominent chemical hydride due to its high hydrogen storage capacities. In relation to the previous studies on NaBH₄/Al₂O₃ nanoparticles/H₂O system with CoCl₂ as a catalyst which presented rate kinetics, this study exclusively deals with the adsorption kinetics in this system. The study includes a series of equations using Langmuir-Hinshelwood adsorption model that represents adsorption phenomenon occurring in the solution in correspondence with the equations from the literature. These equations remarkably lead through in obtaining the surface coverage parameter presenting the adsorption of borohydride ions on catalyst surface. Furthermore, effect of temperature is observed on the concentration of NaBH₄ to obtain experimental hydrogen generation. This parameter calculates [C] that is final concentration against each initial concentration of NaBH₄, amount of adsorbed species (q_e) on catalyst surface, Langmuir-Hinshelwood adsorption constants, surface coverage (θ_A) and enthalpy of the system. Role of chemical behaviour of alumina nanoparticles is also elaborated in this study, which promotes the overall hydrogen generation in combination of rise in temperature.

Keywords: Adsorption, Langmuir-Hinshelwood, Nanoparticles, Enthalpy, Hydrogen generation.

INTRODUCTION

The growing concern about depleting oil reserves and harmful effects of carbon dioxide gas emissions in atmosphere are key factors that encourage the development of new and renewable energy technologies [1]. Hydrogen, the zero carbon fuel, is a resolution considered worldwide for a secure energy future so as to lessen the effect of CO₂ in air [2]. However, many crucial and technical challenges remain to be addressed before hydrogen-based energy can become extensively accessible and economical [3, 4]. Additionally, on-board hydrogen storage has been identified as one of the technical difficulties in the implementation of hydrogen economy on global scale [5, 6]. Technologies for hydrogen storage should be considerably advanced in a hydrogen-based energy system; particularly in the transportation sector [5, 7-9]. Storing hydrogen is relatively difficult because of its low density and critical temperature. There are three ways to store hydrogen: (a) compressed gas, (b) cryogenic liquid hydrogen (LH₂) and (c) solid-state hydrogen storage [10]. The main disadvantage of compressed gas and cryogenic liquid hydrogen storage is that hydrogen can only be stored in pressurized form (up to 700 bar) or cryo-compressed form (down to -253°C).

Additionally, various safety concerns and sophisticated technologies are also required to adopt this mode of hydrogen storage.

Many novel concepts of hydrogen storage had emerged in past decades like chemical hydrogen storage or material-based hydrogen storage. One of them is solid-state hydrogen storage that involves storage of hydrogen in complex chemical hydrides. These hydrides have high hydrogen content and hydrogen can be released from them through several chemical pathways like hydrolysis and thermolysis [11-14]. Hydrolysis of chemical hydrides takes place at comparatively moderate temperatures and gives more promising theoretical hydrogen storage efficiencies than thermolysis [15].

Among all chemical hydrides, sodium borohydride (NaBH₄) has been considered as the most attractive hydrogen storage material, as it provides a safe and practical mean of storing hydrogen and has high hydrogen content. It undergoes hydrolysis reaction like other hydrides and forms the byproduct sodium metaborate (NaBO₂). By dissolving sodium borohydride in a basic solution, a highly stable aqueous solution is formed and further hydrogen release could be initiated with an active catalyst during NaBH₄ hydrolysis reaction.

* To whom all correspondence should be sent:
E-mail: er.arsh87@gmail.com

Moreover, reaction stoichiometry states that 1 g of NaBH_4 solution will produce 2.4 L of hydrogen at normal temperature and pressure (STP). On this basis, it gives gravimetric storage capacity of 10.8 wt%. Furthermore, storing hydrogen in the form of aqueous solutions has many advantages. It is worth mentioning that hydrogen with NaBH_4 could be released at ambient conditions, thus increasing its application for portable fuel cells [16-18]. There is a remarkable progress in manufacturing of proton exchange fuel cells to be used in NaBH_4 hydrogen generation systems [19]. Also, there is a significant progress in compact hydrogen storage that would meet higher hydrogen yields per unit mass and volume and is efficient enough to work at low temperature [20].

A significant research towards synthesizing an active catalyst is a step forward for development of NaBH_4 -based on-board hydrogen generation (HG) systems [21]. Cobalt(II) chloride, nickel(II) chloride, iron(II) chloride, copper(II) chloride and manganese(II) chloride are non-noble catalysts that are investigated with time for NaBH_4 hydrolysis. Besides this, noble metal catalysts like ruthenium and platinum with different supporting materials as platinum loaded on LiCoO_2 or ruthenium loaded on TiO_2 are also studied. Due to cost factors, it is not feasible to make use of noble metal catalysts for widespread applications in hydrogen storage systems. Out of all above, cobalt(II) chloride is found to be highly active for NaBH_4 hydrolysis reaction [21-23].

Various kinetic models are studied with respect to the NaBH_4 -based hydrolysis system like zero order, first order, second order, power law model, Langmuir-Hinshelwood model and Michaelis and Menton models [6]. Zero order kinetic model is based on the linear behaviour of hydrogen generation volume with fixed concentrations of NaBH_4 , NaOH and catalyst. Zero order kinetic model is not reliable because usually zero order kinetics shifts from zero order to non-zero order with respect to NaBH_4 concentrations due to by-product formation and increase in water consumption [5].

Also, first order and second order kinetic models give the dependence on catalyst and NaBH_4 concentrations and are unable to relate hydrogen generation rate (HGR) with NaOH . Michaelis and Menton model is based on constant NaOH and temperature consideration thus limiting its practical use. On the other hand, power law kinetic model is based on the concentration of catalyst, NaBH_4 and NaOH . This model could predict order with respect to each factor independently. It does not require any

assumption, hence making it useful for practical applications [6].

Therefore, the authors have used the power law kinetic model in previous studies to understand the kinetics of $\text{NaBH}_4/\text{H}_2\text{O}$ system with CoCl_2 as catalyst and alumina nanoparticles (20 nm) as promoter. Previous research revealed an incredible high efficiency of 99.34% at a mass ratio of 0.09: 0.7 for Al_2O_3 : NaBH_4 with theoretical hydrogen density of 10.76 wt% and experimental hydrogen density of 10.69 wt%. This value is high enough to ensure the overall conversion of NaBH_4 in terms of hydrogen release in the system [25].

As the previous published studies were specifically based on rate kinetics, the new insight of this research is to observe the adsorption kinetics of $\text{NaBH}_4/\text{Al}_2\text{O}_3$ nanoparticles/ H_2O system with CoCl_2 as a catalyst. Consequently, Langmuir-Hinshelwood (L-H) model is reasonably used to develop novel equations for this system representing the surface coverage of sodium borohydride ions on the catalyst in the solution. Experimentation studies are conducted to observe variation in concentration of NaBH_4 with time at different temperatures and previous studies lacked these measurements. Finally, the observed data are used to calculate the surface coverage of borohydride ions on catalyst surface.

EXPERIMENTAL

The reaction occurs in a three-port 250 mL reactor and reagents NaBH_4 , Al_2O_3 and CoCl_2 are primarily added together in solid form in the reactor before the reaction starts. Then, aqueous solution of NaOH (10 mL) is added by a pressure equalizing funnel connected to the reactor from the central port. Predetermined amounts of reactants are used for the reaction like NaBH_4 (1, 1.25, 1.50, 1.75 moles/L), CoCl_2 (0.02 moles/L), Al_2O_3 (0.09 moles/L) and NaOH (1.4 mole/L). The concentration of Al_2O_3 , CoCl_2 and NaOH is considered on the basis of preliminary experiments conducted to observe the maximum hydrogen rate in previous studies [24, 25]. Left-hand port is used to attach the thermometer to monitor the change in reaction temperature. Evolved hydrogen gas is observed as soon as the aqueous NaOH solution from the central port comes in contact with the reagents (NaBH_4 , Al_2O_3 and CoCl_2) already present in solid form in the reactor. There is continuous stirring action observed by the evolved hydrogen gas bubbles which could lead to homogeneous dispersion of the catalyst in the solution. However, the right-hand port is attached to the cylindrical pipe that guides the generated hydrogen to the inverted cylinder (3L capacity) that

is a part of the water replacement system consisting of a container (4L capacity). The experiments are performed at four different temperatures that are 293, 303, 313 and 323K, thus, a heating mantle is used to control these temperatures whereas, to prevent the fluctuation of temperature during the reaction a water bath is used taking in consideration a variation of $\pm 0.2^\circ\text{C}$.

The figure of experimental setup is similar to the setup used in previous works [24, 25] thus, it is provided in the supplementary section.

Application of Langmuir-Hinshelwood kinetic model

For the present system, Langmuir-Hinshelwood (L-H) model states the adsorption of adsorbate species (BH⁺) on the catalyst surface as the reaction in liquid phase [27]:



Here, BH₄⁻ are borohydride ions and (*) presents the catalytic surface in the solution. It is assumed that for a heterogeneous catalytic reaction, adsorption of reactant molecule occurs on the catalyst surface. Consequently, there is a possibility of formation of a strong chemical bond on the catalyst surface by the phenomenon called as chemisorption. However, few adsorbate and adsorbant combinations are formed because chemisorption involves single layer adsorption of reactant on catalyst surface. Therefore, this heterogeneous catalyst system would depend on the concentration of chemisorbed molecules. Accordingly, the concentration of reactants is related with their respective solid surface coverage on the catalyst [28, 29].

There are series of steps that occur during the hydrolysis reaction of sodium borohydride which would relate to the above theory. Firstly, for simplification, it is supposed that all reactants are in the same phase (liquid), all adsorption sites have similar energies of adsorption and there is no interaction among adsorbed species.

a) The change in concentration of sodium borohydride [C] with time is calculated by equation 2:

$$[C] = C_{A0} \left(1 - \frac{V_{H_2}}{V_{H_2\max}}\right) \quad (2)$$

where, C_{A0} is the initial concentration of NaBH₄ in moles/L. V_{H₂} is the experimental value of hydrogen generated at each time point and V_{H₂max} is the maximum amount of hydrogen that can be generated by the system in litres [27].

b) The maximum amount of hydrogen generated is calculated as follows:

$$V_{H_2\max} = \frac{\text{amount of NaBH}_4 \text{ taken}}{\text{molecular weight of NaBH}_4} \times 4 \times \frac{22.4}{273} \times T \quad (3)$$

where, T = reaction temperature in K, constant (4) is the number of molecules of hydrogen generated by stoichiometry given by equation:



c) further, (q_e) is the concentration of adsorbed species calculated by:

$$q_e = \frac{C_A - C_{A0}}{C_{\text{catalyst}}} \times \text{Volume of the solution (L)} \quad (5)$$

RESULTS AND DISCUSSION

Previous studies presented the role of each individual reagent that promoted hydrogen generation rate. NaBH₄ is the prime component during the reaction and supplier of borohydride ions in the solution.

CoCl₂ is a catalyst precursor; it is reduced by borohydride ions to form catalytically active Co₂B species in the solution [38].

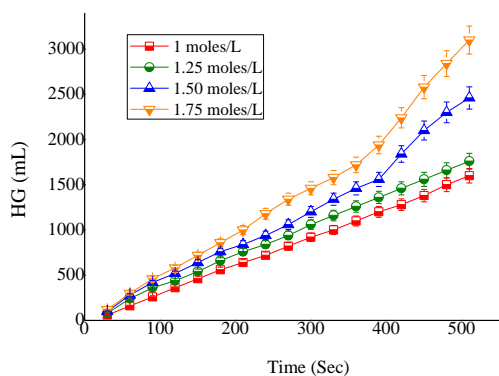
Alumina acts as a catalyst promoter which provides a synergistic catalytic effect because of the formation of Co₂B species and hydroxylates of alumina. This results in the formation of Co/Al complexes like cobalt aluminates which further promote the activity of Co₂B active species resulting in intensifying NaBH₄ hydrolysis in the solution [32, 33]. These interpretations are backed by physiochemical methods like XRD and FTIR characterization analysis used to study the residue left after the completion of the reaction. The results undoubtedly present that cationic adsorption of Co⁺² or Na⁺ occurs on the hydroxide layer of alumina surface that leads to the formation of cobalt and sodium aluminates in the solution (Figures S2 & S3).

Lastly, NaOH helps in preventing passivation of alumina surface which helps alumina to form Co/Al and Co/Na complexes and ultimately promotes hydrolysis of NaBH₄ [24, 25].

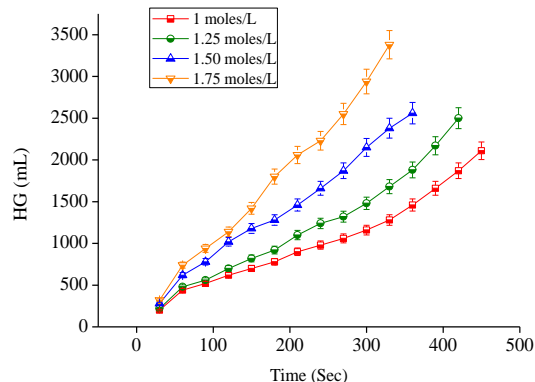
In the present study hydrogen generation is observed at increasing temperatures (293, 303, 313 and 323 K) at different concentrations of NaBH₄ (Figures 1, 2, 3 and 4) with respect to time [30-32]. The figures significantly confer the increasing trend of hydrogen generation (HG) with temperature whereas in previous studies, the trend of increase in HG with respect to NaBH₄ was observed only at room temperature. Additionally, these plots of HG with time also provide the experimental hydrogen generation at each concentration and varying set of temperatures. This experimental hydrogen obtained plays a vital role in observing the adsorption kinetics and ultimately calculating the surface coverage of

borohydride ions on the catalyst surface in this system. The generated experimental hydrogen is used in equation 2 formulated with V_{max} (equation 3) to calculate the final concentration of NaBH_4 (Table 1). Further, the concentration of adsorbed species

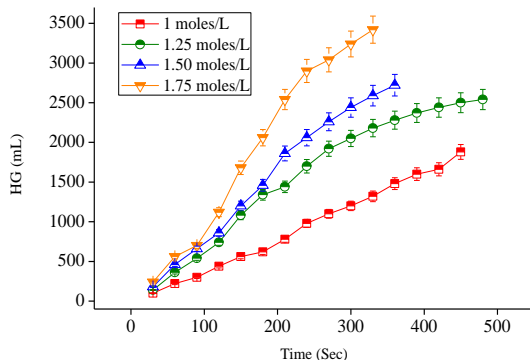
(q_e) is calculated by using equation 5. This finally provides the values of surface coverage of borohydride ions on the catalyst (Table 2) at varying temperatures.



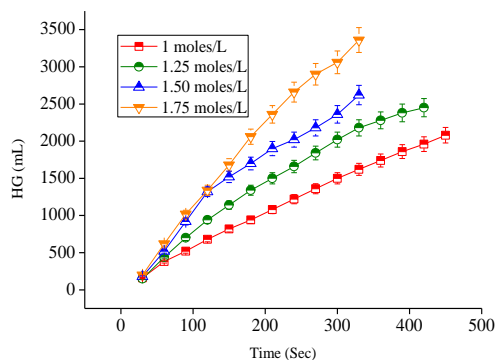
(1) At 293K



(2) At 303K



(3) At 313K



(4) At 323K

Figures 1, 2, 3 & 4. Plots of hydrogen generation with respect to time at various temperatures.

Table 1. Final concentration of NaBH_4 at different temperatures

S. No.	Initial concentration	Final concentration at various temperatures (moles/L)			
	C_{A0} (moles/L)	[C] 293K	[C] 303K	[C] 313K	[C] 323K
1.	1	0.02	0.03	0.04	0.09
2.	1.25	0.05	0.06	0.07	0.08
3.	1.50	0.09	0.18	0.21	0.22
4.	1.75	0.12	0.13	0.16	0.27

Table 2. Values of q_e and θ_A at 293 and 323K

Sample No.	C_{A0} (moles/L)	[C] (moles/L) at 293K	[C] (moles/L) at 323K	q_e (moles/g) at 293K	q_e (moles/g) at 323K	θ_A at 293K	θ_A at 323K
1.	1	0.016	0.019	0.20	0.20	0.4	0.6
2.	1.25	0.05	0.073	0.23	0.24	0.5	0.8
3.	1.50	0.09	0.22	0.28	0.26	0.60	0.9
4.	1.75	0.12	0.27	0.29	0.3	0.8	1

Table 1 gives information of the final concentration of NaBH₄ at various temperatures (293, 303, 313 and 323K) and the mathematical calculations confirm that the final concentration of NaBH₄ in solution increases with an increase in temperature [36, 37].

Table 2 provides the values of q_e (amount of absorbed species) and θ_A (surface coverage). Here, an increasing trend in the values is observed with respect to temperature and NaBH₄ concentration.

Consequently, Langmuir adsorption isotherm constants (k₁, k₂, k₃ and k₄) at 293, 303, 313 and 323K and enthalpy of this system are calculated by Van't Hoff equation 6:

$$\frac{d}{dt} \ln(K_{eq}) = \frac{\Delta H}{RT^2} \quad (6)$$

Here, ln(K_{eq}) signifies the change in equilibrium constant with change in temperature. Thus, by plotting ln(K_{eq}) and 1/T (Figure 5) the enthalpy of the system is calculated as -47 kJ/mole.

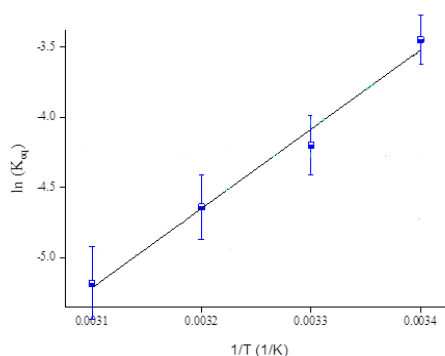


Figure 5. Plot of 1/[T] and ln(Ke_q)

When these results are interrelated with previous interpretations it is understood that temperature is dominantly promoting the role of alumina as a catalyst promoter in the solution and ultimately causing an increase in surface coverage of borohydride species on the catalyst surface. Therefore, the present study would also comprehensively describe the chemical behavior of alumina in the solution to provide a clear vision on how temperature is promoting adsorption kinetics in the solution.

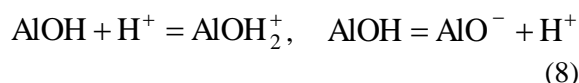
Chemical properties of alumina are elaborated as given below which in combination with rise in temperature have a considerable effect on hydrogen generation.

(a) Hydrophilic nature of alumina. Due to the chemical behaviour of γ-Al₂O₃ in the solution at least a monolayer of water is chemisorbed by alumina. When the surface is hydrated, water molecules are

chemisorbed on the top oxide layer of γ-Al₂O₃ as shown in reaction 7 [33]:



(b) Amphoteric nature of alumina. Reactive functional groups (hydroxyl ions) are coordinated in various ways to aluminum cations on the alumina surface like hydroxyl group with one aluminum ion and hydroxyl groups with two aluminum ions. Basic nature of alumina is given by singly coordinated hydroxyl groups and acidic nature by hydroxyl ions coordinated with two aluminum ions. The ionization reactions presenting the acidic and basic nature of alumina are given in [34]:



The hydroxyl groups in the present system are expected to be singly co-ordinated with aluminum ions thus, developing a basic nature in the solution.

(c) Iso-electric point and pH of the solution. This is explained by the principle of electro-neutrality, as in acidic medium the oxide particle will be positively charged and to compensate this charge a layer of particles with opposite charge (negative charge) will be present in the solution that will surround the oxide particles. Similarly, in basic medium, oxide particles will be negatively charged and a layer of positively charged particles will be present in the solution that surrounds the oxide particle. Furthermore, the iso-electric point is the value of solution pH when the net oxide particle charge is zero. The iso-electric point of alumina is at pH = 8, which implies that alumina will adsorb anions at a solution pH lower than 8 and adsorb cations at a solution pH higher than 8 [34, 35]. The present system is at pH = 9, therefore, adsorption of Co⁺² and Na⁺² cations occurs on alumina surface.

Thus, hydrophilic nature, amphoteric nature, iso-electric point and pH of solution are a few chemical behavioral characteristics of alumina that promote its reactivity as a catalyst promoter in the solution.

Therefore, it is interpreted that increase in temperature speeds up the formation of alumina reactivity and formation of cobalt and sodium aluminates in the solution and results in rise in affinity, as well as diffusion capacity of borohydride ions towards the catalyst resulting in high surface coverage of borohydride ions on the catalyst surface with rise in temperature [36, 37].

CONCLUSIONS

The present research is an exclusive study on the adsorption properties of the NaBH₄/γ-Al₂O₃ nanoparticles/ H₂O system with CoCl₂ as a catalyst. Langmuir-Hinshelwood adsorption model is extensively used predicting the equations in correspondence with the present hydrogen generation system. The effect of increasing temperature is examined at varying concentration of NaBH₄ and thus experimental hydrogen generation is monitored. This ultimately leads to calculate parameters like final NaBH₄ concentration, q_e that is concentration of the adsorbed species, Langmuir adsorption isotherms constants and surface coverage (θ_A). It is observed that all these parameters increase with increase in temperature. Furthermore, Van't Hoff equation calculates the value of enthalpy of this system to be -47 kJ/mole. Mathematical calculations describe the increase in surface coverage of borohydride ions with temperature. This result is also supported by the chemical properties of alumina like hydrophilic nature, amphoteric nature, isoelectric point and pH of the solution as they enhance the rate of hydrogen generation in the system. The study overall describes novel mathematical observations and adsorption studies of the NaBH₄/γ-Al₂O₃ nanoparticles/ H₂O system with CoCl₂ which directly contributes to the use of NaBH₄ for practical fuel cell applications.

Acknowledgements: The authors gratefully acknowledge the support provided by the management of Thapar Institute of Engineering and Technology, Patiala for providing the necessary facilities to carry out this research work and guidance provided by Prof. Pramod K. Bajpai (Ex. Distinguished Professor, Thapar University, India) and Dr. Chitrakshi Goel (Research Officer, Swansea University, Swansea, Wales, U.K.)

REFERENCES

1. S. Kaufman, *J. Chemical Society*, **64**, 307 (1985).
2. H. I. Schlesinger, H. C. Brown, A. E. Finholt, J. R. Gilbreath, H. R. Hoekstra, E. K. Hyde, *J. American Chem. Society*, **75**, 215 (1953).
3. K. Cowey, K. J. Green, G. O. Mepsted, R. Reeve, *Current Opinion in Solid State and Material Science*, **8**, 367 (2004).
4. J. S. Zhang, D. Hazra, T. S. Fisher, P. V. *J. Power Sources*, **32**, 2298 (2006).
5. S. C. Amendola, G. S. L. Sharp, J. M. Saleem, M. T. Kelly, P. J. Petillo, M. Binder, *J. Power Sources*, **85**, 186 (2000).
6. R. Retnamma, A. Novais, C. M. Rangel, *Int. J. Hydrogen Energy*, **22**, 1649 (2011).
7. Y. Shang, R. Chen, *Energy and Fuels*, **20**, 2149 (2006).
8. A. Zuttel, A. Borgschulte, L. Schlapbach, *Int. J. Hydrogen Energy*, **27**, 203 (2002).
9. A. E. Y. Marrero, A. M. Beaird, T. A. Davis, M. A. Matthews, *J. Molecular Catalysis*, **48**, 3703 (2009).
10. U. Eberle, M. Felderhoff, *J. German Society*, **48**, 6608 (2009).
11. R. Chahie, T. K. Bose, *J. Hydrogen Energy*, **19**, 161 (1994).
12. A. C. Dillon, K. M. Jones, T. A. Bekkedahl, C. H. Kiang, D. S. Bethune, M. J. Heben, *Applied Physics*, **72**, 133 (2001).
13. S. Hynek W. Fuller Bentley, *Int. J. Hydrogen Energy*, **22**, 601 (1997).
14. M. Kunowsky, B. Weinberger, F. Lamari Darkrim, G. F. Suarez, A. D. Cazorala, L. Solano, *Int. J. Hydrogen Energy*, **33**, 2975 (2008).
15. B. Sakintuna, F. Lamari, *Int. J. Hydrogen Energy*, **32**, 1121 (2007).
16. B. Bogdanovic, M. Schwickardi, *J. Alloys Compounds*, **36**, 302 (2000).
17. V. Diakov, M. Diwan, E. Shaffirovich, A. Varma, *Chem. Eng. Society*, **62**, 5586 (2000).
18. R. B. Binwale, S. Rayalu, S. Devotta, M. Ichikawa, Chemical hydrides, *Int. J. Hydrogen Energy*, **39**, 1390 (2008).
19. Nagar, A. Schechter, B. B. Moshe, N. Shvalb, *Materials and Design*, **108**, 240 (2016).
20. V. Netskina, T. N. Phillipov, O. V. Komova, V. I. Simagina, *Catal. Sustain. Energy*, **41**, (2018).
21. U. B. Demirci, *Turkish J. Chemistry*, **42**, 193 (2018).
22. S. Kaufman, *J. Power Sources*, **85**, 186 (2000).
23. O. Akdim, U. B. Demirci, D. Muller, P. Miele, *Int. J. Hydrogen Energy*, **34**, 2631 (2009).
24. A. Kaur, D. Gangacharyulu, P. K. Bajpai, *Brazilian J. Chem. Eng.*, **35**, 131 (2016).
25. A. Kaur, D. Gangacharyulu, P. K. Bajpai, *Brazilian J. Chem. Eng.*, **36**, 929 (2019).
26. G. F. Froment, K. B. Bischoff, *Chemical Reactor Analysis and Design*, John Wiley and Sons, New York, 1990.
27. J. S. Zhang, W. N. Delgass, T. S. Fisher, J. P. Gore, *J. Power Sources*, **164**, 772 (2007).
28. D. D. Duong, *Adsorption Analysis: Equilibria and Kinetics*, Imperial College Press, London, 1998.
29. D. Mark, J. D. Robert, *Fundamentals of Chemical Reaction Engineering*, McGraw Hill, New York, 2003.
30. M. Mitov, R. Rashkov, N. Atanassov, A. Zielonka, *J. Material Science*, **42**, 3367 (2007).
31. H. B. Dai, Y. Liang, P. Wang, H. M. Cheng, *J. Power Sources*, **177**, 17 (2008).
32. B. H. Liu, Z. P. Li, S. Suda, *J. Alloys and Compounds*, **415**, 288 (2006).
33. L. Soler, A. M. Candela, J. Macanas, M. Munoz, J. Casado, *J. Power Sources*, **192** (2009).
34. G. Sposito, *The Environmental Chemistry of Aluminum*, Lewis Publishers, 1996.
35. J. P. Brunelle, *Pure and Applied Chemistry*, **50**, 1211 (1978).

36. E. Y. M. Alfonso, A. M. Beard, T.A. Davis, M. A. Matthews, *Industrial and Engineering Chemistry Research*, **48**, 3703 (2009).
37. H. Y. Cheng, H. H. Chih, S. T. Chung, *Aerosol and Air Quality Research*, **12**, 745 (2012).
38. H. B. Dai, G. L. Ma, X. D. Kang, P. Wang, *Catalyst Today*, **170**, 50 (2009).

Supplementary Section

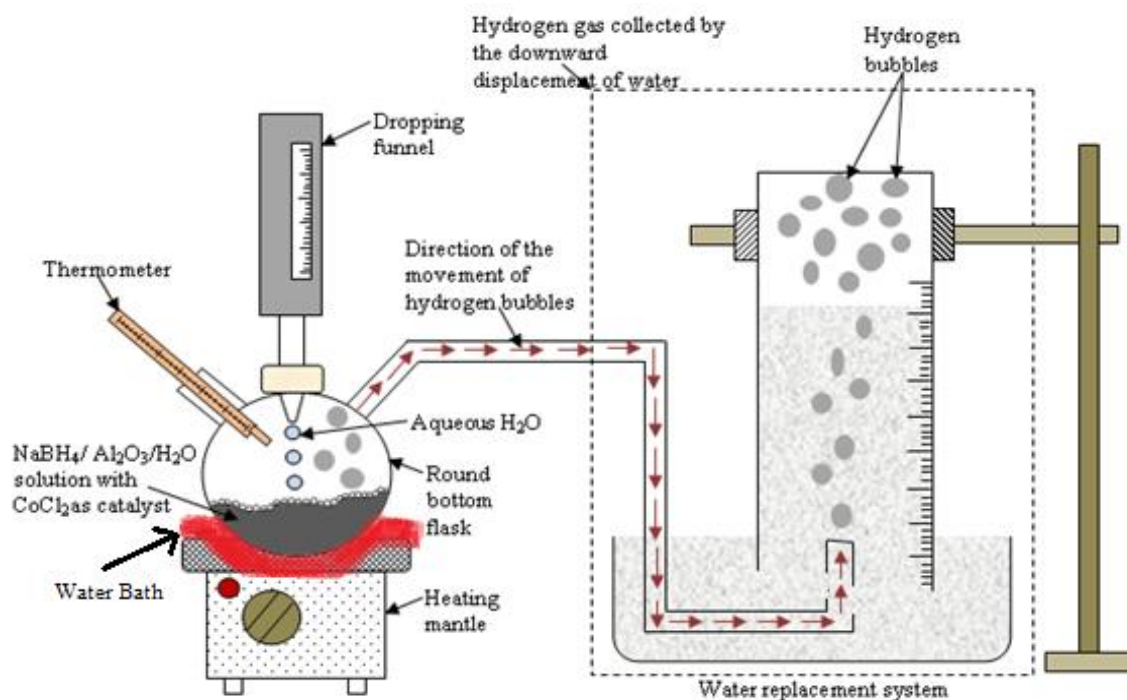


Figure S1. Experimental set up

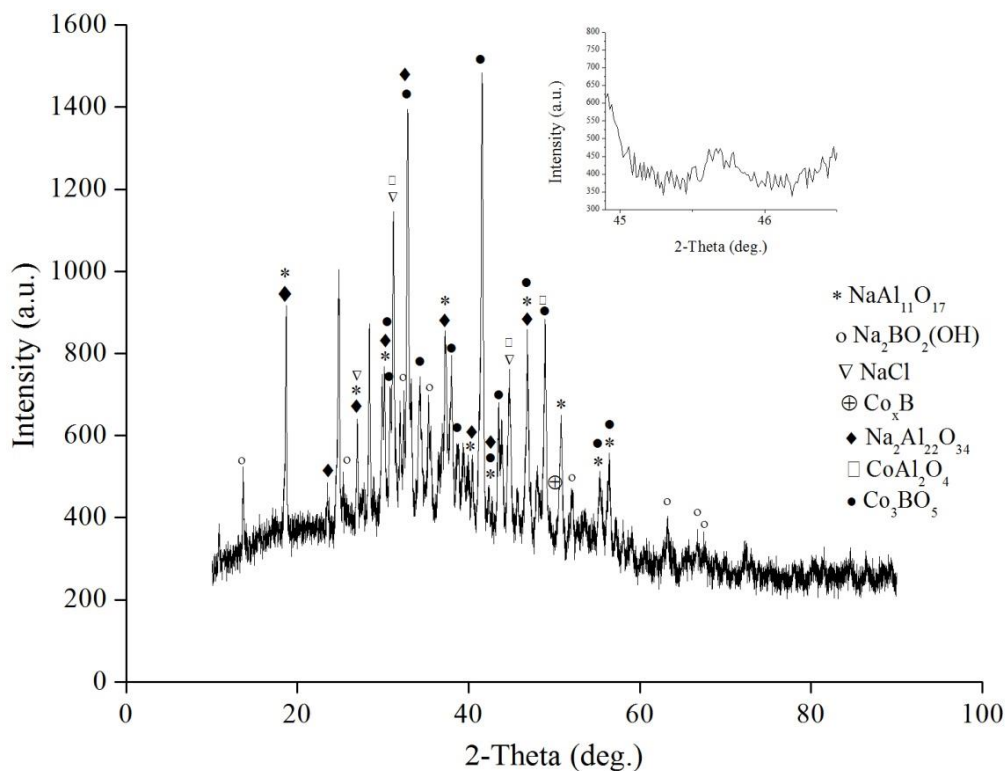


Figure S2. XRD analysis of residue [24]

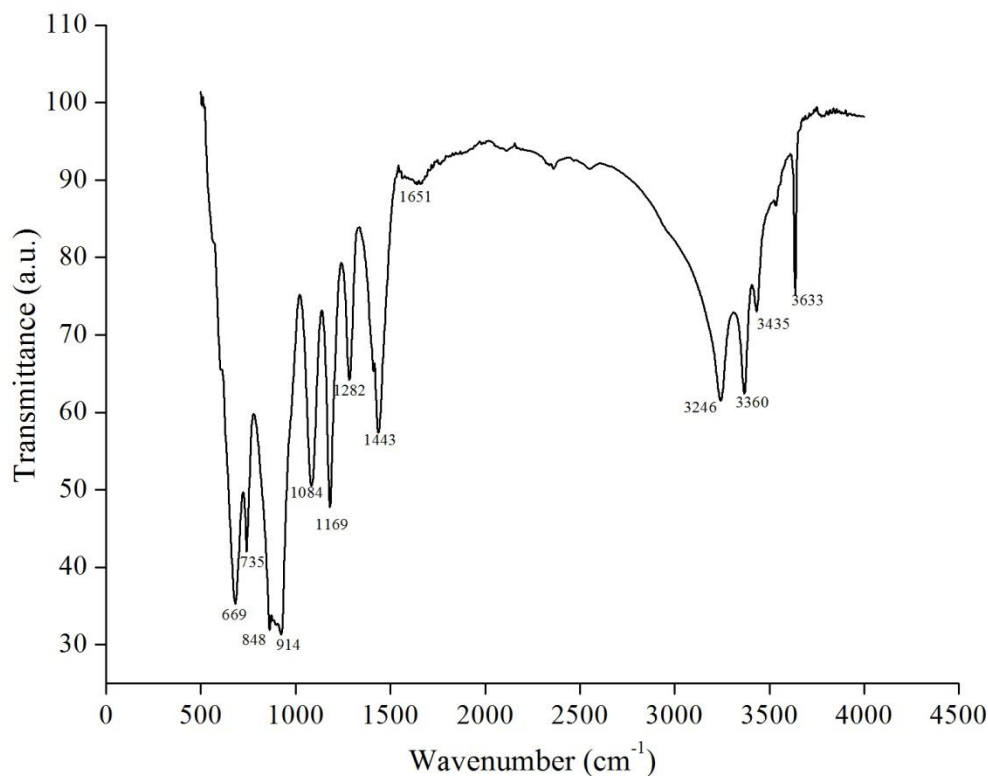


Figure S3. FTIR analysis of residue [24]

Following are the reactions from the literature studies in correspondence with the present system of hydrogen generation.

Active site for chemisorption is given by R with its surface concentration [R]. Adsorption concentration of NaBH₄ is expressed as [C], thus,



Here, [CR] is NaBH₄ that is chemisorbed on the sites of the surface with respect to k_{ads} and k_{ds} that are rate constants signifying the rate of adsorption and desorption. Hence, the net rate of adsorption is given by [28]:

$$r = k_{\text{ad}}[C][R] - k_{\text{de}}[CR] \quad (S2)$$

Hence, the equilibrium relation becomes,

$$K_{\text{ad}} = \frac{k_{\text{ad}}}{k_{\text{de}}} = \frac{[CR]}{[C][R]} \quad (S3)$$

Also, we introduce [R]_I that is concentration of all adsorption sites on the catalyst surface and θ_C that is the surface coverage of reactants on the catalyst surface.

Therefore,

$$[R]_i = [R] + [CR] \quad (S4)$$

$$\theta_C = \frac{[CR]}{[R]_i} \quad (S5)$$

The fractional surface coverage (θ_C) by the adsorbate borohydride ions could also be obtained from equations S3, S4 and S5 [26]:

$$\theta_C = \frac{[C]K}{1 + [C]K} \quad (S7)$$

Here, K is Langmuir adsorption isotherm constant and [C] is concentration of NaBH₄ at time t.

Equations used for calculation of surface coverage of borohydride ions on catalyst surface:

[CR] is written as q_e in moles/g and [R]_i is written as q_m in moles/g for calculation purposes, therefore,

$$\theta_C = \frac{q_e}{q_m} \quad (S8)$$

From equations S7 and S8, the following equation is obtained:

$$\frac{1}{q_e} = \frac{1}{K[C]q_m} + \frac{1}{q_m} \quad (S9)$$

Thus, the plot of $1/q_e$ and $1/q_m$ would give the slope and intercept to calculate k_{ad} and q_m [4].

Theoretical investigation of inclusion complex of 2-methyl mercapto phenothiazine with hydroxy propyl β -cyclodextrin by DFT approaches

Y. Mezari¹, L. Nouar^{2*}, F. Madi², A. Guendouzi^{3,4}, I. Djellala², I. Lafifi², R. Merdes¹,
A. Bouhadiba⁵, B. Houari³

¹Laboratory of Applied Chemistry, Department of Material Sciences, Faculty of Mathematical, Informatics and Material Sciences, University of 8 Mai 1945, Guelma, Algeria

²Laboratory of Computational Chemistry and Nanostructures, Department of Material Sciences, Faculty of Mathematical, Informatics and Material Sciences, University of 8 Mai 1945, Guelma, Algeria

³Laboratory of Chemistry, Synthesis, Properties and Applications, Department of Chemistry, Faculty of Sciences, University of Saïda, Algeria

⁴Laboratory of Applied Thermodynamics and Molecular Modeling, University Abu Bekr Belkaïd of Tlemcen, Algeria

⁵Laboratory of Computational Chemistry and Nanostructures, University of Skikda, Algeria

Received: September 24, 2020; Revised: February 02, 2021

The supramolecular host-guest complexation of 2-methyl mercapto phenothiazine with hydroxy propyl β -cyclodextrin is computationally investigated employing B97-D3 and BP86-D3 levels of theory with 6-31G(d,p) basis set in gas and aqueous phases. The computed binding and interaction energies values reflect the stability of the studied inclusion complexes. EDA, TD-DFT, NBO, QTAIM and NCI analyses were done to give more information about the nature of intermolecular interaction between 2-methyl mercapto phenothiazine and hydroxy propyl β -cyclodextrin. The results show that the inclusion complexes are stabilized by hydrogen bonding and van der Waals interactions. Finally, our theoretical ¹H NMR chemical shift results are in good agreement with the experimental data.

Keywords: Inclusion complex, interaction energies, Fukui function, electronic transitions, non-covalent interactions.

INTRODUCTION

In recent years, quantum chemical approaches have become a valuable tool to understand the nature of interactions in supramolecular systems. These interactions play important roles in molecular properties. A deep understanding of intermolecular non-covalent interactions has been one of the main tasks in theoretical chemistry. Several parameters contribute to quantify the nature of non-covalent intermolecular interactions in supramolecular systems [1]. These parameters can be divided in four categories: energy decomposition analysis (EDA), which provides quantitative analysis for intermolecular interactions *via* dividing total interaction energy into several physically meaningful energy quantities, atoms in molecules (AIM) [2] to inspect the nature of weak interactions in supramolecular complexes; non-covalent interactions (NCI) analysis has been widely used to visualize the interaction in the supramolecular host-guest system [3] and NBO analysis, in which intermolecular interaction energy is estimated by charge transfers between donating and accepting orbitals [4].

Phenothiazines are organic compounds related to the thiazine class of heterocyclic compounds. They have antipsychotic, antiemetic, anthelmintic,

antibacterial, antifungal, insecticidal and anticancer properties [5]. 2-Methyl mercapto phenothiazine (2MMPT) (10-[2-(1-methyl-2-piperidyl)ethyl]-2-(methylthio)-10H-phenothiazine thioridazine) (Fig. 1) is one of the phenothiazine substituents showing strong antiproliferative activity against various breast, ovarian, lungs, and melanoma cell lines [6]. However, phenothiazine derivatives have a low solubility in water [7] possibly limiting its range of applications. Therefore, complexation with cyclodextrin is a significant method to increase the solubility, bioavailability and biological activities of phenothiazine drugs.

Cyclodextrins (CDs), are cyclic oligomers of α -D-glucose units connected through glycosidic α -1,4 bonds, which can form inclusion complexes with a variety of organic compounds [8]. The most widely used CDs are α -, β - and γ -CDs. Compared to α - and γ -cyclodextrins, β -cyclodextrin (β -CD) is most useful. However, the solubility of β -CD is relatively low [9]. Hydroxy propyl β -cyclodextrin (HP β -CD) is a substitute for β -CD and has higher water solubility than β -CD. Hydroxy propyl β -cyclodextrin (Fig. 1) has attracted growing research interest owing to its low toxicity, satisfactory inclusion ability and capacity to improve the physico-chemical properties and the solubility of poorly water-soluble drugs [10].

* To whom all correspondence should be sent:

E-mail: leilanoua@yahoo.fr, nouar.leila@univ-guelma.dz

© 2021 Bulgarian Academy of Sciences, Union of Chemists in Bulgaria

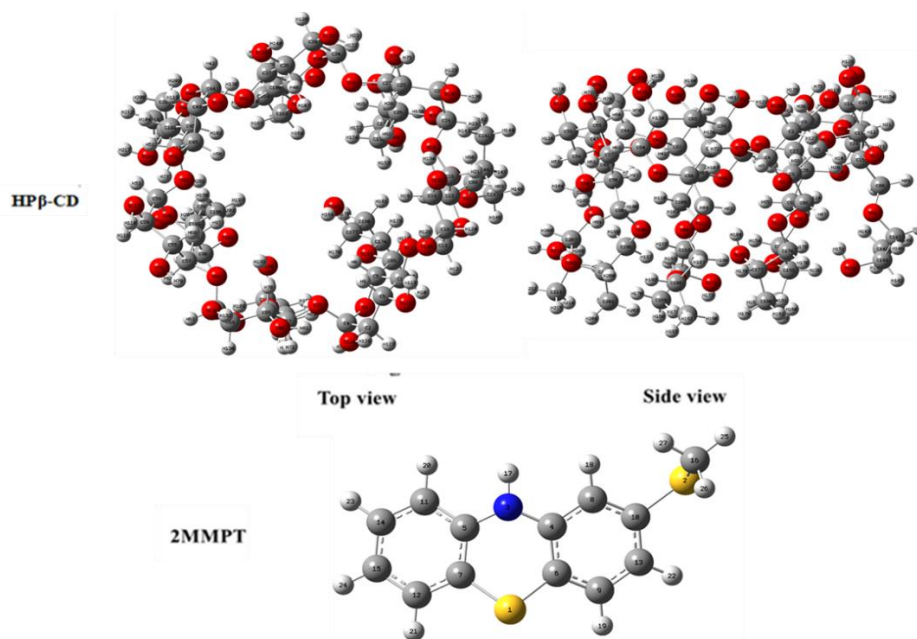


Fig. 1. Molecular structures and atom numbering for HPβ-CD and 2MMPT.

The complexation involving 2MMPT and HPβ-CD has been studied experimentally for improving solubility and bioavailability of the active principle [11]. However, in the latter work, no information about the nature of intermolecular non-covalent interactions between host and guest of the complex was provided.

The aim of this work is to study the nature of non-covalent intermolecular interactions, especially hydrogen bond interaction between 2MMPT and HPβ-CD during inclusion complex formation.

Therefore, the present work is organized as follows: Firstly, in computational details we describe the formation of the complex between HPβ-CD and 2MMPT, using PM3 semi-empirical method to localize the minimum energy structures. Secondly, the most stable complexes, found by PM3 calculations, were re-optimized by the DFT-D3 method. Thirdly, the analysis results of the intermolecular non-covalent interactions are discussed.

Computational details

Geometry optimizations were performed by PM3 and DFT using the dispersion corrected with the Grimme's D3 correction [12-14]. For the complexation process, we followed the method described in our previous studies [15, 16]. The oxygen atoms of glycosidic bond links of HPβ-CD were placed onto the (XY) plane. Their center was set as the center of the coordination system. The secondary (OH) groups of the HPβ-CD were positioned pointing toward the Z-axis in the positive

direction. The 2MMPT molecule was initially oriented along the Z-axis. We considered in this process two possible inclusion models with HPβ-CD. The model in which the phenyl ring of 2MMPT points toward the secondary hydroxyl of HPβ-CD was called the "C1 complex", the other model in which 2MMPT penetrates into the cavity of HPβ-CD from its wide side by the SCH₃ group was called the "C2 complex". The inclusion models can be seen in Fig. 2. The relative position between the host and the guest was determined by the Z-coordinate of the labelled nitrogen atom (N220) of the guest (Fig. 2). Then, the guest was moved into the HPβ-CD cavity along the Z-axis from -6 to +6 Å with 1 Å step. The generated structures at each step were optimized by the PM3 method without imposing any symmetrical restrictions. On the other hand, the generated structures at each step were analyzed by EDA analysis. After that, the obtained global minimas were fully re-optimized within any restriction at B97-D3 and BP86-D3 levels of theory with 6-31G(d, p) basis set in gas and aqueous phases. The solvent effects in water ($\epsilon=78.5$) were evaluated by a conductor polarizable continuum model (CPCM). Harmonic vibrational frequencies were computed for the minimum energy geometries to verify them to be at the minimum on the potential surface. Statistical thermodynamic calculations were carried out at 1 atm and 298.15 K in gas and aqueous phases. The gauge-independent atomic orbital (GIAO) method [17] was used to compute ¹H NMR chemical shifts of free and complexed 2MMPT.

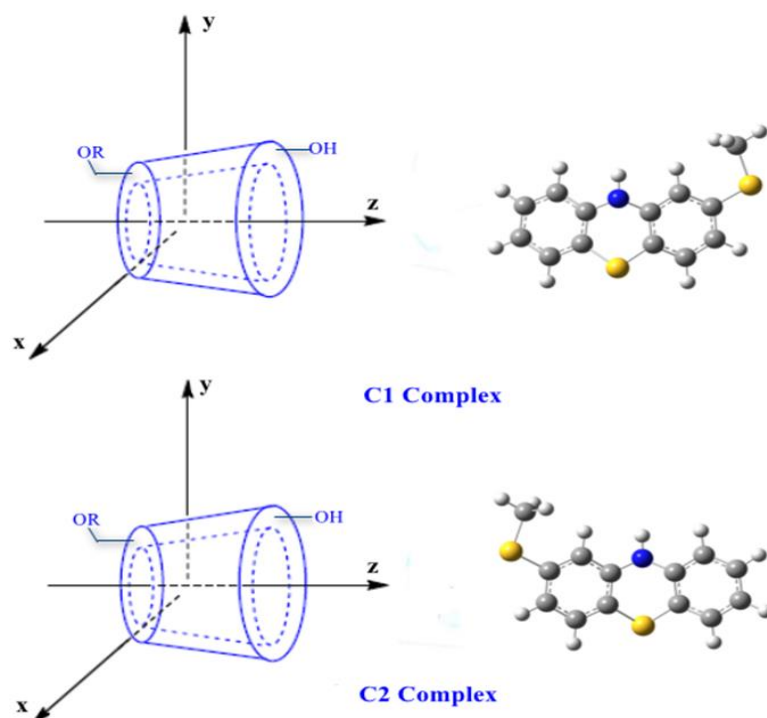


Fig. 2. Proposed structures of 2MMPT @ HPβ-CD inclusion complexes.

Electronic transitions by time-dependent density functional theory (TD-DFT) and the frequency shift in the calculated vibrational spectra were explained. Finally, to identify the nature of non-covalent intermolecular interactions between host and guest on the optimized structures with the lowest energy in aqueous phase at BP86-D3/6-31G(d,p) level of theory, we investigated the natural bond orbital (NBO), atoms-in-molecules (AIM) and the non-covalent interactions in the complexes using the non-covalent interaction-reduced density gradient (NCI-RDG) analyses. Geometry optimizations and NBO calculations were carried out using the Gaussian 09 package [18]. QTAIM and NCI-RDG analyses were envisaged using the Multiwfn program [19] and visualized by the VMD program [20]. EDA analysis was performed using the ADF package [21].

RESULTS AND DISCUSSION

Energies, geometries and thermodynamic parameters

The PM3 calculation was used in this study to localize global minima through Z-axis for C1 and C2 complexes by controlling binding energy during the inclusion process of 2MMPT into HPβ-CD cavity.

To evaluate the stability of the obtained complexes, we calculated binding, interaction and strain energies using the following eqs.:

$$\Delta E_{\text{binding}} = E_{\text{binding}} - (E_{\text{HP}\beta\text{-CD}} + E_{2\text{MMPT}}) \quad (1)$$

where E_{binding} , $E_{\text{HP}\beta\text{-CD}}$ and $E_{2\text{MMPT}}$ represent the total energy of the complex, the free optimized HPβ-CD and the free optimized 2MMPT energy, respectively. The binding energy corresponds to the energy change accompanying the inclusion of 2MMPT in HPβ-CD:

$$\Delta E_{\text{interaction}} = E_{\text{complex}} - (E_{\text{HP}\beta\text{-CD}}^{\text{SP}} + E_{2\text{MMPT}}^{\text{SP}}) \quad (2)$$

where E_{complex} , $E_{\text{HP}\beta\text{-CD}}^{\text{SP}}$ and $E_{2\text{MMPT}}^{\text{SP}}$ are the total energy and the single point energy of the HPβ-CD and 2MMPT molecules in the optimized complexes, respectively.

$$\Delta E_{\text{strain}} = (E_{\text{component}}^{\text{SP}} - E_{\text{component}}^{\text{free}}) \quad (3)$$

where $E_{\text{component}}^{\text{SP}}$ is the single point energy of the component (HPβ-CD or 2MMPT) in the optimized complex and $E_{\text{component}}$ is the energy when it is optimized in free form.

The variation of the binding energy for both complexes is illustrated in Fig. 3. As it can be seen, all values of binding energy are negative, which indicates that the inclusion process of the 2MMPT in the HPβ-CD is thermodynamically favorable. The lowest binding energies were obtained at $Z = -3 \text{ \AA}$ and $Z = -4 \text{ \AA}$ for C1 and C2 complexes, respectively.

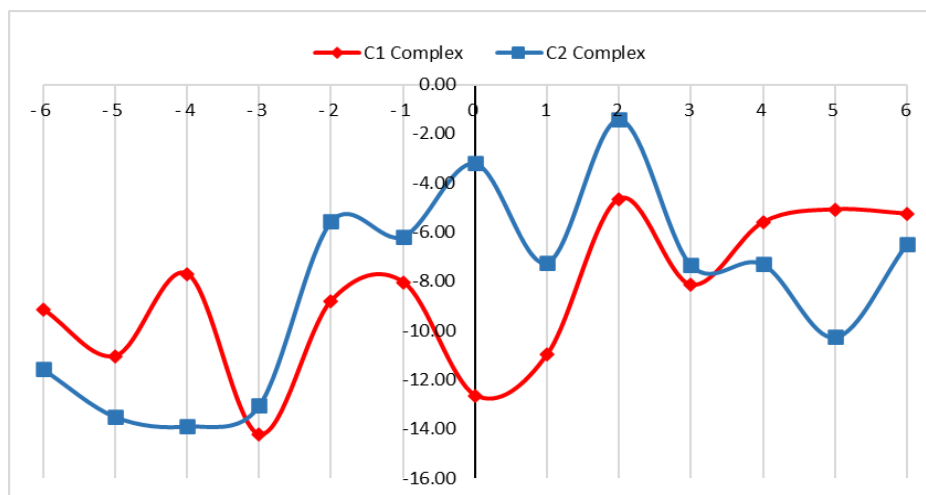


Fig. 3. Variation of the binding energy for both complexes at different positions, PM3 calculations.

The calculated binding, interaction and strain energies for the most stable structures in gas and in aqueous phases are mentioned in Table 1. We noticed that the binding energy in gas phase is in favor of the C1 complex by 1.78 and 4.28 kcal/mol, respectively, by the B97-D3/6-31G(d,p) and BP86-D3/6-31G(d,p) methods. In aqueous phase, the results of calculations listed in Table 1 confirm those obtained in gas phase and the binding energy difference in aqueous phase for B97-D3/6-31G(d,p) and BP86-D3/6-31G(d,p) calculations between the two complexes is 4.11 and 8.62 kcal/mol, respectively, in favor of the C1 complex. These energies are higher in gas phase than in aqueous phase, because the water molecules can weaken the intermolecular interactions between the host and guest molecules.

In addition, interaction energy is an important parameter also measuring the stability of inclusion complexes; it is found more negative for the two complexes in both gas and aqueous phases with BP86-D3/6-31G (d, p) calculations.

Binding and interaction energies in gas and in aqueous phases with two functionals follow the order B97-D3/6-31G (d,p) > BP86-D3/6-31G(d,p). BP86-D3/6-31G (d,p) gave the most negative values of binding and interaction energies for studying our systems.

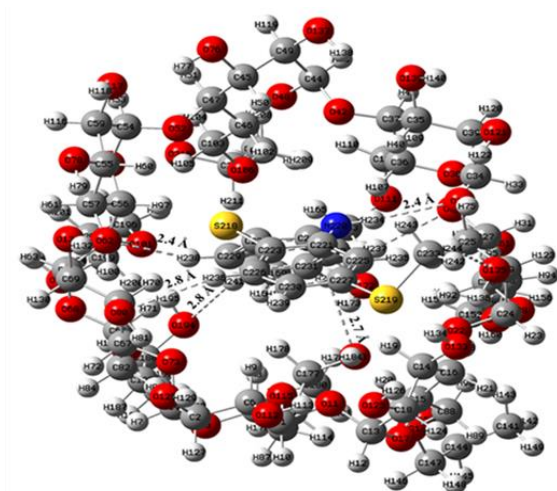
The distortion in the geometry of the 2MMPT and HP β -CD molecules in gas and in aqueous phases is reflected in the calculated strain energy (ΔE_{strain}). The ΔE_{strain} values for the HP β -CD are larger than that of 2MMPT in the two complexes. The great deformation of HP β -CD structure has an important role in increasing the intermolecular interaction of the complexes. From these results it can be

concluded that the distortion in the geometry of the host seems to be one of the driving factors leading to the formation of stable inclusion complexes. In Fig. 4, we illustrated the geometrical structures of the most stable C1 and C2 complexes obtained from B97-D3/6-31G (d,p) and BP86-D3/6-31G(d,p) calculations in both phases. We noticed that the 2MMPT molecule is totally embedded in the HP β -CD cavity. Hydrogen bonds established between the host and guest molecules in the C1 complex are stronger than those in the C2 complex (see Fig. 4 and Table 1S). In this sense, the hydrogen bonds can be considered the driving forces responsible for the difference in binding energies between the two complexes. The structure of the C1 complex agrees well with experimental results, which indicated that the aromatic part of 2MMPT was included into the cavity of HP β -CD from its wide side and formed an inclusion complex [11].

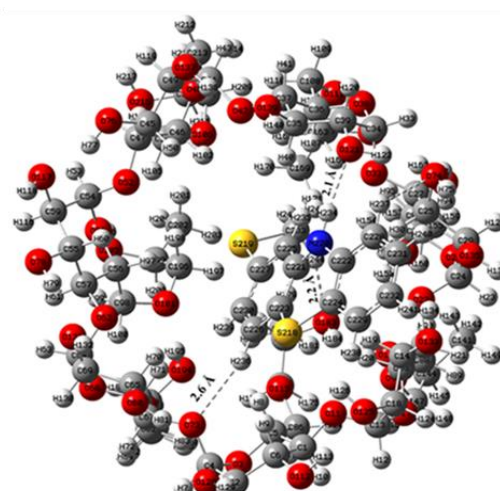
From the vibrational frequency computations and statistical thermodynamics, the standard thermodynamic parameters, *viz.*, enthalpy (ΔH°) and free energy (ΔG°) of the inclusion complexes in gas and in aqueous phases were calculated and are summarized in Table 1. Negative values for ΔH° and ΔG° indicate that the formation of the complexes is an exothermic and spontaneous process. This result is in good agreement with experimental data [11]. However, ΔH° and ΔG° values for the C1 complex obtained from B97-D3/6-31G(d,p) and BP86-D3/6-31G(d,p) functional in gas and in aqueous phases are lower than for the C2 complex, indicating that formation of this complex is a weak exothermic process.

Table 1. Energies (kcal/mol) and thermodynamic parameters for both complexes in gas and in aqueous phases.

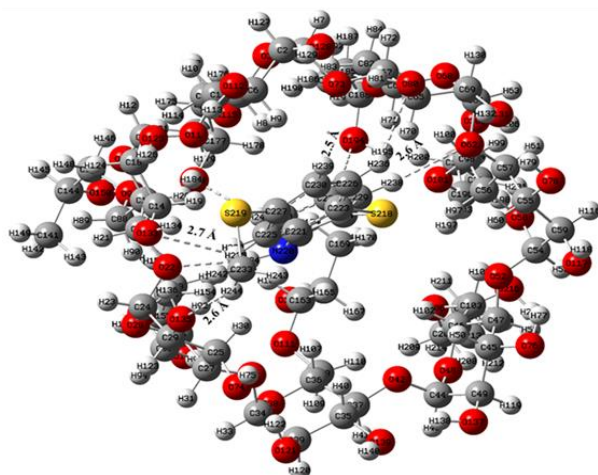
Methods	B97-D3/6-31G(d, p)		BP86-D3/6-31G(d, p)	
	C1	C2	C1	C2
In gas phase				
$\Delta E_{\text{Binding}}$	-42.87	-41.09	-47.46	-43.18
$\Delta E_{\text{Interaction}}$	-56.22	-53.06	-63.32	-63.47
$\Delta E_{\text{Strain (HP}\beta\text{CD)}}$	10.26	9.87	11.72	16.98
$\Delta E_{\text{Strain (2MMPT)}}$	3.11	2.10	4.14	3.31
$\Delta H^\circ(\text{kcal.mol}^{-1})$	-39.78	-32.14	-45.22	-40.79
$\Delta G^\circ(\text{kcal.mol}^{-1})$	-29.69	-16.02	-28.14	-22.94
In aqueous phase				
$\Delta E_{\text{Binding}}$	-38.27	-34.16	-50.87	-42.25
$\Delta E_{\text{Interaction}}$	-47.74	-41.46	-58.94	-54.70
$\Delta E_{\text{Strain (HP}\beta\text{CD)}}$	6.37	6.51	4.41	9.72
$\Delta E_{\text{Strain (2MMPT)}}$	3.10	0.79	3.66	2.74
$\Delta H^\circ(\text{kcal.mol}^{-1})$	-35.85	-33.63	-47.99	-39.50
$\Delta G^\circ(\text{kcal.mol}^{-1})$	-19.19	-17.08	-29.49	-22.06



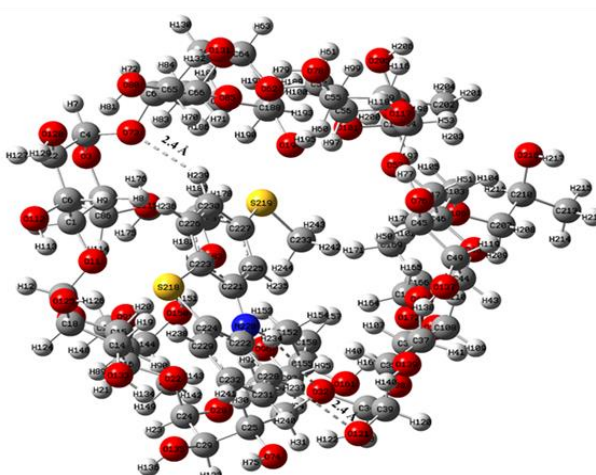
(a)



(b)



(c)



(d)

In gas phase

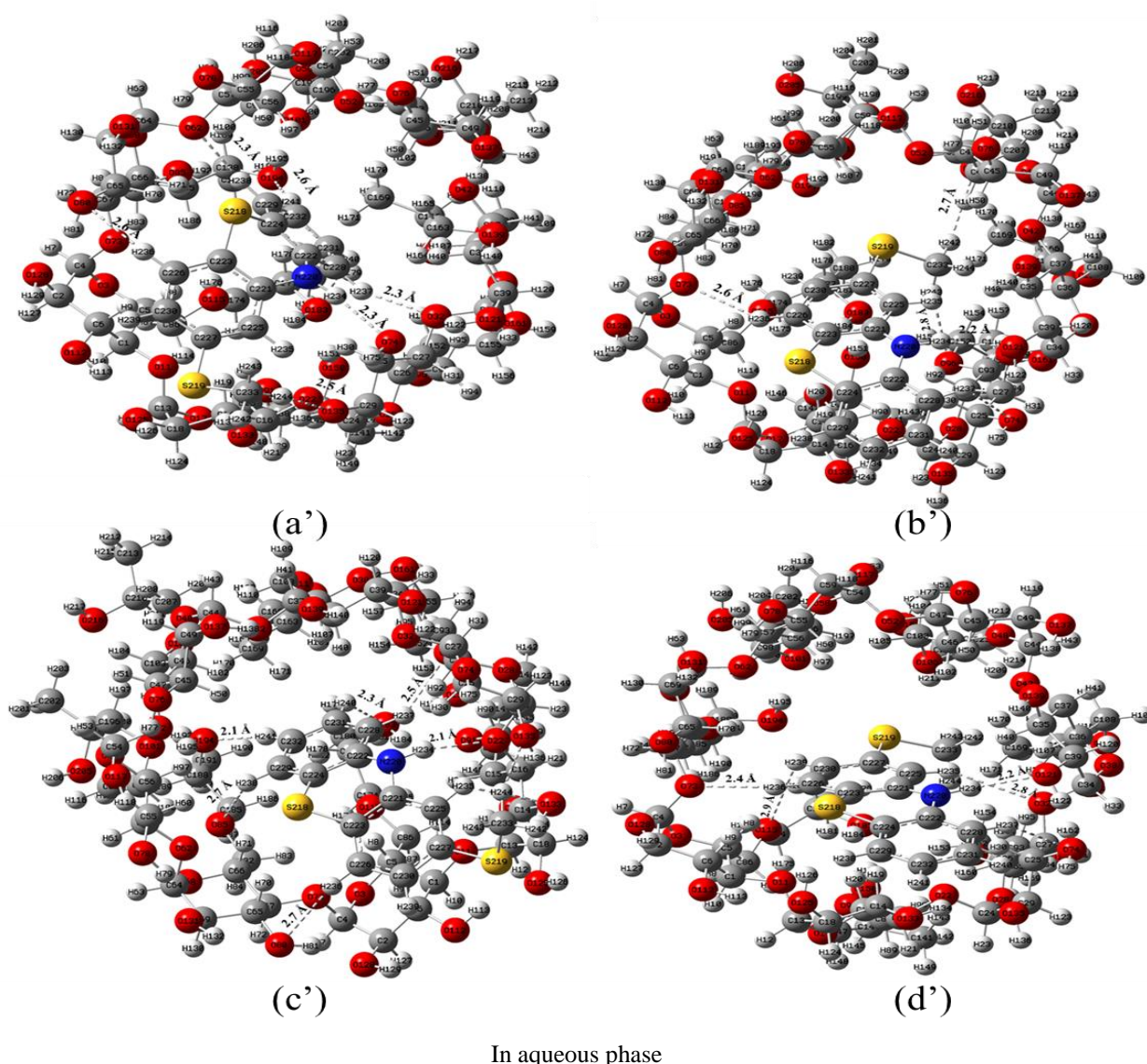


Fig.4. Optimized structures of inclusion complexes obtained from B97-D3/6-31G(d,p) (a, b, a', b') and BP86-D3/6-31G(d,p) (c, d, c', d') calculations. (a, b, c, d) in gas and in aqueous phases (a', b', c', d'), respectively, for C1 and C2 complexes.

Local reactivity descriptors

The local reactivity was analyzed with the aid of the Fukui indices, the condensed Fukui functions [22-24] for the reactive sites of electrophilic and nucleophilic attack on the molecules, which can be expressed as:

$$\text{For nucleophilic attack:} \\ f_k^+ = [q_k(N+1) - q_k(N)] \quad (4)$$

$$\text{For electrophilic attack:} \\ f_k^- = [q_k(N) - q_k(N-1)] \quad (5)$$

$$\text{For radical attack:} \\ f_k^0 = [q_k(N+1) - q_k(N-1)]/2 \quad (6)$$

where +, -, 0 signs refer to nucleophilic, electrophilic and radical attack, respectively.

The Fukui index for electrophilic attack (f_k^-) represents the nucleophilic site of the species and the

Fukui index for nucleophilic attack (f_k^+) represents the electrophilic site of the species [25]. Condensed Fukui functions (f_k^+ , f_k^-) associated with the nucleophilic and electrophilic attacks, using natural population analysis (NPA) of 2MMPT (Scheme 1S) before and after complexation in aqueous phase, are reported in Table 2S. To compare between the possible sites for nucleophilic and electrophilic attacks on any atom, we calculated (Δf_k) which corresponds to the difference ($f_k^+ - f_k^-$). If $\Delta f_k < 0$, then the site is favorable for an electrophilic attack, whereas if $\Delta f_k > 0$, then the site is favorable for a nucleophilic attack. As can be observed, for an isolated 2MMPT molecule S1, S2 and N3 are the most nucleophilic sites, whereas C13 and C14 are the electrophilic sites. After complexation, the values of the dual descriptor are also changed

comparatively to the free 2MMPT. S1, S2 and N3 are the most nucleophilic sites with a slight decrease in values of $f_{(k)}$. C7 and C10 become favorable electrophilic sites. Condensed Fukui functions in the gas phase are illustrated in Table 3S. As can be seen from Table 3S, nucleophilic and electrophilic attacks in gas phase are the same to those obtained in the aqueous phase with difference in values of the Fukui indices. The plots of the Fukui indices for isolated 2MMPT and the two complexes in gas and in aqueous phases are presented in Fig. 5.

Electronic transitions and UV-Vis spectra

The electronic transitions of the two complexes were calculated using the time-dependent density functional theory (TD-DFT) at BP86-D3/6-31G (d, p) level using ground-state geometries in aqueous phase. The calculated excitation energies, oscillator strength (f) and wavelength (λ) and configurations of

excitations are given in Table 4S. For the C1 complex, TD-DFT calculations predict two transitions in the UV-Vis region. A strong transition is observed at 2.9414 eV (421.51 nm) with an oscillator strength $f = 0.0078$. This peak is due to electronic transition from HOMO-1 \rightarrow LUMO. For the C2 complex three transitions are observed, a strong one at 410.59 nm with vertical transitions and oscillator strength equal to 3.0196 eV, respectively. This band is obtained between HOMO \rightarrow LUMO. A careful inspection of molecular plots of encapsulated complexes (Fig. 6) shows that in the C1 complex, the HOMO-1 is localized on the HP β -CD molecule and LUMO is localized on 2MMPT revealing a high charge transfer in the complex. In the C2 complex, the HOMO and LUMO orbitals are localized on the 2MMPT molecule, which shows that this excitation arises from a local excited state.

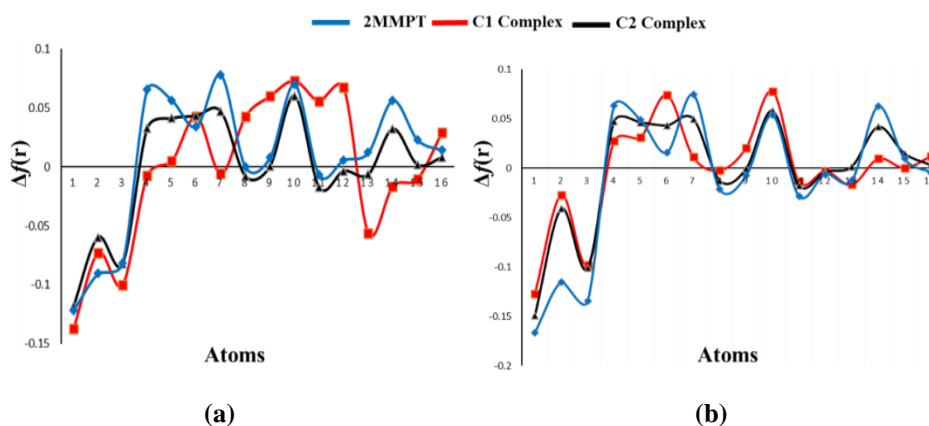


Fig. 5. Plots of the Fukui indices for the isolated 2MMPT and the two complexes in gas (a) and in aqueous (b) phase.

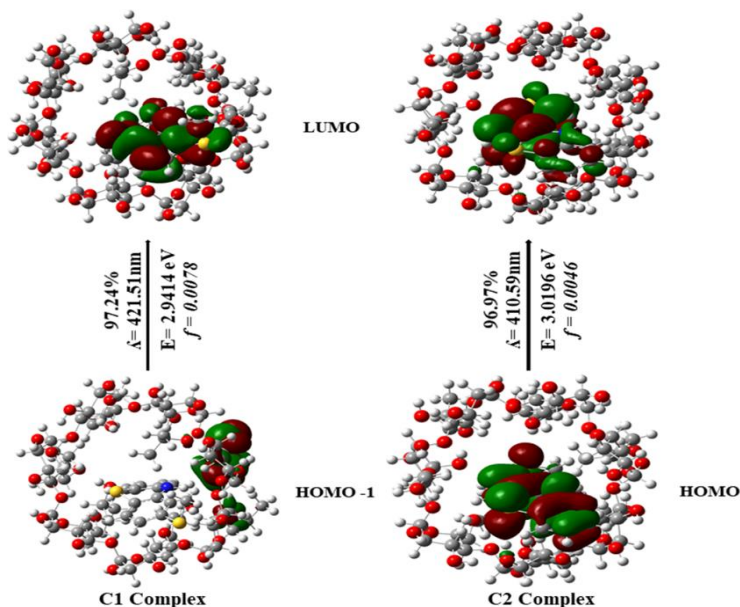


Fig. 6. Plots of molecular orbitals for vertical excitation energies (E , eV), oscillator strengths (f) and wavelength (λ) for C1 and C2 complexes calculated at BP86-D3/6-31G (d,p) in aqueous phase.

NMR spectral studies

Based on BP86-D3/6-31G (d,p) optimized geometries, the gauge-including atomic orbital (GIAO) method was applied for ¹H NMR calculations by employing the density functional theory B3LYP at 6-31G (d,p) basis set by using corresponding TMS shielding calculated at the same theoretical level as the reference. The calculated proton chemical shifts of isolated and complexed 2MMPT (Scheme 1S) are recorded in Table 2. We noticed a significant change in chemical shift values of 2MMPT in the two complexes. This significant chemical shift change confirmed the encapsulation of 2MMPT into the hydrophobic cavity of HPβ-CD and the formation of an inclusion complex between 2MMPT and HPβ-CD. On the other hand, the computed shielding obtained for the optimized

structures from the GIAO theory analysis for C1 and C2 complexes plotted as a function of the experimental chemical shift parameters [11] displayed in Fig. 7 turns out to be linear. The linear regression equation is expressed by the following regression expressions:

$$\delta_{\text{Calculated}} = 1.0704 \delta_{\text{experimental}} - 0.5988,$$

with correlation coefficient $R^2 = 0.96$ for the C1 complex and

$$\delta_{\text{Calculated}} = 0.8106 \delta_{\text{experimental}} + 0.7669,$$

with $R^2 = 0.90$ for the C2 complex.

The best linear correlation between calculated and experimental chemical shift is observed in the C1 complex; however, our theoretical ¹H NMR chemical shift results for the C1 complex are in good agreement with the experimental data [11].

Table 2. ¹H NMR chemical shift (δ, ppm) in D₂O obtained by the GIAO approach for free and complexed 2MMPT as calculated at B3LYP-D3/6-31G(d,p) level of theory and chemical shift displacement Δδ after complexation.

Δδ = δ_{2MMPT in complex} - δ_{2MMPT free}

Proton	2MMPT calculated	2MMP Texp	C 1 complex	C 2 complex	2MMPT@ HPβ-CDexp	Δδ _{C 1} complex	Δδ _{C2} complex	Δδ _{exp}
H _a	5.420	5.798	5.353	5.248	5.802	0.067	0.173	0.004
H _b	6.031	7.254	6.507	5.822	7.262	0.477	0.208	0.008
H _c	6.675	7.001	6.949	6.425	7.011	0.274	0.25	0.01
H _d	6.712	6.894	6.709	6.371	6.904	0.003	0.340	0.01
H _e	6.893	6.732	6.811	6.550	6.743	0.082	0.343	0.011
H _f	6.911	6.542	6.923	6.584	6.542	0.012	0.326	0
H _g	7.014	6.840	6.912	6.725	6.847	0.102	0.289	0.007
H _h	6.464	6.462	6.463	5.912	6.481	0.001	0.552	0.019
H _i	2.402	2.423	1.957	2.681	2.436	0.451	0.279	0.013
H _j	2.137	/	2.452	1.968	/	0.315	0.169	/
H _k	2.137	/	2.573	2.335	/	0.436	0.198	/

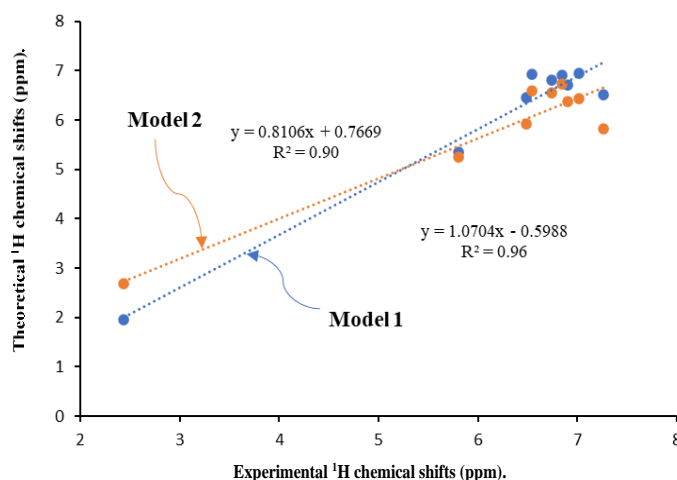


Fig. 7. Correlation between calculated and experimental chemical shifts.

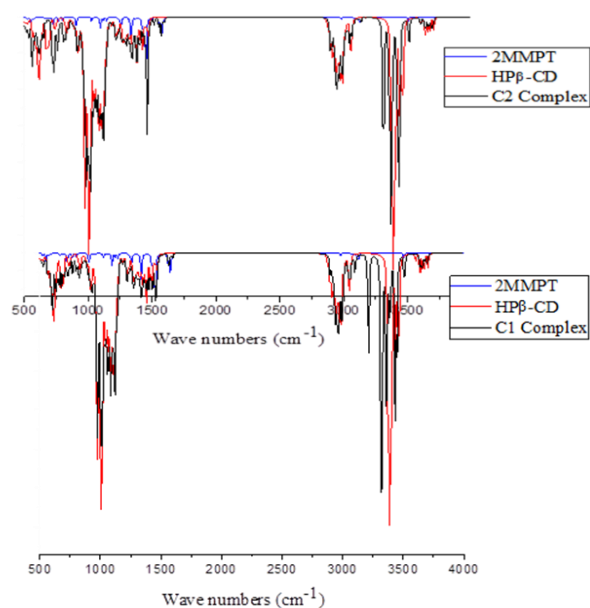


Fig. 8. FT-IR spectra of 2MMPT (in blue), HPβ-CD (in red) and 2MMPT@HPβ-CD (in black) inclusion complexes.

Vibrational spectra

Vibrational frequencies are useful for probing interatomic interactions between host and guest in the two complexes. The infrared spectra of HPβ-CD, 2MMPT, C1 and C2 inclusion complexes are shown in Fig. 8. BP86-D3/6-31G (d,p) computed spectra of the complexes (depicted in black) are compared with the individual HPβ-CD (red) and 2MMPT (blue) spectra. The theoretical and experimental frequencies are presented in Table 5S. As shown in Table 5S and in Fig. 8, for HPβ-CD, peaks were observed at 3398 cm⁻¹, 2950 cm⁻¹, 921 cm⁻¹ and 1120 cm⁻¹, respectively, for O-H stretching, C-H stretching, C-H bending and C-O stretching vibrations. Upon complexation with 2MMPT, these vibrational frequencies reveal up-shift tendencies. In the case of 2MMPT, the bands resulting from inclusion complexes are shifted or their intensities are changed. The highly intense band at 3500 cm⁻¹ assigned to the N-H stretching shows downshift in the two complexes. The C-H stretching and C-S stretching vibrations show down-shift. The C=C stretching, C-C stretching and C-H bending vibrations show up-shift in their vibrational frequencies. N-H bending shows up-shift for the C1 complex and down-shift for the C2 complex. In addition, C-N stretching and C-S-CH₃ stretching vibrations reveal a shift in their frequencies. These results indicated that the 2MMPT was included into the cavity of HPβ-CD and formed an inclusion complex. The selected calculated vibrational

frequencies in the C1 and C2 complexes given in Table 5S are generally in consonance with these obtained in experimental data [11].

Recently, Lane *et al.* [26] demonstrated that the analysis of the kinetic energy density $G(r)$ features at the hydrogen bond critical points could be correlated to spectroscopic features of the X-H stretching involved in hydrogen bond formation. With this view the calculated kinetic energy density $G(r)$ was plotted as a function of the frequency shift in Fig. 2S. The plot reveals an excellent linear correlation.

Natural bond orbital analysis

The natural bonding orbital (NBO) analysis provides an efficient method for studying intra- and intermolecular bonding and for investigating charge transfer or conjugative interaction in molecular systems [27]. Also it can be used to estimate delocalization of the electron density between occupied Lewis-type orbitals and unoccupied non-Lewis NBOs, which corresponds to a stabilizing donor-acceptor interaction [28]. In the NBO analysis the stabilization or second-order perturbation energy $E^{(2)}$ is a value of energy by which the whole of the molecular systems is stabilized through charge transfer from donor to acceptor groups, and the large $E^{(2)}$ value shows the intense interaction between electron donors and electron acceptors and the greater extent of conjugation of the whole system [29]. This second-order perturbation energy $E^{(2)}$ is defined by:

$$E^{(2)} = q_i \frac{F(i,j)}{\epsilon_j - \epsilon_i} \quad (7)$$

where q_i is the donor occupancy, ϵ_i and ϵ_j are diagonal elements (orbital energies), and $F(i,j)$ are off-diagonal elements of NBO Fock matrix. Natural bond orbital (NBO) donors and acceptors and their second-order perturbation energy values $E^{(2)}$ in both gas and aqueous phases for C1 and C2 complexes are tabulated in Table 3. The interactions are classified in two categories: that the $E^{(2)}$ value is larger than 2 kcal/mol for strong hydrogen bond interaction and from 0.5 kcal/mol to 2kcal/mol for weak hydrogen bond interaction [30]. The interactions are detailed as follows: for the C1 complex, the highest interaction energy was observed for the lone pairs interaction LP (S 218)_{2MMPT} → σ*(C 65 - H 70)_{HPβ-CD}, LP (S 219)_{2MMPT} → σ*(O 133 - H 134)_{HPβ-CD}, LP (O22)_{HPβ-CD} → σ*(N 220 - H 234)_{2MMPT} and LP (O194)_{HPβ-CD} → σ*(C 232 - H 241)_{2MMPT}, with stabilization energy ranged between 2.02 to 28.01 kcal/mol.

Table 3. NBO electronic transitions of the intermolecular HBs of host-guest inclusion complexes of 2MMPT with HP β -CD for C1 and C2 complexes and the corresponding stabilization energies ($E^{(2)}$).

Donor	Acceptor	$E^{(2)}$ Bp86-D3/6-31G(d,p)	
		In gas phase	In aqueous phase
C1 complex			
LP (2) S 218	$\sigma^*(C 65 - H 70)$	4.62	2.28
$\sigma(C 26 - H 92)$	$\sigma^*(C 228 - H 237)$	0.25	0.58
$\sigma(C 56 - H 97)$	$\sigma^*(C 229 - H 238)$	0.11	0.08
LP (2) S 219	$\sigma^*(O 133 - H 134)$	28.01	20.61
$\sigma(C 169 - H 171)$	$\sigma^*(C 231 - H 240)$	0.12	0.19
$\sigma(C 225 - H 235)$	$\sigma^*(O 135 - H 136)$	0.08	0.17
$\sigma(C 226 - H 236)$	$\sigma^*(O 80 - H 81)$	0.05	0.05
$\sigma(C 227 - H 237)$	$\sigma^*(C 26 - H 92)$	0.21	0.91
$\sigma(C 229 - H 238)$	$\sigma^*(C 56 - H 97)$	0.31	0.13
LP (1) O 22	$\sigma^*(N 220 - H 234)$	2.02	6.23
LP (2) O 194	$\sigma^*(C 232 - H 241)$	3.10	4.96
$\sigma(C 231 - H 240)$	$\sigma^*(C 169 - H 171)$	0.10	0.30
$\sigma(C 232 - H 241)$	$\sigma^*(O 194 - H 195)$	0.20	0.06
C2 complex			
$\sigma(C 25 - H 30)$	$\sigma^*(N 220 - H 234)$	0.07	0.21
$\sigma(C 35 - H 40)$	$\sigma^*(N 220 - H 234)$	0.10	0.08
$\sigma(C 39 - H 121)$	$\sigma^*(C 228 - H 237)$	0.12	0.12
$\sigma(C 66 - H 71)$	$\sigma^*(C 230 - H 239)$	0.28	0.23
$\sigma(C 225 - H 235)$	$\sigma^*(C 35 - H 40)$	1.06	0.83
LP (2) S 218	$\sigma^*(O 125 - H 126)$	8.38	7.67
$\sigma(C 226 - H 236)$	$\sigma^*(C 6 - H 9)$	0.60	0.19
LP (1) O 73	$\sigma^*(C 226 - H 236)$	2.01	2.09
$\sigma(C 227 - H 230)$	$\sigma^*(O 183 - H 184)$	0.17	0.10
LP (2) O 121	$\sigma^*(N 220 - H 234)$	6.44	6.15
$\sigma(C 228 - H 237)$	$\sigma^*(O 121 - H 122)$	0.43	0.35
$\sigma(C 230 - H 239)$	$\sigma^*(C 5 - H 8)$	0.24	0.06
$\sigma(C 231 - H 232)$	$\sigma^*(O 133 - H 134)$	0.17	0.09
$\sigma(C 233 - H 243)$	$\sigma^*(C 163 - H 164)$	0.18	0.06

For the C2 complex, donor–acceptor interactions are observed between LP (O121)_{HP β -CD} \rightarrow $\sigma^*(N 220 - H 234)$ _{2MMPT}, LP (S218)_{2MMPT} \rightarrow $\sigma^*(O 125 - H 126)$ _{HP β -CD} and LP (O 73)_{HP β -CD} \rightarrow $\sigma^*(C 226 - H 236)$ _{2MMPT} with stabilization energy ranged between 2.09 to 8.38 kcal/mol. Thus, we concluded that the higher $E^{(2)}$ energy for the C1 complex indicates a greater interaction compared to the C2 complex. This result is in agreement with the binding and interaction energies of the C1 complex. The interactions described above are hydrogen bonds. The other types of orbital’s interactions: $\sigma \rightarrow \sigma^*$ are relatively low, in which their stabilization energies vary between 0.05 and 1.06 kcal/mol. These interactions are classified as weak hydrogen bonds. From this NBO analysis, it can be concluded that these complexes are stabilized by strong hydrogen bonds and van der Waals interactions.

Energy decomposition analysis

The generated structures optimized by the PM3 method at each step from -6 to $+6$ Å were analyzed by EDA at BP86-D3/6-31G (d,p) functional. The computed results are depicted in Fig. 9 and in Table 6S in supporting information. The total binding energies are the summation of four terms, *viz.*, Pauli repulsion (ΔE^{Pauli}), electrostatic (ΔE^{elstat}), orbital (ΔE^{orb}) and dispersion (ΔE^{disp}) terms. In the EDA analysis, the 2MMPT is considered as one fragment and the HP β -CD is considered as the other fragment. From Table 6S and Fig. 9 it can be seen that the repulsive term, ΔE^{Pauli} , is positive in value and is responsible for steric repulsion [31, 32]. The term ΔE^{Pauli} provides the repulsive interaction between the occupied orbitals of two interacting fragments. The maximum contribution at each step comes from ΔE^{elstat} and plays a major role in stabilizing the two complexes. The non-covalent term ($\Delta E^{\text{elstat}} + \Delta E^{\text{disp}}$) contributes more largely in the total stabilization

than the covalent term (ΔE^{orb}) confirming the non-covalent nature of the interactions between host and guest. From the EDA results, we can conclude that in the attractive forces, the electrostatic interaction dominates in the intermolecular bonding between the HP β -CD and the 2MMPT.

QTAIM analysis

The intermolecular interactions in C1 and C2 complexes were further discussed through topological QTAIM analysis. Bader [33, 34] developed QTAIM quantum theory. It is based on the study of the topology of the electronic density, which characterizes the distribution of electrons in space.

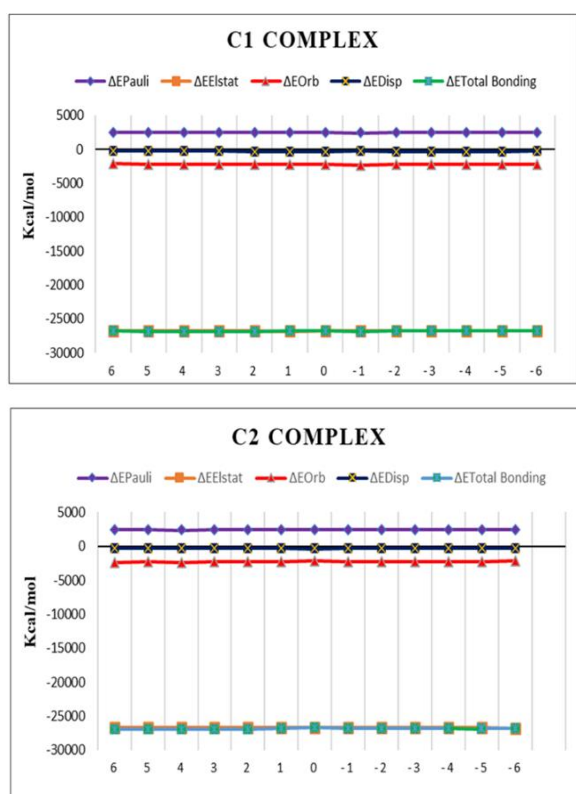


Fig. 9. Energy profiles of the generated structures at each step for C1 and C2 complexes obtained from the EDA analysis at BP86-D3/6-31G (d,p) level of theory.

It is allowed to determine the different characteristics that present the intra- and intermolecular interactions, precisely to find hydrogen bond strengths from different topological properties [35]. The Laplacian, local kinetic energy density $G(r)$, local potential energy density $V(r)$, and local electron energy density $H(r)$ at the BCP are used to summarize the nature of the bond or interaction. According to QTAIM theory, a bond is characterized by the existence of a critical point of

binding (BCP) [36]. The molecular graphs obtained for the studied inclusion complexes are given in Fig. 10. The different intermolecular interactions that exist in both complexes are shown in dotted lines.

The computed topological parameters corresponding to the intermolecular interactions of the two complexes such as electron densities (ρ), Laplacian of electron density ($\nabla^2(\rho)$), local kinetic energy density $G(r)$, local potential energy density $V(r)$, Hamiltonian kinetic energy $H(r)$, $-G(r)/V(r)$ ratio, electron localization function (ELF), localized orbital locator (LOL) and bond energies at the intermolecular bonding BCPs are listed in Table 4.

From Table 4 we observe that the obtained electron density and the Laplacian at the intermolecular BCPs are all positive for both complexes, showing the non-covalent nature of intermolecular bonding. Based on the Rozas *et al.* [37] criterion, the hydrogen bonds are classified as follows:

- Weak hydrogen bonds: $\nabla^2\rho(r) > 0$ and $H(r\text{BCP}) > 0$;
- Moderate hydrogen bonds: $\nabla^2\rho(r) > 0$ and $H(r\text{BCP}) < 0$;
- Strong or very strong hydrogen bonds: $\nabla^2\rho(r) < 0$ and $H(r) < 0$.

For all BCPs, $\nabla^2\rho(r) > 0$, $H(r) > 0$ and the interaction energies E_{HB} do not exceed 10 kcal/mol.

Based on the above topological and energetic results, one may conclude that the intermolecular interactions in the C1 and C2 complexes are weak and approve the electrostatic behavior of these interactions [38]. In addition, the ratio of $-G(r)/V(r)$ is > 1 , supporting the existence of weak intermolecular bonding between host and guest in the two complexes [39]. Additionally, a small value of ELF and LOL confirms the electrostatic nature of the interactions between host and guest molecules, which shows that electrons are not greatly localized at the BCPs.

The important advantage of the QTAIM application lies with the development of models correlating between the electron density $\rho(\text{BCP})$ and the interatomic distance. It has been found that the BCP is typically an excellent descriptor of the strength of the interactions; that is larger for shorter interatomic distances [40]. The plots of the electron density as a function of interatomic distances for C1 and C2 complexes are shown in Fig. 11. It can be seen that the dependence between the electron density and the hydrogen bond distances follows an exponential trend.

Table 4. Topological parameters obtained from QTAIM analysis for C1 and C2 complexes. The following topological parameters are given: the corresponding $d_{H...X}$ distances; the electron density at BCP $\rho(r)$, its Laplacian $\nabla^2(\rho)$, the kinetic electron energy density $G(r)$ and the potential electron energy density $V(r)$. All $\rho(r)$, $\nabla^2(\rho)$, $G(r)$ and $V(r)$ values in atomic units; E_{HB} in kcal/mol; bond length in Å.

	$d_{H...X}$	$\rho(r)$	$\nabla^2(\rho)$	$G(r)$	$V(r)$	$H(r)$	$-G/V$	LOL	ELF	E_{HB}
C1 complex										
N220-H234...O22	2.10	0.0189	0.0189	0.0218	-0.0206	0.0011	1.0583	0.1498	0.03010	6.46
C233-H244...O135	2.43	0.0089	0.0488	0.0095	-0.0068	0.0027	1.3971	0.1032	0.0130	2.13
C225-H235...O135	2.50	0.0082	0.0433	0.0082	-0.0056	0.0026	1.4643	0.1037	0.0132	1.76
C2 complex										
N220-H234...O121	2.15	0.0167	1.8	0.0189	-0.0171	0.0018	1.1053	0.1415	0.0264	5.37
C233-H244...O96	2.66	0.0052	2.9	0.0058	-0.0036	0.0022	1.6111	0.0726	0.0061	1.13
C228-H237...O121	2.50	0.0078	0.0455	0.0086	-0.0058	0.0028	1.4810	0.0937	0.0105	1.82



Fig. 10. Molecular topography analysis obtained from the AIM analysis of C1 and C2 complexes in aqueous phase at BP86-D3/6-31G (d,p) level of theory.

The corresponding relationships are given in Fig. 11. Excellent correlation is seen between $\rho_{(BCP)}$ and the hydrogen bond distances. Also, QTAIM characteristics are further described through hydrogen bond energies (E_{HB}) at the intermolecular BCPs estimated by using Espinosa equation [41] (see Table 4) and the kinetic electron energy density ($G(r)$). Fig. 12 displays E_{HB} as a function of the kinetic electron energy density ($G(r)$) showing a

linear dependence. corresponding linear regression equations for C1 and C2 complexes are as follows:

$$E_{HB} = 555.28 G(r) - 1.8111,$$

$$E_{HB} = 528.37 G(r) - 1.4315.$$

An excellent linear correlation ($R^2 = 0.9998$ and 0.9972 , respectively, for C1 and C2 complexes) is obtained between the hydrogen bond energies and the kinetic electron energy density ($G(r)$).

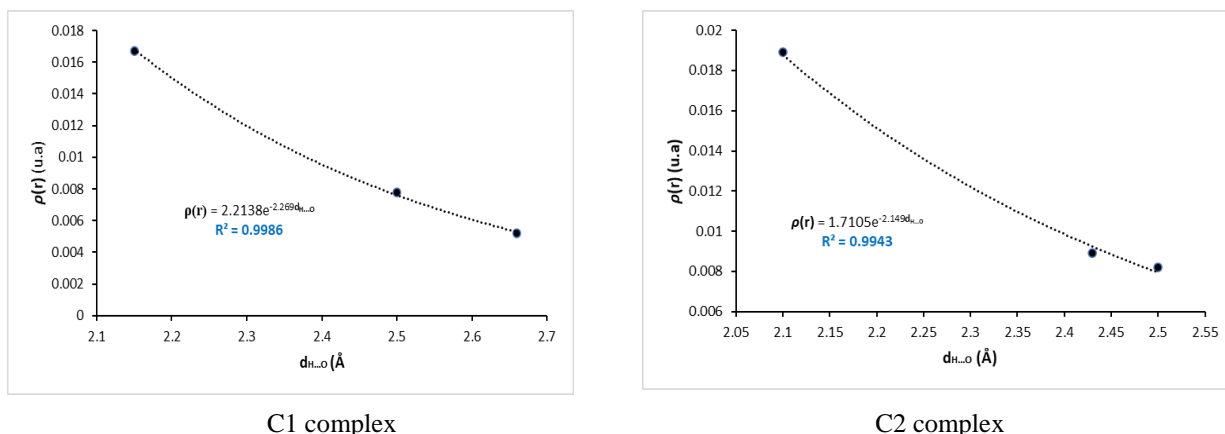


Fig. 11. Electron densities (in au) as a function of the hydrogen bond distances (in Å) for C1 and C2 complexes.

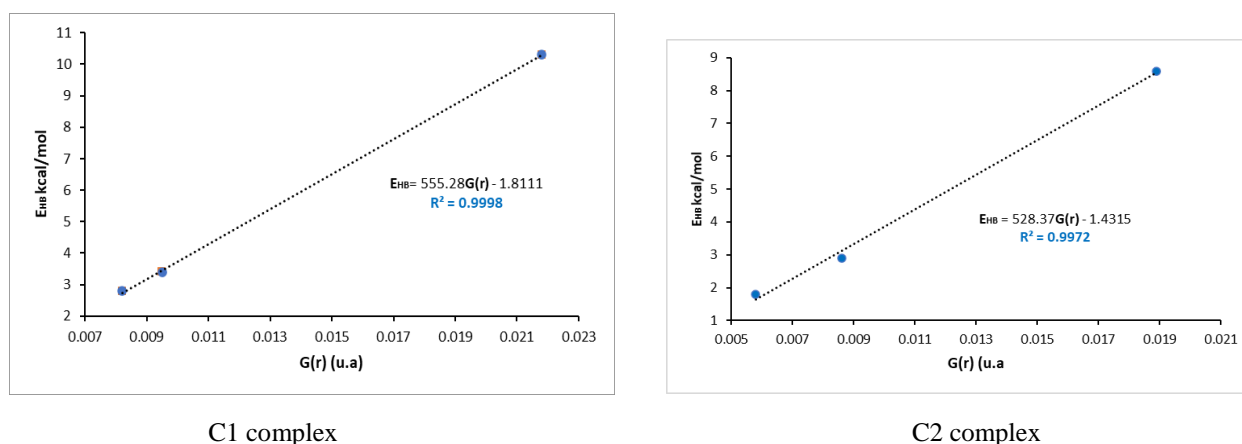


Fig. 12. E_{HB} (in kcal/mol) as a function of kinetic electron energy density ($G(r)$ in au) for C1 and C2 complexes.

Non-covalent interactions-reduced density gradient analysis

NCI-RDG analysis presents a graphical visualization of the region where non-covalent interactions occur in real-space, and is capable of distinguishing hydrogen bonds, van der Waals interactions and repulsive steric interactions through simple color codes [42]. NCI is expressed in terms of the electron density, its Laplacian, and the reduced gradient of density. According to NCI analysis, the interaction types are determined by examination of the sign of the second eigenvalue λ_2 . The strength and nature of interactions can be interpreted by the product sign λ_2 times ρ as given by RDG iso surfaces. (Sign λ_2) $\rho < 0$ for attractive interaction, (sign λ_2) $\rho > 0$ for a repulsive interaction, whereas the weak van der Waals types reveal (sign λ_2) $\rho \approx 0$ which are designed in the RDG isosurface with blue, red and green color, respectively [43]. Blue, green, and red color codes are used to describe stabilizing H-bonding, van der Waals, and destabilizing steric interaction, respectively [38]. The NCI plots for the two complexes are depicted in Fig. 13. The red areas observed indicate a steric

repulsion and are localized mostly in the middle of the benzene rings and near the oxygens of carbonyl groups of HP β -CD. The green areas observed between host and guest molecules indicate the existence of van der Waals and electrostatic interactions.

CONCLUSION

We applied a dispersion corrected density functional methodology to study non-covalent intermolecular interactions leading to the complex formation of 2MMPT with HP β -CD. The calculated binding and interaction energies are in favor of the C1 complex where the guest molecule is totally encapsulated in the HP β -CD cavity. Our theoretical ^1H NMR chemical shift results are in good agreement with the experimental data. The results of NBO analysis show that C1 and C2 were stabilized by weak and strong hydrogen bonds. Energy decomposition analysis indicated that the electrostatic interaction dominated among the attractive interactions in both complexes.

From the AIM results, one can conclude that the obtained electron density and the Laplacian at the

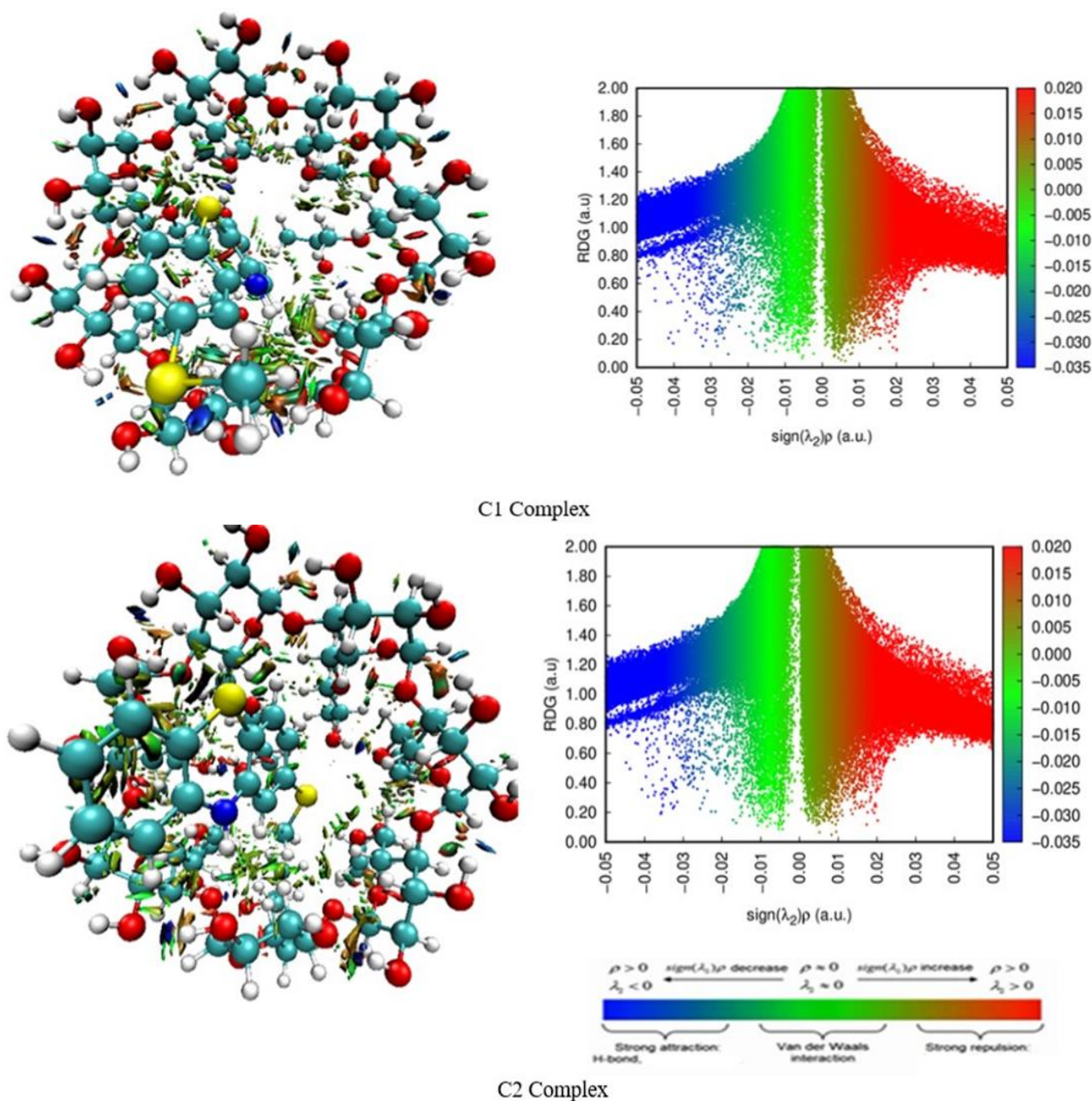


Fig. 13. Plots of RDG(s) versus the electron density multiplied by the sign of the second Hessian eigenvalue ($\text{sign}(\lambda_2)\rho$) and the corresponding H-bond interaction for both complexes

intermolecular BCPs were all positive for both complexes, showing the non-covalent nature of intermolecular bonding. Finally, the NCI analysis shows that the van der Waals interactions and hydrogen bonds are the driving forces in stabilizing the complexes.

Acknowledgement: The Algerian Ministry of Higher Education and Scientific Research supported the investigation.

Conflict of interest: The authors declare no conflict of interest.

Supplementary Data File

REFERENCES

1. P. Sua, Z. Chena, W. Wu, *J. Chem. Phys. Lett.*, **635**, 250 (2015).
2. R. F. W. Bader, *J. Chem. Rev.*, **91**, 893 (1991).
3. F. Fuster, S. J Grabowski, *J. Phys. Chem. A*, **115**, 10078 (2011).
4. C. R. Landis, F. Weinhold, *Discovering chemistry with natural bond orbitals*, John Wiley & sons, 2012.
5. T. R. Ragia, K. Sivakumar, *J. Mater. Tod. Proc.*, **14**, 395 (2019).
6. M. Krstic, S. P. Sovilj, S. Grguric-Sipka, I. Radosavljevic Evans, S. Borozan, J. F. Santibanez, J. Kocic, *Eur. J. Med. Chem.*, **45**, 3669 (2010)
7. A. Lutka, B. Golda, *Acta Pol. Pharm.*, **63**, 3 (2006).

8. Y. Fu, L. Liu, Q. X. Guo, *J. Phen. Macro. Chem.*, **43**, 223 (2002).
9. M. E. Davis, M. E. Brewster, *Nat. Rev. Drug. Discov.*, **31**, 1023 (2004).
10. L. Wang, J. Yan, L. Li, K. Xu, S. Li, P. Tang, H. Li, *J. Pharm. Biomed. Anal.*, **117**, 453 (2016).
11. T. R. Ragia, K. Sivakumar, *Mater. Tod. Process.*, **14**, 395(2019).
12. S. Grimme, J. Antony, S. Ehrlich, H. Krieg, *J. Chem. Phys.*, **132**, 154104 (2010).
13. S. Grimme, *J. Comput. Chem.*, **27**, 1787 (2006).
14. S. Grimme, *J. Wires. Comput. Mol. Sci.*, **1**, 211 (2011).
15. H. Bouchemela, F. Madi, L. Nouar, *J. Inclus. Pheno. Macro. Chem.*, **25**, 247 (2019).
16. S. Himri, I. Lafifi, A. Guendouzi, M. Cheriet, L. Nouar, F. Madi, *J. Mol. Liq.*, **280**, 218 (2019).
17. P. L. Verma, S. P. Gejji, *J. Mol. Liq.*, **293**, 111548 (2019).
18. M. J. Frisch, G. W. Trucks, B. Schlegel, G. E. Scuseria, M. A. Robb, J. R. Cheeseman et al., Gaussian 09, revision A.01, 2013.
19. T. Lu, Chen, F. Multiwfn, *J. Comput. Chem.*, **33**, 580 (2011).
20. W. Humphrey, A. Dalke, K. Schulten, *J. Mol. Graph.*, **14**, 33 (1996)
21. ADF2017, SCM, Theoretical Chemistry, Vrije Universiteit, Amsterdam, The Netherlands, <http://www.scm.com>.
22. K. Fukui, *J. World.Scientific*, **150-170** (1997) (1981-1990).
23. F. De Proft, J. M. Martin, P. Geerlings, *J. Chem. Phys. Lett.*, **256**, 400 (1996).
24. R. R. Contreras, P. Fuentealba, M. Galván, P. Pérez, *J. Chem. Phys. Lett.*, **304**, 405 (1999).
25. R. Arora, U. Issar, R. Kakkar, *J. Comput. Theor. Chem.*, **1138**, 5765 (2018).
26. D. N. Lande, S. A. Bhadane, S. P. Gejji, *J. Phys. Chem., A*, **121**, 1814 (2017).
27. M. Snehalatha, C. Ravikumar, I. H. Joe, N. Sekar, V. S. Jayakumar, *Spectrochim. Acta A*, **72**, 646 (2009).
28. C. James, A. A. Raj, R. Reghunathan, V. S. Jayakumar, I. H. Joe, *J. Spectrosc. J. Raman. Spectrom.*, **37**, 1381 (2006).
29. H. Ghalla, N. Issaouia, F. Bardak, A. Atac, *Computational Materials Science*, **149**, 291 (2018).
30. G. Uccello-Barretta, F. Balzano, G. Sicoli, C. Fríglola, I. Aldana, A. Monge, D. Paolino, S. Guccione, *Bioorg. Med. Chem.*, **12**, 447 (2004).
31. T. Ziegler, A. Rauk, *Theor. Chim. Acta* **46**, 1 (1977).
32. N. S. Venkataramanan, A. Suvitha, Y. Kawazoe, *J. Mol. Liq.*, **260**, 1829 (2018).
33. R. F. W. Bader, M. A. Austen, *J. Chem. Phys.*, **107**, 427 (1997).
34. R. F. W. Bader, *Atoms in molecules: A. Quantum theory*, Oxford Univ. Press, 1990, p. 12.
35. S. Gatfaoui, N. Issaoui, T. Roisnel, H. Marouani, *Journal of Molecular Structure*, **1191**, 183 (2019).
36. O. Nouredine, S. Gatfaoui, S. A. Brandan, A. Sagaama, H. Marouani, N. Issaoui, *Journal of Molecular Structure*, **1207**, 127762 (2020).
37. I. Rozas, I. Alkorta, J. Elguero, *J. Am. Chem. Soc.*, **122**, 11154 (2000).
38. M. Tahenti, S. Gatfaoui, N. Issaoui, T. Roisnel, H. Marouani, *Journal of Molecular Structure*, (2020), doi: <https://doi.org/10.1016/>.
39. N. S. Venkataramanan, A. Suvitha, Y. Kawazoe, *J. Mol. Graph. Model.*, **78**, 48 (2017).
40. S. J. Grabowski, W. Andrzej Sokalski, J. Leszczynskin, *Chem. Phys.*, **337**, 68 (2007).
41. E. Espinosa, E. Molins, C. Lecomte, *J. Chem. Phys. Lett.*, **285**, 170 (1998).
42. E. R. Johnson, S. Keinan, P. Mori-Sánchez, J. Contreras-García, A. J. Cohen, W. Yang, *J. Am. Chem. Soc.*, **132**, 6498 (2010).
43. G. Saleh, C. Gatti, L. Lo Presti, J. Contreras-Garcia, *J. Chem.*, **18**, 15523 (2012).

Heavy metal accumulation of water, sediment and some organisms in the Marmara Sea (Turkey)

S. M. Arat, B. Çamur-Elipek*, B. Öterler

Trakya University, Faculty of Science, Department of Biology, Edirne, Turkey

Received: October 16, 2020; Revised: February 02, 2021

Increasing human populations and activities depending on the industrial and agricultural improvements cause worldwide disappearance of usable water resources. The harmful effects from polluted waters reach the human body by the food chain. In particular, heavy metals, which are known as some of the most important pollutants to nature, can stay in the ecosystem for a long time, lead to harmful effects in food chain by accumulations, and have direct or indirect toxic effects on aquatic organisms. These metals can be deposited in the body of the organisms which are an important ring in food chain in aquatic environments. In this study, a total of five heavy metals (Cu, Fe, Zn, Cd, and Pb) in water, sediment, some macroinvertebrates and fish at the Sea of Marmara (Turkey), which is a bridge between Black Sea and Aegean Sea, were investigated. For this aim, water, sediment and organism samplings were done in 2009, the date before the planned construction of a channel in the Marmara Sea. Thus, it was aimed to contribute to the researches which have been performed in the Marmara Sea. According to the results, while the levels of Cd and Zn were determined to have high values in the water samples, the obtained concentration levels in sediment and accumulation rates in the organisms were compared in this study.

Keywords: Marmara Sea, heavy metal, accumulation, essential elements

INTRODUCTION

Environmental pollution has negative effects on the living things. Especially the pollution of water resources leads to uncontrolled problems in both aquatic environments and human economy-social life. Among the pollutants, heavy metals stay in the first order depending on their harmful and destroying effects. Although living things need some trace elements like Cu, Zn, Fe for their biological systems, some of them like Cd, Pb, As, and Hg cause very high toxic effects at very low concentrations. Furthermore, a lot of studies reported that these metals accumulate in the bodies of different organisms [1–4].

In recent years, a lot of studies have been performed on the accumulation of heavy metals in aquatic environments. The Marmara Sea is located on north-west of Turkey and it is surrounded by settlements, agricultural and industrial areas. Also, the Marmara Sea, a small inner sea, is a bridge between Black Sea and Aegean Sea *via* Bosphorus Strait and Dardanelles Strait, respectively. Thus, the Marmara Sea separates two important continents, Asia and Europe. Also, the Marmara Sea is an important immigration way between Black Sea and Mediterranean Sea for fish which are fed on benthic invertebrates. Fisheries are very important bazaar for the economy of the local people living around the Marmara Sea. But the Sea is under the influence of anthropogenic effects due to the discharges from

settlements, industrial and agricultural activities [5]. There is a project on opening a channel between the Marmara Sea and Black Sea [6]. Therefore, environmental studies on water and sediment quality of the Marmara Sea gain importance day by day. Thus, we can assess environmental effects of the channel on the Sea by the before/after researches.

There are a lot of studies on heavy metal accumulation in the water column or sediment of Marmara Sea [7–28]. Also, some heavy metal accumulations in mollusc species which are a very important group in benthic macroinvertebrates and the other groups, were studied in Marmara Sea [5, 7, 9, 10, 15, 17, 18, 20, 21, 23–25, 28–36]. Physicochemical analyses can inform on the current water quality at a particular time of an aquatic environment. Therefore, to monitor the changes in the chemicals like heavy metals in aquatic environments, samplings made by seasonal intervals at least will be useful. But benthic macroinvertebrates and fish are useful organisms to follow heavy metal pollution in an aquatic ecosystem by the accumulation talents of the heavy metals in their bodies. They can tell us past and present situation of the ecosystem.

In this study, it was intended to contribute to the researches which have been performed in the Marmara Sea. For this aim, the heavy metal concentrations in both water/ sediment and some tissues of different macroinvertebrates (starfish, crab and shrimp) / fish in the Sea of Marmara at the same time samplings were determined.

* To whom all correspondence should be sent:

E-mail: belginelipekcamur@trakya.edu.tr

Thus, different organism groups in the Sea were evaluated for their roles on heavy metal accumulations in this study.

EXPERIMENTAL

The samplings were made in December 2009 in Marmara Sea between the coordinates 41.01968N - 28.36683E and 40.96936N - 28.51225E. The organisms belonging to invertebrate (starfish *Astropecten* sp., shrimp *Parapenaeus* sp., and crab *Carcinus* sp.) and fish (*Gobius* sp., *Trigla* sp., *Hippocampus* sp., *Spicara* sp.) were sampled by a beam trawl (3 m mouth width, 60 cm length and 3 m bag length, 40 mm pore diameter). The sampling for the organisms was started at the bottom four km from the shore and the beam trawl was used during 15 km (Fig. 1).



Fig. 1. The location of Marmara Sea and the sampling locality

The obtained materials belonging to the macroinvertebrates and fish were put into sterile plastic bags and transported to the laboratory for their dissection. Also, the water samples were obtained from 40 m depth by a Nansen water sampler (1.5 L) and the sediment materials were taken from 50 m depth by an Ekman grab (15 × 15 cm). The water and sediment samples were put into polypropylene bottles that were cleaned by 1:1 HCl and 1:1 HNO₃, separately and transported to the laboratory to perform the heavy metal analyses.

In the laboratory, a total of 10 mL of water samples was put into a solution of HNO₃/HCl (5:2) with 8 mL of pure water and was filtered before measuring the concentrations of heavy metals. The sediment samples were homogenized and about 1 g of sediment samples was taken and dried in a drying oven at 85°C for 48 h before putting into a solution of HNO₃/HCl (5:2) with 3 mL of pure water and the

residue was filtered. The sampled organisms were measured by a calliper and scales. The dissection was made in the laboratory and some tissues of them (muscle tissue, bowel, liver, and gills) were obtained and about 1 g parts of the organs were put into a solution of HNO₃/HCl (5:2) with 3 mL of pure water. All prepared samples were drained by filter paper and were preserved at a temperature of -20°C until measuring the heavy metal contents.

The concentrations of Cu, Fe, Zn, Cd, and Pb were determined on an Analyst 800 Model Perkin Elmer AAS flame atomic absorption spectrometer (FAAS) with deuterium lamp and air acetylene burner. All values were expressed as the mean of three replicate analyses for each sample.

RESULTS AND DISCUSSION

In this study, a total of five heavy metal (Cd, Fe, Zn, Cu, and Pb) contents were determined in water, sediment and some tissues of organisms living in the Sea of Marmara (Table 1).

Table 1. Length and weight sizes of sampled organisms

Material		Length (cm)	Weight (g)
<i>Astropecten</i> sp.	INVERTEBRATES	4.5	13.20
<i>Carcinus</i> sp.		2.0	3.729
<i>Parapenaeus</i> sp.		13.0	12.0
<i>Gobius</i> sp.	FISH	11.5	15.273
<i>Trigla</i> sp.		18.0	59.071
<i>Hippocampus</i> sp.		10.0	4.84
<i>Spicara</i> sp.		12.0	21.0

Water samples

The literature suggests to measure the concentration levels of Cd, Pb and Cu in sea water for determining the pollution level [28]. In this study, the concentrations of Pb and Cu were determined as UAL (under analysable limit) in the water samples (Table 2 and Fig. 2).

But the levels of Cd and Zn were found at high rations in the sea water samples according to the limits in the WPCR of Turkey (Water Pollution Control Regulation) and the limits in the literature [28, 37] (Fig. 2). It is reported that Cd is more likely related to anthropogenic effluents and Zn is widely detected in industrial and mining wastewater [38]. Also, they can enter the sea from the settlements.

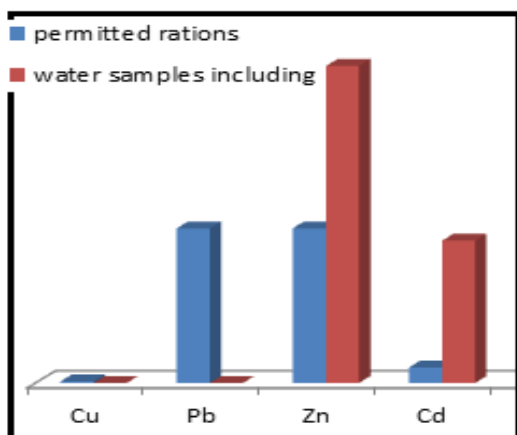


Fig. 2. Comparison of the heavy metal levels in sea water as permitted and measured ratios.

Sediment samples

It is reported that many heavy metal concentrations in sediment are higher than the those in the surrounding water [18]. The heavy metals in the sediments of aquatic environments which they tend to transport to the water column are the results of urban discharge and industrial wastes. Therefore, the analysis of heavy metals in the sediment helps in the interpretation of water quality [39]. In the previous study performed by Balkis *et al.* [18] in the Marmara Sea, it was reported that Cd is rather high in the sediments of Bosphorus and Marmara Sea. Also, Otansev *et al.* [24] reported a widespread heavy metal enrichment in sediments of the Marmara Sea.

Table 2. Measured levels of some heavy metals in water, sediment and some organisms in the Sea of Marmara (ppm)

Sample	Cd	Cu	Zn	Pb	Fe
Water	0.092	UAL	0.205	UAL	3.138
Sediment	0.176	2.043	4.179	2.373	81.770
<i>Astropecten</i> sp. (muscle)	0.227	0.808	0.643	0.170	5.147
<i>Carcinus</i> sp. (muscle)	0.122	1.648	1.092	UAL	3.362
<i>Parapenaeus</i> sp. (gill)	0.134	4.626	1.455	UAL	13.440
<i>Parapenaeus</i> sp. (bowel)	0.126	0.185	2.255	UAL	1.710
<i>Parapenaeus</i> sp. (muscle)	0.128	0.809	1.122	UAL	1.549
<i>Gobius</i> sp. (gill)	0.142	0.294	2.242	UAL	28.830
<i>Trigla</i> sp. (liver)	0.132	UAL	1.350	UAL	11.28
<i>Trigla</i> sp. (gill)	0.141	0.121	1.977	UAL	10.63
<i>Hippocampus</i> sp. (gill)	0.152	UAL	2.782	UAL	5.479
<i>Spicara</i> sp. (gill)	0.145	UAL	1.464	UAL	9.735

UAL: Under Analysable Limit

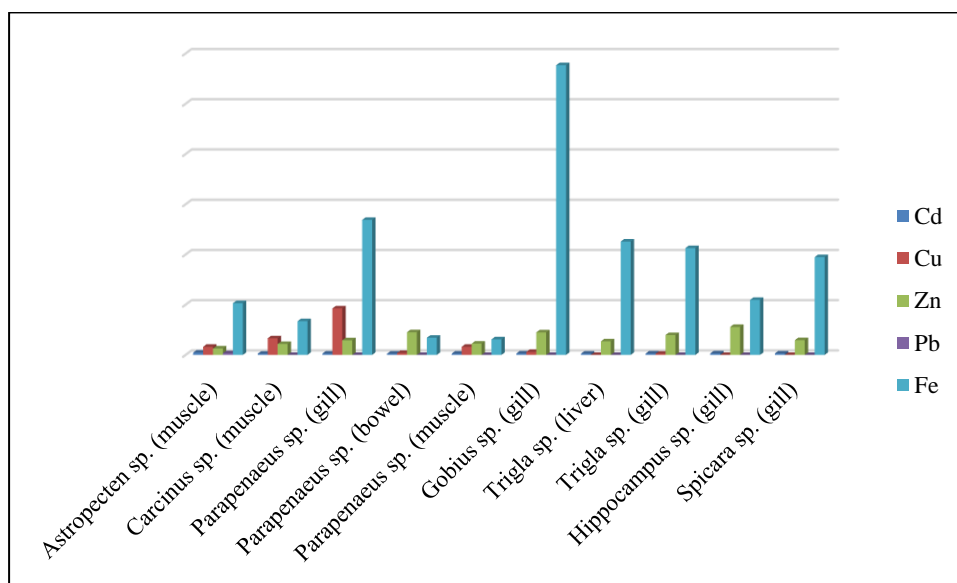


Fig. 3. Comparison of the heavy metal levels in the organisms at measured ratios.

Turkish Thrace region has highly intensive agricultural and industrial activities which lead to continuous pollution of water resources. In the previous study carried out by Balkis and Çağatay [16], the heavy metal distributions and sources were investigated in the sediments of Marmara Sea. The results show that the erosion products by two rivers from the south are the main sources to the relatively high metal concentrations in the studied area [16]. In our study, the concentrations of the heavy metals were found at 0.176 mg/kg for Cd, 2.043 mg/kg for Cu, 4.179 mg/kg for Zn, 2.373 mg/kg for Pb and 81.770 mg/kg for Fe. These ratios were found as very low levels compared with the literature [40]. But the measured heavy metal concentrations in the sediment samples were found higher than in the water samples (Table 2).

Organism samples

The heavy metal contents of the tissues in some marine species were also studied in this study. Although, Cd and Zn concentration levels were found similar to those in the tissues of the macroinvertebrate samples, Cu and Fe concentrations in the gills of shrimps (*Parapenaeus* sp.) were found higher than in the muscles and bowels. The Pb concentrations in the macroinvertebrate samples were found at UAL except starfish muscle (Table 2). When the heavy metal findings were evaluated according to their accumulation in the gills of the fish samples, the levels of Cd, Zn, Cu were found at similar ratios and the Pb concentrations were found at UAL (Table 2). The concentrations of Fe were found at high levels in demersal goby fish (*Gobius* sp.) (Fig. 3).

In a study performed on heavy metal concentrations in the sea water, sediment and starfish of Marmara Sea, it was reported that industrial activities lead to heavy metal accumulation [32]. In another study performed in shrimps (*Parapenaeus longirostris*) living in the Sea of Marmara, some heavy metal concentrations were reported at high ratios [22].

The studies which were performed on heavy metal accumulations in the organisms show that the different accumulation ratios can be observed in different tissues depending on the species and age. The gills are an important way to enter the heavy metal inside the organisms. In this study, the concentrations of Cu and Fe in shrimp gills were found higher than in the other tissues. Also, the measured heavy metal concentrations in sediment were found at a higher level than in water samples. It was observed that the concentration of Fe was at a

high level in goby fish which is living and feeding depending on sedimental material.

Heavy metals are among the important environmental pollutants and they can enter the aquatic surroundings by different ways. Their accumulations have increased due to the settlements, industrial and agricultural wastes. Although other pollutants can be removed from the natural environments by biological degradation, the heavy metals can accumulate [41]. The studies reported that the toxicity and accumulation of heavy metals in the aquatic environments lead to serious problems for ecosystems. These ecological problems can affect human health directly or indirectly because heavy metals can enter the biological structures by the food chain. It was reported that the heavy metal Cd had led to Itai-itai disaster in Japan by feeding on contaminated rice. This heavy metal affects the kidneys in humans and leads to chronic poisoning. The other heavy metals Pb and Zn can be transmitted by superficial water flood to sea, and they can accumulate in the tissues of aquatic organisms. Although Zn is needed for the physiology of living things, it can cause toxic effects at high concentrations. Pb is toxic for aquatic organisms [28].

As a result, to prevent the accumulation of the heavy metals in human body, their transporting to the aquatic environments must be prevented. Also, it is suggested that similar studies should be repeated periodically in the Marmara Sea before opening a channel between Marmara Sea and Black Sea. Thus, controlled monitoring can be provided for sustainable usage and rational management of the Marmara Sea.

REFERENCES

1. G. Ramelov, S. Tugrul, M. A. Özkan, G. Tuncel, C. Saydam, T. I. Balkas, *Int. J. Envir. Anal. Chem.*, **5**, 125 (1978).
2. N. C. Fung, J. C. W. Lam, G. J. Zheng, D. W. Connell, I. Monirith, S. Tanabe, B. J. Richardson, P. K. Lam, *Envir. Pollution*, **127** (2), 203 (2004).
3. C. Skinner, N. J. Turoczy, P. L. Jones, D. Barnett, R. Hodges, *Food Chem.*, **85**, 351 (2004).
4. C. K. Yapp, A. Ismail, H. Omar, S. G. Tan, *Food Chem.*, **84**, 569 (2004).
5. S. Topcuoğlu, Ç. Kırbaçoğlu, Y. Z. Yılmaz, *Envir. Mon. Assess.*, **96**, 183 (2004).
6. M. D. Kantarcı, Istanbul Barosu Yayınları, 2000, p. 60 (in Turkish).
7. S. Topcuoğlu, N. Erentörk, N. Saygı, D. Kut, N. Esen, A. Başsarı, E. Seddigh, *Toxic and Envir. Chem.*, **29**, 95 (1990).
8. M. Ergin, C. Saydam, Ö. Baştör, E. Erdem, R. Yörök, *Chemical Geology*, **91**, 269 (1991).

9. K. C. Göven, N. Saygı, B. Öztürk, *Botanica Marina*, **36**, 175 (1993).
10. N. Saygı, S. Topcuoğlu, N. Ö. Taşcı, *J. Faculty of Science, Ege University, Series B*, **16(1)**, 49 (1994).
11. M. N. Bodur, M. Ergin, *Chemical Geology*, **115**, 73 (1994).
12. N. Esen, S. Topcuoğlu, E. Eğilli, D. Kut, *The Journal of Radioanalytical and Nuclear Chemistry*, **240**, 673 (1999).
13. O. Algan, N. Çağatay, H. Z. Sarıkaya, N. Balkıs, E. Sarı, *Turkish JEEs*, **23**, 39 (1999).
14. O. Algan, N. Balkıs, N. Çağatay, E. Sarı, Turkey. *Environmental Geology*, **46**, 932 (2004).
15. D. Kut, S. Topcuoğlu, N. Esen, R. Küçükcezzar, K. C. Güven, *Water, Air, Soil Pollution*, **118**, 27 (2000).
16. N. Balkıs, M. N. Çağatay, *Environment International*, **27**, 1 (2001).
17. G. Altuğ, N. Güler, *TRJFAS*, **2**, 141 (2002).
18. S. Topcuoğlu, Ç. Kubaşlıoğlu, Y. Z. Yılmaz, *Environmental Monitoring and Assessment*, **96**, 183 (2004).
19. N. Balkıs, S. Topcuoğlu, K. C. Güven, B. Öztürk, B. Topaloğlu, Ç. Kırbasoğlu, A. Aksu, *Black Sea/Mediterranean Environment*, **13**, 147 (2007).
20. İ. Marangoz, Master Thesis, Namık Kemal University, 2009, p. 54 (in Turkish).
21. S. Mol, D. Uçok-Alakavuk, *Biological Trace Element Research*, **141(1-3)**, 184 (2011).
22. A. H. Dokmeci, T. Yildiz, A. Ongen, N. Sivri, *Envir. Monit. Assess.*, **186**, 2449 (2014).
23. M. Topkaya, Master Thesis, Marmara University, 2015, p. 138 (in Turkish).
24. P. Otansev, H. Taşkın, A. Başsarı, A. Varinlioğlu, *Chemosphere*, **154**, 266 (2016).
25. Z. Ü. Yümün, *Geophysical Research Abstracts*, **19**, 17211 (2017).
26. A. H. Dokmeci, *15th International Conference on Environmental Science and Technology, Greece*, 31 August to 2 September 2017, p. 144.
27. I. I. Ozyigit, O. L. Uyanık, N. R. Sahin, I. E. Yalcin, G. Demir, *PJES*, **26 (2)**, 773 (2017).
28. ÇŞB, TUBITAK MAM, Final report, 2017, p. 78 (in Turkish).
29. N. Demir, G. Akkuş, *Turk. J. of Agricult. and Nat. Sci.*, **5 (4)**, 659 (2018).
30. E. Bozkurt-Kopuz, G. Kara, B. Dinçer, Y. Gurtug, *J. Indian Chem. Soc.*, **96**, 1189 (2019).
31. S. Türk-Çulha, F. Koçbaş, A. Gündoğdu, M. Çulha, *40th CIESM Congress, Marsilya*, October 2013, vol. 40.
32. B. Uçar, Master Thesis, Marmara University, 2019, p. 136. (in Turkish)
33. N. Uzunören, PhD Thesis, İstanbul University, 1987, p. 112 (in Turkish).
34. S. Atayeter, Master Thesis, Ankara University, 1991, p. 54 (in Turkish).
35. F. Şentürk, Master Thesis, İstanbul University, 1993, p. 72 (in Turkish).
36. S. Türk- Çulha, M. Y. Çelik, *International Eurasian Conference on Biological and Chemical Sciences, Turkey*, 26 - 27 April 2018, p. 199.
37. WPCR (Water Pollution Control Regulations). Official Gazette on 31 December 2004, No. 25687, 2004 (in Turkish).
38. A. Zhang, L. Wang, S. Zhao, X. Yang, Q. Zhao, X. Zhang, X. Yuan, *Regional Stud. in Marine Sci.*, **11**, 32 (2017).
39. S. Yemenicioğlu, I. Salihoğlu, *Transactions on Ecology and the Environment*, **14**, 1743 (1997).
40. A. Türkmen, *Karadeniz Fen Bilimleri Dergisi*, **2 (1)**, 1 (2011).
41. V. Wepener, J. H. J. Van Vuren, H. H. Dupprez, *Water SA.*, **27(1)**, 99 (2001).

Surface treatment of electro galvanized steel in modified zinc phosphating solutions

D. I. Ivanova

University of Chemical Technology and Metallurgy, 8 "Kliment Ohridski" Blvd., 1756 Sofia, Bulgaria

Received: October 25, 2020; Revised: March 22, 2021

The effects of calcium, nickel and manganese modified zinc-phosphating baths on phosphating of electro galvanizing low-carbon steel surfaces were studied. The phosphating concentrates were characterized by their density; pH; conductivity; total and free acidity. Gravimetric, chemical, electrochemical and physical methods were used to determine the thickness, phase and chemical composition, structure, corrosion resistance and protective ability of the phosphate coatings. The results indicate that the coatings obtained with the modified solutions are thinner than the ones formed in the initial solution at the same experimental conditions: concentrations (5 %-15 % vol.) and temperatures (20°C-60°C). The phosphate coatings obtained contain mainly hopeite and the partial replacement of Zn by Ca, Ni and Mn did not affect new crystal phase formation. The corrosion resistance of the crystalline phosphate coatings was determined in model aqueous solutions of 0.01 M NaCl, 0.6 M NaCl and 0.6 M NH₄NO₃. The protective properties of the phosphate coatings were determined electrochemically by measuring the maximum anodic potential during galvanostatic polarization in a model electrolyte, as well as through neutral salt spray tests.

Keywords: zinc coatings, zinc phosphating, surface treatment.

INTRODUCTION

The production of electro galvanized steels with deposited organic (paint, polymer) coatings has been significantly increased in last years. The most important indicator of the organic coating quality is its adhesion, the main factors of which are the roughness and surface tension of the zinc surface. Therefore, the best preliminary zinc surface treatment when organic coatings are applied is the phosphating procedure that increases its roughness and surface tension about 3-4 times. The adequate phosphating and subsequent surface painting can lead to optimal corrosion protection [1].

The formation of a phosphate coating is a complex process involving subsequent dissolution of the substrate, nucleation and growth of phosphate crystals [1, 2]. The intensification of the phosphating process and the improvement of phosphate coatings deposited can be achieved by adding activators and other substances to the working solutions [3]. Commonly, addition of various metal cations such as Ca²⁺, Ni²⁺, Mn²⁺, etc. [4-7], as well as post-sealing with silicate solution [8], results in improved coating characteristics. In this context, applying the calcium-modified zinc phosphating, the presence of Ca²⁺ in the solution significantly changes the crystal structure, grain size and the corrosion resistance of the coatings [9, 10]. Otherwise, when manganese and nickel containing zinc phosphating solutions are used, the coating surface roughening decreases that results in raised corrosion resistance [11].

The phosphating of zinc surface increases its resistance several times with respect to the case of Cr⁶⁺- passivation [2]. Moreover, the phosphate coatings are more stable at high temperature in comparison with the chromate films.

The present work reports data on the phosphating process of zinc surfaces with calcium, nickel and manganese modified zinc phosphating baths. The densities, pH, conductivities, as well as the total and free acidity of the phosphating concentrates were determined. The effects of bath concentration and temperature on the coating thicknesses, structures, phase and chemical composition were studied. The corrosion resistance and the protective properties of the phosphate coatings obtained were investigated, too.

EXPERIMENTAL

Materials and samples

Disc-shaped specimens (26 mm in diameter, thickness of 1 mm and working surface area S=0.1 dm²) of low-carbon steel (0.17 % C) were coated by zinc in a conventional acid ammonium-chloride electrolyte Entobrite CLZ 953 and used for the gravimetric experiments. The electrochemical experiments were carried out with plate-shaped specimens with dimensions in accordance with ISO 17475:2005 and a fixed working surface area of 0.01 dm². In addition, square plate samples (10×10 mm) were used as specimens in all physical methods applied, while the tests of the corrosion resistance and the protective properties of the phosphate coatings on zinc surfaces were carried

* To whom all correspondence should be sent:
E-mail: dimkaivanova@uctm.edu

out with square plate coupons (50×50 mm). The thickness of the zinc coatings for all types of investigations was about 12 µm.

The preliminary treatment of the specimens prior to the phosphating included subsequent alkaline degreasing, rinsing, acid pickling, rinsing and drying [11, 14].

Solutions and working conditions

Aqueous solutions of Zn,CaPh, Zn,NiPh, and Zn,MnPh were used as working media for the crystalline phosphating depositions. They were prepared on the base of an initial ZnPh zinc phosphating concentrate through replacement of 10% of the present zinc phosphate by nickel, calcium and manganese phosphates, respectively. Thus, they were in fact concentrated solutions of the components containing acid phosphates of the corresponding metals, free phosphoric acid, inorganic salts, stabilizers, etc. The ratio $P_2O_5:NO_3^- = 1:3$ was used.

The working conditions were as follows:

- Concentration values of 5.0 vol. %, 10.0 vol. % and 15.0 vol. %;
- Temperature values of 20.0°C, 40.0°C and 60.0°C;
- Process duration of 5.0 min, 7.5 min, 10.0 min, 12.5 min and 15.0 min.

The model media used for the electrochemical characterization of the coatings were chosen in correspondence with the literature data. They were as follows: 0.01 M NaCl, 0.6 M NaCl, and 0.6 M NH_4NO_3 [13].

The protective properties of the phosphate coatings were determined in a model ($NaCl + Na_2SO_4$; 6 g l^{-1} + 94 g l^{-1}) electrolyte [15].

Methods of investigation

Gravimetric method. The method was used to investigate the influence of various factors on the kinetics of phosphate coatings formation. Its application requires careful determination of the samples mass (in grams) after phosphatizing (m_1), as well as their mass after the coating removal (m_2). Using the following equation allows determination of the phosphate coating thickness, M [11]:

$$M = \frac{(m_1 - m_2)}{S}, g m^{-2},$$

where, S - sample surface area, m².

Open circuit potential determination. Metals or metal-coated substrates immersed in liquid electrolyte media resulted in establishment of non-equilibrium, i.e. the so-called corrosion potentials. The corrosion potentials are not indicative with respect to the resistance attained but their values and time variations provide enough information about

the character of the corrosion process, the behavior of both the metal and metal coating in different media under various conditions. The experiments were performed with an automatic device EG&G Princeton Applied Research, potentiostat/galvanostat, model 263A.

Potentiodynamic polarization method. The polarization curves recorded potentiostatically or potentiodynamically allow determination of various corrosion characteristics such as E_{corr} , i_{corr} , etc. The cell employed was a three-electrode one with compartments for the test electrode (0.11), the counter Pt-electrode (0.2 cm²) and the saturated calomel reference electrode (SCE). The experiments were carried out with EG&G Princeton Applied Research potentiostat/galvanostat, model 263A, provided with the specialized software package PowerCORR[®].

Scanning electron microscopy (SEM). This is the most widely used method of surface topography investigation. The analyses were put through a scanning electron microscope JEOL JSM 6390 equipped with a scanning system of ultra-high resolution (ASID-3D).

Energy-dispersive spectroscopy (EDS). This local X-ray spectral investigation method providing qualitative and quantitative analysis of the composition of surface microvolumes of the order of several µm³ was carried out by the scanning electron microscope JEOL JSM 6390 equipped for EDS.

X-ray photoelectronic spectroscopy (XPS). The method allows direct investigation of the electrons situated in the valence, as well as in the inner electron layers. The measurements were carried out with the Escalab II system equipped with an X-ray source of AlK_{α} (1486.6 eV) and a maximum instrumental resolution of 1 eV.

X-ray phase analysis (XRD). The method allows quantitative determination of the phases in the system (of 1 % – 3 % content), their chemical composition, the structure of the phase unit cell, etc. Philips APD-15 (1030) X-ray diffractometer equipped with Bragg-Brentano focusing system was used.

Atomic force microscopy (AFM). The method allows determination of the surface topography through a direct contact with a probe fixed at the end of the microscopic beam. The measurements were carried out with the Nano Scope V system (Veeco Instruments Inc.). The data obtained were treated by WSxM5.0 Develop 3.0 Software.

Electrochemical determination of the protective properties of the specimens. The method uses measurements of the maximum anodic potential, E_{Amax} under galvanostatic polarization in a model

electrolyte solution ($\text{NaCl} + \text{Na}_2\text{SO}_4$; $6 \text{ g l}^{-1} + 94 \text{ g l}^{-1}$) with the assumption that higher values of E_{Amax} correspond to better corrosion resistances [16]. Corrosion tester characterized the anodic behavior of the coatings. The time variations of the anodic potentials were recorded by EG&G Princeton Applied Research potentiostat/galvanostat, model 263A and treated by the corrosion software Softcorr II.

Neutral salt spray (NSS) corrosion investigations. The NSS corrosion tests were carried out in accordance with ISO 9227:2012 recommendations. The test carried out in an NSS chamber included 4 cycles lasting 24 hours each, i.e. totally 96 hours. The corrosion resistance (the coating corrosion in this case) and the corrosion protection ability (i.e. the steel substrate corrosion) were evaluated after each cycle. Such corrosion studies could be extended up to 8 cycles in order to evaluate the corrosion behavior of each series of coating tests. NSS chamber commercially provided by VSN 1000 Heraeus-Vötsch GmbH was used.

RESULTS AND DISCUSSION

The data summarized in Table 1 show the most important indicators characterizing the phosphating concentrates used in the experiments: density, ρ ; pH; conductivity, σ ; total, K_{ta} , and free, K_{fa} , acidity. The data indicate that the densities of all concentrates are almost identical.

Table 1. Phosphating concentrate characteristics

Solution	ρ , g cm^{-3}	pH	σ , mS cm^{-1}	K_{TA}	K_{FA}
ZnPh	1.330	0.32	110.7	304	35
Zn,CaPh	1.320	0.31	110.5	304	40
Zn,NiPh	1.330	0.41	105.4	302	33
Zn,MnPh	1.325	0.21	113.2	304	44

In the case of Zn,NiPh, the phosphating concentrate containing Ni has the lowest conductivity and the highest pH, while Zn,MnPh modified by Mn has the lowest pH. The solution K_{TA} values differ insignificantly, while K_{FA} is higher in cases of Zn,CaPh and Zn,MnPh. The greater difference in some of the characteristics of the phosphating concentrates studied can be attributed only to the nature and properties of the various cations used for modification of the initial zinc-containing concentrate ZnPh.

Gravimetric investigations

The method was used to elucidate the effect of the operating conditions (concentration and temperature of the phosphating solutions, as well as duration of the process) on the coating thickness M . The values of the concentration and temperature are selected experimentally. Figures 1, 2, 3 and 4 indicate typical thickness/mass, M vs. time, τ relationships of the coatings obtained in solutions of different concentrations at different temperature values.

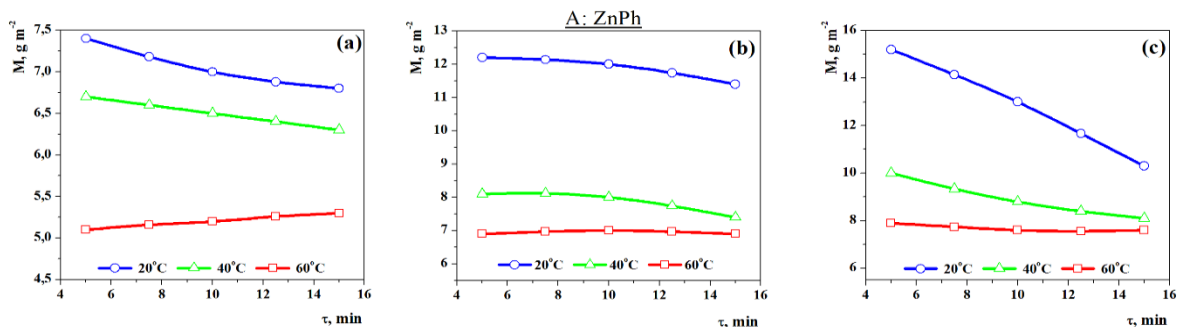


Figure 1. Effect of the phosphating duration, τ , on the thickness/mass of the phosphate coating obtained, M : a – 5 %; b – 10 %; c – 15 % (A: ZnPh)

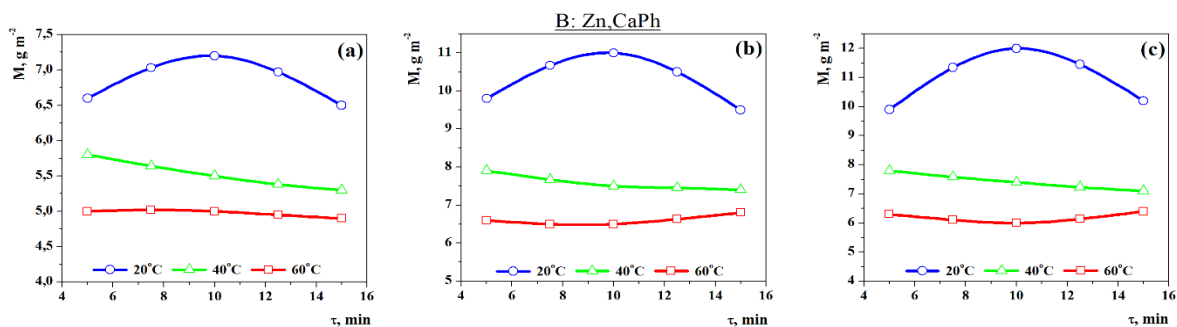


Figure 2. Effect of the phosphating duration, τ , on the thickness/mass of the phosphate coating obtained, M : a – 5 %; b – 10 %; c – 15 % (B: Zn,CaPh)

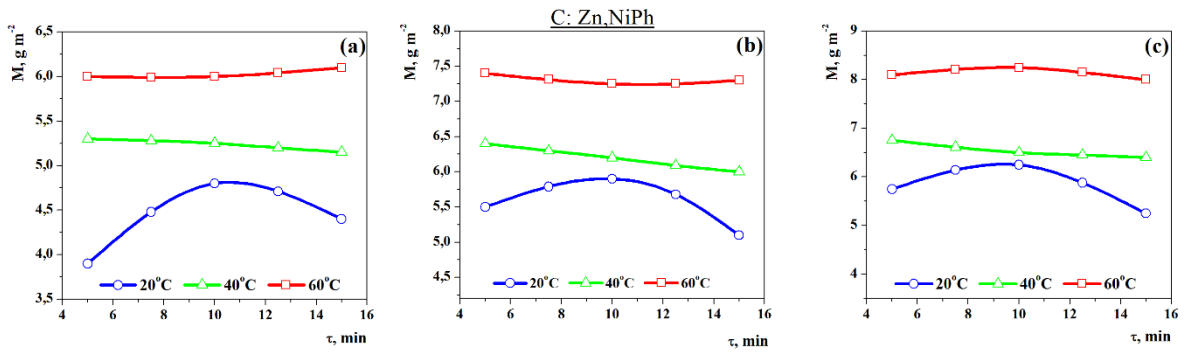


Figure 3. Effect of the phosphating duration, τ , on the thickness/mass of the phosphate coating obtained, M : a – 5 %; b – 10 %; c – 15 % (C: Zn,NiPh)

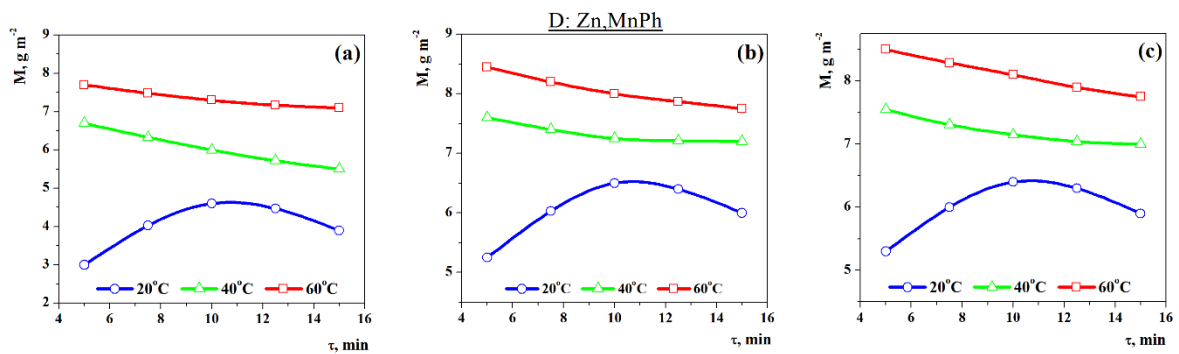


Figure 4. Effect of the phosphating duration, τ , on the thickness/mass of the phosphate coating obtained, M : a – 5 %; b – 10 %; c – 15 % (D: Zn,MnPh)

The shapes of the curves in Figures 1 and 2 indicate that the coatings of highest thickness correspond to the shortest time runs of 5 min in ZnPh and Zn,CaPh irrespective of the concentration and the temperature of the working solutions. The thickness of the coating decreases or stays relatively unchanged at longer duration. These facts suggest that the phosphate coatings on the zinc surfaces are growing with the highest rate in the initial stage (up to 5 min). Then their reorganization proceeds – exchange with the solution’s components resulting in increase of their density, homogenization and mass decrease. An exception was observed in the thickness (M) variation when the specimens were treated at 20°C in Zn,CaPh solutions irrespective of the variations in the concentration (Figure 2). In this case, the top values of M were reached in the first 10 minutes of the phosphating process. This is most probably due to the effect of the calcium cations on the processes of crystal nuclei formation and the consequent growth of the crystals in the course of phosphatizing, owing to the variations in their rates mainly at low temperatures [17].

Figures 1 and 2 also show that the thickness of the coatings increases with the concentration rise in both solutions studied. It is highest at 20°C and

lowest at 60°C. The presence of calcium cations in the phosphating bath Zn,CaPh results in a decrease of the coatings thickness under all experimental conditions considered when compared to the changes observed in the initial zinc phosphating solution. The visual observations ($\times 10$) of the phosphated zinc surfaces indicate that the homogeneity and the density of the coatings obtained in both solutions increase with increase in the temperature.

The modification of ZnPh by nickel and manganese cations, Zn,NiPh and Zn,MnPh, brings about essential variations of the thickness, M vs. time, τ dependences (see Figures 3 and 4). In this case, the crystalline phosphate coatings of the highest thickness were obtained in the first 5 min of the process, in both solutions at the highest temperature value studied, i.e. at 60°C. The lowest thicknesses were obtained at the temperature of 20°C. The thicknesses of the coatings obtained at 40°C and 60°C decreased gradually with the increase in the phosphatizing duration and the effect could be most probably attributed to the coating reorganization taking place. At the lowest temperature of the solution (20°C), the thickest coatings were obtained up to the 10th min of the phosphatizing process.

Electrode potential measurements

The electrode potentials of the phosphated steel specimens were measured in the course of the crystalline coatings formation in the corresponding phosphating baths and at their testing in model aqueous media. The change in the potential in the course of phosphating is related to the nature and the homogeneity of the coating obtained, whereas the stabilization of the electrode potentials indicates in fact the end of the phosphating procedure. The time-variation of the electrode potentials in the course of the phosphate coatings growth is shown in Figure 5.

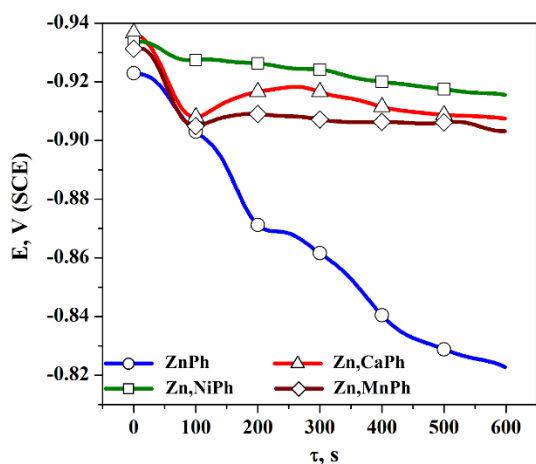


Figure 5. Potential vs. time relationships recorded in the course of crystalline phosphate coatings formation: 10 vol.%, 60°C, 10 min.

The potential, E vs. time, τ relationships were recorded under identical experimental conditions, that is: working solution concentration of 10 vol.%, temperature of 60°C and duration of 10 min. The shape of the curves indicates that within the initial short period (20 – 25 s) constant potentials were observed and followed by their shift in a positive direction. This is most clearly demonstrated by the

results obtained with the ZnPh solutions containing only zinc phosphate, while in the modified phosphating solutions it is more slightly expressive and is in the following order: $E_{Zn,NiPh} < E_{Zn,CaPh} < E_{Zn,MnPh}$. The course of the curves allows suggesting that the nuclei formation, the consequent growth and density of the coatings are stimulated in the modified phosphating solutions.

The corrosion resistance, i.e. the respective protective ability of the crystalline phosphate coatings was determined in model aqueous solutions of 0.01 M NaCl, 0.6 M NaCl and 0.6 M NH_4NO_3 . The experiment itself refers to dipping of the phosphated specimens in the solutions studied. The coatings are determined to be corrosion resistant if no changes on the specimens' surface or model solution coloring are observed within one hour after the dipping. The tests carried out indicate that there are no changes in all phosphate coatings and they are determined as highly resistant against corrosion in these media.

The corrosion potentials of the phosphated specimens in the model media were determined and compared to those corresponding to cold galvanized steel surfaces (without phosphate coatings). The potentials of the crystalline phosphate coatings in both NaCl media are shown in Figure 6 (a) and (b). In this case, the potentials shift to more negative values and after some period remain almost constant. The potentials of the non-phosphated zinc specimens attain intermediate values but they are more negative than the potentials of the specimens treated in the nickel-modified and the initial (non-modified) zinc phosphating solutions. The potentials of the specimens treated in calcium and manganese modified solutions attain more positive values. The results allow classifying the phosphate coatings with respect to their protective abilities although the differences in the potential values are relatively small.

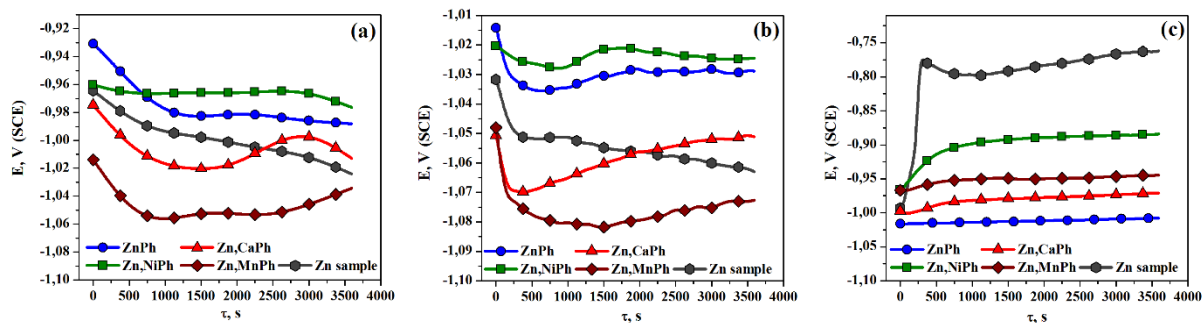


Figure 6. Potential vs. time (E- τ) dependence of phosphate coatings recorded at 20°C in: a – 0.01 M NaCl; b – 0.6 M NaCl; c – 0.6 M NH_4NO_3

The electrode potentials variations obtained in 0.6 M NH_4NO_3 solution are shown in Figure 6 (c).

The initial slight shift in a positive direction is followed by a certain period where the values of the

potentials remain almost constant. The coatings formed in ZnPh solutions exhibited the most negative potentials, followed by those formed in ZnCaPh, Zn,MnPh and Zn,NiPh solutions – the potentials gradually shifted in a positive direction. The curve demonstrating the time-variation of potential of non-phosphated zinc surface within the first 200-250 s indicates an average shift of about 250 mV in a positive direction. This shift, which is essentially greater than that in the cases with phosphated surfaces, is followed by a period where the potential remains almost without alteration.

Potentiodynamic polarization investigations

The potentiodynamic polarization studies of the crystalline phosphate coatings were carried out at 20°C in model aqueous solutions of 0.01 M NaCl, 0.6 M NaCl and 0.6 M NH₄NO₃.

The scanning rate of 10 mV s⁻¹ was chosen based on preliminary test runs. The target of these experiments was to obtain information about the corrosion behavior of the crystalline phosphate coatings formed in the corresponding model media in the course of their cathodic and anodic polarization and consequently to compare them.

The potentiodynamic polarization relationships of the phosphate coatings (Figure 7) obtained in the model solutions of NaCl and NH₄NO₃ allow estimating both the corrosion potentials and the corresponding corrosion currents summarized in Table 2. The modifications of the zinc phosphate baths by nickel, calcium and manganese result in shifts of the coating potentials of about 25 mV-100 mV in a positive direction in both NaCl solutions tested. This effect is not so well demonstrated when solutions with higher sodium chloride concentrations were used. The more positive potentials of the modified phosphate coatings indicate higher corrosion resistances and improved protective abilities when they are compared to the reference zinc surfaces despite the fact that the corrosion currents slightly differ.

The corrosion potentials and the corresponding currents related to the crystalline phosphate coatings developed in 0.6 M NH₄NO₃ solutions are also summarized in Table 2. These corrosion potentials are more positive while the corrosion currents are higher with respect to those determined in NaCl solutions.

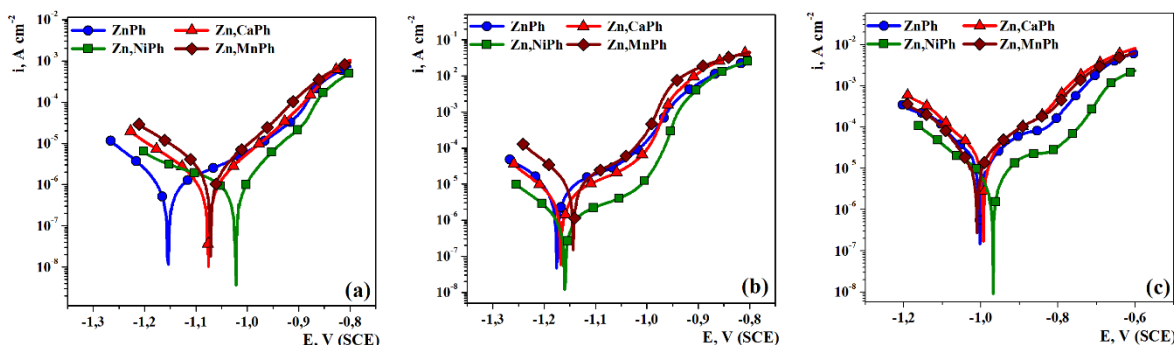


Figure 7. Potentiodynamic polarization relationships of crystalline phosphate coatings at 20°C in: a – 0.01 M NaCl; b – 0.6 M NaCl; c – 0.6 M NH₄NO₃

Table 2. Corrosion current and potential values

Model medium	ZnPh		Zn,CaPh		Zn,NiPh		Zn,MnPh	
	E _{corr} , mV	i _{corr} , A cm ⁻²	E _{corr} , mV	i _{corr} , A cm ⁻²	E _{corr} , mV	i _{corr} , A cm ⁻²	E _{corr} , mV	i _{corr} , A cm ⁻²
0.01 M NaCl	-1154	7.1×10 ⁻⁷	-1076	8.2×10 ⁻⁷	-1022	8.6×10 ⁻⁷	-1072	9.1×10 ⁻⁷
0.6 M NaCl	-1175	4.6×10 ⁻⁶	-1168	4.1×10 ⁻⁶	-1159	2.4×10 ⁻⁶	-1143	6.4×10 ⁻⁶
0.6 M NH ₄ NO ₃	-1051	6.4×10 ⁻⁵	-1035	3.2×10 ⁻⁵	-986	1.6×10 ⁻⁵	-1022	4.2×10 ⁻⁵

SEM analysis

The microphotographs (SEM) of the phosphate coatings obtained on electrogalvanized steel in ZnPh, Zn,CaPh, Zn,NiPh and Zn,MnPh, developed for 10 min at 60°C in a solution of 10 vol. % concentration, reveal that the habitus of the coatings is almost the same (Figure 8). Precisely, the crystals are formed at a single center with a growing mode similar to that of spherulites. The crystal dimensions are within the range of 2 µm-200 µm. There are relatively well-displayed differences that could be attributed to the presence of some better and greater leaf-like crystals grown in Zn,NiPh and Zn,MnPh.

EDX analysis

The quantities of the main elements found in the coatings obtained for 10 min at 60°C in solutions of a concentration of 10 vol.% are summarized in Table 3. The EDX data indicate almost identical amounts of O, P and Zn in all coatings tested. Presence of Ca, Ni and Mn was not detected in the composition of the coating grown in ZnPh solutions but quantities of these elements were discovered in the coatings formed in the modified zinc-phosphating baths.

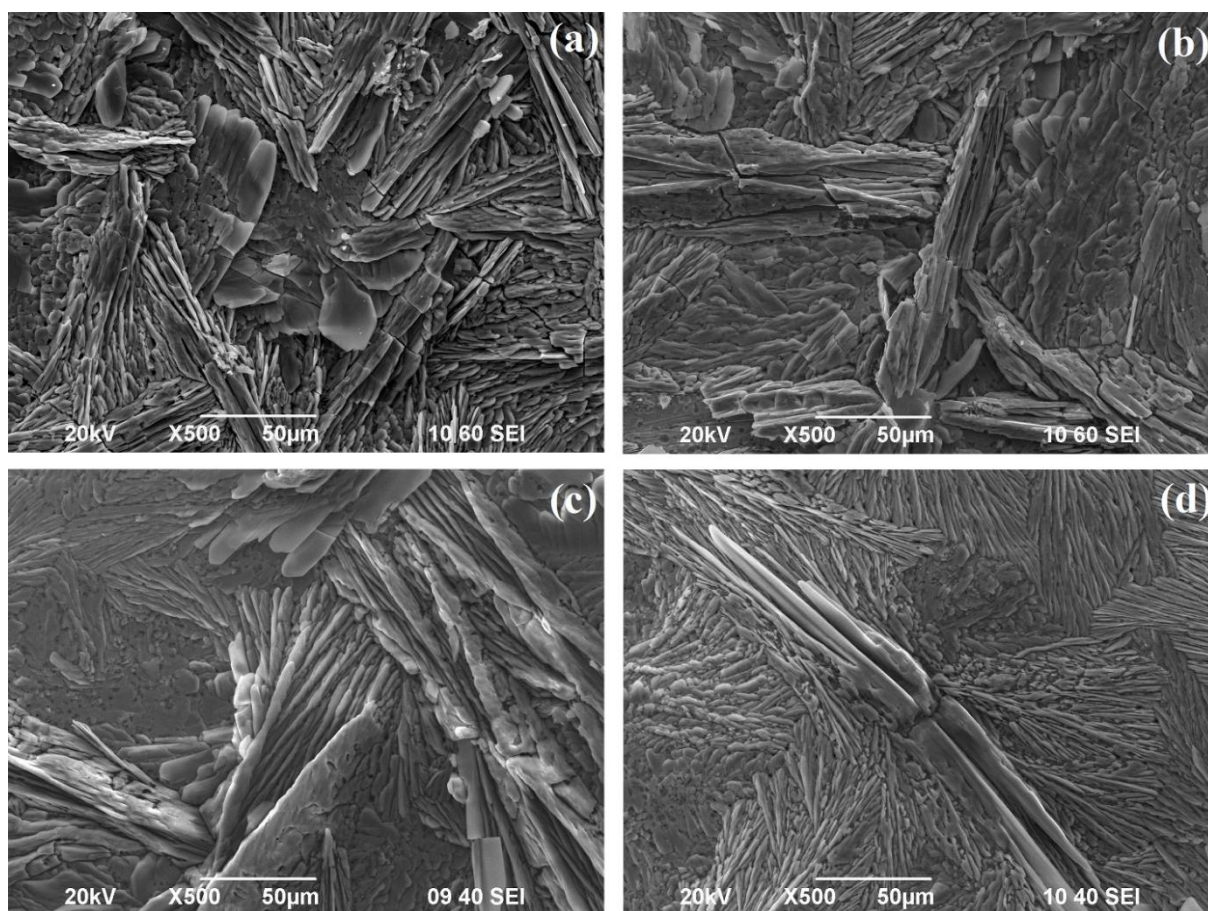


Figure 8. Microphotographs of phosphate coatings grown in: a – ZnPh; b – Zn,CaPh; c – Zn,NiPh; d – Zn,MnPh

Table 3. Elemental composition of the phosphate coatings obtained by EDX – analysis

Elements	ZnPh		Zn,CaPh		Zn,NiPh		Zn,MnPh	
	Wt %	At %	Wt %	At %	Wt %	At %	Wt %	At %
O	43.24	70.96	37.90	67.00	37.94	64.26	35.40	65.13
P	13.99	11.86	12.60	11.51	11.85	0.37	11.43	10.86
Zn	42.76	17.18	48.38	20.93	46.39	19.23	52.50	23.65
Ni	-	-	-	-	3.82	6.14	-	-
Ca	-	-	1.12	0.56	-	-	-	-
Mn	-	-	-	-	-	-	0.67	0.36
Total	100	100	100	100	100	100	100	100

XRD analysis

The XRD spectra of the crystalline coatings grown in the initial and the modified phosphating solutions are shown in Figure 9. The XRD analysis principally indicates the presence of hopeite – $Zn_3(PO_4)_2 \cdot 4H_2O$ in the coatings. There are shifts of some of the peaks in the spectra corresponding to coatings obtained in the modified solutions, as well as changes in their intensities when compared to the data obtained with coatings formed in the initial zinc-containing solution. These shifts suggest partial displacement of Zn in the hopeite by Ca, Ni and Mn but this does not lead to appearance of new phases. In fact, quasi-hopeites of calcium, nickel and manganese, are formed.

X-ray photoelectron spectroscopy (XPS)

The X-ray photoelectron spectroscopy was applied to determine both the nature and the valent state of the elements present on the coatings surfaces. The peaks observed refer to Zn2p, O1s, P2p and Fe2p as it is shown in Figure 10. The binding energies of Zn2p and O1s were estimated as 1021.6 eV and 532.0 eV, respectively and

corresponded to ZnO. The estimated binding energy of P2p was about 134.2 eV. This suggests that the element existing in its V-valent state is incorporated in a compound of the form of P_2O_5/PO_4^{-3} . The Fe2p peak was found in the spectra of all crystalline phosphate coatings. The presence of small quantities of iron (see Table 4) could be attributed to the zinc coating of the sample substrate. The peaks corresponding to Ca2p, Ni2p and Mn2p peaks are shown in Figure 11. Precisely, they were detected in the photoelectron spectra of the coatings developed in the modified phosphating solutions. The values of the binding energies are as follows: 348.2 eV for Ca2p, 855.0 eV and 861.2 eV for Ni2p, and 642.4 eV for Mn2p. These values suggest that the coatings are mainly in the form of oxides and the calcium and nickel cations are in their second-valent states, while the manganese cations are in their fourth-valent state.

The concentration values corresponding to the elemental analysis of the different phosphate coatings obtained by XPS analysis are summarized in Table 4.

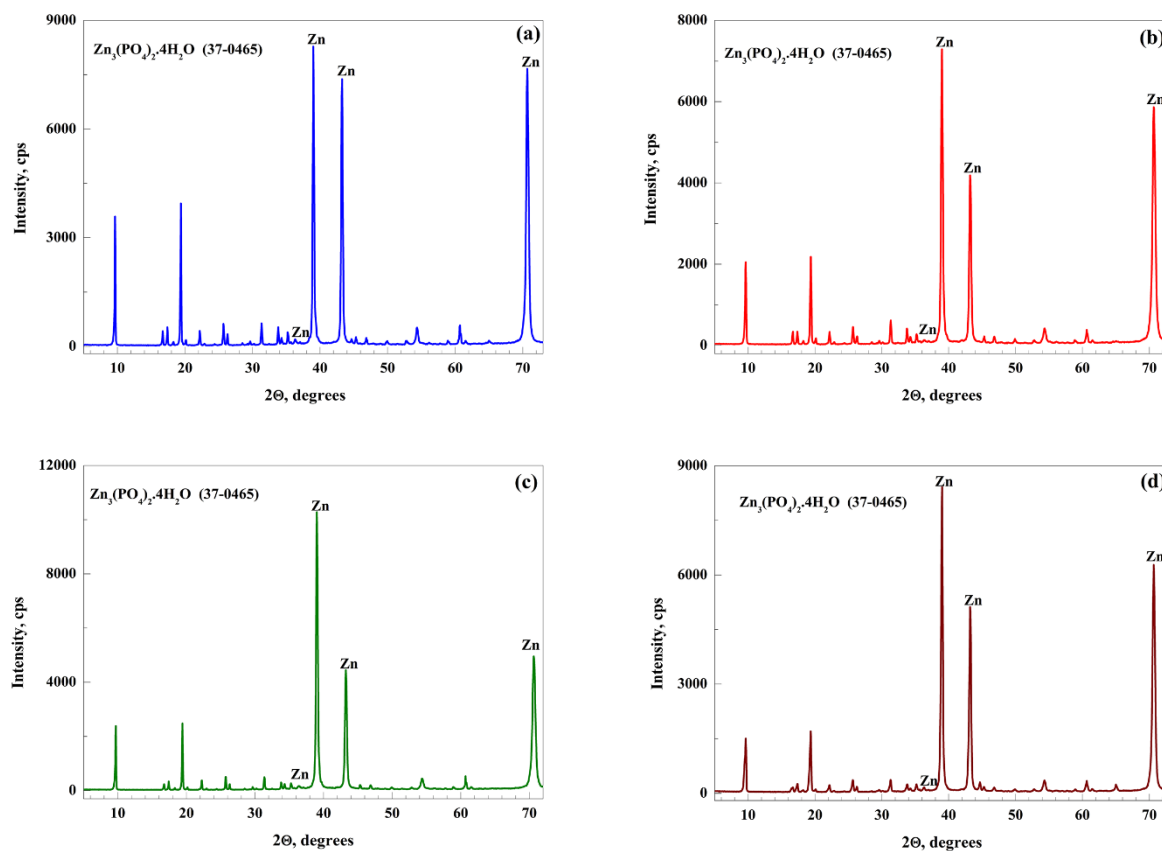


Figure 9. XRD spectra of the crystalline phosphate coatings grown in: a – ZnPh; b – Zn,CaPh; c – Zn,NiPh; d – Zn,MnPh

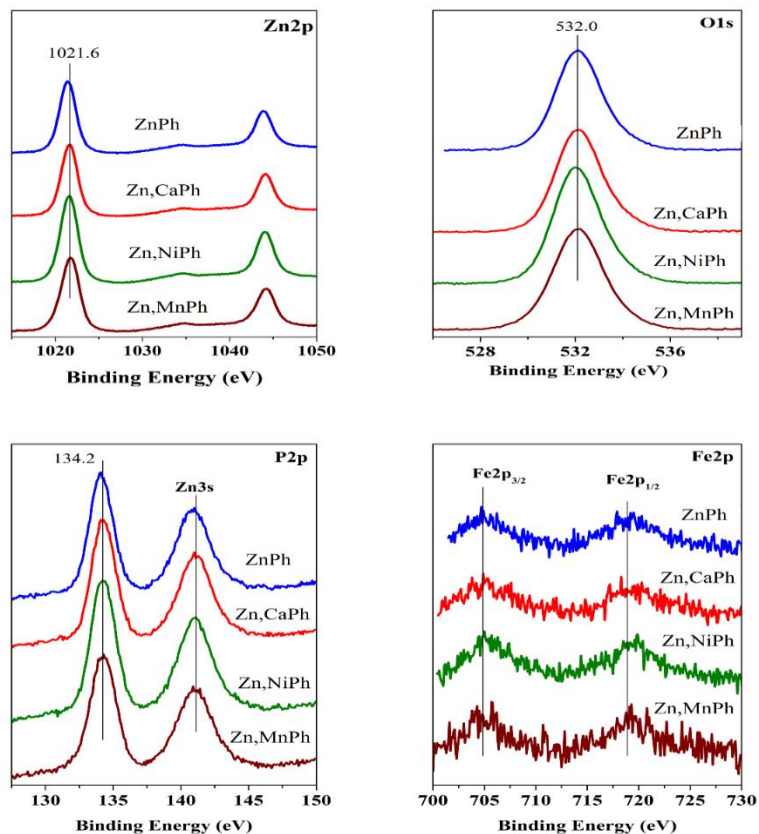


Figure 10. XPS spectra of the crystalline phosphate coatings illustrating the presence of Zn2p, O1s, P2p and Fe2p peaks.

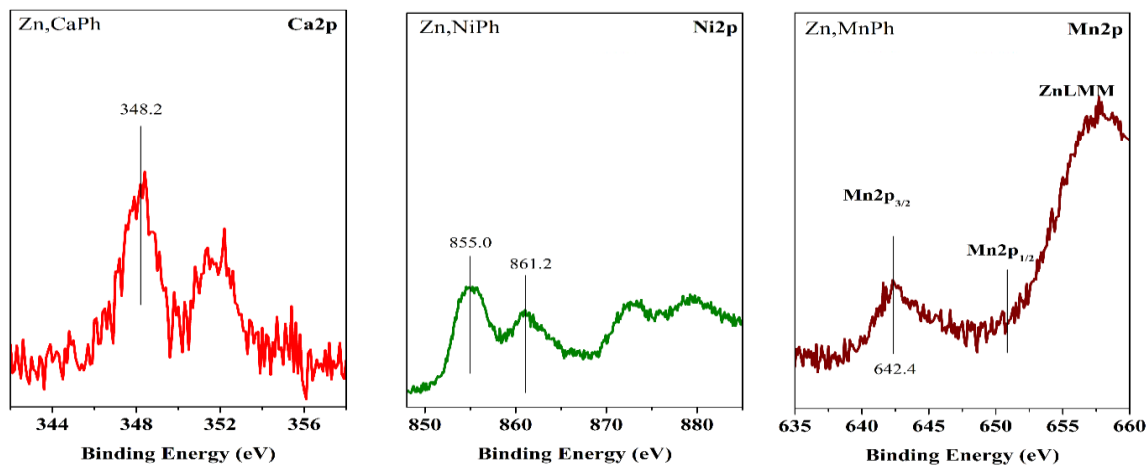


Figure 11. XPS spectra illustrating the presence of Ca2p, Ni2p and Mn2p peaks in the coatings grown in: a – Zn,CaPh; b – Zn,NiPh; c – Zn,MnPh

Table 4. Elemental composition of the phosphate coatings obtained by XPS – analysis

Elements	ZnPh	Zn,CaPh	Zn,NiPh	Zn,MnPh
	At %	At %	At %	At %
O	64.9	65.0	64.0	64.4
P	20.1	19.4	19.3	18.9
Zn	14.6	13.6	14.8	14.6
Fe	0.4	1.0	0.7	0.9
Mn	–	–	–	1.2
Ni	–	–	1.2	–
Ca	–	1.0	–	–

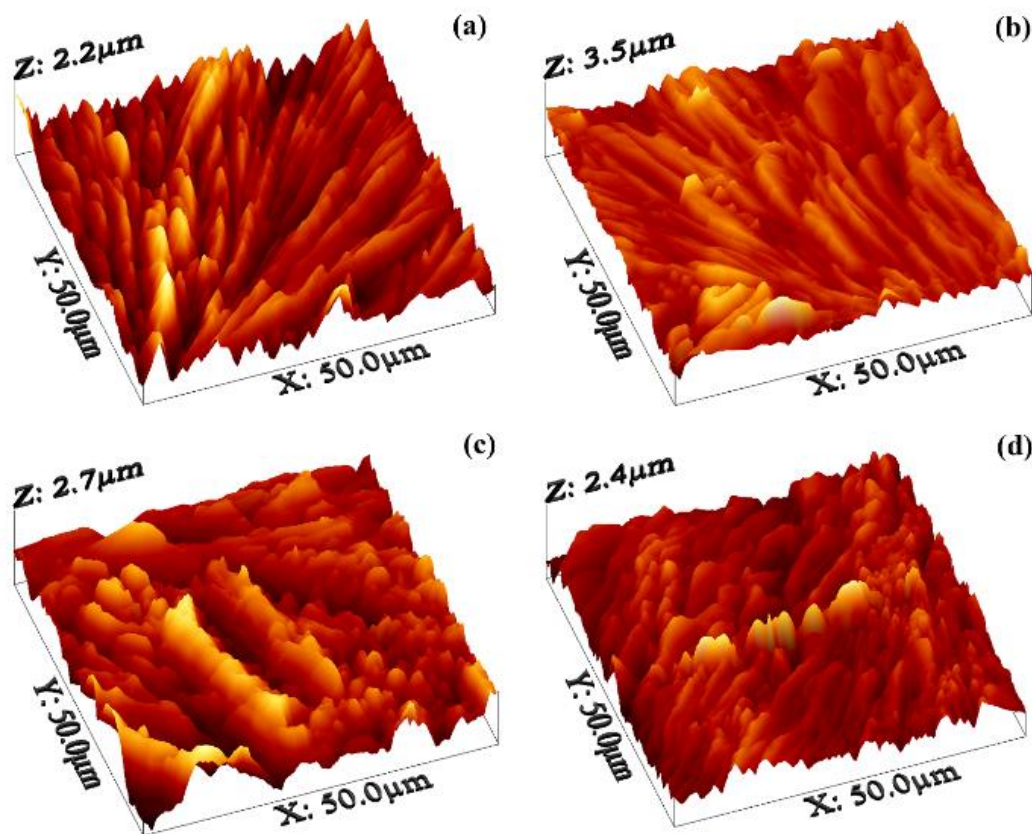


Figure 12. AFM three-dimensional images of the surface of the crystalline phosphate coatings grown in: a – ZnPh; b – Zn,CaPh; c – Zn,NiPh; d – Zn,MnPh

Atomic force microscopy (AFM) data

The three-dimensional contour maps determined by AFM (see Figure 12) indicate well-developed crystalline structures of the coatings. The latter determined the dimensions ($50\mu\text{m} \times 50\mu\text{m}$) of the scanned area used for the analysis.

Electrochemical determination of the phosphate coatings protective properties

The electrochemical determination of the protective properties of phosphate coatings consist in measuring the maxima of the anodic corrosion potential, E_{Amax} during galvanostatic polarization in a model electrolyte ($\text{NaCl} + \text{Na}_2\text{SO}_4$; $6 \text{ gl}^{-1} + 94 \text{ gl}^{-1}$). Three samples from each series of specimens with identical coatings were tested aiming higher precision and at least three replicates were measured of each sample. Some of the profiles of the polarization potentials against time are shown in Figure 13.

The better corrosion protective properties correspond to the higher E_{Amax} and to the bigger integral area under the maxima. The data presented show that close values of E_{Amax} correspond to coatings formed in ZnPh and Zn,CaPh.

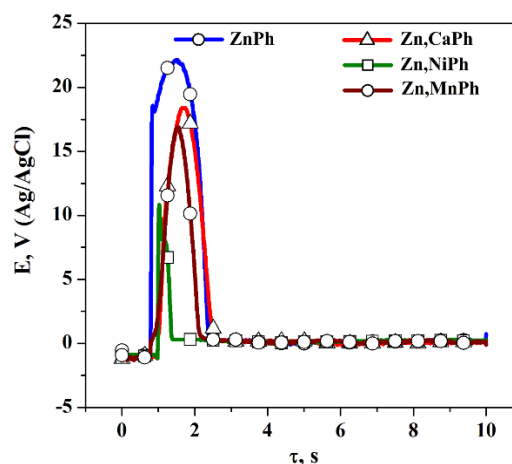


Figure 13. Potential vs. time ($E, V - \tau, s$) dependences of the crystalline coatings obtained during galvanostatic polarization.

Corrosion tests in a neutral salt spray (NSS)

The NSS corrosion tests were carried out in accordance with the procedure described in ISO 9227:2012. The initial visual observations of the specimens indicated acceptable homogeneities of the surfaces. The corrosion tests addressed one side of the samples, while the opposite ones were used for electrochemical experiments. Three specimens of each coating series were examined.

A. Corrosion resistance of the coatings. Essential changes in the outer appearances of all specimens were observed immediately after the first cycle. Precisely, the samples became covered to varying extents by white corrosion products (*white rust*) indicating the zinc corrosion in NSS. The most aggressive white rust appeared when samples with zinc coating only were tested, which is an expected result.

B. Corrosion protection provided by the coatings investigated. Specimens of all series (including three with a zinc coating only) do not corrode until the appearance of *red rust* formation (0% affected area) irrespective of the significant corrosive impact of the *white rust* on some of the series. Examination marks of 10 were assigned to these samples, evaluating in this way their corrosion resistances in comparison with the steel substrate until the end of the corrosion tests (the end of the 8-th corrosion cycle).

The experiments with phosphated coatings developed in different native and modified solutions allowed to outline the main results among them: the tests indicated that all samples became covered by white rust after the first corrosion cycle. This effect was stronger with specimens with no phosphate coatings while the samples with phosphate coatings (of the 5-th÷8-th series) were almost identically affected by white rust on both sides of the plates. The latter can be attributed to the fact that the crystalline phosphate coatings do not participate alone in the corrosion test but as layers attached to sublayers better adhere to the substrates.

The tests with almost all crystalline phosphate coatings revealed that corrosion products formed on the surfaces after the first run remained practically unchanged until the end of the experiments. No red rust appeared on the specimens of all series until the end of the 8-th cycle.

The results related to the corrosion behavior in a neutral salt spray and the electrochemical experiments demonstrate satisfactory correlations and interrelations, which allows obtaining reliable characteristics of the phosphate coatings investigated.

CONCLUSIONS

On investigating the phosphating of electro galvanized low carbon steel surfaces in calcium, nickel and manganese modified zinc-phosphating baths (ZnPh), it was established that:

The phosphating in Zn,NiPh and Zn,MnPh, as well as in Zn,CaPh leads to the formation of thinner coatings under all experimental conditions investigated when compared to those grown in the zinc phosphating bath – ZnPh.

The modification of the zinc phosphate bath by calcium, nickel and manganese results in shifts of the coating potentials of about 25 mV-100 mV in a positive direction in all tested media.

The crystals of the coatings are formed at a single center with a growing mode similar to that of spherulite. The crystal dimensions are within the range of 2 µm-200 µm.

The EDX data indicate almost identical amounts of O, P and Zn in all coatings tested. Presence of Ca, Ni and Mn was not detected in the composition of the coating grown in ZnPh solutions.

The X-ray phase analysis showed the presence of mainly hopeite – $Zn_3(PO_4)_2 \cdot 4H_2O$ in the phosphate coatings. Weak removing to some of the diffraction pattern peaks was observed. The latter is probably due to partial replacement of the zinc in hopeite by calcium, nickel and manganese, but it is not sufficient to clearly characterize the differentiation of new phases.

The protective properties of the phosphate coatings were determined electrochemically by measuring the maximum anodic potential, $E_{A,max}$ during galvanostatic polarization in a model ($NaCl + Na_2SO_4$; 6 $g\ l^{-1} + 94\ g\ l^{-1}$) electrolyte, as well as through neutral salt spray tests.

REFERENCES

1. D. Rausch, The Phosphating of Metals, Finishing Publications Ltd, Teddington, Middlesex, England, 1990, pp. 47, 151.
2. D. B. Freeman, Phosphating and Metal Pretreatment, Woodhead-Foulkner, Cambridge, 1986, pp. 9, 118.
3. Zh. Gao, D. Zhang, X. Li, Sh. Jiang, Q. Zhang, *Colloids and Surfaces A: Physicochemical and Engineering Aspects*, **546**, 221 (2018).
4. J. Donofrio, *Metal Finishing*, **98** (6) 57, 60 (2000).
5. U. B. Nair, *Metal Finishing*, **93**, 40 (1995).
6. A. S. Akhtar, D. Susac, P. Glaze, K. C. Wong, P. C. Wong, K. A. Mitchell, *Surf. and Coat. Tech.*, **187**, 208 (2004).
7. M. Tamilselvi, P. Kamaraj, M. Arthanareeswari, S. Devikala, J. Arockia Selvi, *Intern. J. of Adv. Chem. Sci. and Applications*, **3** (1), 25 (2015).
8. K. An, Ch. An, Ch. Yang, Y. Qing, Y. Shang, Ch. Liu, *Int. J. Electrochem. Sci.*, **12**, 2102 (2017).
9. G. N. Bhar, N. C. Debnath, S. Roy, *Surf. and Coat. Tech.*, **35** (1-2), 171 (1988).

10. W. P. Kripps, in: *Metals Handbook*, ASM, Ohio, 13, 9th edn., 1978, p. 380.
11. Fachikov L., D. Ivanova, D. Dimov, *J. UCTM, Sofia*, **41** (1), 15 (2006).
12. N. A. Perekhrest, K. N. Pimenova, V. D. Litovchenko, L. I. Biryuk, *Zashchita Metallov*, **28** (1), 134 (1992), (in Russian).
13. T. Sugama, T. Takahashi, *J. Mater. Sci.*, **30** (3), 809 (1995).
14. D. Ivanova, L. Fachikov, *Bulg. Chem. Commun.*, **43** (1), 54 (2011).
15. Ts. Dobrev, M. Monev, I. Krastev, W. Richtering, R. Zlatev, St. Rashkov, *Trans. IMF*, **74** (2), 45 (1996).
16. Ts. Dobrev, M. Monev, I. Krastev, R. Zlatev, St. Rashkov, Bulgarian Patent, Registration № 99469, 1995.
17. T. S. N. Sankara Narayanan, *Rev. Adv. Mater. Sci.*, **9**, 130 (2005).

Simplified synthetic procedure for (Z) to (E)-cyclooct-4-enol photoisomerization

S. S. Stanimirov*, B. R. Todorov

Faculty of Chemistry and Pharmacy, Sofia University, Sofia, Bulgaria

Received: October 30, 2020; Revised: January 27, 2021

This article is a proof of the principle of a new synthetic procedure for sensitized photoisomerization of *cis*-cyclooct-4-enol in the corresponding *trans* isomer. By irradiation of the organic solution containing ethyl benzoate as sensitizer, which is part of a two-phase cyclohexane/water system, during irradiation a continuous extraction of the resulting *trans*-cyclooct-4-enol in the form of a silver complex is carried out. A theoretical model describing the thermodynamic equilibrium of this two-phase system is also derived. This model was used as a tool to optimize the experimental conditions of the photolysis. In this model, the stability constants of the silver complexes of the cyclooct-4-enol isomers, as well as the distribution constant of this compound between the organic and aqueous phases, participate as parameters, which parameters were experimentally established in the present study as well.

Keywords: Click chemistry, photoisomerization, (E)-cyclooct-4-enol

INTRODUCTION

The term “Click Chemistry” [1-4] involves interactions between pairs of functional groups that rapidly and selectively react (“click”) with each other in mild, aqueous conditions. This concept has developed into a convenient and reliable two-step coupling procedure of two molecules widely used in biosciences [5], drug discovery [6, 7] and material science [8]. Especially biomolecule labelling requires reaction procedures that can be performed under physiological conditions (neutral pH, aqueous solution, ambient temperature) with low reactant concentrations to ensure non-toxic, low background labelling at a reasonable time scale while still preserving biological function. Among the plethora of possible reactions only a few generally fit the necessity of fast reactivity, selectivity, catalyst-free and biocompatibility criteria [9]. An example of such coupling is the inverse electron demand Diels–Alder (IEDDA) reaction [10] which goes between 1,2,4,5-tetrazines (s-tetrazines, Tz) and various dienophiles ([4+2] cycloaddition). It was observed that the use of *trans*-cyclooctene (TCO) as a precursor gave a tremendous rate difference compared to *cis*-cyclooctene and most importantly to the other cyclic alkenes with higher ring strain.

Unfortunately, synthesis of the *trans* isomer of cyclooctene derivatives is not easy and usually proceeds with low yields. This fact determines the high price of these compounds. The most common synthesis of the *trans* isomers follows the photochemical synthetic procedure described by Royzen *et al.* [11]. By this procedure,

corresponding Z isomer of cyclooctene is dissolved in a nonpolar aprotic solvent as cyclohexane and is placed in a photochemical reactor where it is irradiated with UV light in presence of sensitizer. During irradiation, the solution is continuously recirculated through a chromatography column filled with silica gel the top of which is covered by an additional amount of silica gel impregnated with AgNO₃. In this way, the E isomer, obtained by photoisomerization of the Z cyclooctene, is retained over the silica gel doped with silver ions due to the formation of a silver complex and the Z isomer is transmitted through this layer given that its silver complex is by two orders of magnitude weaker than the former one. After unknown amount of time [11] recirculation is suspended and the captured E-cyclooctene is liberated by dissolving the silica gel containing its silver complex in 25% ammonium hydroxide and the compound is then re-extracted from the aqueous solution with an organic solvent. After evaporation of the organic solvent the E isomer is collected.

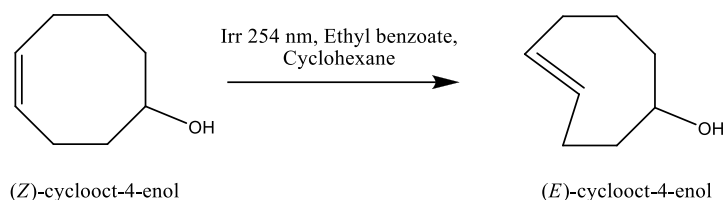
Some drawbacks of the procedure described [11, 12] are observed, though it leads to good yields of isomerization. First, the experimental setup used is not the simplest. A circulating pump is required and consumables such as hundreds of grams of silica gel and liter amounts of organic solvent are used. This makes the procedure unusable for milligrams of the substrate because it will spread throughout the system and this will lead to a significant reduction in yields. Second, before the start of photolysis, unknown circulation time might be required to achieve a concentration equilibrium of

* To whom all correspondence should be sent:
E-mail: sstanimirov@chem.uni-sofia.bg

the substances dissolved in the organic solvent. Depending on the nature of the solutes and the polarity of the eluent, different rates of passage through the silica gel column can be obtained for the solvent and for the solutes. This leads to the attenuation of concentration fluctuations in the solution over time, as they are different for the substrate and for the sensitizer. After reaching the equilibrium some substrate will be retained on the

column causing unknown reduction of the concentration of the substrate in the irradiated solution.

In this paper, we suggest a simplified method for *cis* to *trans* isomerization of cyclooctene derivatives using (Z)-cyclooct-4-enol (*cis*-CO-4-OH) (CAS number: 4277-34-3) as sample compound (Scheme 1).



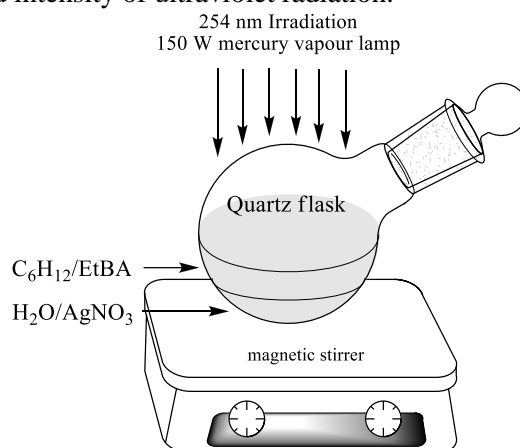
Scheme 1.

The advantage of this method is that it uses an extremely simple experimental setup, which allows the use of mg amounts of substrate and small amounts of organic solvent without affecting the yields for photoisomerization. In addition, precise control of the substrate and sensitizer concentrations in the irradiated solution can be performed. This is extremely important because it results in photoisomerization yields. With this method we obtain yields comparable to the more complex procedure using silica gel [11, 12] and 3 to 5 times higher yields than those of single-phase photosensitized isomerization with different sensitizers [13-15].

The experimental setup of the method is presented on

Scheme 2. We use a two-phase system consisting of two layers of liquids – an upper organic layer of cyclohexane in which the cyclooctenol and the sensitizer (ethyl benzoate) are dissolved and an aqueous layer containing silver nitrate on the bottom of the flask. Thus, by continuously stirring of the solutions during irradiation from the top of the flask, a continuous extraction of the resulting *trans*-CO-4-OH (CAS number: 85081-69-2) is ensured, and it is retained in the aqueous layer in the form of a silver complex. The progress of the photoisomerization was monitored by titration of the resulting *trans*-CO-4-OH in the aqueous layer over a period of time with 3,6-di(pyridin-2-yl)-1,2,4,5-tetrazine (TzPy) (CAS Number 1671-87-0). In the article we develop and discuss a theoretical model for the distribution of the different forms under which CO-4-OH exists in the two-phase system, taking into account different thermodynamic parameters of the system, such as

equilibrium and stability constants, constants of phase distribution and photostationary state. This model helps us to adjust the experimental conditions of the method such as to achieve maximum efficiency of photoisomerization for the specific conditions of the experiment, such as irradiation area and intensity of ultraviolet radiation.



Scheme 2.

EXPERIMENTAL

cis-Cyclooct-4-enol (10 g 98% purity Career Henan Chemical Co) and 3,6-di(pyridin-2-yl)-1,2,4,5-tetrazine (54 g 98% purity Career Henan Chemical Co) are trade products which were purified prior to use by column chromatography. The photoisomerization was monitored by the amount of the *trans*-cyclooct-4-enol produced in the aqueous phase or that left in the organic phase by titration of the ethanol solution of tetrazine with known concentration. Quantity of the *trans*-cyclooct-4-enol was calculated by the change of the absorption band of the tetrazine at 540 nm in pure ethanol or at 570 nm in presence of silver ions. Absorbance was

recorded using UV-Vis-NIR Agilent Cary 5000 spectrophotometer. The same instrument was used for determination of the thermodynamic parameters of the system such as distribution and stability constants. $K_D = 0.92 \pm 0.05$ constant of cyclooct-4-enol for the system cyclohexane/water was determined by measuring the absorbance shoulder at 200 nm of the solution of cyclooct-4-enol in cyclohexane before and after water extraction. The constant K_{AgZ} was calculated to be $2.5 \pm 0.3 \text{ M}^{-1}$ by UV spectroscopy monitoring of the amount of cyclooct-4-enol left in cyclohexane after extraction with aqueous solutions of AgNO_3 with different concentrations. The same approach was used for determination of the $K_{AgE} = 2100 \pm 100 \text{ M}^{-1}$ constant. In this case the amount of *trans*-cyclooct-4-enol left in cyclohexane was determined by titration with tetrazine.

The photolysis of *cis*-cyclooct-4-enol to *trans*-cyclooct-4-enol was carried out by irradiation from the top under continued stirring and constant temperature of 20 °C with a 150 W mercury vapor lamp of the quartz flask filled with air saturated cyclohexane/water mixture containing substrate and the sensitizer ethyl benzoate. In all experiments the concentration of ethyl benzoate in cyclohexane was

such as to ensure optical density 1 at a wavelength 272 nm and optical path 1 cm.

cis-Cyclooct-4-enol: ^1H NMR (500 MHz, CDCl_3) δ 5.72 – 5.67 (m, 1H), 5.63 – 5.56 (m, 1H), 3.85 – 3.78 (m, 1H), 2.36 – 2.22 (m, 1H), 2.19 – 2.07 (m, 3H), 1.98 – 1.81 (m, 2H), 1.76 – 1.46 (m, 5H).

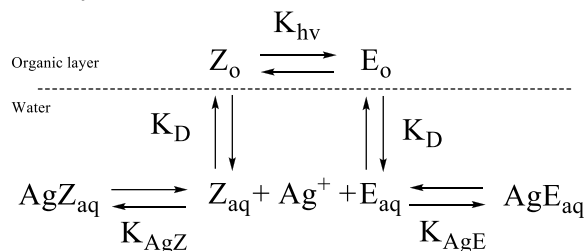
trans-Cyclooct-4-enol: ^1H NMR (500 MHz, CDCl_3) δ 5.64 – 5.51 (m, 1H), 5.45 – 5.32 (m, 1H), 3.51 – 3.41 (m, 1H), 2.31 (m, 3H), 2.02 – 1.88 (m, 4H), 1.72 – 1.53 (m, 3H).

RESULTS AND DISCUSSION

Theoretical background

Assuming that at the ultimate time of irradiation the isomerization of *cis*-CO-4-OH to *trans*-CO-4-OH and *vice versa* leads to reaching a photostationary state, the global equilibrium and the distribution of the components between the two-phase system can be expressed by the equations on

Scheme 3.



Scheme 3.

where letters Z and E denote the corresponding π -diastereomers of CO-4-OH and subscripts “o” and “aq” denote organic and aqueous phase at which the compounds exist, respectively. AgZ and AgE are the silver complexes of the *cis*- and *trans*-CO-4-OH, respectively. K_{hv} is the equilibrium constant of the photostationary state in presence of sensitizer, which is equal to $K_{hv} = E_o/Z_o$, where Z_o and E_o are the moles of *cis* and *trans* isomer, respectively. The equilibrium constant which presents the distribution of the CO-4-OH isomers in the two immiscible solvents can be written as follows:

$$K_D = \frac{Z_o V_{aq}}{Z_{aq} V_o} = \frac{E_o V_{aq}}{E_{aq} V_o},$$

where V_o and V_{aq} are the volumes of the organic and aqueous phase, respectively. The stability

constants K_{AgZ} and K_{AgE} of the corresponding silver complexes are equal to:

$$K_{AgZ} = \frac{\text{AgZ}_{aq} \cdot V_{aq}}{Z_{aq} \cdot (C_{Ag} - \text{AgZ}_{aq} - \text{AgE}_{aq})}$$

and

$$K_{AgE} = \frac{\text{AgE}_{aq} \cdot V_{aq}}{E_{aq} \cdot (C_{Ag} - \text{AgZ}_{aq} - \text{AgE}_{aq})}$$

where C_{Ag} is the total mole amount of silver ions.

We made two approximations presenting the global equilibrium of the system with this model.

First, we neglected the amount of silver complexes in the organic phase, assuming that they are almost completely dissolved only in water, and second, that

the distribution constant K_D has the same value for the E and Z isomers. The thermodynamic model of the two-phase system at equilibrium presented on

Scheme 3 can be expressed by the following system of equations:

$$\begin{aligned} E_o &= K_{hv} Z_o \\ Z_{aq} &= \frac{Z_o V_{aq}}{V_o} \\ E_{aq} &= \frac{E_o V_{aq}}{K_D V_o} \\ K_{AgZ} &= \frac{AgZ_{aq} \cdot V_{aq}}{Z_{aq} \cdot (C_{Ag} - AgZ_{aq} - AgE_{aq})} \\ K_{AgE} &= \frac{AgE_{aq} \cdot V_{aq}}{E_{aq} \cdot (C_{Ag} - AgZ_{aq} - AgE_{aq})} \\ (Ca &= Z_o + E_o + Z_{aq} + E_{aq} + AgZ_{aq} + AgE_{aq}) \end{aligned}$$

By solving this system of equations, the mole fractions of the components of the two-phase model can be represented as a function of the total amount of CO-4-OH available in the system – Ca, as follows:

$$\begin{aligned} A &= K_{AgZ} + K_{AgE} K_{hv} \\ B &= K_D V_o + V_{aq} \end{aligned}$$

$$\begin{aligned} \chi_{Z_o} &= \frac{(K_D V_o (-K_D (1 + K_{hv}) V_o V_{aq} + V_{aq} ((Ca - C_{Ag}) A - (1 + K_{hv}) V_{aq})) \\ &+ \sqrt{V_{aq}^2 (4 Ca (1 + K_{hv}) A B + (A (C_{Ag} - Ca) + (1 + K_{hv}) B)^2))}{(2 Ca (1 + K_{hv}) A V_{aq} B)} \end{aligned}$$

Hence, by replacing the term for Z_o into the equations above, the mole fractions of the other components of the system as functions of Ca can be easily deduced. These functions are represented graphically in Figure 1 and represent a specific case for the corresponding values of the equilibrium constants and volumes of the phases specified in the figure inset.

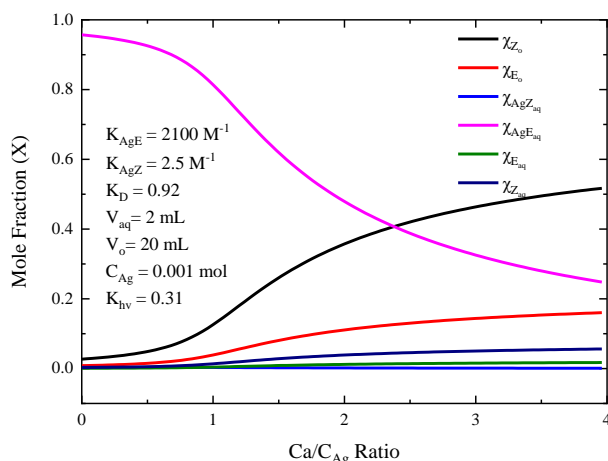


Figure 1. Mole fractions of the components of the system at global equilibrium as a function of CO-4-OH total mole – Ca, which follow the thermodynamic model of the two-phase system at global equilibrium presented on

Scheme 3.

As can be seen from Figure 1 under these conditions and an equimolar ratio between the amounts of CO-4-OH and silver ions, about 80% of the total amount of cyclooctenol will be in the form of a silver complex of the *trans* form, upon reaching global equilibrium. Thus, this theoretical model illustrates the advantage of the two-phase system in the photoisomerization of *cis*-CO-4-OH by providing a convenient way to synthesize *trans*-CO-4-OH, which can be isolated after treatment of the aqueous phase with 25% ammonium hydroxide and subsequent re-extraction. Although this procedure predicts 100% *cis* to *trans* conversion at optimal experimental conditions, as a result of side reactions between substrates and photoactive species, the predicted theoretical yield can never be reached. However, this model helps us to select the experimental conditions such as to minimize the rates of side reactions and thus maximize the yield of sensitized photoisomerization.

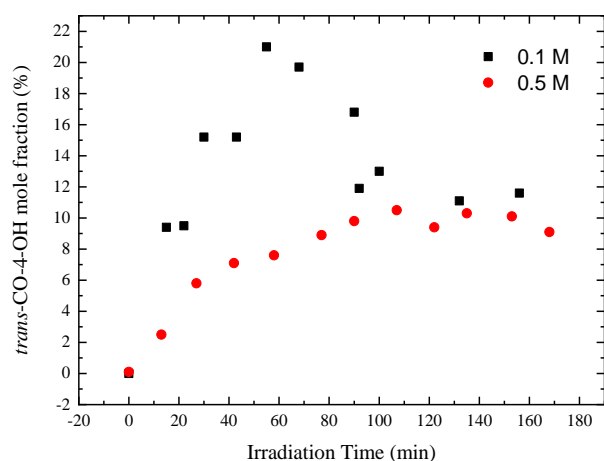


Figure 2. Sensitized photoisomerization of *cis*-CO-4-OH to *trans*-CO-4-OH in cyclohexane at two different initial concentrations of the substrate as a function of time.

RESULTS AND DISCUSSION

Figure 2 presents the isomerization process of *cis*- in *trans*-CO-4-OH as a function of time for two different initial concentrations of *cis*-CO-4-OH. Photolysis of the *cis* form of CO-4-OH was performed in cyclohexane in the presence of ethyl benzoate. The amount of sensitizer was such that the optical density of the solution in the cuvette with an optical path length of 1 cm is equal to 1 at 272 nm wavelength. The amount of the *trans* isomer obtained was monitored by titration with a solution of TzPy in ethanol with known concentration. As can be seen from the figure, the initial concentration of cyclooctenol affects both the percentage of maximum transformation of *cis*- to *trans*-cyclooctenol and the shape of the function. This is an effect known in the literature [13, 15, 16], which is confirmed by our experiments. The reason for the concentration dependence of the photostationary state is the participation of substrates in side reactions, whose rate constants depend on the total concentration of cyclooctenol. These are polymerization reactions or interactions with radicals that are the product of photodestruction. All of these processes are bimolecular, but they follow pseudo-first-order kinetics because the concentration of the starting cyclooctenol that is a component of the reaction is orders of magnitude higher than that of short-lived radicals or photoexcited particles formed during photolysis. Thus, at high concentrations of cyclooctenol, the rates of side reactions become commensurate or even higher than those of *cis-trans* isomerization, since the concentration is a coefficient by which the rate constant of the side reaction is multiplied. For this reason, due to the continuous losses of cyclooctenol, the true photostationary equilibrium in

the isomerization of *cis*- and *trans*-cyclooctenol can be reached and determined by absorption spectroscopy only at low concentrations of the substrate. For this reason, single-phase photolysis of *cis*- to *trans*-cyclooctenol on a gram scale can only be done with large amounts of solvent, which requires subsequent concentration of the dilute solutions. The use of the two-phase method proposed in this article allows maintaining a low concentration of the substrate in the organic phase where photolysis takes place. By an appropriate ratio between the volumes of the two phases, a concentration of the substrate in the organic layer, by one or two orders of magnitude lower than the amount of all cyclooctenol distributed throughout the system, can be easily ensured.

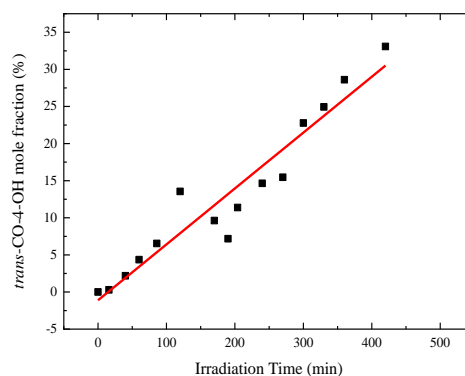


Figure 3. Sensitized photoisomerization of *cis*-CO-4-OH to *trans*-CO-4-OH in a two-phase system as a function of time. Volume ratio of cyclohexane/water is 10. The initial concentration of the substrate is 0.074 M (0.174 mL *cis*-CO-4-OH in 20 mL cyclohexane).

To test the advantage of the two-phase photoisomerization of *cis*-CO-4-OH in the *trans* isomer over the single-phase one, we conducted an experiment, the results of which are presented in Figure 3. The figure shows the progress of photoisomerization of *cis*-CO-4-OH in the *trans* isomer as a function of time in a two-phase cyclohexane/water system in the presence of ethyl benzoate sensitizer. The experiment was performed at a phase volume ratio of 1:10 in favor of the organic layer. Under these conditions, about 70% of the total amount of *cis*-CO-4-OH (0.074 M, 0.00147 mol in 20 mL cyclohexane) is present in the organic layer as a free ligand. As can be seen (Figure 3), the dependence can be approximated by a straight line, which represents the kinetics of a zero-order reaction. This is because the substrate concentration is kept relatively constant over a wide range due to the global equilibrium between the forms distributed between the two phases. If we compare the experiments performed with approximately the same

total concentration of *cis*-CO-4-OH (about 0.1M) in single-phase (Figure 2) and two-phase (Figure 3) photoisomerization, we see that in the second case we have a 10% increase in the yield of the *trans* form, namely from 25% in the single-phase to 33% in the two-phase system. This result is probably due, on the one hand, to the decrease in the concentration of the substrate in the irradiated solution, which reduces the competitiveness of the side reactions and, on the other hand, to the continuous removal of the *trans* product from the organic to the aqueous phase, where it is retained in the form of a silver complex.

From the analysis of the experimental data in combination with the theoretical predictions for the distribution of the substrate in the different forms of the system, coming from the model described above, it is clear that the yield of the *trans* isomer increases at lower concentrations of the irradiated solution, which is achieved by increasing the volume of the aqueous phase compared to that of the organic. This, in turn, slows down the transformation process, as the slope of the dependence shown in Figure 3 depends inversely on the equilibrium concentration of *cis*-CO-4-OH in the irradiated solution. Finding the optimal experimental conditions and the maximum ratio (yield of the *trans* isomer in %) vs. (time) will be the goal of a future publication. In this article we wanted to illustrate the advantage of heterophase photoisomerization as a method for the synthesis of *trans* isomers of cyclooctene derivatives over other procedures already described in the literature.

CONCLUSIONS

In conclusion, we point out a 3- to 5-fold increase in the yield of *trans*-CO-4-OH through photosensitized isomerization, as a result of the use of our proposed two-phase method. Thanks to the simplified experimental setup and with knowledge of the thermodynamic properties of the particular compound, better yields of sensitized photoisomerization can be achieved by precise control of the substrate concentration in the

irradiated solution carried out by changing the volume ratio of the organic and water phases, using the proposed two-phase method for the synthesis of *trans* derivatives of cyclooctene. That increase of the photoisomerization yields was achieved by using a very simple experimental setup consisting only of quartz flask and magnetic stirrer.

Acknowledgement: the authors are thankful for the support by the National Science Fund, Bulgarian Ministry of Education and Science (Contract no. KP-06-H29/4).

REFERENCES

1. C. R. Becer, R. Hoogenboom, U. S. Schubert, *Angewandte Chemie*, **48**, 4900 (2009).
2. J. Han, Q. Chen, Y. Shen, Z. Liu, X. Hao, M. Zhong, Z. Zhao. M. R. Bockstaller, *Biomacromolecules*, **21**, 3512 (2020).
3. C. D. Hein, X. M. Liu, D. Wang, *Pharmaceutical Research*, **25**, 2216 (2008).
4. S. O. Pereira, T. Trindade, A. Barros-Timmons, *Polymers*, **12**, (2020).
5. S. Hvilsted, *Polymer International*, **61**, 485 (2012).
6. H. Li, R. Aneja, I. Chaiken, *Molecules*, **18**, 9797 (2013).
7. J. Hou, X. Liu, J. Shen, G. Zhao, P. G. Wang, *Expert Opinion on Drug Discovery*, **7**, 489 (2012).
8. H. Nandivada, X. Jiang, J. Lahann, *Advanced Materials*, **19**, 2197 (2007).
9. B. L. Oliveira, Z. Guo, G. J. L. Bernardes, *Chemical Society Reviews*, **46**, 4895 (2017).
10. A. C. Knall, C. Slugovc, *Chemical Society Reviews*, **42**, 5131 (2013).
11. M. Royzen, G. P. Yap, J. M. Fox, *Journal of the American Chemical Society*, **130**, 3760 (2008).
12. D. Svatunek, C. Denk, V. Rosecker, B. Sohr, C. Hametner, G. Allmaier, J. Fröhlich, H. Mikula, *Monatshefte für Chemie*, **147**, 579 (2016).
13. Y. Inoue, T. Kobata, T. Hakushi, *The Journal of Physical Chemistry*, **89**, 1973 (1985).
14. Y. Inoue, K. Moritsugu, S. Takamuku, H. Sakurai, *Journal of the Chemical Society, Perkin Transactions*, **2**, 569 (1976).
15. Y. Inoue, S. Takamuku, H. Sakurai, *The Journal of Physical Chemistry*, **81**, 7 (1977).
16. Y. Inoue, S. Takamuku, H. Sakurai, *Synthesis*, **1977**, 111 (1977).

Structuring of water clusters depending on the energy of hydrogen bonds in electrochemically activated waters Anolyte and Catholyte

I. Ignatov^{1*}, G. Gluhchev², N. Neshev³, D. Mehandjiev⁴

¹Scientific Research Center of Medical Biophysics, 32 N. Kopernik Str., Sofia 1111, Bulgaria

²Institute of Information and Communication Technologies, Bulgarian Academy of Sciences, Acad. G. Bonchev Str., Bl. 2, Sofia 1113, Bulgaria

³Sofia University "St. Kliment Ohridski", Faculty of Physics, Sofia, Bulgaria

⁴Institute of General and Inorganic Chemistry, Bulgarian Academy of Sciences, Acad. G. Bonchev Str., Bl. 11, Sofia 1113, Bulgaria

Received: January 26, 2021; Revised: March 21, 2021

Experiments with alkaline (Catholyte), acidic (Anolyte) components of electrolyzed water, and control sample were carried out using NES and DNES methods. Clusters of different energy of hydrogen bonds were obtained. They were modeled with dodecahedral structures consisting of 20 water molecules having a diameter of circumscribed spheres equal to 0.822 nm. Lower number of clusters and increased average number of molecules per cluster in Catholyte and Anolyte compared to control water points to their better structuring. Higher average energy of hydrogen bonds in Catholyte and lower energy in Anolyte than that in control water, points to increased/decreased energy density, respectively, which could be related to different physiological effects. Thus, a new point of view to the processes of electrochemically activated water and its physiological action is suggested.

Keywords: Anolyte, Catholyte, NES, DNES, hydrogen bonds, clusters

INTRODUCTION

It is well known that energetic influence on a water solution causes alterations of its physicochemical properties, intermolecular forces and formation of configurations of different numbers of molecules [1, 2]. Thus, new properties of water could be obtained. These changes, together with the underlying physicochemical processes, have been studied during the last decades. Different hypotheses about the water structure have been launched assuming the existence of clusters and numbers of molecules in specific configuration [3-10]. For experimental proof different methods, such as far-infrared (FIR) [11], vibration-rotation-tunneling (VRT)[12], EXAFS- and X-ray spectroscopy [13], ¹H-NMR [14], neutron diffraction [15] and SCC-DFTB method [16] have been used.

However, to the best of our knowledge, there is no satisfactory description of the processes taking place during the electrolysis of water with a semipermeable membrane, leading to different properties of the obtained fractions, Catholyte at the cathode chamber, and Anolyte at the anode one. Their physiological effects as anti-oxidation, immune system stimulation, tissue regeneration of the Catholyte; anti-bacterial, anti-viral, anti-fungal, anti-inflammatory action of the Anolyte, have been confirmed by many researchers [17-23]. In this respect very interesting is the question about the

structure of Catholyte and Anolyte, i.e. formation of clusters, distribution of molecules according to the energy of hydrogen bonds and, as a result, energy redistribution between the two fractions. For this the methods NES (Non-equilibrium Energy Spectrum) and DNES (Differential Non-equilibrium Energy Spectrum) developed by Antonov [24] for the evaluation of molecule distribution depending on the energy of hydrogen bonds seem to be promising [25].

The methods are based on a unique physical effect where, during drop evaporation the wetting angle θ decreases discreetly to 0, while the diameter of the drop base area changes slightly.

Measurements of this angle at regular time intervals allows for determination of the distribution function $f(\theta)$ of the number of water molecules according to the energy of hydrogen bonds. $f(\theta)$ is called *water state spectrum* [24, 25]. Subsequently, the average energy $E(\theta)$ of hydrogen bonds in the sample can be derived for every measured value of the wetting angle θ . Derivation is based on Luck's model [26] according to which water is composed of O-H...O groups. The greater part of these groups contribute to hydrogen bond energy ($-E$), while the rest are not bound ($E=0$). The shape of $E(\theta)$ function also depends on external influencing factors. Its measurement unit is reciprocal electronvolt (eV^{-1}).

* To whom all correspondence should be sent:
E-mail: mbioph@abv.bg

Some results concerning the measurement of hydrogen bonds energy spectrum have already been published by the authors [27]. The present work is a continuation of the analysis of energy redistribution between Catholyte and Anolyte on the basis of data from [27].

MATERIALS AND METHODS

Water samples

Catholyte and Anolyte samples of water were produced in an electrolytic cell consisting of cathode and anode with a semipermeable membrane between them (Fig. 1). The membrane separates the water fractions: an alkaline one (Catholyte) and an acidic one (Anolyte) [17]. When direct electric current passes through both water-filled chambers, electrons from the cathode, as well as those extracted from water at the anode cause a series of redox reactions on the surface of both electrodes, and induce changes in the water structure, resulting in high pH and negative ORP values of the Catholyte, and low pH and positive ORP values of the Anolyte. It is worth noting that the mechanism of such changes is still not clear, but in any case it relates to the redistribution of electrical charges, i.e. energy. For comparison a control sample of non-processed water is used.

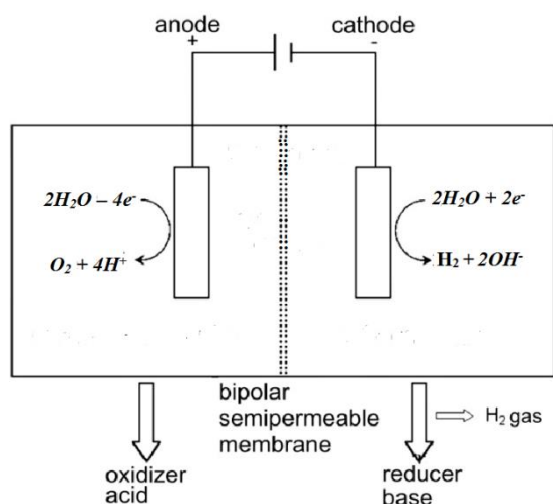


Figure 1. Electrolyzer scheme

NES and DNES spectral analysis

This study assumes a model of water molecule structuring based on average hydrogen bonds energy in the interval (-0.0912 eV to -0.1387 eV).

Measurements were performed with the optical device invented by Antonov for NES and DNES spectral analysis [24]. Water drops were evaporated in a hermetic camera, on a glass plate covered with transparent mylar foil.

The device characteristics are:

1. Monochromatic filter: wave length $\lambda = 580 \pm 7$ nm (yellow color in the visible spectrum);
2. Wetting angle of water drops: from 72.3° to 0° ;
3. Temperature range: $(+22 - 24^\circ \text{C})$;
4. Energy range of hydrogen bonds: $E = -0.08 - -0.1387$ eV (corresponding to $\lambda = 8.9 - 13.8$ μm).

Characteristics of NES and DNES water state spectra

The energy ($E_{H...O}$) of hydrogen O...H-bonds between H_2O molecules in water is measured in eV. The $f(\theta)$ function is called *energy distribution spectrum*. It is characterized by the non-equilibrium process of water droplets evaporation.

Figure 2 shows the operating principle of the method for measurement of wetting angle of liquid drops on a hard surface.

The relation between $f(\theta)$ and the energy of hydrogen bonds between water molecules $f(E)$ is expressed as follows:

$$f(E) = \frac{14.33f(\theta)}{[1-(1+bE)^2]^2} \quad (1)$$

where b depends on the number of water molecules at the surface layer of water per unit area, on the water surface tension and on the initial contact angle of the drop.

The water state spectrum is obtained from the non-equilibrium process of evaporation of water drops and, due to this, the term Non-equilibrium spectrum of water (NES) is used [24]. The evaluated measurement error for E is ± 0.0011 eV.

The difference:

$$\Delta E(\theta) = E(\theta)_{\text{sample}} - E(\theta)_{\text{control sample}} \quad (2)$$

is called Differential Non-equilibrium Energy Spectrum (DNES) [2, 24].

DNES is a measure of the alteration of water structure as a result of a certain influencing factor. The combined effect of all other influencing factors besides the examined one is the same for the control and the sample, that is why it is canceled out.

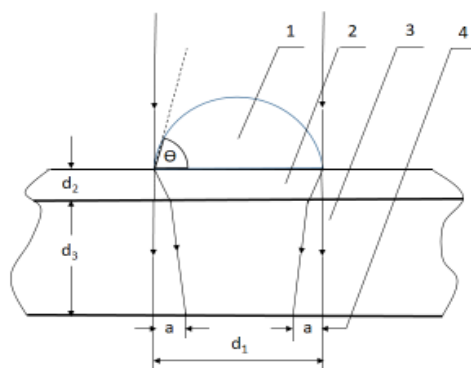


Figure 2. Operating principle of the method for measurement of wetting angle of liquid drops on a hard surface: 1 – drop, 2 – thin maylar foil, 3 – glass plate, 4 – refraction ring width. The wetting angle θ is a function of a and d_1 .

Electrical measurements

A HANNA Instruments HI221 meter equipped with Sensorex sensors was used for measurement of oxidation reduction potential (ORP) in mV, and pH. Its measurement ranges are: pH: (2.00 – 16.00 ± 0.01); ORP: ($\pm 699.9 \pm 0.01$ – $\pm 2000 \pm 0.1$) mV.

RESULTS AND DISCUSSION

Water samples

Following parameters were measured for the three samples of water: pH = 9.5, ORP = -400 mV for the Catholyte; pH = 3.5, ORP = +800 mV for the Anolyte, and pH = 7.2, ORP = +260 mV for the control sample (Table 2).

Results with NES and DNES methods for Catholyte, Anolyte and the control

The average energy ($\Delta E_{H...O}$) of hydrogen H...O-bonds between individual H₂O molecules was calculated for Catholyte, Anolyte and the control by NES- and DNES-methods. The result for Catholyte in the NES-spectrum is $E = -0.1251$ eV, for Anolyte it is $E = -0.1144$ eV and for control water $E = -0.1191$ eV. Calculations of $\Delta E_{H...O}$ for Catholyte with the DNES method lead to (-0.0060 eV), and to (+0.0047 eV) for the Anolyte (Table 1). These results point to restructuring among individual H₂O molecules with a significant increase of local extrema in Catholyte and Anolyte spectra (Table 2).

Characteristics of water molecules and hydrogen bonds

Water, as a weak electrolyte, dissociates into the hydrogen cations H⁺ and hydroxide anion OH⁻. Splitting up of the H–OH bond is accompanied by formation of new disordered bonds between

“fragments” of the initial molecules, leading to formation of areas with density fluctuations different from those in aqueous solutions.

The water molecule has a size of 0.27 nm. Hydrogen bond length is 1.5-2.6 Å or 0.24-0.26 nm [28]. The covalent bond length is 0.096 nm. Hydrogen bond strength between two water molecules is 5-6 kcal/mol or 0.22-0.26 eV [29].

In spectral analysis using NES and DNES methods, the working range is from (-0.0912) to (-0.1387) eV. The outermost layer of water drops evaporates at hydrogen bonds energy of -0.0912 eV. The last water molecules evaporate at hydrogen bonds energy of -0.1387 eV.

We adopted Saykally’s [4] model according to which the total number of available hydrogen bonds is maximum for 100 water molecules (Fig. 3).

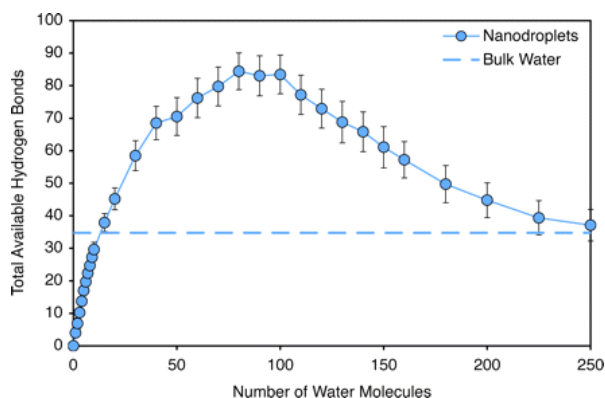


Figure 3. Saykally’s model of total available hydrogen bond numbers

Table 1 shows the distribution of numbers of water molecules according to the energy of hydrogen bonds per each 100 water molecules in the bulk volume of Anolyte, Catholyte and control water (data for Catholyte and Anolyte are taken from Table 2

[27]). These distributions are due to the spatial arrangement of H₂O molecules with equal energies of hydrogen bonds. This is a feasible mathematical model for explaining the behavior of Anolyte and Catholyte, by showing how their H₂O molecules are grouped in clusters.

In particular, at hydrogen bonds energy $E = -0.1387$ eV, we estimated that the biggest stable clusters can consist of 21 water molecules for Catholyte and of 22 water molecules for Anolyte at $E = -0.1212$ eV. Their hydrogen bonds were measured last during evaporation of water according to the wetting angle. Such preliminary considerations lead to a realistic model of stable clusters with 20 water molecules in both cases, arranged in dodecahedral structures shown in Fig. 4.

Their size can be estimated using the diameter of circumscribed spheres, provided that nuclei of oxygen atoms are located at dodecahedron vertices.

It should be pointed out that, according to Ignatov [30, 31], the local maximum at -0.1212 eV in Anolyte is related to anti-inflammatory effects, while the local maximum -0.1387 eV in Catholyte is related to inhibition of tumor cells development on molecular level [2, 23].

Measured values of pH and ORP, as well as derived values of cluster numbers and average energy of hydrogen bonds for Catholyte, Anolyte and control water are shown in Table 2.

Table 1. Values of pH, ORP, number of clusters and average energy of hydrogen bonds for Catholyte, Anolyte and control water.

Parameter	Catholyte	Anolyte	Control water
pH	9.5	3.5	6.7
ORP	- 400 mV	+ 800 mV	+170 mV
Number of clusters	11	11	15
Average number of molecules per cluster	9	9	6.7
Average energy of hydrogen bonds $\langle E \rangle$	-0.1251 (eV)	+0.1144 (eV)	-0.1191(eV)

Table 2. Distribution of numbers of water molecules according to the energy of hydrogen bonds

-E(eV)	Catholyte	Anolyte	Control water	-E(eV)	Catholyte	Anolyte	Control water
0.0912	0	0	0	0.1162	9	7	8
0.0937	0	15	9	0.1187	0	7	7
0.0962	0	0	5	0.1212	9	22	0
0.0987	0	11	0	0.1237	0	7	7
0.1012	0	0	6	0.1262	9	0	0
0.1037	9	0	8	0.1287	9	4	5
0.1062	4	0	0	0.1312	13	4	9
0.1087	4	15	11	0.1337	0	0	7
0.1112	4	0	6	0.1362	9	4	3
0.1137	0	0	7	0.1387	21	4	2

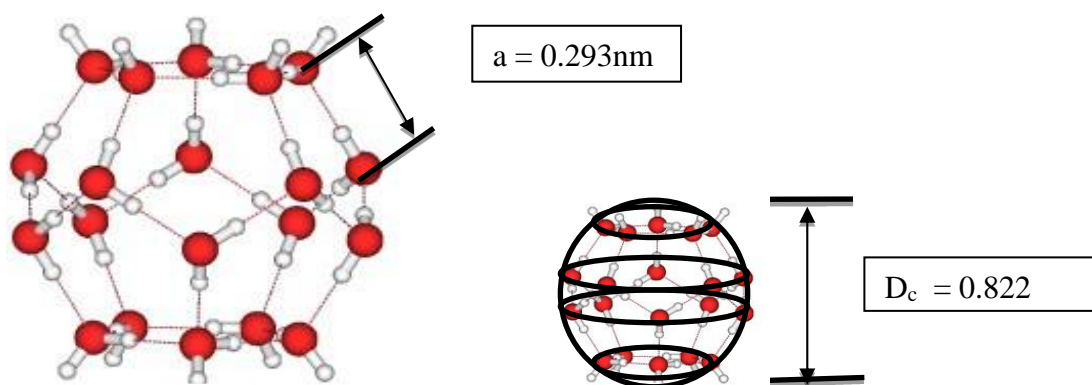


Figure 4. Dodecahedral cluster structure with 20 water molecules and the diameter of its circumscribed sphere

Average energy $\langle E \rangle$ of hydrogen bonds is calculated as:

$$\langle E \rangle = - \frac{1}{n} \sum_i^k n_i E_i$$

where n is the total number of molecules according to the adopted model, k is the number of clusters, n_i is the number of molecules in the i -th cluster, and E_i is the energy of hydrogen bonds corresponding to the i -th cluster.

DISCUSSION

The obtained data show a decreased number of clusters and an increased number of molecules per cluster in Catholyte and Anolyte solutions compared to control water, i.e. Catholyte and Anolyte are better structured. However, it is interesting to note that despite of this the average energy of the Anolyte is lower than the energy of the control sample which means that clusters in Anolyte are predominantly formed in the lower part of the energy spectrum, while the clusters of non-processed water are more spread. The increased average energy of Catholyte could be related to its stimulating immune system effect and inhibition of tumor growth due to energy adding, while the decreased energy of Anolyte could be connected to its biocidal effect due to energy sucking out. Also, many researchers from different countries have registered quite interesting and inexplicable Catholyte effects in stock-breeding and plant-growing, consisting in faster growing of plants and animals without additional nutrition, and increased production from them. Also, it was noticed that drying up flowers started refreshing in Catholyte. Possible explanation could be related to the higher energy in the Catholyte.

Increased pH and decreased ORP values of Catholyte compared to Anolyte do not affect cluster numbers and average number of molecules per

cluster in both fractions, but relate to the changes in average energy of hydrogen bonds. It is interesting to investigate this relationship at different values of pH and ORP which could be a subject of a future work. This may elucidate their inexplicable behavior in different periods of time. While in Catholyte they change rapidly and reach the values of the non-processed water in a couple of days, in Anolyte they remain quite stable during a few months regardless of the preservation conditions (decrease of less than 10% after half a year).

Information about the number of clusters and molecules could help to better understand the effect of nascent hydrogen and oxygen stabilization in electrochemically activated water – Catholyte and Anolyte, respectively. This process could relate to generation of clusters with a specific number of molecules in a specific configuration. Promising results about the nascent hydrogen in Catholyte have already been obtained [32]. However, to be fully verified, such a hypothesis requires further investigations.

CONCLUSIONS

The evaluation of hydrogen bonds energy of electrochemically activated fractions of water – Catholyte and Anolyte, and a sample of non-processed water, was carried out using the methods NES and DNES. The obtained spectra of energies allowed estimation of the possible number of clusters and the number of molecules in them. Also, the AVERAGE energy of each of the three samples was calculated.

The energetic position of the clusters with the maximal number of molecules corresponds to already establish physiological effects of Catholyte and Anolyte, respectively. This allows connecting these effects to the changed cluster structure and

redistributed energy between both fractions, which gives a new point of view on the processes of electrochemical activation of water and its useful effects.

An idea of adding/extracting energy to/from living things seems to be working, since some phenomena could be easily explained on its base.

The obtained results could be used for further investigation of the processes of electrochemical activation of water that are still quite unclear, including the stability of nascent hydrogen and oxygen in it [32].

REFERENCES

1. P. Gramatikov, A. Antonov, M. Gramatikova, *Fresenius Journal of Analytical Chemistry*, **343** (1), 134 (1992).
2. A. Yu, P. Carlson, G. Pollack, *The European Physical Journal Special Topics*, **223**, 947 (2014).
3. A. V. Nemuhin, *Russian Chemical Journal*, **40**(2), 48 (1996).
4. J. Smith, C. Cappa, K. Wilson, R. Cohen, P. Geisler, R. Saykally, *PNAS*, **102** (40), 14171 (2005).
5. O. Loboda, V. Goncharuk, *Chemical Physics Letters*, **484** (4-6), 144 (2010).
6. F. Keutsch, R. Saykally, *PNAS*, **98** (19), 10530 (2011).
7. M. Chaplin. The water molecule, Liquid water, hydrogen bonds and water networks, in: Water the Forgotten Biological Molecule, D. Le Brihan, H. Fukuyama (eds.), Pan Stanford Publishing Pte. Ltd, Singapore, 2011, p. 3.
8. I. Ignatov, O. V. Mosin, *Journal of Mathematical Theory and Modeling*, **3** (11), 72 (2013).
9. L. Shu, L. Jegatheesan, V. Jegatheesan, C. Q. Li, *Fluid Phase Equilibria*, **511** (2020).
10. I. Ignatov, G. Gluhchev, S. Karadzhov, I. Yaneva, N. Valcheva, G. Dinkov, T. Popova, T. Petrova, D. Mehandjiev, I. Akszonovich, *Physical Science International Journal*, **24** (1), 46 (2020).
11. K. Liu, R. Fellers, M. Viant, R. McLaughlin, M. Brown, R. Saykally, *Review of Scientific Instruments*, **67** (2), (1998).
12. K. Liu, J. Cruzan, R. Saykally, *Science*, **271** (5251), 929 (1996).
13. P. D'Angelo, A. Zitolo, G. Aquilanti, V. Migliorati, *The Journal of Physical Chemistry B*, **117** (41), 12516 (2013).
14. V. Turov, T. Krupskaya, V. Barvinchenko, N. Lipkovska, M. Kartel, L. Suvorova, *Colloids and Surfaces A: Physicochemical and Engineering Aspects*, **499**, 97 (2016).
15. K. Yoshida, S. Ishuda, T. Yamaguchi, *Molecular Physics*, **117** (22), 3297 (2019).
16. T. Choi, K. Jordan, *The Journal of Physical Chemistry B*, **114** (20), 6932 (2010).
17. V. F. Prilutsky, V. M. Bakhir, *All Russian Scientific Research and Experimental Institute of Medical Engineering (VNIIMT)*, *UDK 621.357*: **541.13** (1997).
18. M. Henry, J. Chambron, *Water*, **5**(4), 2094 (2013)
19. C.-N. Cha, E.-K. Park, J.-Y. Jung, C.-Y. Yoo, S. Kim. H.-J. Lee, *Korean Journal of Veterinary Service*, **39** (2), 117 (2016).
20. S. Shirahata, T. Hamasaki, K. Teruya, *Trends in Food Science and Technology*, **23**, 124 (2012).
21. G. Gluhchev, I. Ignatov, S. Karadzhov, G. Miloshev, N. Ivanov, O. V. Mosin, *European Journal of Molecular Biotechnology*, **7**(1), 12 (2015).
22. T. P. Popova, T. Petrova, S. Karadzhov, *Int. J. Curr. Microbiol. Appl. Sci.*, **5** (1), 624 (2016).
23. R. Toshkova, E. Zvetkova, I. Ignatov, G. Gluhchev, *Bulgarian Journal of Public Health*, **11** (3), 60 (2019).
24. A. Antonov, Research of the non-equilibrium processes in the area in allocated systems, Dissertation thesis for degree "Doctor of physical sciences", Blagoevgrad, 1995.
25. S. Todorov, A. Damianova, I. Sivriev, A. Antonov, T. Galabova, *Comptes Rendus de l'Academie Bulgare des Sciences*, **61** (5251), 857 (2008).
26. W. Luck, D. Schioberg, U. Siemann, *J. Chem. Soc., Faraday*, **76**, 136 (1980).
27. I. Ignatov, G. Gluhchev, S. Karadzhov, I. Yaneva, N. Valcheva, G. Dinkov, T. Popova, T. Petrova, D. Mehandjiev, I. Akszonovich, *Physical Science International Journal*, **24** (1), 46 (2020).
28. Sh. Zhou, L. Wang, *Chemical Science*, **33** (2019).
29. B. E. Rocher-Casterline, L. C. Ch'ng, A. K. Mollner, H. Reisler, *Journal of Chemical Physics*, **115**, 6903 (2011).
30. I. Ignatov, S. Karadzhov, A. Atanasov, E. Ivanova, O. V. Mosin, *Journal of Health, Medicine and Nursing*, **8**, 1 (2014).
31. I. Ignatov, S. Karadzhov, G. Gluhchev, I. Yakimov, *Bulgarian Journal of Public Health*, **10** (4), 63 (2018).
32. P. Vassileva, D. Voykova, I. Ignatov, S. Karadzhov, G. Gluhchev, N. Ivanov, D. Mehandjiev, *Journal of Medicine, Physiology and Biophysics*, **52**, 7 (2019).

Prediction of ^1H -NMR shifts with Ambit-HNMR softwareN. T. Kochev^{1*}, S. H. Tsoneva¹, M. V. Frenkeva¹, N. G. Jeliaskova²¹University of Plovdiv "Paisii Hilendarski", Department of Analytical Chemistry and Computer Chemistry,
24 Tzar Asen Str., 4000 Plovdiv, Bulgaria²Ideaconsult Ltd, 4 A Kanchev Str., Sofia 1000, Bulgaria

Received: February 11, 2021; Revised: March 29, 2021

We present a new software tool, Ambit-HNMR, for automatic calculation of ^1H -NMR chemical shifts of organic compounds. Ambit-HNMR is an open-source software, written in Java, part of the chemoinformatics platform Ambit. Ambit-HNMR software uses a CDK-based molecule presentation as a connection table where H atoms are implicitly treated. The chemical shifts for each H atom are calculated by means of so called H-atom environments which describe different types of resonance protons. Each H-atom environment consists of: (1) a SMARTS pattern defining a molecular substructure; (2) base H shift, Z_0 ; (3) atom positions $\{a_1, a_2, \dots, a_n\}$ and topological distances within the structure; (4) a set of possible substituents $\{S_1, S_2, \dots, S_k\}$ described by SMARTS patterns and (5) associated chemical shifts, $\{Z_{i1}, Z_{i2}, \dots, Z_{in}\}$, for each substituent, S_i , respectively for all atoms' positions of the H-atom environment ($i=1, 2, \dots, k$). For an input target structure, all H-atom environments and all substituents $\{S_{r1}, S_{r2}, \dots, S_{rn}\}$ attached to the corresponding environment positions are identified by means of substructure searching. The chemical shift for a given H atom is calculated by means of an additive scheme: $Z_0 + Z_{r,1} + Z_{r,2} + \dots + Z_{r,n}$. We created a knowledge base with H-atom environments for the main classes of organic compounds based on the additive schemes of Pretsch. Additionally, Ambit-HNMR calculates the H atom multiplicity using the information of molecule classes of equivalent atoms. Ambit-HNMR module is available for download as a Java library or as a command line application (<https://doi.org/10.5281/zenodo.4506289>). Software example usage and test results are presented.

Keywords: Ambit, ^1H -NMR, chemical shifts, additive scheme, software, open-source.

INTRODUCTION

NMR spectroscopy is a powerful analytical technique for structure elucidation and study of molecular structure and is the preferred method due to its advantages: non-destructive, fast, with minimal sample preparation. ^1H -NMR interpretation can be assisted or automated by computer-based calculation of chemical shifts. The chemical shifts for different types of H atoms can be estimated with the help of additivity rules using the shift values of increments for substituents in various positions.

The spectra interpretation, namely full assignment of chemical shifts, is a pivotal task in analyzing any molecular structures and one that can be achieved by a number of means: (1) a library search that matches an unknown spectrum to one contained in the particular library; (2) application of additive rules for each considered atom and comparing the calculated to the experimental chemical shifts or (3) using dedicated ^1H -NMR predictor software.

A number of such software tools exist, both open-source and commercial. NMRShiftDB is a NMR predictor which can be used free of cost *via* web interface. The site credits the work of Binev and Aires-de-Sousa, developers of the FCT-Universidade NOVA de Lisboa tool [1]. The

SPINUS (Structure-based Predictions In Nuclear magnetic resonance Spectroscopy) program, <http://neural.dq.fct.unl.pt/spinus/>, uses a feed-forward neural network (FFNN) system and a series of empirical proton descriptors. The prediction is then corrected by Associative Neural Network (ASNN) on the basis of observed errors for the k nearest neighbors.

Some of the most widely used commercial softwares in general, ChemDraw [2] and Chem3D, developed by PerkinElmer and part of the ChemOffice package [3], also offer ^1H -NMR and ^{13}C -NMR predictions as a fully integrated tool in their versions. Their main advantage is the easy to use interface, but the quality of the estimated shifts can sometimes be challenged. Both programs use GAMESS software for performing general quantum chemistry calculations, such as HF, DFT, GVB and others, that can then be subject to correlation correction [4]. ACD/Labs' NMR Predictor software [5] takes it further by allowing the prediction of solvent specific spectra for both ^1H -NMR and ^{13}C -NMR, predicting multiplicity, recognizing tautomers prior to predicting and even simulating exact experimental conditions (frequency, line width). A very useful feature is the user's access to the complete calculation protocol. ACD/Labs' NMR Predictor uses HOSE code and neural net algorithms

* To whom all correspondence should be sent:

E-mail: nick@uni-plovdiv.net

to predict the chemical shifts while taking into account stereochemistry. It also provides with the ability to train predictions with new experimental data [5].

Another commercially available software is NMRPredict [6] distributed by Modgraph Consultants Ltd. It predicts chemical shifts using two prediction methods: (1) additivity rules developed by Pretsch, as well as several stages of approximation and (2) predictions based on functional groups parametrized by Abraham and then automatically chooses “best” proton prediction. In the first case, chemical shifts are predicted for each proton with available additivity rules by assigning substructures following a hierarchical list. Thus the base value of the final shift is given. If there are no available data for a given substructure, e.g. ring system, it is to be disassembled so that a base value can be approximated. For each substructure the remaining part of the molecule is treated as substituents that contribute to the final shift by adding their increments to the base value. In the second case each functional group is identified and treated separately using CHARGE [7] by first generating 3D conformers and then predicting the proton spectra for all of them giving a weighted average spectrum.

Mestrelab offers a similar product, Mestrenova [8], using HOSE code, that starts at a given hydrogen/carbon atom and tries to find the environment one bond away in its database. This process is repeated for every hydrogen/carbon atom until reaching the boundary of the molecule or coming across environment not represented in the database. Gaussian software [9] has by far the widest array of modeling methods including HF, DFT, MP2, CCSD, etc. The accuracy of the predicted shifts depends on the basis set used and the application of adequate solvent correction. An alternative free option is ORCA *ab initio* program with its variety of methods ranging from semi-empirical methods and density functional theory to correlated single- and multi-reference wave-function based methods [10]. Downloading and running these or other similar programs may be viewed as necessary, especially when using your own confidential data, but with the growing numbers and popularity of Web browser applications it may not be actually requisite. AMBIT chemoinformatics platform is one such open-source platform for predictive models [11].

We present Ambit-HNMR, a new software tool for automatic calculation of ¹H-NMR chemical shifts of organic compounds. It is an open-source tool and is part of the chemoinformatics module

Ambit-GCM [12] which facilitates interoperability with external software packages, thus making running predictions and sharing online resources much easier without installing any additional software. We have implemented a knowledge base with H-atom environments for the main classes of hydrocarbon compounds based on the additive schemes of Pretsch [13] and the knowledge base is being updated with new rules.

Software characteristics and architecture

Ambit-HNMR is implemented in object-oriented programming language Java. It is an open-source, OS independent software module distributed under LGPL license [14]. Ambit-HNMR is an extension of Ambit-GCM [12] (previously developed by us software tool) part of the chemoinformatics platform Ambit [11] where it is integrated as a separate module (`ambit2-groupcontribution.nmr`). Ambit integration allows the usage of plenty of chemoinformatics functionalities from other Ambit modules [11] developed by our group, as well as utilities from external open-source resources. The full capability of Ambit-HNMR could be accessed when using it as a Java library with APIs. In addition, we have developed a console tool, Ambit-HNMR, available as a command-line interface (CLI) Java application, as well as a GUI application. Detailed information about Ambit software platform, as well as the source code of the Java library (`ambit2-groupcontribution.nmr`) is available at <http://ambit.sourceforge.net/>. Executable *.jar files with the latest Ambit-HNMR knowledge base can be downloaded from the Zenodo repository: <https://doi.org/10.5281/zenodo.4506289>. Ambit-HNMR implementation includes the following basic components:

(1) *Data input/output utilities.* Ambit modules are developed on top of the CDK (Chemistry Development Kit) [15, 16] library. CDK provides input and output for basic structure presentation formats thus Ambit-HNMR supports most popular chemoinformatics formats: SMILES [17, 18] and InChI [19] linear notations, CML chemical format, MOL/SDF file formats, CSV and TXT file formats. The software configuration can be done from command-line interface options. The variety of supported file formats allows easy integration of our tool with other software applications.

(2) *Structural information management.* The basic structure management in Ambit-HNMR is developed on top of CDK classes. The chemical structure representation relies on the CDK Java class `AtomContainer` which implements the molecular connection table (CT).

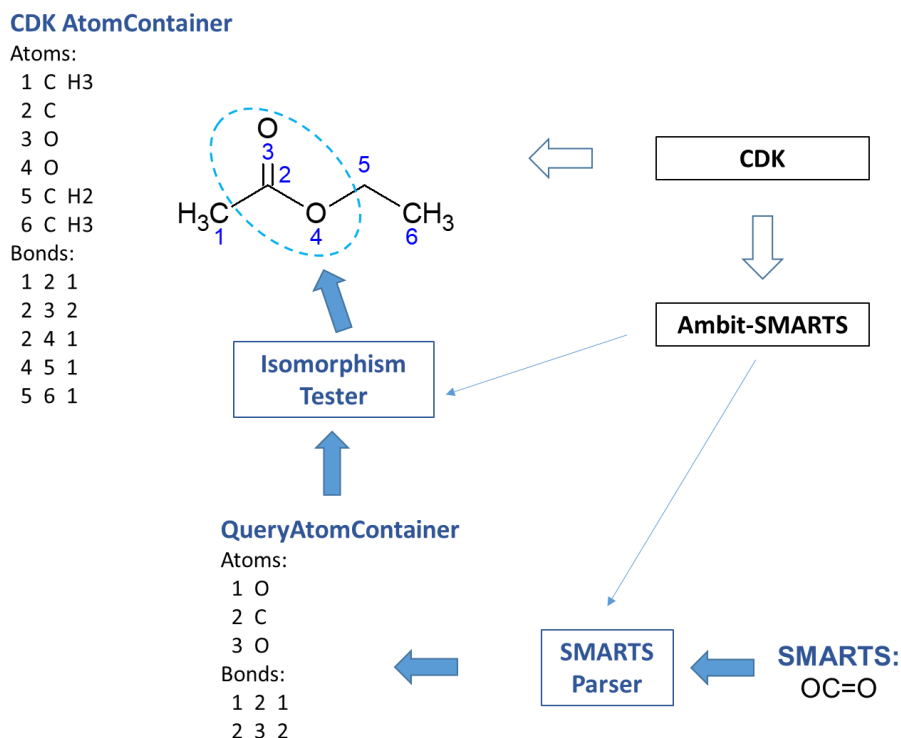


Figure 1. Chemical object management in Ambit-HNMR

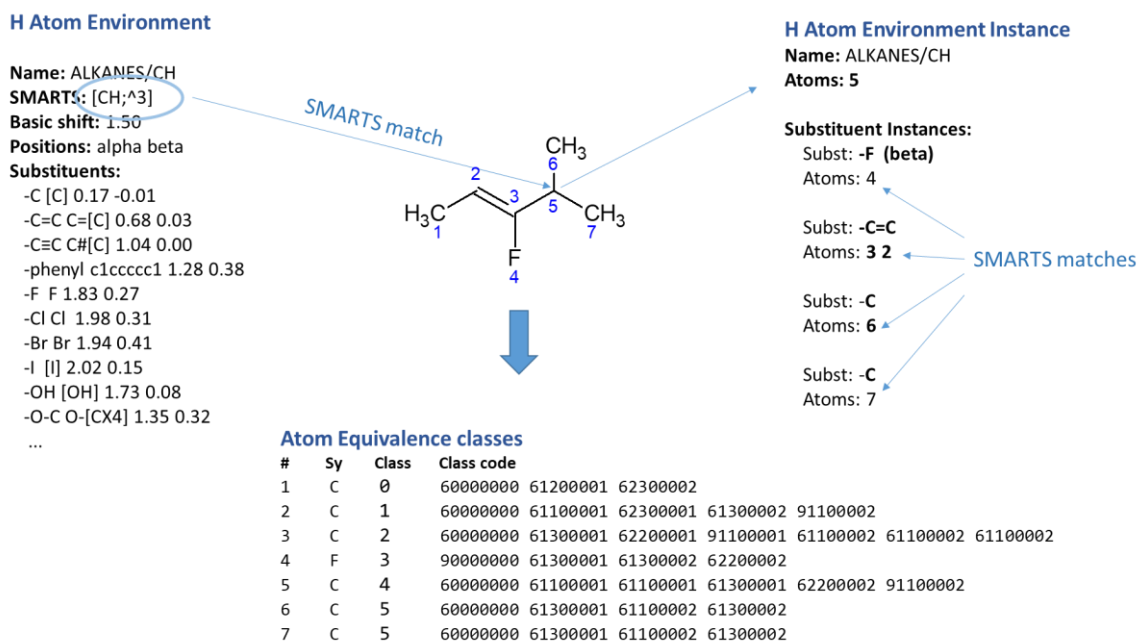


Figure 2. H Atom Environment and atom equivalence classes management

Ambit-HNMR processing requires handling of the two basic types of chemical objects shown in Figure 1: chemical structures (basic CT) and chemical fragments or substructures (represented by means of specialized CT) plus dedicated data structures for H atom environments and classes of equivalent atoms. H atom environment management includes multiple SMARTS linear notations used for definition of the heavy atoms associated to a given

proton (H atom) and SMARTS definitions for corresponding substituents (see Figure 2). Atom equivalency within a molecule is determined by Ambit-SMARTS [20] module using specially designed atomic codes also illustrated in Figure 2.

(3) *Substructure searching.* Ambit-SMARTS [20] module is also developed by our group and implements the key substructure search algorithm (see in Figure 1, Isomorphism Tester is applied to

match OC=O against the target molecule). It is used for finding all matchings (called instances) of a given H atom environment and the matchings (instances) of substituents. Figure 2 illustrates the H atom environment for tertiary sp³ carbon atoms and matching of an instance at atom 5 with four substituents at three alpha and one beta positions at atoms {3, 2}, {6}, {7} and {4} respectively.

(4) *Chemical shift calculation.* This is the most crucial software component. The calculation of H-shifts is based on exhaustive searching of all possible instances of all H atom environments from the Ambit-HNMR knowledge base described in following sections.

HNMR shifts calculation algorithm

Ambit-HNMR algorithm for H-shift calculation includes the following main stages:

(i) loading of a knowledge base with H-shift rules formalized as H atom environments (see example in Figure 2 and format syntax example below);

(ii) target molecule input using one of the popular molecular formats (e.g. SMILES linear notation) and conversion into the internal CDK representation;

(iii) calculation of topological distance matrix of the target molecule;

(iv) finding of all groups mappings for all SMARTS definitions from the knowledge base;

(v) determination of all H Atom Environment Instances;

(vi) finding all substituents for each H Atom Environment Instance;

(vii) calculation of H-shifts using additive schemes;

(viii) determination of atom equivalence classes;

(ix) calculation of multiplicity.

The basic workflow of Ambit-HNMR is summarized in Figure 3 illustrating stages (i), (ii), (v), (vi) and (vii).

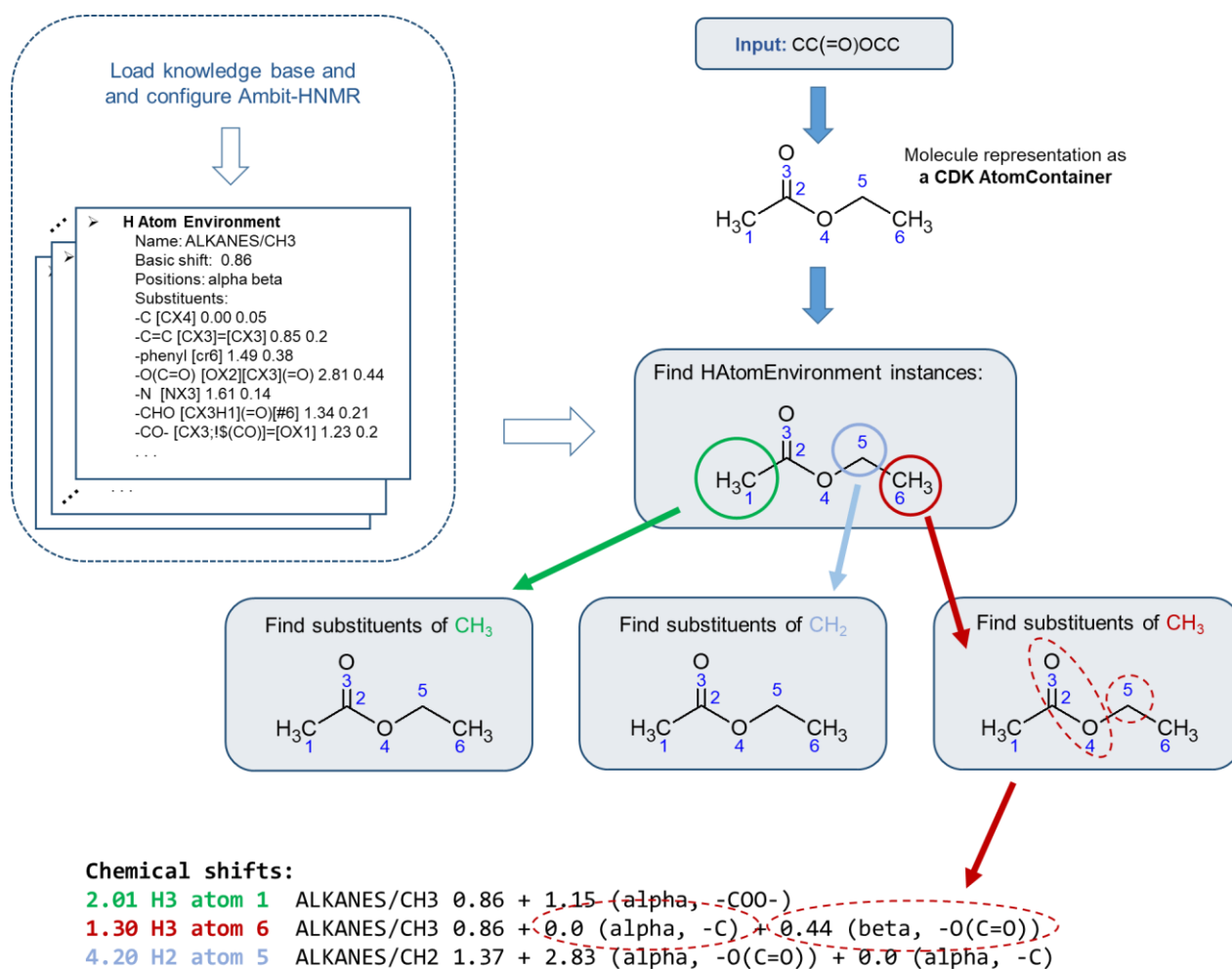


Figure 3. Flow chart of the Ambit-HNMR H-shift calculation algorithm

Ambit-HNMR knowledge base is configurable and stored in an external text file. It contains additivity rules described as H atom environments with the following syntax:

```

$$H_ATOM_ENVIRONMENT=
$$NAME= ALKANES/CH2
$$SMARTS= [CH2;^3]
$$BASIC_SHIFT= 1.37
$$IMPLICIT_H_ATOMS_NUMBER= 2
$$SHIFT_DESIGNATIONS= alpha beta
$$SHIFT_ASSOCIATION
SUBSTITUENT_POSITION =
$$SUBSTITUENT_POS_ATOM_INDICES= 1 1
$$POSITION_DISTANCES = 1 2
$$SUBST= -C [C] 0.00 -0.04
$$SUBST= -C=C C=[C] 0.63 0.00
$$SUBST= -C#C C#[C] 0.70 0.13
$$SUBST= -phenyl c1ccccc1 1.22 0.29
    
```

H-atom environment consists of: (1) a SMARTS pattern defining a molecular substructure or an atom used for topological identification of the H atoms (e.g. [CH2;^3] defines a secondary carbon); (2) base H shift, Z_0 (key word BASIC_SHIFT) is the value used for unsubstituted substructure/atom; (3) possible substituents atom positions $\{a_1, a_2, \dots, a_n\}$, given as atomic indices within the defined substructure and associated topological distances from the substituents to the substructure; (4) a set of possible substituents, $\{S_1, S_2, \dots, S_k\}$ described by SMARTS patterns; and (5) associated chemical shift contributions, $\{Z_{i1}, Z_{i2}, \dots, Z_{in}\}$, for each substituent, S_i , respectively for all atoms' positions and distances of the H-atom environment ($i=1, 2, \dots, k$). Points (4) and (5) are given by means of a list of substituents with additive contributions for the chemical shifts described in the form:

```

$$SUBST= <name> <smarts>
<contribution 1> <contribution 2> ...
    
```

For the example given above, row “\$\$SUBST= -phenyl c1ccccc1 1.22 0.29” means that benzene ring will have additive contribution 1.22 ppm in alpha position and 0.29 ppm in beta position added to the basic chemical shift, 1.37 ppm of H atoms of CH₂ carbon atom.

The default knowledge base contains rules based on the Pretsch additives schemes. The piece of default knowledge base shown above describes an additive scheme for secondary sp³ carbon atom, CH₂, in the form:

$$\delta[\text{CH}_2] = 1.37 + \sum_i Z_{\alpha_i} + \sum_j Z_{\beta_j},$$

where Z_{α_i} are the contributions to the chemical shift of the substituents at alpha position (topological

distance 1 from the carbon atom) and respectively Z_{β_j} are the contributions of substituents at beta positions (topological distance 2). The default knowledge base includes H atom environments for basic atoms of hydrocarbon chains (e.g. carbons with different numbers of H atoms and different hybridizations) with a rich set of possible substituents: alkyl, phenyl, halogens, chemical groups and fragments containing oxygen, nitrogen and sulfur atoms, etc. The full list of the possible substituents can be seen in the knowledge base file available at the Zenodo repository (<https://doi.org/10.5281/zenodo.4506289>). In the current knowledge base version, we have also included H atom environments for mono substituted benzene rings and pyridines. The user can enrich the knowledge base with additional rules or, if needed, completely replace the default rules. *Ambit-HNMR* calculates multiplicity for all predicted H-shifts using the atom equivalence classes. Atom equivalence is determined by calculating so called atomic codes which include information about a predefined number of topological layers of an atom (default number of layers is 2). The atomic code is composed of pieces of information for each atom in each topological environment encoding: atom element, bond type, topological degree, charge, isotope and topological layer number (i.e. distance from the center atom). All atoms having the same atomic code are considered as equivalent. For example, in Figure 2, atoms 6 and 7 (the terminal methyl groups) have exactly the same atomic code, “60000000 61300001 61100002 61300002”, hence they are identified as equivalent atoms (class 5). The multiplicity of a particular H atom is determined by counting the number of H atoms, $\{n_1, n_2, \dots, n_s\}$, for each neighbor atom equivalence class. Then multiplicity is $(n_1+1) \times (n_2+1) \times \dots \times (n_s+1)$.

RESULTS AND DISCUSSION

Ambit-HNMR software usage

Ambit-HNMR software version 1.2 is available as a command-line interface application with following options:

```

HNMR shifts predict
usage:
ambit2.groupcontribution.cli.HNMRPredictCli
-c, --config <config>           HNMR
database configuration file
-e, --explanation <on|off>      Switch
on/off H shift calculation
    
```

explanation. Default explanation is on

```
-h,--help           Shows this help info
-i,--input <input>  Input molecule file
-l,--log <on|off>   Switch on/off log printing. Default log is off
-p,--multiplicity <on|off> Switch on/off H multiplicity feature.
```

Default is on

```
-s,--smiles <smiles>  Input molecule smiles
```

Example of Ambit-HNMR application for the molecule of ethyl acetate inputted as a SMILES notation from the command line is given below:

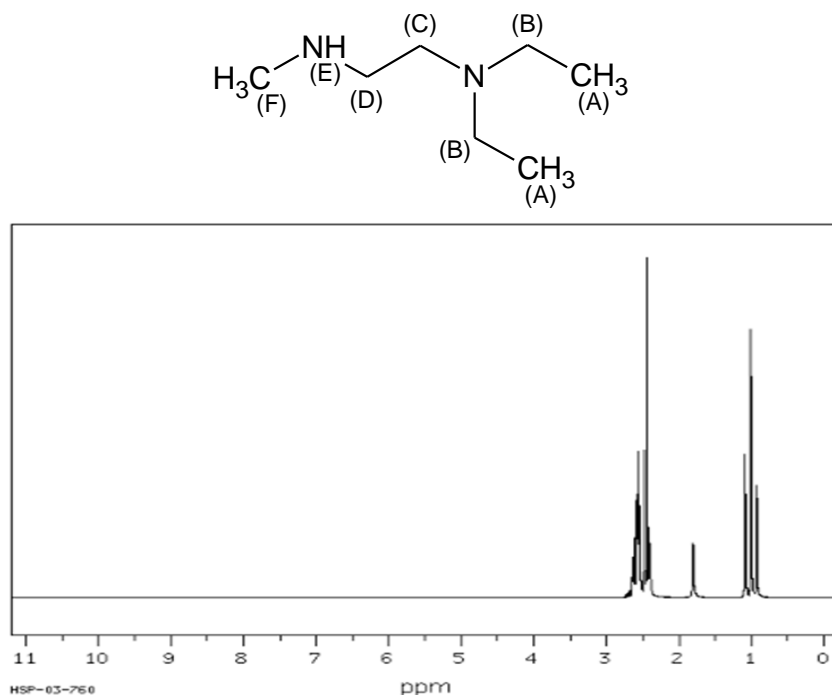
```
java -jar ambit-hnmr.jar -s CC(=O)OCC
```

Using default HNMR database: ./hnmr-knowledgebase.txt

```
Input smiles: CC(=O)OCC
2.01 H3 atom 1 multiplicity 3
ALKANES/CH3 0.86 + 1.15 (alpha, -COO-)
1.30 H3 atom 6 multiplicity 3
ALKANES/CH3 0.86 + 0.0 (alpha, -C_alkyl) + 0.44 (beta, -O(C=O))
4.20 H2 atom 5 multiplicity 4
ALKANES/CH2 1.37 + 2.83 (alpha, -O(C=O)) + 0.0 (alpha, -C_alkyl)
```

Ambit-HNMR can also be applied in a batch mode for a set of molecules specified by means of *-i* option. Executable *.jar file, detailed documentation and more usage examples are available at: <https://doi.org/10.5281/zenodo.4506289>.

We present a comparison of Ambit-HNMR calculated chemical shifts with the experimental ¹H-NMR spectra of organic compounds from the public database SDBS [21] and four different software tools for prediction of ¹H-NMR chemical shifts.



Protons	Shifts ¹ H-NMR spectrum (ppm)	Ambit-HNMR (ppm)	Diff (ppm)	Chem Draw (ppm)	Diff. (ppm)	nmrdb.org (ppm)	Diff. (ppm)	Mestrenova (ppm)	Diff. (ppm)	Gaussian (ppm)	Diff. (ppm)
H(A, A)	1.01	1.00	0.01	1.00	0.01	0.96	0.05	1.09	0.08	1.01	0.00
H(B, B)	2.51	2.61	0.10	2.40	0.11	2.63	0.12	2.45	0.06	2.10	0.41
H(C)	2.54	2.83	0.29	2.48	0.06	2.83	0.29	2.59	0.05	2.07	0.47
H(D)	2.62	2.87	0.25	2.65	0.03	2.8	0.18	2.72	0.10	2.35	0.27
H(E)	1.81							1.14	0.67	0.43	1.38
H(F)	2.47	2.52	0.05	2.47	0.00	2.31	0.16	2.56	0.09	2.34	0.13

Figure 4. H-NMR spectrum of N,N-diethyl-N'-methylethylenediamine and comparison with the calculated shifts from Ambit-HNMR, ChemDraw, nmrdb.org, Mestrenova and Gaussian

Figure 4 shows the structure and spectrum of N, N-diethyl-N'-methylethylenediamine (measurement conditions: 89.56 MHz, solution 0.04 ml: 0.5 ml CDCl_3) and comparison of the experimental and predicted chemical shifts. The structure of N,N-diethyl-N'-methylethylenediamine is non-cyclic with secondary and tertiary amino groups in it. There are two methyl (A) and two methylene (B) groups that are chemically equivalent with each other that have the same chemical shifts in the $^1\text{H-NMR}$ spectrum. According to the positions of the H atoms in the structure of the compound and the calculated

distances it is seen in the spectrum that there is a certain number of multiplets. The comparison between spectrum and *Ambit-HNMR* shows that chemical shift differences are with deviation less than 0.3 ppm. Figure 4 also shows a comparison between chemical shifts predicted with *Mestrenova* and *Gaussian* and their difference in ppm from the experimental $^1\text{H NMR}$ spectrum. *Mestrenova* simulates full spectra with their chemical shifts and multiplicity with the help of the *NMRPredict Desktop*.

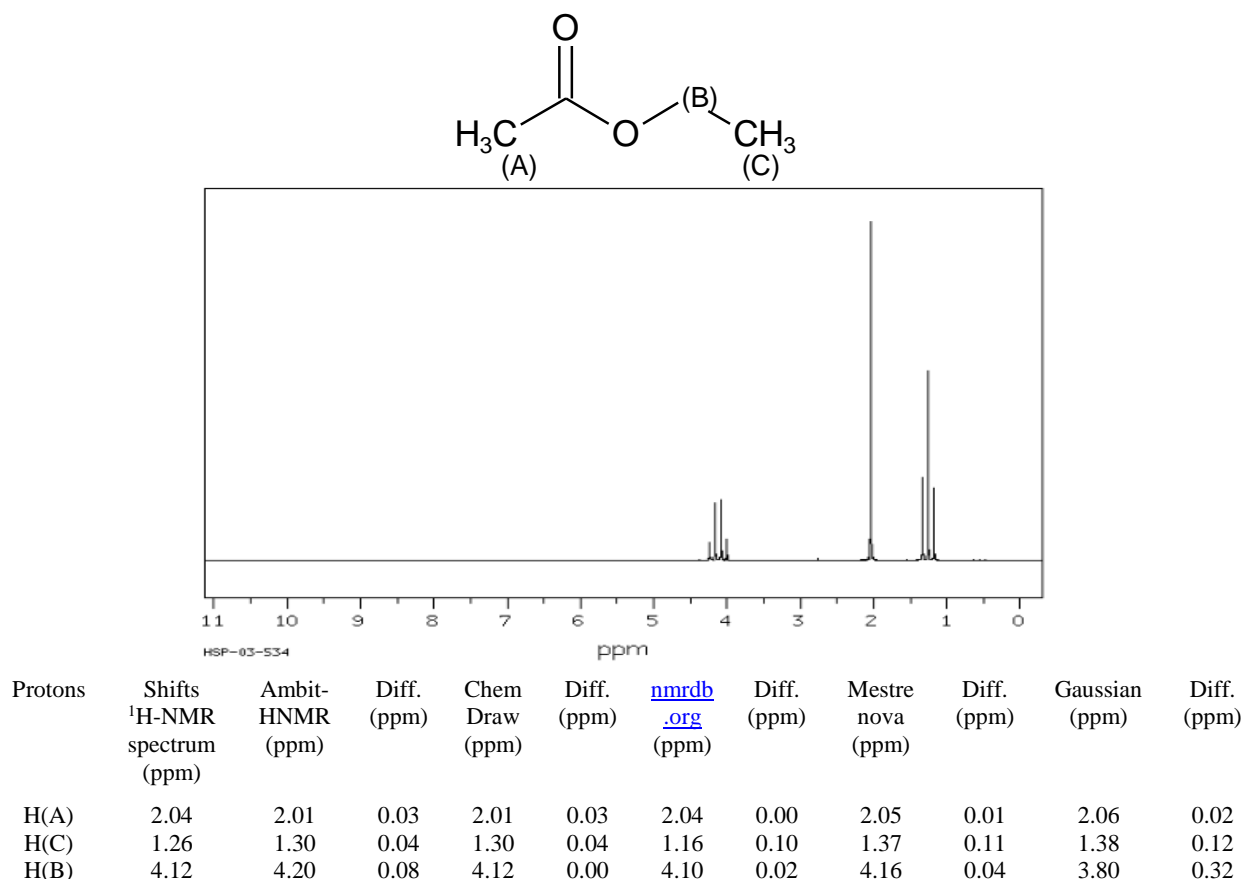


Figure 5. HNMR spectrum of ethyl acetate and comparison with the calculated shifts from *Ambit-HNMR*, *ChemDraw*, *nmrdb.org*, *Mestrenova* and *Gaussian*

The calculations were quick and fairly accurate for all protons except for the one in the NH group. For the purpose of comparing the capabilities of *Gaussian 98*, Revision A.7, the geometries of all molecules (N,N-diethyl-N'-methylethylenediamine and ethyl acetate and styrene, presented below) were optimized on B3LYP (Becke three-parameter Lee–Yang–Parr) exchange-correlation functional with 6-31g basis set with subsequent calculations carried out on HF with 6-311+g (2d, p) basis set for the ^1H NMR spectra prediction.

The structure, HNMR spectrum and predicted H-shifts of ethyl acetate are shown in Figure 5. The compound has two methyl (A, C) groups that are not

chemically equivalent with each other and have different chemical shifts in the H-NMR spectrum as it is shown in Figure 5. According to the positions of the H atoms in the structure and the topological distances, the spectrum has a triplet and a quadruplet, which are correctly calculated by *Ambit-HNMR* (see the multiplicity in the console output for the molecule of ethyl acetate shown previously in this section). Chemical shifts comparison shows that the differences are with deviation less than 0.1 ppm.

Figure 6 shows the GUI (graphical use interface) application with the result screen for the molecule of styrene.

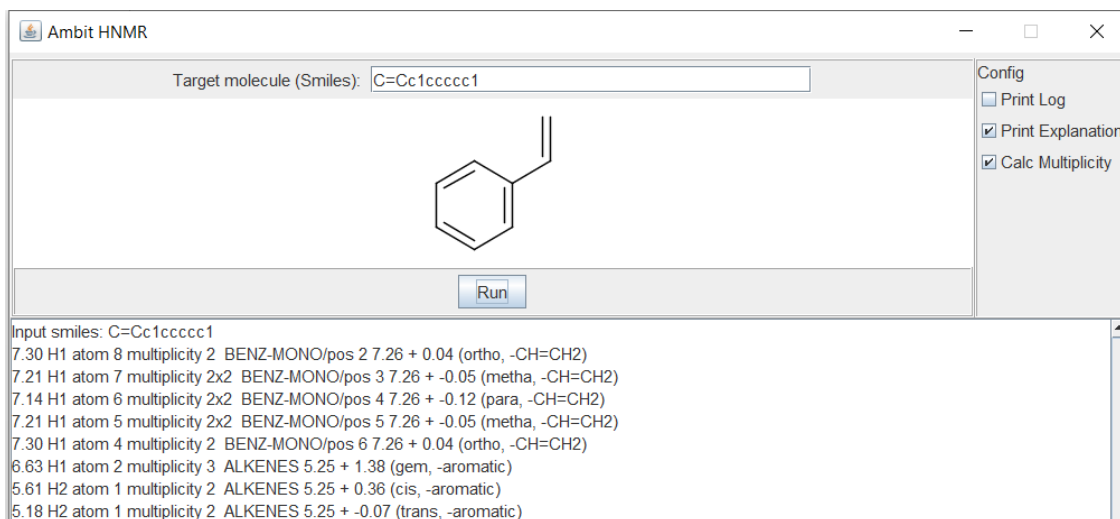


Figure 6. Ambit-HNMR-GUI screen with the calculated shifts for the molecule of styrene.

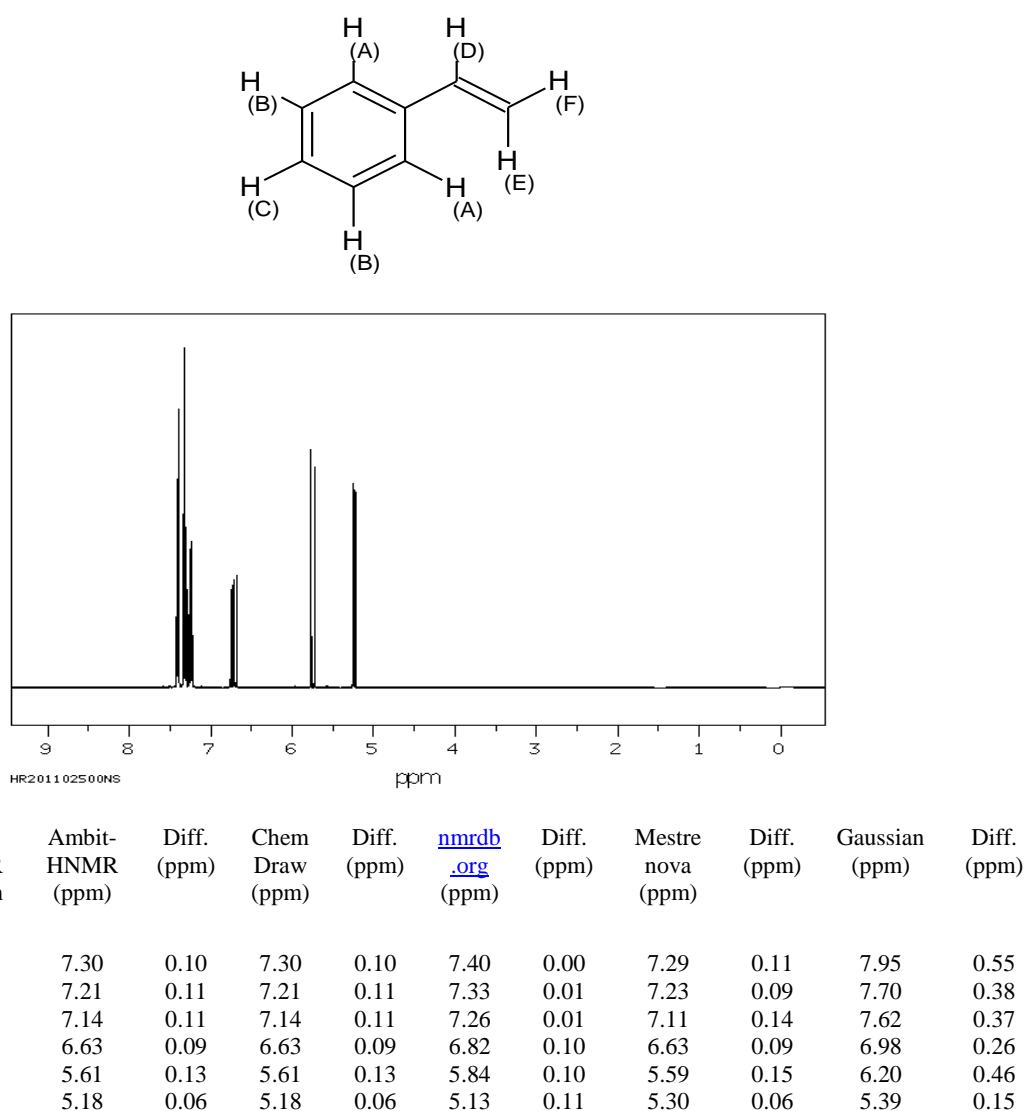


Figure 7. HNMR spectrum of styrene and the calculated shifts from Ambit-HNMR, ChemDraw, nmrdb.org, Mestrenova and Gaussian.

Full comparison of the experimental H-NMR spectrum shifts and the calculated chemical shifts from Ambit-HNMR tool and four other testing

software tools is given in Figure 7. For the molecule of styrene, the average chemical shift difference of Ambit-HNMR is 0.1 ppm. The corresponding

difference averages of the other tools are: ChemDraw - 0.1 ppm, nmrdb.org - 0.55, Mestrenova - 0.11, and Gaussian - 0.36, showing that the Ambit-HNMR performance is comparable with the considered test software tools.

A major challenge of the additive scheme methods is the problems of missing fragments. i.e. the cases of organic compounds containing fragments which have no additive contributions in the knowledge base (e.g. the missing secondary amine in Figure 4). That is why continuous improvement of the knowledge base is required. In this context, one advantage of the Ambit-HNMR software is that the knowledge base rules are not hardly encoded but are configurable and externally stored so that the user can update, enrich or replace the default rules.

CONCLUSION

A new software tool, Ambit-HNMR, for prediction of ¹H-NMR chemical shifts is developed. The software uses a configurable knowledge base, which can be modified by the user. The command line application can be applied for organic compounds inputted directly from the console as SMILES linear notations or in a batch mode for an input molecular file. Software performance is demonstrated with examples. Ambit-HNMR source code is available at <http://ambit.sourceforge.net/> and the software can be easily integrated as part of a bigger scientific workflow. Executable jar file with the latest software version and knowledge base, additional usage examples and full documentation is present at: <https://doi.org/10.5281/zenodo.4506289>. Our team is continuing the improvement of default knowledge base rules and new releases will be available at the Zenodo repository.

Acknowledgement: This work was supported by the University of Plovdiv Scientific Fund under project MU19-HF-003.

REFERENCES

1. Y. Binev, M. M. Marques, J. Aires-de-Sousa, *J. Chem. Inf. Model.*, **47**(6), 2089 (2007).
2. N. Mills, *J. Am. Chem. Soc.*, **128** (41), 13649 (2006).
3. A. Zielesny, *J. Chem. Inf. Model.*, **45** (5), 1474 (2005).
4. M. W. Schmidt, K. K. Baldrige, J. A. Boatz, S. T. Elbert, M. S. Gordon, J. H. Jensen, S. Koseki, N. Matsunaga, K.A. Nguyen, S. Su, T. L. Windus, M. Dupuis, J. A. Montgomery, *J. Comput. Chem.*, **14**, 1347 (1993).
5. E. E. Kwan, *J. Chem. Inf. Model.*, **52** (7), 1898 (2012).
6. J. Abraham. M. Mobli, Modelling ¹H NMR Spectra of Organic Compounds: Theory, Applications and NMR Prediction Software, John Wiley & Sons Ltd, 2008.
7. R. J. Abraham, M. Mobli, *Spectroscopy Europe*, **16**(4), (2004).
8. T. Claridge, M. Nova, *J. Chem. Inf. Model.*, **49**(4), 1136 (2009).
9. M. J. Frisch, G. W. Trucks, H. B. Schlegel, G. E. Scuseria, M. A. Robb, J. R. Cheeseman, G. Scalmani, V. Barone, G. A. Petersson, H. Nakatsuji, X. Li, M. Caricato, A. V. Marenich, J. Bloino, B. G. Janesko, R. Gomperts, B. Mennucci, H. P. Hratchian, J. V. Ortiz, A. F. Izmaylov, J. L. Sonnenberg, D. Williams-Young, F. Ding, F. Lipparini, F. Egidi, J. Goings, B. Peng, A. Petrone, T. Henderson, D. Ranasinghe, V. G. Zakrzewski, J. Gao, N. Rega, G. Zheng, W. Liang, M. Hada, M. Ehara, K. Toyota, R. Fukuda, J. Hasegawa, M. Ishida, T. Nakajima, Y. Honda, O. Kitao, H. Nakai, T. Vreven, K. Throssell, J. A. Montgomery, Jr., J. E. Peralta, F. Ogliaro, M. J. Bearpark, J. J. Heyd, E. N. Brothers, K. N. Kudin, V. N. Staroverov, T. A. Keith, R. Kobayashi, J. Normand, K. Raghavachari, A. P. Rendell, J. C. Burant, S. S. Iyengar, J. Tomasi, M. Cossi, J. M. Millam, M. Klene, C. Adamo, R. Cammi, J. W. Ochterski, R. L. Martin, K. Morokuma, O. Farkas, J. B. Foresman, D. J. Fox, Gaussian 16, Revision C.01, Gaussian, Inc., Wallingford, CT, 2016.
10. F. Neese, F. Wennmohs, U. Becker, C. Riplinger, *J. Chem. Phys.* **152**, 224108 (2020).
11. N. Jeliazkova, V. Jeliazkov, *J. Cheminform.*, **3**(1), 18 (2011).
12. N. Kochev, V. Paskaleva, O. Pukalov, N. Jeliazkova, *Molecular Informatics*, **38**(8-9), e1800138 (2019).
13. E. Pretsch, P. Buhlmann, M. Badertscher, Structure Determination of Organic Compounds, Springer, 2009.
14. LGPL, GNU Lesser General Public License, <https://www.gnu.org/licenses/lgpl-3.0.en.html>, last accessed on 04.02.2021.
15. E. L. Willighagen, J. W. Mayfield, J. Alvarsson, A. Berg, L. Carlsson, N. Jeliazkova, S. Kuhn, T. Pluskal, M. Rojas-Chertó, O. Spjuth, G. Tarrance, C. T. Evelo, R. Guha, C. Steinbeck, *J. Cheminform.*, **9**(1), 33 (2017).
16. Chemistry Development Kit, <https://cdk.github.io/> accessed 04.02.2021.
17. D. Weininger, *J. Chem. Inf. Comput. Sci.*, **28**(1), 31 1988.
18. <https://www.daylight.com/dayhtml/doc/theory/theory.smiles>, Daylight Theory: SMILES, accessed 04.02.2021.
19. S. Heller, A. McNaught, I. Pletnev, S. Stein, D. Tchekhovskoi, *J. Cheminform.*, **7**(23), 2 (2015).
20. N. Jeliazkova, N. Kochev, *Molecular Informatics*, **30**(8), 707 (2011).
21. Spectral Database for Organic Compounds, SDBS, https://sdb.sdb.aist.go.jp/sdb/cgi-bin/cre_index.cgi, accessed 04.02.2021.

Preparation and thermal stability evaluation of GNP/CNT doped poly(lactic acid) and high-density polyethylene nanocomposites

V. F. Georgiev*

Institute of Catalysis, Bulgarian Academy of Sciences, Sofia 1113, Bulgaria
Institute of Mechanics, Bulgarian Academy of Sciences, Sofia 1113, Bulgaria

Received: February 11, 2021; Revised: March 16, 2021

Melt mixing was used to obtain two series of composite materials based on poly(lactic acid) (PLA) and high-density polyethylene, reinforced with 1.5% graphene nanoplatelets and multi-walled carbon nanotubes. Analysis methods such as infrared spectroscopy, wide-angle X-ray diffraction, and scanning electron microscopy were used to determine the materials' structural and chemical properties. Studies showed no intercalation or interaction of the polymer molecules with the fillers, approved by the absence of shift of the main diffraction peak of the fillers appearing at 26.3°, and the same wavenumbers of pure high-density polyethylene absorption bands compared to these of the composite materials. The differential scanning calorimetry showed that the addition of fillers did not affect the glass transition temperature and the melting temperature of PLA but had a slight effect on melt crystallization which increased by 7° for the 1.5% GNP/1.5% CNT/PLA sample. Thermal stability was improved for the 1.5% GNP/PLA material as the decomposition onset temperature increased by 2 °C, determined by thermogravimetric analysis. High-density polyethylene-based composite materials with the presence of graphene nanoplatelets are characterized by a 2 °C increase in melting point and an 8 °C increase in the onset of decomposition temperature for the bifiller ones. It can be attributed to the high aspect ratio of GNPs that served as a barrier and then prevented the emission of gaseous molecules during thermal degradation.

Keywords: thermal stability, composite, graphene.

INTRODUCTION

The increased interest to polymer stability research has been discussed in a great number of papers [1-3]. High-density polyethylene (HDPE) and poly(lactic acid) (PLA) possess a combination of favorable physical properties, chemical resistance, and economic characteristics that make them incredibly versatile and suitable in various applications. Poly(lactic acid) is well known as a biodegradable polymeric material produced from agricultural resources that has recently found application in fused deposition modeling [4]. At the same time, HDPE has found widespread use in products designed for outdoor applications where degradation from sunlight and other weathering conditions becomes an essential factor. For the polymers successfully to withstand degradative oxidation accelerated by high processing and service temperatures, as well as outdoor weathering conditions, a stabilizer or combination of stabilizers must be incorporated. Due to the controlled combination of the components, new materials with distinct properties are obtained from the individual components [5]. The typical fillers used in polymeric composites are graphene [6, 7] graphene oxide [8-10], silica [11, 12], and carbon nanotubes (CNTs) [13, 14]. Carbon nanotubes and graphene exhibit unique and unusual electrical, mechanical and thermal properties making them attractive fillers for

reinforcing polymers to form functional and structural composite materials with high performance. The effective enhancement of mechanical, electrical and thermal properties by adding CNTs and graphene nanoplatelets (GNPs) in the polymer composites has been approved [15-17]. The main factor that could control the composite's potential properties is the degree of dispersion, percolation threshold, and interfacial interactions. Better dispersion and stronger interfacial interaction of both 2D and 1D fillers in the matrix polymer resulted in higher values of thermal conductivity, due to stronger suppressing of phonon scattering [18]. Unfortunately, carbon nanofillers with large surfaces and proportions are usually poorly dispersed in organic solvents and polymers. Neat carbon nanotubes CNTs and GNPs tend to form bundles or agglomerates due to the strong van der Waals interaction between them, which leads to weak interphase interactions between nanotubes and polymer matrix. The dispersion of carbon fillers in solvents and polymers can be improved by mechanical mixing and chemical functionalization. The melt mixing process employs high temperature and intense shear forces to disperse nanofillers in the molten polymer using rotating screws of an extruder. Its simplicity and low cost make it a promising technique for producing polymer composites with improved properties.

* To whom all correspondence should be sent:

E-mail: vlado@ic.bas.bg

In this paper we report the effect of multiwalled carbon nanotubes and graphene nanoplatelets addition into poly(lactic acid) and high-density polyethylene on the resulting nanocomposites' thermal stability. Hot melt mixing was applied for fabrication of composites with filler content of 1.5%wt. denoted as 1.5% GNP/PLA, 1.5% CNT/PLA, 1.5% GNP/HDPE, 1.5% CNT/HDPE, 1.5% GNP/1.5% CNT/PLA and 1.5% GNP/1.5% CNT/HDPE.

MATERIALS AND METHODS

Materials

The poly(lactic acid) (PLA-3D850) with MFR 7–9 g/10 min (210 °C, 2.16 kg), peak melt temperature 165–180 °C, and glass transition temperature 60–65 °C was supplied by Nature Works, USA. Industrial GNPs and industrial grade OH-functionalized multiwall carbon nanotubes adopted as nanofillers were supplied from Times Nano, China. GNPs purity is 90% and true density is 2.2 g/cm³, whereas CNT purity is 95%, true density is 2.1 g/cm³ and its OH-content is 2.48%.

Preparation of Nanocomposites

Two series of nanocomposite materials based on PLA and HDPE with GNPs and CNTs content of 1% wt. were produced by melt mixing using the twin-screw extruder, COLLIN Teach-Line ZK25T, with a screw speed of 40 rpm for PLA composites and Thermo Scientific twin screw extruder at 100 rpm and temperatures of 170–180 °C. Before mixing with the fillers, the PLA pellets were ground and then used as a powder for 9% masterbatch preparation while the HDPE mixture was prepared by wrapping technique in a ball mill for two hours at a speed of 70 rpm. Then, the formulations with lower filler contents of 1.5 wt. % were prepared by diluting the respective masterbatches with neat PLA and HDPE through a second extrusion run.

Experimental Methods

Wide-angle X-ray diffraction (WAXD) was employed for characterization of the samples. The measurements were performed on a DX-1000 X-ray diffractometer (Dandong Fangyuan Instrument Co., Ltd., Dandong, Liaoning Province, China) employing copper line focus X-ray tube producing K α radiation by a generator operating at 45 kV and 25 mA. The diffraction patterns were taken in the range from 5° to 70° at a 1°/min rate. The specimens being analyzed were powders for the fillers, GNPs and MWCNTs and pellets for the nanocomposites. The data from WAXD were processed using MDI Jade software capable of analyzing the crystal

structure of materials. The KBr technique was applied for recording the FT-IR spectra in the scanning range from 4000 to 400 cm⁻¹ using a Nicolet 6700 spectrometer. The morphology and structures were visualized using scanning electron microscopy (SEM) on a Quanta 250 instrument (FEI Co. Ltd, USA).

DSC Q20 (TA Instruments), was used for the DSC measurements. The test sample with a weight of ~10 mg was placed in an aluminum pan and hermetically sealed in order to prevent gas emissions into the instrument or in the environment. Tests were performed in two cycles (one heating and one cooling scan). During the heating cycle, the temperature was raised from room temperature to 200 °C, with a ramp of 10 °C/min, and held for 1 min. Afterward, the temperature was lowered from 200 °C to 20 °C in order to register the DSC curve through the cooling cycle. Upon these conditions, the glass transition temperature (T_g), melt crystallization temperature (T_c) and melting peak temperature (T_m) were determined from the heating and cooling DSC curves. TGA Q50 (TA Instruments) was used for the thermo-gravimetric analysis (TGA) measurements. It was done to assess the composite thermal stability defined by the characteristic decomposition temperatures of the samples. The trials were performed in nitrogen atmosphere by heating a 10 mg specimen from room temperature to 600 °C in an aluminium pan, with a heating step of 10 °C/min.

RESULTS AND DISCUSSION

WAXD analysis was used to characterize the nanocomposites as it provided accurate information on the phase composition and crystallinity of the test materials. Fig. 1 shows pure graphene nanoplatelets characterized by a main reflection (002) peak at $2\theta = 26.35^\circ$, sharper than that of the carbon nanotubes' peak at $2\theta = 26^\circ$ from the corresponding diffraction plane, indicating a more crystalline structure of GNPs. The shifting of the nanotubes diffraction peak (002) to lower degrees ($2\theta = 26^\circ$) means a larger interplanar spacing between the lattice fringes which could be assigned to higher functionalization of the CNTs in comparison to GNPs. By applying the Scherer equation, $L_{hkl} = k \lambda / (\beta_{hkl} \cos \theta)$, where: β is the FWHM of the reflection (in radians) located at 2θ , with an appropriate value of the shape factor of $k = 0.9$, it was found that the GNPs powders have a stack thickness of about 18 nm. The addition of carbonaceous fillers does not increase the PLA's crystallinity for both series, which is evident from the comparison of the WAXD spectra of the pure polymer and those of the composite materials (Fig. 1). It is seen that there is no appearing of a sharp peak

in the composites' patterns containing 1.5% CNTs or GNPs at around 16.8 degrees [19], which would be due to crystal areas' formation, but only the wide halo characteristic of amorphous PLA with a steepest point at $2\theta = 15.5^\circ$ remains unchanged.

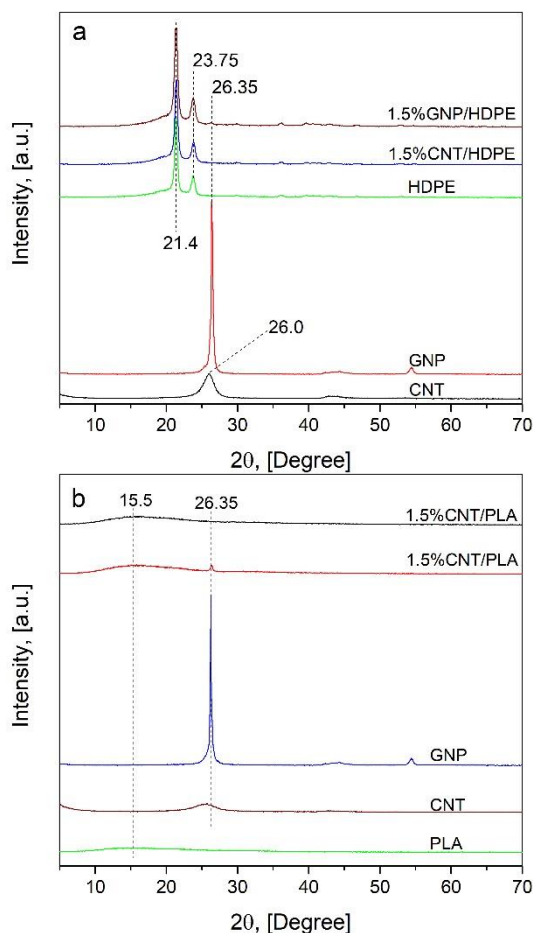


Fig. 1. X-ray diffraction spectra of (a) series of HDPE and (b) series of PLA.

This is attributed to the insufficient fillers nucleation effect to cause a significant increase in the crystallinity of the PLA. In the spectra of 1.5% CNT/PLA and 1.5% CNT/HDPE, no additional peaks were found due to filler presence in the mixed materials, probably because of its small particle size and homogeneous dispersion in the volume of the polymer. Characteristic of the composite materials spectra containing 1.5% GNP is the appearance of a peak at 26.35° which is attributed to pure GNPs. Since a shift of this peak was not observed, it can be concluded that no intercalation of polymer molecules occurred in the stacks of graphene particles.

SEM micrographs of 1.5% GNP/HDPE and 1.5% GNP/PLA are shown in Fig. 2. The images show that the filler particles are distributed in the polymer's volume with any spatial orientation for 1.5% GNP/HDPE. It was reported [20] that GNPs have intrinsic properties to orient predominantly in-plane that impedes the practical application, which was

observed for 1.5% GNP/PLA. Such anisotropy mostly affects the thermal conductivity (the thermal conductivity of in-plane is much higher than that of through-plane) in GNP-based thermal composites.

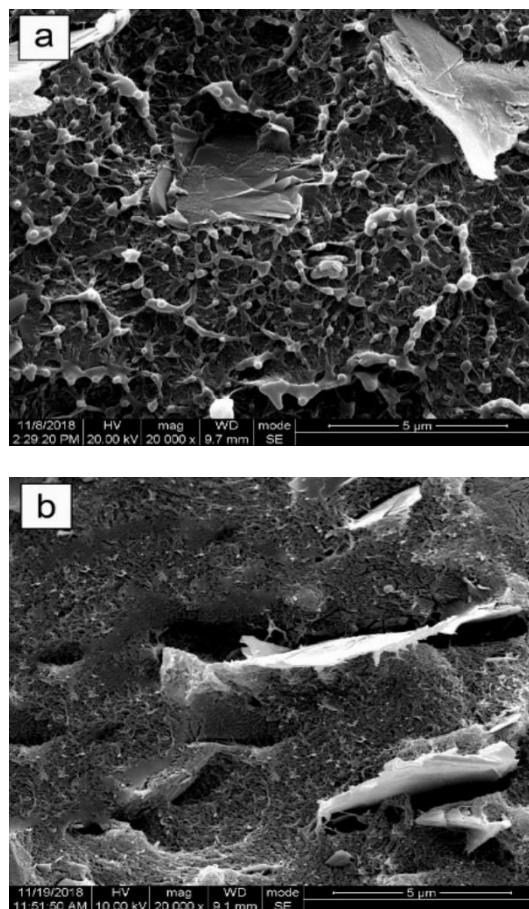


Fig. 2. SEM micrographs of (a) 1.5% GNP/HDPE and (b) 1.5% GNP/PLA samples.

To monitor the functionalization of GNPs and CNTs, FTIR analysis was conducted. Fig. 3 presents the FT-IR spectra in the scanning range from 4000 to 400 cm^{-1} for the tested samples of both series.

It is seen that characteristic bands appearing in the spectra of both fillers are at the same wavenumbers, which means that they possess the same functional groups. In the IR-spectra of GNP and CNT bands corresponding to stretching vibrations of the CH group at 2850 cm^{-1} and 2920 cm^{-1} are observed. The bands at 3436 cm^{-1} , 1630 cm^{-1} , 1110 cm^{-1} and 1052 cm^{-1} are due to stretching vibrations of the $-\text{OH}$, $\text{C}=\text{O}$ and $\text{C}-\text{O}$ adsorption groups, respectively. By comparing the spectra of the pure fillers and those of the composite materials, it is noticed that the peaks characteristic for the fillers are not present in the spectrum of the composite materials, probably due to their low concentration. Analysis of the IR spectra also shows no changes in the frequency of the vibration bands assigned to pure PLA or HDPE compared to the corresponding ones in the spectra of

the composite materials containing 1.5% filler. It follows that no new bonds are formed between the filler and the polymer, such as hydrogen bonding or strong van der Waals forces due to a direct interaction of a specified group and the adsorption site of the liquid matrix.

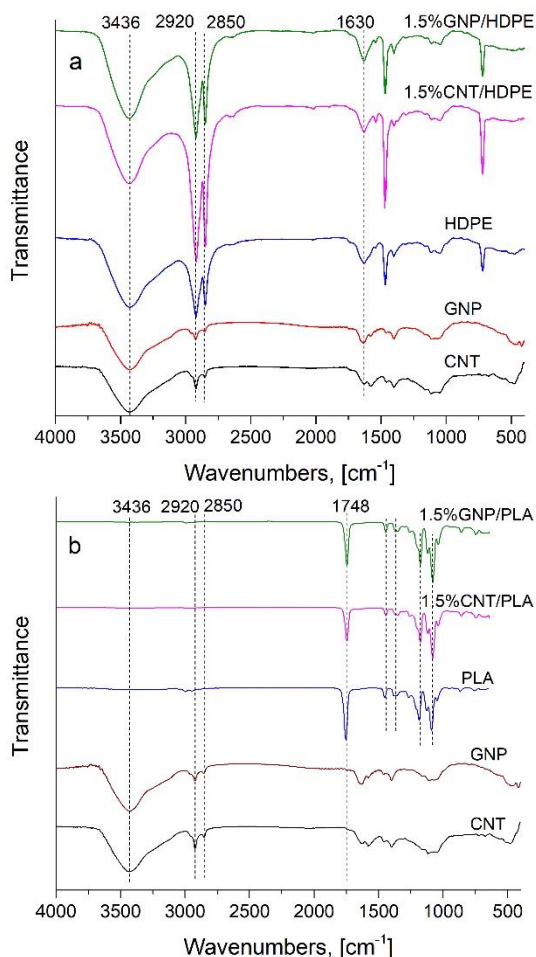


Fig. 3. IR spectra of (a) series of HDPE and (b) series of PLA.

Figures 4a and 4b present results from the DSC analysis of monofiller (GNP/PLA, CNT/PLA) and bifiller (GNP/CNT/PLA) nanocomposites containing 1.5 wt% carbon particles. The glass transition temperature for all nanocomposites is around 64-65°C. The transition region in which an amorphous glassy polymer changes from its glassy state into a rubber-like state is important because dramatic changes in the polymer's physical properties are observed during this transition. These changes are completely reversible as the transition from a glassy into a rubbery state. When considering the T_g of reinforced polymers, it should be had in mind that it depends mainly on the interaction of the polymer with the filler that impedes the relaxation [21]. The T_g increases, and

vice versa if there is a repulsion between the filler and the polymer chain.

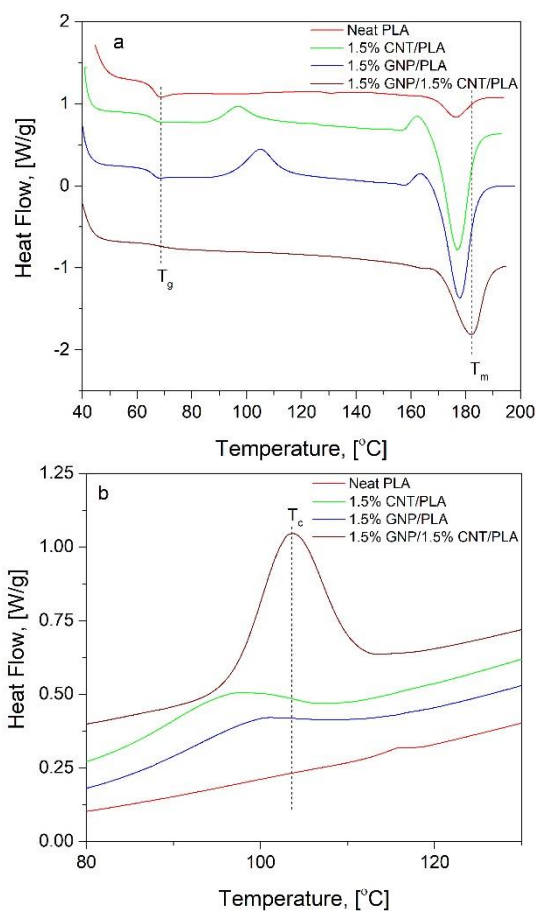


Fig. 4. DSC thermograms of (a) PLA, 1.5wt% GNP/PLA, 1.5wt% MWCNT/PLA and mixed composites during heating cycle and (b) during cooling cycle.

The similar T_g values of the samples (Table 1) imply either that the amount of nanofiller is insufficient to influence the composite T_g temperature or there is no strong interaction of attraction or repulsion between the carbon nanoparticles and the polymer.

Table 1. Thermal properties of samples after melting at 200° for pure PLA, monofiller (GNP/PLA, CNT/PLA) and bifiller (GNP/CNT/PLA) nanocomposites.

Samples	T_g [°C]	T_m [°C]	T_c [°C]
PLA	63.8	178.4	96.2
1.5% CNT/PLA	65.0	177.1	97.8
1.5% GNP/PLA	64.5	177.8	99.7
1.5% GNP/1.5% CNT/PLA	64.9	178.9	103.4

The melting temperatures for all tested PLA composite samples are in the range of 177-179 °C, and it can be concluded that the presence of nanofillers does not lead to a change compared to that of the pure PLA. Since the addition of fillers to the polymer does not increase the crystallinity of the

resulting materials, which is confirmed by XRD, in this case the melting temperature does not change significantly, because when considering semi-crystalline polymers, crystallinity directly affects the melting temperature. It can be seen from Fig. 4b that the melt crystallization of 1.5% GNP/CNT/PLA is higher by around 7°C compared to the pure PLA ($T_c = 96.2^\circ\text{C}$). This observation is attributed to the synergic effect of GNPs and CNTs promoting the crystallization through heterogeneous nucleation during the cooling run.

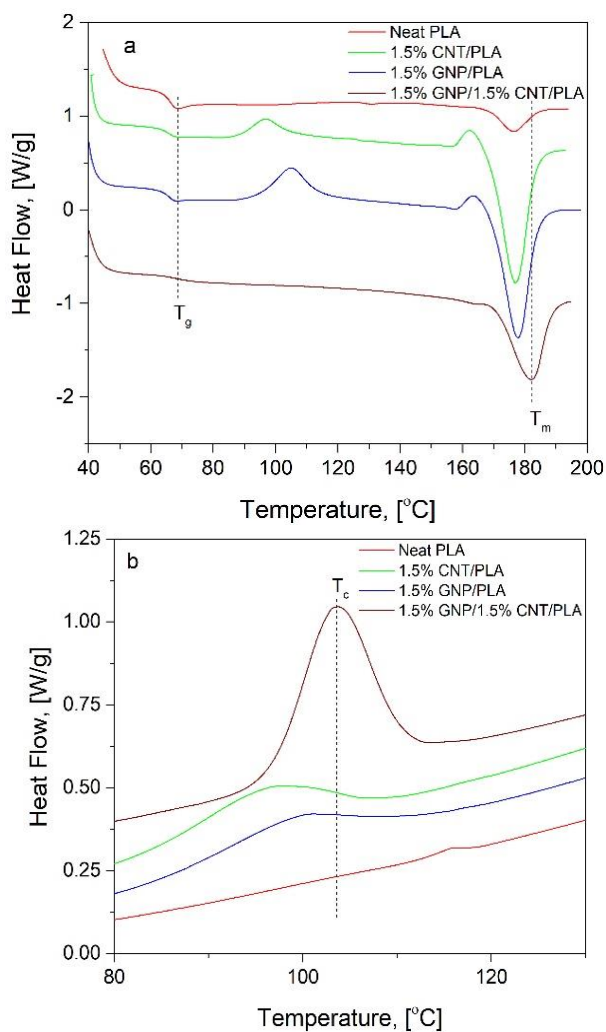


Fig. 4. DSC thermograms of (a) PLA, 1.5wt% GNP/PLA, 1.5wt% MWCNT/PLA and mixed composites during heating cycle and (b) during cooling cycle.

Figures 5a and 5b present DSC analysis results of pure HDPE and nanocomposites on its base containing 1.5wt% of carbon fillers. The melting temperature (T_m) of composite materials is by about 3 degrees higher than that of the pure polymer.

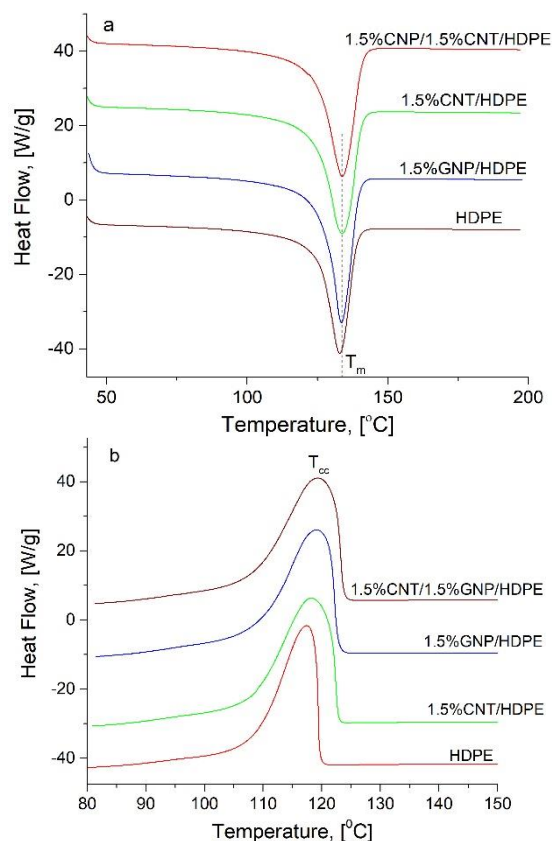


Fig. 5. DSC thermograms of (a) HDPE, 1.5wt% GNP/HDPE, 1.5wt% MWCNT/HDPE and mixed composites during heating cycle and (b) during cooling cycle of the same specimens.

The T_m of the pure HDPE is 132.1°C , while those of the composites 1.5% GNP/HDPE and 1.5% GNP/1.5% CNT/HDPE are around 134°C (Table 2). The melt crystallization slightly increases with adding fillers as for pure polymer, $T_c = 116^\circ\text{C}$, while for the composites, it reaches 119.1°C for 1.5% GNP/HDPE. The shift of the crystallization and melting peaks to higher temperatures is due to an increased crystal size distribution due to nucleation.

Table 2. DSC thermal properties of samples after melting at 200° for monofiller (GNP/HDPE, CNT/HDPE) and bifiller (GNP/CNT/HDPE) nanocomposites.

Samples	T_g [°C]	T_m [°C]	T_c [°C]
HDPE	n/a	132.1	116.0
1.5% CNT/HDPE	n/a	133.7	118.2
1.5% GNP/HDPE	n/a	134.1	119.1
1.5% GNP/1.5% CNT/HDPE	n/a	133.7	118.2

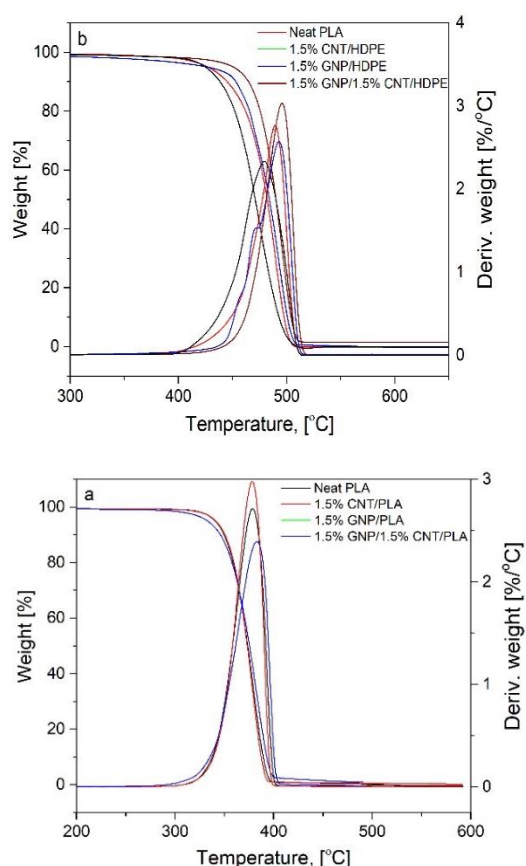


Fig. 6. TGA curves of (a) pure PLA, mono- and bifiller GNP/CNT composites and (b) pure HDPE, 1.5wt% GNP/HDPE, 1.5wt% MWCNT/HDPE, 1.5% GNP/1.5% CNT/HDPE

Thermogravimetry (TG), was applied to monitor mass loss as a function of the temperature at a constant heating rate in order to get a quick impression of the composite materials' thermal stability. The results are presented in Figure 6 and Table 3. Variation in weight percentage of the samples with respect to the temperature was observed. The values summarized in Table 3 represent the TGA characteristics of monofiller and bifiller composites. The thermal degradation process of PLA begins at 310.8 °C (onset temperature according to ASTM E2550) due to intra-molecular

trans-esterification [22]. Afterward, a major degradation proceeds wherein the polymer chain breaks at a high rate in the range from 330 to 395 °C. Concerning the composites, the results apparently disclose that the composite 1.5% GNP/PLA improves the thermal stability of PLA with 2 °C as a result whereof T_{onset} raises to 312.9 °C. A possible explanation for this delayed breakdown can be the assumption that graphene nanoplatelets impede the diffusion of the gaseous low-mass degradation products from the bulk to its surface creating a labyrinth effect [23]. Another important point characterizing the thermal behavior is the pattern of the TGA curve depicting the overall mechanism of degradation. From Fig. 6a is visible that the samples undergo one-step destruction caused by C-C cleavage. Maximum improvement of the thermal degradation stability regarding the highest decomposition rate was observed for bifiller composites. Combining both fillers (GNPs and CNTs) the peak of polymer degradation T_p shifts to the higher temperatures with almost 9°C, due to the better spatial structure in the composite volume suppressing the heat distribution.

From the weight loss plots of HDPE's series (Fig. 6b) is seen that the onset of thermal degradation (T_{onset}) for neat HDPE is 354 °C. T_{onset} increases by about 4 K on the addition of 1.5%GNP and by 8 K on 1.5% addition for both fillers. The composite material containing 1.5% CNT shows the lowest T_{onset} , which is by about 40 K lower than that of the pure polymer. This behavior would suggest that at low CNT loadings, the CNTs accelerate the thermal degradation of HDPE and may be associated with the high thermal conductivity of CNTs and more effective dissipation of thermal energy. It has been proposed that CNTs create a 'barrier effect' by preventing the release of volatiles and decomposed products from the composite material, resulting in the retardation of the thermal decomposition of the composites, but a critical concentration of CNTs is required to enhance the thermal stability of HDPE.

Table 3. Values of T_{onset} , $T_{50\%}$, T_p , for PLA and HDPE monofiller (GNP, CNT) and bifiller (GNP/CNT) composites.

Samples	T_{onset} [°C]	$T_{50\%}$ [°C]	Peak of polymer degradation T_p [°C]
PLA	310.8	381.0	378.6
1.5% CNT/PLA	288.2	375.4	383.1
1.5% GNP/PLA	312.9	373.2	378.2
1.5% GNP/1.5% CNT/PLA	311.1	379.1	386.9
HDPE	354.2	482.1	489.4
1.5% CNT/HDPE	309.5	484.2	479.6
1.5% GNP/HDPE	357.8	471.6	492.7
1.5% GNP/1.5% CNT/HDPE	362.6	490.1	495.7

The thermal stability of HDPE is better demonstrated by examining the derivative weight as a function of temperature. Here, the peak maximum (T_p) is decreased for 1.5% CNT content, suggesting that the onset of thermal degradation of HDPE is shifted to lower temperatures. The unpredictability of HDPE/CNT composites' thermal stability implies that this property is controlled by a combination of factors, including CNT dispersion and distribution, the properties of the thermal conductivity of CNTs, polymer–CNT interactions and polymer crystallinity. The thermal stability increased for the GNP-added composites, attributed to the high aspect ratio of GNP that served as a barrier and then prevented the emission of gaseous molecules during the thermal degradation. Besides, the radical scavenging function of GNP could inhibit the degradation process of the polymer.

CONCLUSION

The thermal properties of two series of mono- and bifiller composite materials based on PLA and HDPE with 1.5% carbonaceous fillers content were evaluated. Test results showed that fillers addition to the base polymer had a small effect on the investigated materials' thermal properties. Glass transition temperature (T_g) for the PLA series was not affected by the presence of fillers, which is explained by the absence of interaction between the individual components of the composite. The same applies to the melting temperature (T_m), which for all samples is in the range of 178–179 °C, but melt crystallization of 1.5% GNP/CNT/PLA is higher by around 7 °C compared to the pure PLA ($T_c = 96.2$ °C). The decomposition's onset temperature (T_{onset}) obtained from the TGA analysis was increased by 2 °C for the 1.5% GNP/PLA sample. As for the HDPE series, the melting temperature of the composite materials is by about 3 °C higher than that of pure polymer and T_{onset} increased by about 4 °C on the addition of 1.5% GNP and by 8 °C on 1.5% addition of both GNP and CNT fillers.

Acknowledgement: The author gratefully acknowledges financial support from Project BG05M2OP001-1.001-0008 National center on mechatronics and clean technologies; the H2020-FET-Graphene Flagship-881603-Graphene Core 3; and the Bulgarian National Science Fund contract KP-06-COST-11 (to CA19118).

REFERENCES

1. A. Hassan, A. Akbari, N. Hing, Ch. T. Ratnam, *Polym Plast Technol Eng*, **51**(5), 473 (2012).

2. D. W. Sauter, M. Taoufik, Ch. Boisson, *Polymers*, **9**, 185 (2017).
3. J. Yu, L. Sun, Ch. Ma, Yu Qiao, H. Yao, *Waste Management*, **48**, 300 (2016).
4. A. Mushtaq, A. Israr, M. Fahad, J. Ahmed, *Bulgarian Chemical Communications*, **52**(1), 29 (2020).
5. I. Plesa, P. V. Notingher, S. Schlögl, Ch. Sumereder, M. Muhr, *Polymers*, **8**, 173 (2013).
6. S. Chatterjee, F. Nafezarefi, N. H. Tai, F. A. Nüesch, B. T. T. Chu, *Carbon*, **50**(15), 5380 (2012).
7. X. Huang, C. Zhi, P. Jiang, *J. Phys. Chem. C*, **116**(44), 23812 (2012).
8. N. Jha, P. Ramesh, E. Bekyarova, M.E. Itkis, R. Haddon, *Adv. Energy Mater.*, **2**(4), 438 (2012).
9. F. Mohandes, M. Salavati-Niasari, *RSC Adv.*, **4**, 25993 (2014).
10. F. Mohandes, M. Salavati-Niasari, *J. Nano Res.*, **16**, 2604 (2014).
11. J. W. Brinke, S. C. Debnath, L. A. Reuvekamp, J. W. Noordermeer, *Compos. Sci. Technol.*, **63**(8), 1165 (2003).
12. W. Kaewsakul, K. Sahakaro, W. K. Dierkes, J. W. Noordermeer, *Rubber Chem. Technol.*, **85**(2), 277 (2012).
13. H.D. Bao, Z.X. Guo, J. Yu, *Polymer*, **49**(17), 3826 (2008).
14. T. Fukushima, A. Kosaka, Y. Yamamoto, T. Aimiya, S. Notazawa, T. Takigawa, T. Inabe, T. Aida, *Adv. Sci.*, **2**(4), 554 (2006).
15. R. Kotsilkova, I. Petrova-Doycheva, D. Menseidov, E. Ivanov, A. Paddubskaya, P. Kuzhir, *Compos. Sci. Technol.*, **181**(8), 107712 (2019).
16. G. Spinelli, P. Lamberti, V. Tucci, R. Kotsilkova, E. Ivanov, D. Menseidov, C. Naddeo, V. Romano, L. Guadagno, R. Adami, D. Meisak, D. Bychanok, P. Kuzhir, *Materials*, **12**(15), 2369 (2019).
17. E. Ivanov, R. Kotsilkova, H. Xia, Y. Chen, R. K. Donato, K. Donato, A. P. Godoy, R. Di Maio, C. Silvestre, S. Cimmino, V. Angelov, *Applied Sciences*, **9**(6), 1209 (2019).
18. R. Kotsilkova, E. Ivanov, V. Georgiev, R. Ivanova, D. Menseidov, T. Batakliiev, V. Angelov, H. Xia, Y. Chen, D. Bychanok, P. Kuzhir, R. Di Maio, C. Silvestre, S. Cimmino, *Polymers*, **12**(6), 1208 (2020).
19. E. Teixeira, A. Campos J.M. Marconcini, T.J. Bondancia, D. Wood, A. Klaczcynski, L. Mattoso, G. Glenn, *RSC Advances*, **4**, 6616 (2014).
20. Q. Li, X. Tian, M. Wu, Y. Li, J. Pan, B. Zhang, Y. Duan, Sh. Wang, Y. Li, *J. Appl. Polym. Sci.*, **138**, e49781 (2020).
21. K. Hagita, H. Morita, *Polymer*, **178**, 121615 (2019).
22. R. B. Valapa, G. Pugazhenthii, V. Katiyar, *RSC Adv.*, **5**, 28410 (2015).
23. I. Armentano, E. Fortunatu, N. Burgos, F. Dominici, F. Luzi, S. Fiori, A. Jimenez, K. Yoon, J. Ahn, S. Kang, J. M. Kenny, *Express Polymer Letters*, **9**(7), 583 (2015).

Instructions about Preparation of Manuscripts

General remarks: Manuscripts are submitted in English by e-mail. The text must be typed on A4 format paper using Times New Roman font size 11, normal character spacing. The manuscript should not exceed 15 pages (about 3500 words), including photographs, tables, drawings, formulae, etc. Authors are requested to use margins of 2 cm on all sides.

Manuscripts should be subdivided into labelled sections, e.g. **Introduction, Experimental, Results and Discussion, etc.** The **title page** comprises headline, author's names and affiliations, abstract and key words. Attention is drawn to the following:

a) **The title** of the manuscript should reflect concisely the purpose and findings of the work. Abbreviations, symbols, chemical formulas, references and footnotes should be avoided. If indispensable, abbreviations and formulas should be given in parentheses immediately after the respective full form.

b) **The author's** first and middle name initials and family name in full should be given, followed by the address (or addresses) of the contributing laboratory (laboratories). **The affiliation** of the author(s) should be listed in detail by numbers (no abbreviations!). The author to whom correspondence and/or inquiries should be sent should be indicated by asterisk (*) with e-mail address.

The abstract should be self-explanatory and intelligible without any references to the text and containing not more than 250 words. It should be followed by key words (not more than six).

References should be numbered sequentially in the order, in which they are cited in the text. The numbers in the text should be enclosed in brackets [2], [5, 6], [9–12], etc., set on the text line. References are to be listed in numerical order on a separate sheet. All references are to be given in Latin letters. The names of the authors are given without inversion. Titles of journals must be abbreviated according to Chemical Abstracts and given in italics, the volume is typed in bold, the initial page is given and the year in parentheses. Attention is drawn to the following conventions: a) The names of all authors of a certain publication should be given. The use of “*et al.*” in the list of references is not acceptable. b) Only the initials of the first and middle names should be given. In the manuscripts, the reference to author(s) of cited works should be made without giving initials, e.g. “Bush and Smith [7] pioneered...”. If the reference carries the names of three or more authors it should be quoted as “Bush *et al.* [7]”, if Bush is the first author, or as “Bush and co-workers [7]”, if Bush is the senior author.

Footnotes should be reduced to a minimum. Each footnote should be typed double-spaced at the bottom of the page, on which its subject is first mentioned. **Tables** are numbered with Arabic numerals on the left-hand top. Each table should be referred to in the text. Column headings should be as short as possible but they must define units unambiguously. The units are to be separated from the preceding symbols by a comma or brackets. Note: The following format should be used when figures, equations, etc. are referred to the text (followed by the respective numbers): Fig., Eqns., Table, Scheme.

Schemes and figures. Each manuscript should contain or be accompanied by the respective illustrative material as well as by the respective figure captions in a separate file (sheet). As far as presentation of units is concerned, SI units are to be used. However, some non-SI units are also acceptable, such as °C, ml, l, etc. The author(s) name(s), the title of the manuscript, the number of drawings, photographs, diagrams, etc., should be written in black pencil on the back of the illustrative material (hard copies) in accordance with the list enclosed. Avoid using more than 6 (12 for reviews, respectively) figures in the manuscript. Since most of the illustrative materials are to be presented as 8-cm wide pictures, attention should be paid that all axis titles, numerals, legend(s) and texts are legible.

The authors are required to submit the text with a list of three individuals and their e-mail addresses that can be considered by the Editors as potential reviewers. Please, note that the reviewers should be outside the authors' own institution or organization. The Editorial Board of the journal is not obliged to accept these proposals.

The authors are asked to submit **the final text** (after the manuscript has been accepted for publication) in electronic form by e-mail. The main text, list of references, tables and figure captions should be saved in separate files (as *.rtf or *.doc) with clearly identifiable file names. It is essential that the name and version of the word-processing program and the format of the text files is clearly indicated. It is recommended that the pictures are presented in *.tif, *.jpg, *.cdr or *.bmp format.

The equations are written using "Equation Editor" and chemical reaction schemes are written using ISIS Draw or ChemDraw programme.

EXAMPLES FOR PRESENTATION OF REFERENCES

REFERENCES

1. D. S. Newsome, *Catal. Rev.–Sci. Eng.*, **21**, 275 (1980).
2. C.-H. Lin, C.-Y. Hsu, *J. Chem. Soc. Chem. Commun.*, 1479 (1992).
3. R. G. Parr, W. Yang, *Density Functional Theory of Atoms and Molecules*, Oxford Univ. Press, New York, 1989.
4. V. Ponec, G. C. Bond, *Catalysis by Metals and Alloys (Stud. Surf. Sci. Catal., vol. 95)*, Elsevier, Amsterdam, 1995.
5. G. Kadinov, S. Todorova, A. Palazov, in: *New Frontiers in Catalysis (Proc. 10th Int. Congr. Catal., Budapest, (1992)*, L. Guzzi, F. Solymosi, P. Tetenyi (eds.), Akademiai Kiado, Budapest, 1993, Part C, p. 2817.
6. G. L. C. Maire, F. Garin, in: *Catalysis. Science and Technology*, J. R. Anderson, M. Boudart (eds), vol. 6, SpringerVerlag, Berlin, 1984, p. 161.
7. D. Pocknell, *GB Patent 2 207 355* (1949).
8. G. Angelov, PhD Thesis, UCTM, Sofia, 2001, pp. 121-126.
- 9 JCPDS International Center for Diffraction Data, Power Diffraction File, Swarthmore, PA, 1991.
10. CA **127**, 184 762q (1998).
11. P. Hou, H. Wise, *J. Catal.*, in press.
12. M. Sinev, private communication.
13. <http://www.chemweb.com/alchem/articles/1051611477211.html>.

Texts with references which do not match these requirements will not be considered for publication!!!

CONTENTS

<i>F. Ghasemi, A. Naghizadeh, G. A. M. Ali, V. K. Gupta, Shilpi Agarwal, B. Mansouri</i> , Evaluation of sonocatalytic degradation of phenol in the presence of zirconium oxide and cerium oxide nanocatalysts	127
<i>J. M. Veličković, S. D. Stevanović, M. Lutovac</i> , The effect of effluent on the water quality in the Nišava	134
<i>M. Thirumalaikumar</i> , Green corrosion inhibitors in various corroding media	142
<i>M. K. Dutta, R. K. Sarkar, S. Karmakar</i> , Fabrication and characterization of CdS-Cu ₂ S thin film heterojunction diode using chemical bath deposition technique	158
<i>R. K. Yaghoobi, Masoud Khajenoori, Maryam Khajenoori</i> , Modeling and simulating of heat transfer for three-layer skin using an external thermal pulse	163
<i>K. Fattahi, M. Farahi, B. Karami, R. Keshavarz</i> , Design of sodium carbonate functionalized TiO ₂ -coated Fe ₃ O ₄ nanoparticles as a new heterogeneous catalyst for pyrrole synthesis	174
<i>M. K. Mladenov</i> , Potential of municipal solid waste generated in Bulgaria for energy production	180
<i>A. Sudan, A. Kaur, D. Gangacharyulu, R. K. Gupta</i> , Experimental and modelling studies of hydrogen generation from NaBH ₄ /Al ₂ O ₃ nanoparticles/H ₂ O system with CoCl ₂ as a catalyst	188
<i>Y. Mezari, L. Nouar, F. Madi, A. Guendouzi, I. Djellala, I. Lafifi, R. Merdes, A. Bouhadiba, B. Houari</i> , Theoretical investigation of inclusion complex of 2-methyl mercapto phenothiazine with hydroxy propyl β-cyclodextrin by DFT approaches	196
<i>S. M. Arat, B. Çamur-Elipek, B. Öterler</i> , Heavy metal accumulation of water, sediment and some organisms in the Marmara Sea (Turkey).....	211
<i>D. I. Ivanova</i> , Surface treatment of electro galvanized steel in modified zinc phosphating solutions	216
<i>S. S. Stanimirov, B. R. Todorov</i> , Simplified synthetic procedure for (Z) to (E)-cyclooct-4-enol photoisomerization	228
<i>I. Ignatov, G. Gluhchev, N. Neshev, D. Mehandjiev</i> , Structuring of water clusters depending on the energy of hydrogen bonds in electrochemically activated waters Anolyte and Catholyte	234
<i>N. T. Kochev, S. H. Tsoneva, M. V. Frenkeva, N. G. Jeliazkova</i> , Prediction of ¹ H-NMR shifts with Ambient-HNMR software	240
<i>V. F. Georgiev</i> , Preparation and thermal stability evaluation of GNP/CNT doped poly(lactic acid) and high-density polyethylene nanocomposites	249
<i>INSTRUCTIONS TO AUTHORS</i>	256